UNIVERSITAT DE BARCELONA

Inversion of multichannel seismic data by combination of travel-time and full-waveform tomography

Clàudia Gras Andreu

Aquesta tesi doctoral està subjecta a la llicència ***Reconeixement- CompartIgual 4.0. Espanya de Creative Commons***.

Esta tesis doctoral está sujeta a la licencia ***Reconocimiento - CompartirIgual 4.0. España de Creative* Commons**.

This doctoral thesis is licensed under the ***Creative Commons Attribution-ShareAlike 4.0. Spain License***.

Inversion of multichannel seismic data by combination of travel-time and full-waveform tomography

Memòria de tesi doctoral presentada per

Clàudia Gras Andreu

Per optar al Grau de Doctor per la Universitat de Barcelona

Aquesta memòria s'ha dut a terme dins del programa de doctorat de Ciències de la Terra de la Universitat de Barcelona,

sota la direcció de:

Dr. Valentí Sallarès Casas
Prof. César Rodríguez Ranero

Tutelada per:

Dr. Alejandro Marcuello Pascual

Barcelona, Setembre de 2019

No Surrender

(Bruce Springsteen)

Agraïments / Acknowledgments

M'agradaria donar les gràcies als meus directors de tesis, Valentí i César, que en aquests moments de falta d'inversió en el sector de la investigació van trobar la manera d'oferir-me la possibilitat per fer aquest doctorat. Gràcies per la confiança dipositada en les meues capacitats, les recomanacions, directrius donades, la paciència i els ànims. En especial, volia agraïr-li al Valentí la seva dedicació i esforç que han permès fer d'aquesta tesi, una versió millor.

Agraïr als membres del grup d'inversió els seus consells i propostes: Adrià, desitjo que sempre siguis tant robust com el TTT; Dani, ha estat un plaer utilitzar els teus programes, no deixis d'afegir comentaris graciosos; Slaven, el meu germà bessó acadèmic que s'ha acabat convertint com en un de veritable, i Estela, gràcies per TOT (ajuda, consells, suport... tant en el treball, com en la vida, gràcies per estar sempre al meu costat!). També dono gràcies a tots els membres que actualment formen o han format part del grup Barcelona-CSI i ICM perquè ja sempre formaran part de mi: a na Laura, tú y yo poco necesitamos para montarnoslo genial, molamos, te quiero y punto; na Marina i en Sergio, sou els meus gochos i esportistes preferits; en Miquel, ets l'artista que m'ha acompanyat i posat ritme en aquest dur camí; en Davide, gràcies per estar sempre disposat a fer la stafa; les meves girlies, Cristina, Marta i Irene, gràcies sou monísimes; els antics companys (Jhon, Albert, Guille...), les noves incorporacions (Sergio, Sergi...) i els que retornen (Manel, Jaume, Sara...); aquells que per un període curt però intens han marcat la meva vida (Laura, Pedro, Domo, Cyril, Joao, Florence, Morgan...); als meus tècnics de campanya preferits (Héctor, Marc, David...); als posdoc. i seniors del grup que tot i el seu rang superior, això no ha impedit que tinguem un tracte igualitari i d'amic (Xavi, Alci, Héctor, Rafa, Claudio...), i a tots els ICM young researchers, per il·luminar i destacar la bellesa de la ciència en la etapa final del doctorat, la de més foscor.

Vull agraïr al meu tutor de la UB (Àlex) la seva ajuda, disponibilitat i ànims, així com altres professors, en especial la Pilar, sense tu i les teves recomanacions no hagués fet cap al ICM. A més, m'agradaria donar les gràcies als meus companys d'universitat, grans genis i persones (Òscar, Fransesc, Jordi, Laia, Ricard, Rubén, Alejandro, Genís, Mariona...).

També m'agradaria agraïr sincerament el suport i ànims dels meus amics de Tortosa (Laura, Núria, Pau,...), del swimming (Carles, Raül,...), les esportistes i aventureres (Montse, Cristina, Nat...)... I en particular a la Raquel, que s'ha convertit en una part essencial de la meva vida actual, gràcies per escoltar-me, entendre'm, i inclourem sempre en els teus plans, t'estimo molt.

Gràcies a les meves companyes de pis que m'han facilitat la vida, sempre disposades a pujar-me els ànims: Blanca, ets superespecial per mi llucet, gràcies per ser com ets i apareixer a la meva vida, pels mil i un cafès a casa lolo, les nits en vela, el teu companyerisme, somriure...; Carme, gràcies per recordar-te de mi des de la guarderia, per ser espontània, directa, sincera, m'encanten les teues anades de bola i les nostres aventures, ja mai m'oblidaré de tu; Laura, gràcies per les teves abraçades sinceres, els tuppers, i la teva enegia "vinga que ja hem tumbat la tesi!"; Marina, Ened...

Finalment, vull donar les gràcies a la meva família, que tot i no entendre molt bé què és i implica fer un doctorat, sempre m'han donat tot el seu suport. En especial, gràcies als meus pares, pel seu amor, per fer-me de guia (amb bona música) i mai posar barreres al què vull fer; tot i que a vegades us faig patir, sé que sempre esteu allí, per ajudar-me i aclocar-me. I ja per rematar-ho a les meves germanes, que tant m'agrada xinxar, gràcies per aguantar-me i ser com sou, sou un orgull de germanes per a mi.

Contents

Summary

This thesis presents the implementation and application of a procedure combining different geophysical techniques to extract high-resolution information that helps characterizing the structure and properties (p-wave velocity, Vp) of the subsurface by using marine multichannel seismic (MCS) data alone. The challenge is overcoming the inherent non-linearity and non-uniqueness of inverse methods, in general, and of full-waveform inversion (FWI), in particular, which are especially critical for short-offset, band-limited seismic data. I have applied an in-house modelling workflow consisting of three steps: (1) data re-datuming or downward continuation (DC) by back-propagation of the recorded seismograms to the seafloor; (2) travel-time tomography (TTT) using the first arrivals of the re-datumed shot gathers (synthetic data), combined with those of a reflecting boundary in the original data (field data); and (3) FWI of the original shot gathers using the model obtained by TTT as initial reference. This workflow is first tested with synthetic data, and then applied to field data acquired in the Alboran Sea Basin (SE of Iberia).

Due to the relatively short source-receiver offset of 6 km and the ~2 km depth of the seafloor, refractions are identified only in a few farthermost channels as first arrivals. To solve this problem, I changed the reference datum of the data set from the sea surface to the seafloor, by implementing a DC code that uses a solver of the acoustic wave equation developed at the Barcelona-CSI (Dagnino et al., 2016). The DC code follows the steps proposed by Berryhill (1979, 1984) and the scheme of McMechan (1982, 1983). By modifying the MCS records to simulate a seafloor-type acquisition it is possible to recover refracted phases, crucial in Vp modelling, as first arrivals.

Then, I performed TTT using the travel times of the DC first arrivals to obtain a coarse, but kinematically correct, Vp model. This TTT Vp model has the correct low-wavenumber information because the waveforms simulated with the inverted model and the recorded ones are not cycle-skipped. To better constrain the result, particularly in the deep parts of the model, I have incorporated the seismic phases corresponding to a major reflecting interface (top of the basement, TOB) and performed a joint refraction and reflection TTT combining the original and the DC field data.

Finally, finer structural details are progressively introduced in the initial model by applying iterative, multi-scale FWI to the original MCS data. The results confirm that the combination of data re-datuming and TTT provides reference models that are accurate enough to apply FWI to relatively short offset streamer data in deep-water settings as the ones used here, even if records lack low frequencies (< 4 Hz). I also show that, when the initial model is not kinematically correct, the FWI falls into a local minimum.

The application of the workflow to the Alboran field data reveals a number of geological structures in the FWI Vp model that cannot be appreciated in the TTT Vp model, nor

easily interpreted based on MCS images alone. A sharp strong velocity contrast defines the geometry of an irregular TOB that includes high velocity volcano-like structures. The model clearly images steeply dipping Vp changes at the flanks of the basin that appear to correspond to faults. Moreover, it displays a 200–300 m thick high-velocity layer that could probably correspond to evaporites deposited during the Messinian crisis in the Mediterranean. The result is validated by comparing the two-way time-transformed Vp model and the time-migrated MCS image, showing that velocity changes coincide with major reflectivity contrasts.

In summary, this study shows that by using an appropriate workflow, in our case including DC of MCS data to the seafloor, joint refraction and reflection TTT, and FWI, accurate, geologically meaningful Vp models can be obtained even for sub-optimal data sets. In particular, our results provide information that improves the geological characterization and interpretation of the subsurface structure of the Alboran Basin. The main results are presented in Gras et al. (in press).

In order to present the results in a clear structure, I organized this volume in six parts that follow the Motivation and Working hypothesis sections. The Motivation section shows the characteristics, benefits and drawbacks, of the seismic data sets and inverse methods to obtain high-resolution information of the medium of interest. Then, the Working hypothesis exposes the evidences and our ideas to tackle the above-mentioned issues, which in our case is a strategy that combines a suite of processing and modelling techniques. Part I is the introductory section. Chapter 1 briefly describes the main geophysical techniques and its potential to recover subsurface information. One of the most powerful tools is the seismic method, which it is the one used in this thesis. Chapter 2 is devoted to describe the fundamentals of the seismic exploration methods. Part II describes the objectives, which are listed in Chapter 3. During this thesis, I had to design, implement, and apply the above-described in-house modelling sequence. That leads to part III, in which each of these methods is presented. Chapter 4 describes the DC, and Chapter 5, the tomographic techniques (TTT and FWI). The aim of part IV is to expose the results. Chapter 6 presents the synthetic tests (target models and acquisition settings). Chapter 7 shows the synthetic result after applying DC. In Chapter 8 I present the TTT models recovered using the first arrivals of the synthetic DC results obtained in Chapter 7. Chapter 9 displays the FWI results for the synthetic tests, emphasizing the importance of building a kinematically correct initial model. Then, Chapter 10 presents the application of the whole strategy to field data, acquired in this case in the Alboran Basin (SE Iberia). Part V includes the discussion (Chapter 11), which is focused on the assessment of the procedure implemented by evaluating the DC shot gathers, TTT, and FWI models, as well as the geological analysis of the final high-resolution Vp model shown in Chapter 10. Finally, part VI includes the conclusions (Chapter 12) and the forward look (Chapter 13).

Motivation

Seismic tomography techniques are one of the most powerful tools to obtain information on the geological structure and physical properties of the Earth's subsurface. These techniques use seismic recordings as input to extract subsurface distribution of physical properties, generally P-wave velocity (Vp) or, less frequently, other parameters of interest (S-wave velocity, density, anisotropy, attenuation, etc.). Modelling techniques, and particularly inverse methods, have limitations to retrieve accurate models of the complex reality that depend on both the method itself and on the type of data used. A well-known example concerns the usage of a few km long offset (3-9 km), relatively high-frequency (~4-60 Hz) streamer data acquired with conventional marine multichannel seismic (MCS) systems. In this case, the combination of the lack of both first arrival refracted waves and low-frequency components in the seismic records make it difficult to apply the most common seismic tomography techniques.

Traditionally, studies designed for tomography work use long offset data sets, particularly those acquired with wide-angle reflection and refraction (WAS) acquisition settings, where the source-receiver distance can be as large (often tens to > hundred km) as required for the target (e.g. as in offshore ocean bottom seismometer (OBS) surveys). The large offsets of the WAS acquisitions allow to record refracted phases as first arrivals (i.e. beyond the critical distance) so that they can be used in the inversion, either alone or combined with wide-angle reflections. This is highly relevant, because while reflection travel times depend on both velocity field and reflector location (so there is an intrinsic trade-off between these two parameters), refraction travel times depend uniquely on the velocity field, so they are the best suited to provide accurate Vp information. Therefore, including first arrival travel times in the inversion helps improving the accuracy of the retrieved Vp model and reducing, in turn, the velocity-depth trade-off. In contrast, the length of the streamer limits the maximum offset in marine MCS systems, which is of 10-15 km at most with current equipment, but typically <6 km. This makes that in >~1-2 km deep water environments refractions are not usually recorded as coherent first arrivals, because the critical emerging distance is beyond the streamer length. Therefore, Vp models for MCS data, which are needed to depth image the record sections and hence recovering the correct geometry and location of the seismic reflectors, are constructed through velocity analysis based on reflection travel times alone. These models are therefore of low resolution and are subject to intrinsic uncertainty due to the velocity-depth trade-off of reflections.

This situation poses a severe problem to apply state-of-the-art tomography techniques such as full-waveform inversion (FWI), to MCS data. While FWI has proved to be a powerful technique that allows producing Vp models with a resolution of up to one order of magnitude better than travel time-based ones, it is an inherently non-linear technique. This means that successful FWI through gradient-based approaches is subject to many factors, and in particular, to the availability of an initial Vp model that is "kinematically correct", in the sense that the simulated seismograms are not cycle-skipped with respect to the real data (i.e. they are out of phase by less than half a cycle). Experience indicates that reflection travel time-based Vp models require a comparatively large amount of detailed work to satisfy this condition and of rapidly decreasing resolution in depth, whereas refraction travel time-based ones are generally more accurate and less time-consuming. It must also be noted that MCS data normally lack low-frequency signal (no signal below ~4-5 Hz), which exacerbates the problem of cycle skipping for FWI, thus the need to obtain an accurate initial Vp model by other means. This situation is however paradoxical, because the spatial sampling and data redundancy of MCS data is higher than that of WAS acquisition systems, so that the potential resolution of their Vp models is higher. Finding a robust and time-efficient way to modify the MCS

data so that refractions appear as first arrivals in the shot gathers, and hence tomography methods (including travel time- and waveform-based approaches) can be applied, stands as a first order challenge on the utilization of streamer seismic data.

The main motivation of this work is to explore and develop a methodological approach combining state-of-the-art processing and modelling techniques that allow overcoming the above-mentioned issues, and to test it with synthetic and real MCS streamer data.

As above-mentioned, having a correct Vp model is essential to depth-imaging of record sections and to obtain the real geometry of the seismic reflectors. The data migration from time to depth is key to an improved image of the subsurface structure and, ultimately, to produce the correct geological interpretation. Models that are more accurate reduce the number of artefacts and improve the definition of contacts, discontinuities, faults and rock bodies (sedimentary and not sedimentary). The knowledge of the location and geometry of geological boundaries and their reflections below and above are crucial to reconstruct the geological evolution of the area. Besides the structural information contained in seismic reflections, Vp provides additional information on rock properties, which can be used to determine lithology, porosity and/or fluid content. Therefore, building a reliable and accurate Vp model is crucial to characterize geologically the studied area and evaluate its potential seismic hazard.

With the above-mentioned motivation in mind, I have investigated possible methodologies for MCS streamer data so that they can be used as input for seismic tomography techniques and produce high-quality Vp models in a pseudo-automatic way. The strategy, steps and technical details of the proposed workflow combines data processing or re-datuming techniques, joint refraction and reflection travel-time inversion and adjoint full-waveform inversion (FWI) using codes developed and implemented at the Barcelona-CSI, and are described in the next chapters.

Working hypothesis

As stated in the Motivation section, the main goal of my thesis is to develop a strategy to overcome the major issues related with limited-offset acquisition geometry and lack of low-frequency content in streamer MCS data, so that we are able to apply seismic tomography techniques to obtain high-resolution Vp models of the surveyed area in a pseudo-automatic way.

Our working hypothesis is that it is possible overcame the main issues by applying a three-step workflow that combines a suite of processing and modelling techniques. The first step is the back-propagation of the recorded wave field so that we simulate a seafloor acquisition geometry of receivers and source in which first arrivals are visible from zero offset to the end of the streamer. Second, applying travel-time tomography (TTT) to recover a coarse, but kinematically correct, Vp model. Third, incorporating high-resolution Vp details on the TTT result by applying FWI.

This hypothesis is based on our and other group's previous experience using TTT and FWI codes, and on the knowledge of their advantages and drawbacks. The rationale of our hypothesis is the following:

A first evidence is that FWI requires an accurate starting Vp model that allows overcoming cycle skipping at the lowest available frequency, typically 4-5 Hz in field data sets. However, this model cannot efficiently be obtained applying common forward velocity analysis techniques using seismic reflection data. Then, it is convenient to find an alternative that exploits the information available in the recorded wave field to construct this initial model.

A second evidence is several published works showing that the best suited initial models for FWI are typically those constructed by TTT of refracted (and eventually reflected) phases. However, as stated previously no refractions are commonly visible in limited-offset MCS acquisition geometries (especially in deep water settings), so conventional TTT cannot be easily and efficiently applied to the recorded seismic data.

Thus, the main goal of my working hypothesis is that we should be able to apply robust TTT followed by FWI to streamer MCS data, provided that we find an accurate way for unraveling the refracted waves present in the seismic records, but obscured by the higher amplitude reflections.

In other words, MCS systems are designed to obtain images of the Earth's subsurface but, as they are based on reflected arrivals alone, are affected by velocity-depth trade-off and are not well-suited to obtain Vp information, so Vp models are tedious of constructing and can potentially have significant errors due to offset limitations. Therefore, if this model is used as a initial of FWI, the Vp uncertainty intrinsic to the initial model can produce strong artefacts in the inverted model. The idea is mitigating this situation using refracted phases, because they depend only on the Vp field. If refractions are included as input, then we should be able to recover a coarse, but kinematically correct, background Vp model that will help overcoming the non-linearity issues of FWI. Afterwards, finer structural details will be sequentially incorporated in the model following a hierarchical multi-scale FWI strategy. Such a strategy should provide a Vp model approaching the resolution of seismic reflection images and thus noticeably improving the geological interpretation in terms of physical properties and lithology.

The key problem is thus the lack of first arrivals in the limited-offset records. In this case, the fact is

that this information exists in the recordings, but it is encoded and hidden by more energetic reflected phases in deep water environments. These encoded refractions should be extracted as first arrivals in the shot gathers by means of wave field propagation techniques. The critical emerging distance, in which refractions start arriving before reflections at the receiver positions, can be reduced by re-datuming the recorded wave field to the seafloor level. The extrapolation of the seismic wave field to another surface, closer or at the seafloor itself so that the effect of the water column is eliminated, is the key in the workflow to unravel refraction travel times.

In summary, our hypothesis can be tested as follows: 1) extract the refractions of the shallow subsurface by re-datuming the MCS data to the seafloor, 2) carry out TTT to obtain a kinematically correct model that allows overcoming the velocity-depth trade-off of the reflection-based Vp models. This result will be an appropriate initial model for FWI, making the inversion well-posed and allowing to retrieve a realistic Vp model. 3) FWI to provide a detailed model of the structure and properties of the subsurface.

Part I

INTRODUCTION

Is there anybody alive
out there?!

(Bruce Springsteen)

Chapter 1. Geophysical methods

Geophysical techniques study the structure and properties of the subsurface on land and offshore at different resolution and depth using observables and indirect measurements normally acquired with non-destructive, remote sensing methods. Therefore, these kind of data sets allow the construction of a hand or computer generated model to interpret the nature and physical properties of rocks under the ground.

These techniques allow covering extensive areas in a faster and more economical way than *in situ* methods such as excavations or perforations. Usually, in petroleum exploration geophysical information is used together with *in situ* measurements such as core samples or logging data to better assess the reservoir location and its properties (e.g. porosity) before drilling.

Therefore, geophysical methods aim at characterizing the physical properties of rocks and minerals. Some examples of the most typical physical fields modelled currently are the gravitational, magnetic, electrical, electromagnetic and seismic wave fields. The methods that use measures of these fields to extract meaningful information of rock properties are described in the next sections of this chapter.

Gravity method

The gravity method is useful to infer the rock density (mass "δm" per unit volume "δx'δy'δz'") distribution of the subsurface. As gravity (g) is directly proportional to the distribution of the masses in the Earth, it is also directly related with density (ρ).

$$\Delta g = Gmz/r^3 \quad \rightarrow \quad \delta g = G\rho\left(z'-z\right)\delta x'\delta y'\delta z'/r^3 \quad (1.1)$$

This equation describes the attraction δg at a point outside the body (x,y,z), at a distance r from the element. Where G is the universal Gravitational Constant ($6.67\text{x}10^{-11} m^3 kg^{-1} s^{-2}$).

This method is characterized for being a fast and cheap technique. However, the resulting model has a relatively poor resolution and depth definition, and its interpretation is inherently ambiguous if gravitational information is used alone. Map density variations is valuable when it is combined with other techniques, such as seismic methods. This density information adds to other constraints coming from complementary methods such as crustal thickness, velocity and porosity, i.e. the petrological nature of the rocks. Usually, empirically-derived relationships of density as a function of other physical properties such as Vp of the rocks, and vice versa, are used to combine different data sets

and explain them with a single structural model (Brocher, T. M., 2005; Mavko, et al., 1998) (Fig. 1.1). Therefore, if the velocity distribution of the surveyed area is available, it can be converted to density assumed a given lithology and compared to the observations to check the validity of the assumptions/interpretations within parameter uncertainty bounds.

The acceleration of gravity is the observable measured by a gravimeter (Fig. 1.2). This instrument must be located over the target area at different positions spaced from a few meters in the case of detailed studies to several kilometers in regional surveys. In marine experiments, the stations are on a vessel so they must be stabilized from its movements.

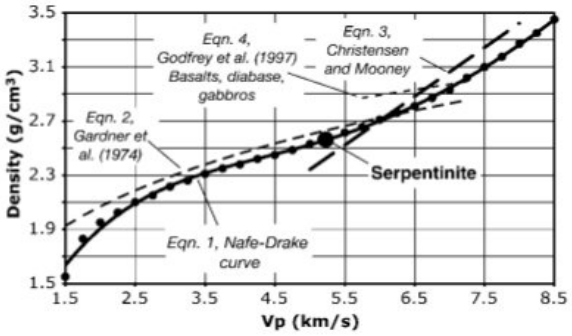

Figure 1.1: Comparison of published density versus Vp relations used compiled by Brocher, T. M. (2005). Filled circles show handpicked values from the curve published by Ludwig et al. (1970). Solid line corresponds to the Nafe-Drake curve (Ludwig et al.,1970) which shows a polynomial regression to these picks. This function is valid for all rocks excepting mafic crustal and calcium-rich rocks. Other lines show more relations for other types of rocks, Gardner et al. (1974) for sedimentary rocks, Christensen and Mooney (1995) for crystalline rocks and Godfrey et al. (1997) for basalt, diabase, and gabbro.

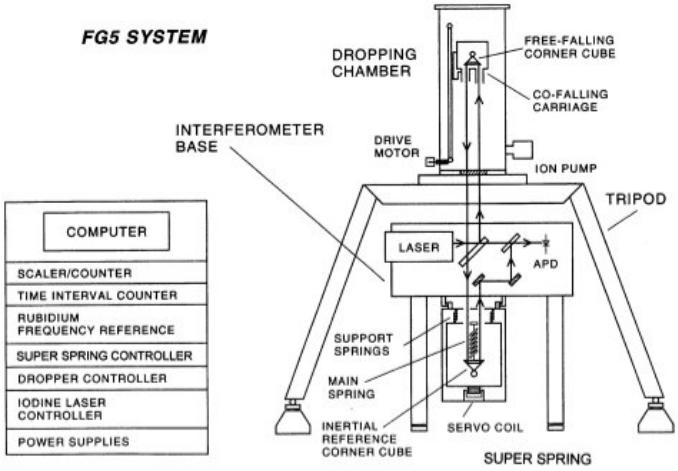

Figure 1.2: Schematic diagram of key systems in the FG5 absolute gravimeter (Niebauer, et al., 1995). This absolute gravimeter employ laser interferometers that measure the free-fall trajectory of an optical element within a vacuum chamber.

The gravity varies not only with rock densities, but also with elevation, latitude and topography. Thus, the raw observations (g_{obs}) must be corrected for the other effects to obtain the rock density distribution. In offshore experiments, the corrections that have to be applied come from sea level changes and variations on heading, speed and gyro of the ship. Once the values are corrected a residual gravity is obtained (Fig. 1.3 a). The gravity at sea level is about 980 cm/s^2 (Gadallah, et al., 2009), whilst residual gravity values are of the orders of 0.01 cm/s^2. Then, the units used for the residual gravity are the milligal (mgal), and it is equivalent to 0.001 cm/s^2, or the gravity unit (gu), and it is equivalent to 0.0001 cm/s^2. Gravimeters can detect changes of ± 10 - 0.1 gu depending on the survey characteristics.

$$BA = g_{obs} - g_{lat} + FAC \pm BC + TC(\pm EC) \quad (1.2)$$

Where BA corresponds to the Bouger anomaly, g_{lat} is the gravity to latitude on the reference spheroid at the recording point, FAC is the free-air correction, BC is the Bouguer correction, TC is the tidal correction and EC is the Eötvös correction which is taken on a moving vehicle.

A rock unit of different density from its surroundings will produce a variation in the residual gravity. If we represent the residual gravity at each station location, then contours of equal values can be displayed showing the distribution of the gravity anomalies over the surveyed area (Fig. 1.3 b). Using that image of lateral and vertical variations in density one can infer location and properties of subsurface geologic structures by forward or inverse modelling. Therefore, the shape and size of the resultant gravity anomalies are compared to the ones generated by Earth models of different rock distributions. These models are obtained changing the geometrical shapes of the subsurface layers, depths and densities. The gravity anomaly will be positive or negative depending on whether the body is more or less dense than its surroundings. There are some codes to calculate the gravity anomaly of the different models, such as the ones used by Li and Chouteau (1998), Farquharson and Mosher (2009), Xu and Chen (2018), among others for direct modelling and *grav2d* (Korenaga, et al., 2001) for inverse modelling. As mentioned, this method is often complemented with the available external constraints, because the inverse problem of potential field interpretation is not univocal and a wide range of geological models can explain to the observed gravity anomalies.

(a) (b)

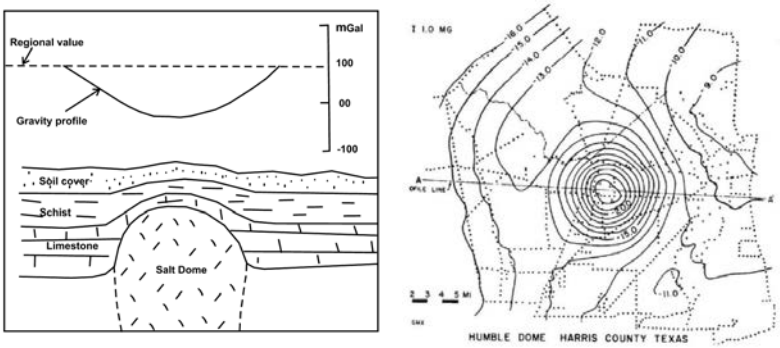

Figure 1.3: (a) Residual gravity profile across a buried salt dome showing lower density compared to the surrounding country rocks (Haldar, 2013). (b) Gravity map example where the gravity anomaly values are displayed and contoured over the surveyed area (Gadallah, et al., 2009). Gravity decreases due to the presence of a humble dome.

Magnetic method

The magnetic method is useful to provide the magnetic susceptibility distribution of the subsurface. This technique is widely employed because can be performed on land, at sea and from the air. Additionally, as gravity surveying, it is also a fast and cost-effective geophysical technique. However, as in the case of gravitational and other potential field methods, the derived models of physical properties have poor resolution and depth definition, and it is not usually possible to identify with certainty the causative lithology from magnetic information alone (Kearey, et al., 2002). Generally, the information of the horizontal magnetic variations in susceptibility are very useful in mapping the basement composed by igneous or metamorphic rocks, and locating intrusions into sediments, such as dykes, lava flows..., or ferromagnetic mineral deposits. Historically, magnetic surveying has helped in the understanding of the formation of oceanic lithosphere, and thus the development of the plate tectonic theory.

The intensity or field strength of the magnetic field (B) (Fig. 1.4 a, and b) is the observable of this method.

$$B=\mu_0 m/\left(4\pi \mu_R r^2\right) \quad (1.3)$$

Where, μ_0 is the constant corresponding to the magnetic permeability of vacuum, μ_R is the relative magnetic permeability of the medium separating the poles, and m is the magnetic pole strength at a distance r.

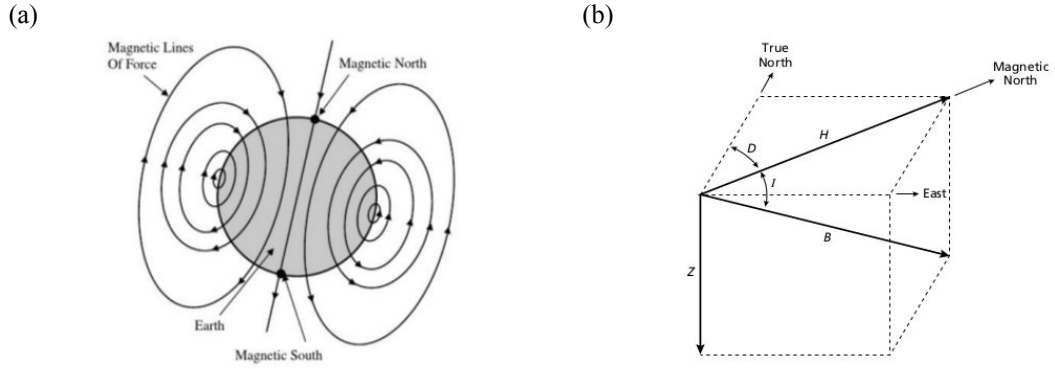

Figure 1.4: (a) Lines of force caused by the Earth's magnetic field (Gadallah, et al., 2009). (b) Orientation of the geomagnetic field (B) at a particular point on the Earth's surface, where Z and H are the vertical and horizontal components respectively, D is the declination and I is the inclination (Kearey, et al., 2002).

The magnetic field is measured by a magnetometer (Fig. 1.5). The sensor does not have to be accurately oriented. Consequently, this instrument is often located at airplanes

recording continuously the magnetic field through predefined paths over the studied area. Marine surveying is slower than aeromagnetic surveying, but is frequently carried out together with other geophysical methods.

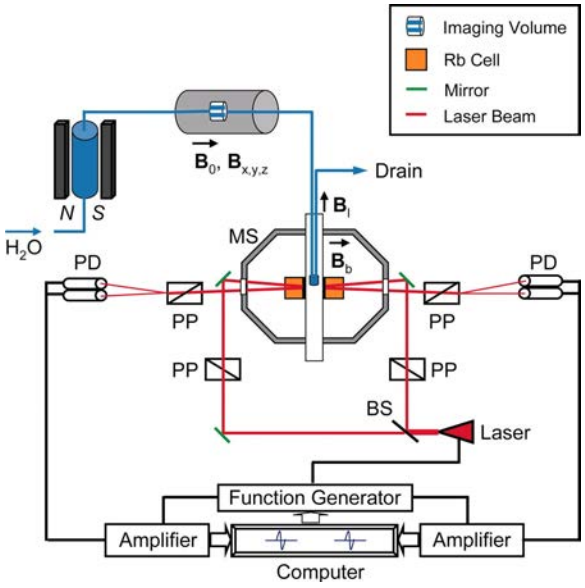

Figure 1.5: Schematic of the experimental set-up (Xu, et al., 2006). This instrument is an example of one type of magnetometer that measures the earth's magnetic field at a specific location. Typically, the magnetometers measure the induced electromagnetic field in a closed conducting coil, but this device consists of two rubidium vapor cells forming a first-order gradiometer. The cells are cubic, with a 1-cm side length, and maintained at 43ºC. The beam from a single laser (whose wavelength is resonant with the rubidium D1 transition) is split equally into two, one for each cell. For each arm of the gradiometer, polarizing and analyzing prisms are oriented at 45º to each other to detect optical rotation occurring in the vapor cell. The intrinsic resonance linewidth is ≈5 Hz. A piercing solenoid provides a 0.05-mT leading field (Bl). The geometry is such that the rubidium atoms are not subject to this field. A bias field of 70 nT (Bb) gives a resonance frequency of ≈1000 Hz for the modulation of the laser when no sample is introduced. The magnetometer measures the magnetic field change along the direction of the bias field. The magnetized sample in the detection region produces magnetic fields of opposite direction in the two cells. The frequency of magneto-optical resonance on one arm of the gradiometer is fed back to the laser modulation to maintain this arm on resonance. Thus the optical rotation in the other cell represents the difference field between the two cells, equal to twice the magnetic field produced by the sample. N, north pole; S, south pole; PD, photo diode; PP, polarization prism; MS, magnetic shield; BS, beam splitter.

The magnetic field recorded varies not only locally due to the subsurface minerals, but also due to the geomagnetic field. This field depends on the location of the Earth's surface where the field is measured, the secular variation, which is periodic and it is produced as a result of the shifting of the magnetic poles, and other annual, diurnal, or daily variations, caused by the influence of the Sun and Moon. Thus, the reduction of magnetic raw observations is necessary to remove all these effects and thus obtain the magnetic susceptibility distribution alone. Once the values are corrected a residual field is obtained (Fig. 1.6 a). The magnetic field is measured in Tesla (T), whilst the residual field is about

six up to nine orders of magnitude lower. Then, the unit used for the residual magnetic field is the nanoTesla (nT) or gammas (γ), and it is equivalent to 10^{-9} T. Generally, the total magnetic field measurements accurate to ±0.1 nT.

If the values of the residual magnetic field are represented on a map, then contours of equal values can be displayed showing the distribution of the magnetic anomalies over the surveyed area (Fig. 1.6 b). Using that image of lateral and vertical variations in magnetic susceptibility one can infer location and shape local ferromagnetic bodies or changes in depth to the basement. Sediment-covered areas with relatively deep basements are typically represented by smooth magnetic contours, whilst igneous and metamorphic regions often display patterns that are more complex.

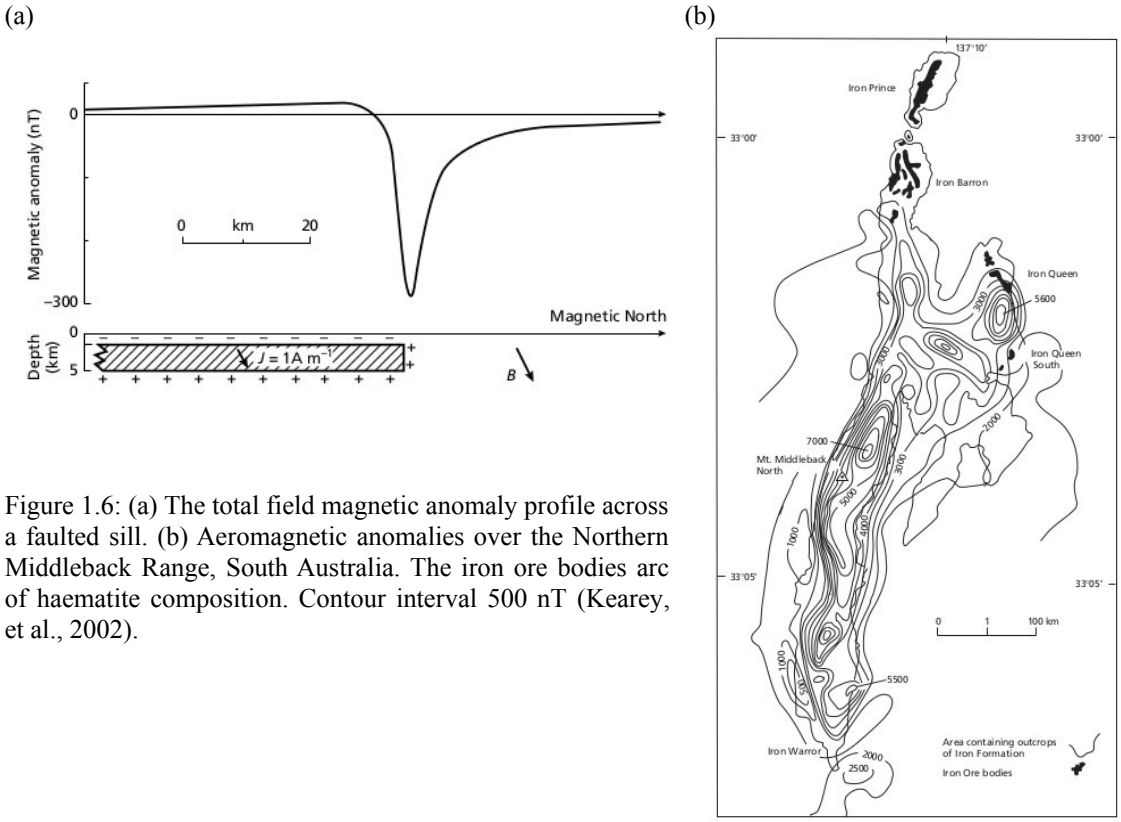

Figure 1.6: (a) The total field magnetic anomaly profile across a faulted sill. (b) Aeromagnetic anomalies over the Northern Middleback Range, South Australia. The iron ore bodies arc of haematite composition. Contour interval 500 nT (Kearey, et al., 2002).

Forward or inverse modelling techniques are used to explain the shape and size of the resulting magnetic anomalies. Observed anomalies are then compared to the ones generated by Earth models of different rock types and also different amount, size, shape and distribution of ferrimagnetic minerals in each rock type. The fact that the intensity of magnetization is a vector highly increases the complexity of the process to find the correct model. Thus, the ambiguity related to the non-uniqueness of the solution that characterizes the inverse problem is also encountered here. For this reason, this method, as most potential field ones, has to be also complemented by additional constraints from other method (e.g. seismic ones).

Electrical method

The electrical methods utilize direct currents or low-frequency alternating currents to investigate the ability to conduct electricity over a target area. Inside electrical methods there are three different branches depending on the origin of the electrical current and their response to the subsurface rocks under investigation: the resistivity method, induced polarization (IP) method and self-potential (SP) method. An example of their different responses is shown in Fig. 1.7. The electrical methods in general are well-suited to investigate the shallow subsurface geology, and therefore they are widely used in engineering and hydrogeological investigations tracking the subsurface water table and locating water-bearing sands, among other applications.

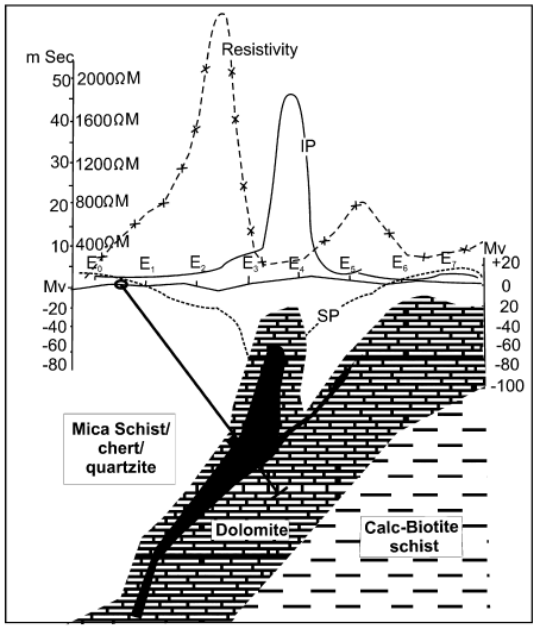

Figure 1.7: Geophysical interpretation of SP, IP and resistivity survey and confirmed by drill testing of rich sulfide orebody in Rajasthan. E0, E1, E2 … are measurement points on survey lines across the expected causative body (Haldar, 2013).

Resistivity

In the resistivity method, artificially-generated electrical currents are introduced into the ground to study the horizontal and vertical discontinuities and detect bodies of anomalous electrical conductivity (Fig. 1.8). Resistivity is one of the most variable physical properties of rocks, thus identification of a rock type is not possible using this data alone. Resistivity is closely related with porosity because most rocks conduct electricity by electrolytic processes, and generally increases as porosity decreases. Thus, it is widely employed in hydrogeological applications.

The resistivity of the ground (ρ), that is, the ratio of the potential difference (δV) between

two electrodes and the power of the current injected (I),

$$\delta V/\delta L = -\rho I/\delta A \quad (1.4)$$

where, δA is the cross-section area and δL the length of the conductor. The resistance is the observable measured by a resistivity meter. Moreover, the instrument can measure the resistance of the electrodes when there is no current flowing to correct the effect of contact resistance of the electrodes with the ground. The SI unit of resistivity is the ohm-metre (Ωm).

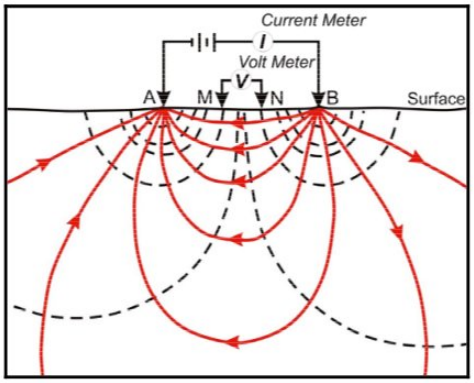

Figure 1.8: Schematic illustration of the resistivity method in which artificially electrical current is introduced into the ground to then measure the resulting potential difference with a volt meter at the surface. Solid red lines represent current flow. Dashed black lines contour electrical potential (voltage). (Clark and Page, 2011).

The resulting potential difference measured at the surface with different electrode separations give information on the form and electrical properties of subsurface inhomogeneities. The apparent resistivity is computed from the potential difference, the current introduced and the electrode configuration (Telford, et al., 2004). The depth of the experiment depends on the separation of the current electrodes and the power injected. As much separation and lower is the frequency of the current, deeper is the current penetration. The practical depth limit for most surveys is about 1 km.

Depending on the electrode configuration, which characterize the lateral and depth sampling of a survey, two main different procedures in resistivity methods exist, namely vertical electrical sounding (VES) and constant separation traversing (CST) systems. While VES is used to map horizontal interfaces, CST systems determine lateral variations of resistivity. The main difference between them are the electrode separation, in CST systems are constant, whilst in VES increases gradually.

An example of measured apparent resistivity values from a sounding survey is shown in Fig. 1.7. Interpretation of data from 1-D profiling surveys is mainly qualitative. However, it is commonly used due to the lack of proper field equipment to carry out the more data

intensive 2-D and 3-D surveys, and the lack of high performance computing tools. A more accurate model of the subsurface is a two-dimensional (2-D) model where the resistivity changes in the vertical direction, as well as in the horizontal direction along the survey line (Loke, 2001). The costs of a typical 2-D survey could be several times higher than the costs of a 1-D sounding survey. Figure 1.9 shows the typical set-up for a 2-D survey with a number of electrodes along a straight line attached to a multi-core cable.

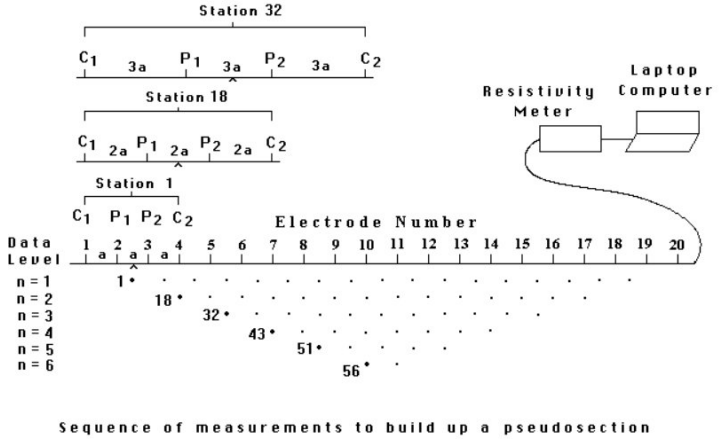

Figure 1.9: The arrangement of electrodes for a 2-D electrical survey and the sequence of measurements used to build up a pseudosection for the Wenner electrode array for a system with 20 electrodes (Loke, 2001). The spacing between adjacent electrodes is "a". The first step is to make the measurements with an electrode spacing of "1a". Electrode 1 is used as the first current electrode C1, electrode 2 as the first potential electrode P1, electrode 3 as the second potential electrode P2 and electrode 4 as the second current electrode C2. For the second measurement, electrodes number 2, 3, 4 and 5 are used for C1, P1, P2 and C2 respectively. The total number of electric measurements with a system of 20 electrodes is 17. The next step in order to obtain deeper information is increase the electrode spacing to "2a". Thus, electrodes 1, 3, 5 and 7 are used for C1, P1, P2 and C2 respectively for the first measurement. This process is repeated down the line and for measurements with increasing spacings.

The interpretation of 2-D data surveys provides a cross-section of the studied area limited to simple structural configurations of zones of different resistivity values (Fig. 1.10). The interpretation of the resulting models is complex and, as it involves a potential field, ambiguous. Indirect interpretations follow the same modelling principles as for gravity and magnetic fields, in which simulated observations are compared with the recorded ones and the model properties are varied until a good match is obtained. Non-uniqueness of solution is also a problem in this case, there is more than one model that can give the same resistivity curve. The models generated can differ in the location, shape and resistivity of the bodies. Possible errors arise from undetected layers masked by noise, irregular-shaped bodies, discontinuities, topography, near-surface resistivity variations, etc. Consequently, independent geophysical and geological controls are necessary to discriminate between valid alternative interpretations of the resistivity data.

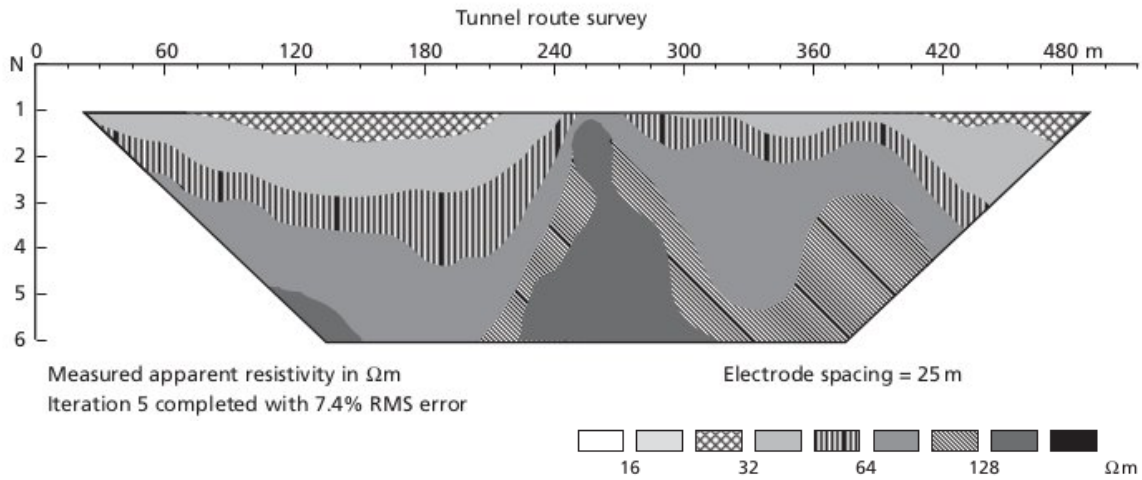

Figure 1.10: Example of electrical imaging or electrical tomography illustrating a contoured apparent resistivity pseudosection along the route of a proposed tunnel (Kearey, et al., 2002). The data was acquired using an electrode spacing of 25 m. Different apparent resistivity areas are represented with different gray patterns. The pseudosection shown is obtained after 5 iterations inverting VES data into a full, two-dimensional geoelectric model. The final RMS error is 7.4%.

Induced Polarization

The IP method measures the capacitive action of the subsurface to locate zones where conductive minerals are disseminated within their host rocks. Unlike resistivity methods, the IP technique distinguishes chargeable and non-chargeable bodies, even if both are similarly conductive. The electrical energy is stored in rocks mainly by electrochemical processes. One of the processes is known as membrane polarization or electrolytic polarization, and it is based on the electrolytic flow in the pore fluid. The other is named electrode polarization or overvoltage and it appears in all minerals that are good conductors. In particular, the latter is interesting in prospecting applications for metallic ores.

The capacity property of the ground can be investigated by using two different survey methods. The time-domain IP surveying is the one that measures a decaying voltage (ΔV_c) over a certain time interval ($t_1 - t_2$) (Fig. 1.11). In this case, the apparent chargeability (M) is the parameter measured in milliseconds (ms).

$$M = A/\Delta V_c \quad (1.5)$$

Where, A is the area beneath the decay curve (Fig. 1.11).

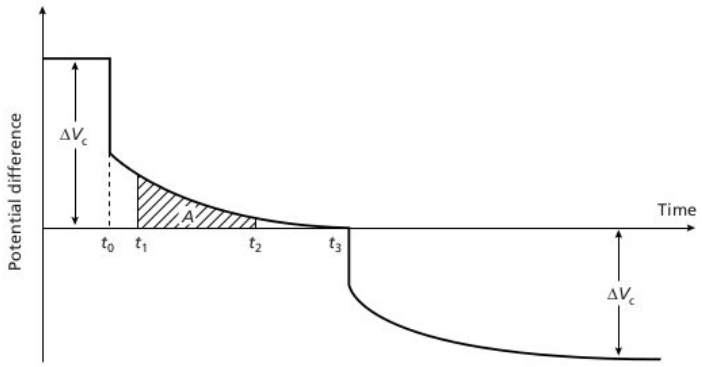

Figure 1.11: The phenomenon of induced polarization (Kearey, et al., 2002). At time t_0 the current is switched off and the measured potential difference, after an initial large drop from the steady-state value ΔV_c, decays gradually to zero. A similar sequence occurs when the current is switched on at a time t_3. A represents the area under the decay curve for the time increment $t_1 - t_2$.

On the other hand, the frequency-domain IP surveying measures the apparent resistivity at two or more low alternate currents frequencies (Kearey, et al., 2002). The instrument used is similar to the resistivity meter but more powerful to inject higher intensity currents.

A pseudosection is usually displayed presenting the IP measurements of the profile with depth. Measured values are plotted at the intersections of lines sloping at 45º from the centres of the potential and current electrode pairs. According to this way of data representation, the dip of the anomalies displayed can present variations and not be the exact one. Much IP interpretations have to be used to provide an estimate of the anomalies distribution, so mostly qualitative information. This method is poorly efficient because despite slow field operations and considerable survey costs, it does not give reliable results of economic importance for most applications. One exception is base metal exploration where the IP method is extensively used in due to the strong IP response of buried metal deposits.

Self-potential

The self-potential or spontaneous polarization (SP) is the ability to generate an electrical voltage. In the self-potential method, natural currents flowing in the ground that are generated by electrochemical processes are measured to locate shallow bodies of anomalous electrical conductivity (Fig. 1.12). The self-potential method was the first electrical method used for mineral exploration and is still used therein. In the oil industry, SP is used in boreholes to find porous zones, which is where the oil can exist. Because of the limited depth of investigation of SP methods (30 m) and the fact that other

geophysical techniques can give more information of the area, nowadays SP is being less used.

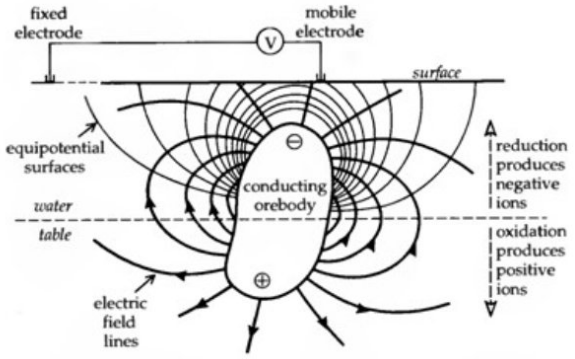

Figure 1.12: A schematic model of the origin of the self-potential anomaly of an orebody. The mechanism depends on differences in oxidation potential above and below the water table. The electric voltage is measured at the surface with a pair of non-polarizing electrodes. (Lowrie, 1997).

The instrument to measure the SP of the ground consists of a pair of non-polarizing electrodes, generally separated less than 30 m, connected via a high-impedance millivoltmeter. Thus, the SP anomalies are expressed as millivolts (mV) in SI units. The SP anomaly is negative with a magnitude over hundred millivolts with respect to background and it is stable over long periods (Fig. 1.7). As the previously mentioned potential field methods, the SP also provides a qualitative interpretation of the subsurface anomalies distribution over the target area but lacks resolution and definition of depth and boundaries of the different bodies. Although, it is a useful method in rapid ground reconnaissance for base metal deposits when used in conjunction with other geophysical techniques.

Electromagnetic method

In contrast to the electric methods presented above, the electromagnetic (EM) methods utilize alternating electromagnetic fields of higher frequency to retrieve the electrical conductivity and inductance distribution over a surface area. Some examples of electromagnetic radiation used in these methods are radar, radio waves and infrared radiation.

In the presence of a conducting body, the magnetic component of the electromagnetic field penetrating the ground induces alternating currents, or eddy currents, to flow in the conductor. The eddy currents generate their own secondary electromagnetic field which travels to the receiver (Fig. 1.13). Thus, electromagnetic fields of the source and the ones generated by the conductors arrive at the receiver. The difference between both EM fields reflect the presence of the conductor and provide information on its location, shape and electrical properties.

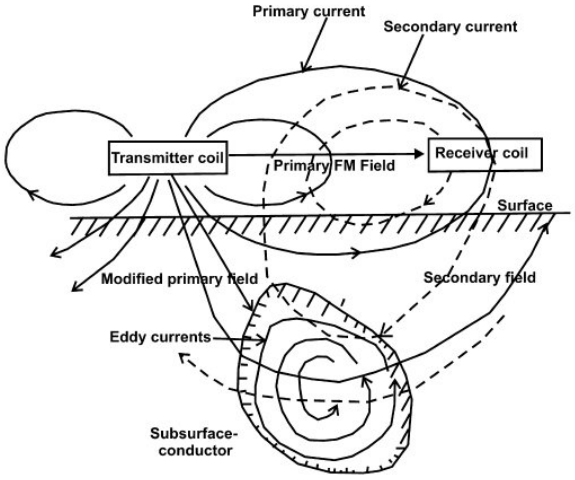

Figure 1.13: Conceptual diagram of electromagnetic induction processing system generating eddy currents in subsurface conductive mass, showing the EM surveying. (Haldar, 2013).

The detection of conducting bodies can be done through the angular deviation or tilt-angle measurements between transmitter and receiver electromagnetic fields (Fig. 1.14). More sophisticated EM surveying systems measure the phase and amplitude relationships between primary, secondary and resultant EM fields.

An additional advantage of EM methods versus electrical ones is that EM instruments do not need ground contact of either transmitter or receiver, for this reason EM methods have a faster field operation than electrical surveys, where electrodes must be introduced into the ground. Therefore, EM methods, as the magnetic ones, can be performed on land, at sea and in the air. In the EM measurements the orientation and position of the instruments has to be constant and very well defined unless only phase shifts are considered.

The results are difficult to interpret, the theoretical computations are quite complex and limited to simple geometric shapes. As the rest of geophysical methods described above, just a qualitative interpretation of EM anomalies is usually performed. Contour maps of real or imaginary components provide information on the length and conductivity of conductors while asymmetry of the profiles provides an estimate of the inclination of the bodies. The depth of penetration increases as both the frequency of the electromagnetic field and the conductivity of the ground decrease. The depth of investigation is maximum about half the transmitter-receiver separation. The typical penetration depth is of the order of 500 m and 50 m in airborne work. However, it can be limited and lower in the presence of shallow high conductivity layers. This technique is useful in the location of conducting ore bodies and also to geological mapping and hydrogeological studies, for example detecting near surface features such as ancient rivers.

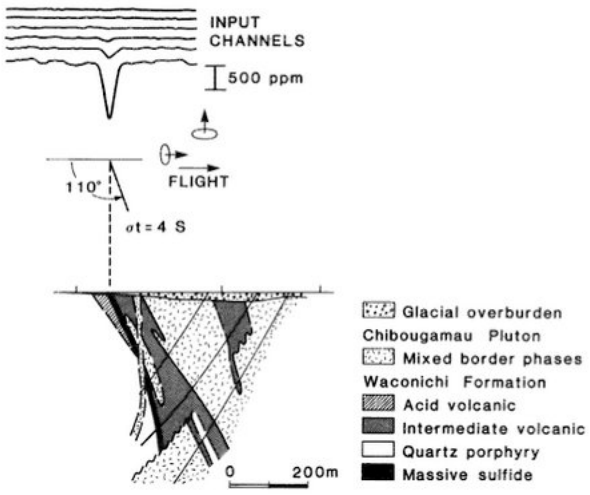

Figure 1.14: Geologic section and Input Airborne Electromagnetics response of the Scott Zn-Ag-Cu volcanic-associated massive sulfide deposit (Nabighian, et al., 1988). The Scott orebody is located 20 km of Chibougamau, Québec, Canada, in a Precambrian greenstone belt. It was descobered as a result of an Airborne Electromagnetics survey (after Questor Surveys, 1984). Massive sulfides occur at the contact of felsic and intermediate volcanic rocks of the Waconichi formation. The anomaly was typical of massive sulfides: small, isolated, and with magnetic association, even though the ground follow-up identified the magnetic zone to be distinct 100m distant from the sulfide body. The target was selected for follow-up despite its low conductance (4S).

Telluric and magnetotelluric

Telluric and magnetotelluric field methods are two particular EM techniques that use natural fields in prospecting. Telluric currents are induced by the magnetotelluric fields that penetrate the ground. The magnetotelluric fields are belived to result from the flow of charged particles in the ionosphere. The main advantage of these methods compared to other potential field ones is the variable frequency range of the fields recorded. As lower frequencies are available, telluric method has a higher penetrating depth than the other electrical methods (potentially unlimited). The depth of investigation is also dependent on the electrode separation.

The potential gradient is measured at the Earth's surface and its value is about 10 mV/km. As in electric methods, anomalous potential gradients measured at the surface permits the location of subsurface areas of distinctive conductivity (Fig. 1.15). The telluric method is widely used in oil exploration to detect potential hydrocarbon traps, such as salt domes and anticlinal structures, but can be also useful to mineral exploration and in many other academic applications to unveil the properties of the Earth’s interior at a lithospheric scale.

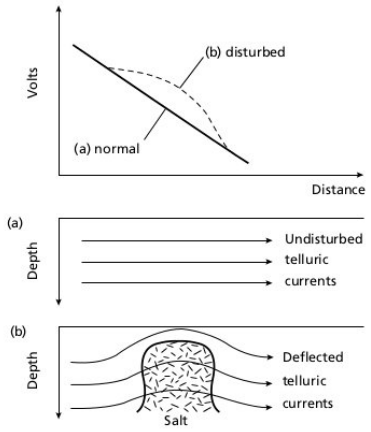

Figure 1.15: The instantaneous potential gradient associated with telluric currents. (a) Normal, undisturbed gradient. (b) Disturbed gradient resulting from deflection of current flow by a salt dome. (Kearey, et al., 2002).

In the magnetotelluric method, in addition to the telluric currents monitoring, the magnetic field must be also measured by a sensitive fluxgate magnetometer. Apart from the frequency, the subsurface resistivity of the media affects the depth of penetration of the survey. Generally, deeper information is obtained with decreasing frequency and increasing apparent resistivity. Interpretation of magnetotelluric data is similar to the resistivity methods explained, is essentially a form of VES. Thus, this method is mainly useful in mapping horizontal interfaces, and less efficient at identifying vertical boundaries.

Ground-penetrating radar (GPR)

Ground-penetrating radar (GPR) is a particular technique that uses radar waves to image the shallow subsurface with high-resolution. The GPR method consists on send a short radar pulse in the 10-1000MHz frequency band, this pulse is transmitted into the ground and when it arrives to a contrasts in dielectric properties part of the pulse is reflected back and recorded to a receiving antenna (Fig. 1.16 a). The data obtained can be displayed on a radargram, which contains all the observables or returned radar waves (Fig. 1.16 b). As in seismic methods, this data has to be processed to eliminate effects of multiples, noise, etc.

Additionally to the high quality and high-resolution results that can be obtained, another advantage of the GPR method is that it is a non-destructive method so it can be used in urban and sensitive environments. As the previous EM methods, the depth penetration of radio waves increases with increasing resistivity of the media surveyed and with the lower frequencies. Typical GPR applications can be resolved until a depth of the order of 20 m, although can increase to 50 m in the presence of low conductivity media. There is a trade-off between depth of penetration and resolution.

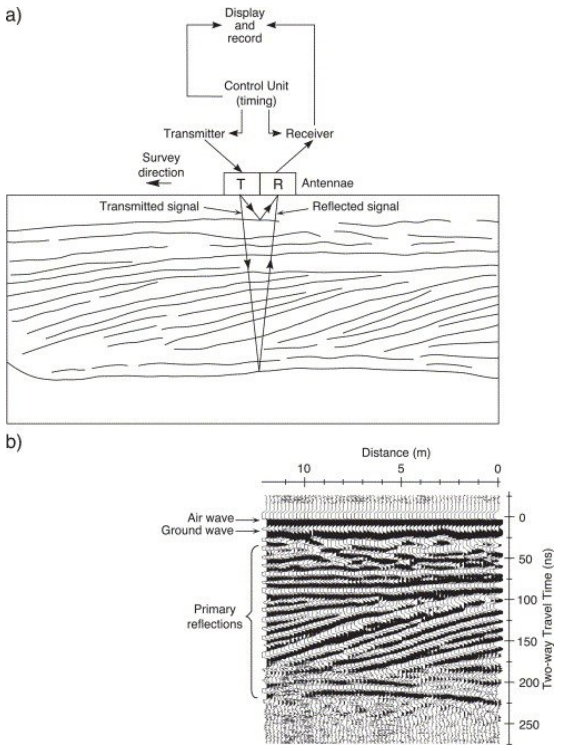

Figure 1.16: GPR data acquisition and the resulting radar reflection profile. (a) Data acquisition at an individual survey point, showing GPR system components and subsurface reflector configuration. (b) Radar reflection profile resulting from sequential plotting of individual traces from adjacent survey points. Position of the air wave, ground wave and primary reflections are indicated (Neal, 2004).

GPR survey is widely applied in imaging shallow soil and rock structures, locating buried channels and mapping the water table. Moreover, it has non-geological applications such as in archaeology. In this last case, the instruments used can have a depth of penetration of only a few centimetres to locate buried objects such as treasure trove (Kearey, et al., 2002).

Seismic method

Seismic methods use elastic waves to image the subsurface. It is useful to provide the distribution of the wave propagation velocity (rate at which seismic waves are transmitted in the earth) among other physical properties of the subsurface such as density, attenuation, anisotropy or other related ones. This technique is characterized for having higher costs than others such as gravity or magnetic methods. However, the result provides detailed information about the subsurface, including location, depth and shape of the different geological layers and bodies to large depths, particularly through the so-called seismic reflection experiments. As electric methods, it is also well-suited to tracking the subsurface water table and locating water-bearing sands. It is the most

extensively-used geophysical method by both oil industry and academia, and has many different applications at a very wide range of spatial scales. This is the method used and developed in this work, so it deserves a detailed explanation that is presented in the next chapter.

Chapter 2. Fundamentals of the seismic exploration method

2.1. Seismic waves

When seismic waves are produced by a source, that energy is transmitted as a three-dimensional phenomenon throughout the Earth's surface and subsurface (see Fig. 2.1) by continuous and progressive elastic displacement of adjacent particles in the medium. In this way, the wave propagation depends on the elastic properties of the media. The theory of elasticity relates the forces applied to a body and its deformation. The measure of the intensity of these balanced internal forces and consequent change of shape and/or size of a body are expressed in terms of the stress and strain respectively. In the elastic field, the ratio of a particular type of stress to the resultant strain is specified for any material by its various elastic moduli. In this thesis, the bulk modulus κ , or its inverse called the compressibility, describes the stress-strain when the stresses produced by the inwards hydrostatic pressure P is equal in all directions applied to a cubic element, being the resultant strain or dilatation experienced the change of volume Δv divided by the original volume v .

$$\kappa = \frac{P}{\Delta v / v} \quad (2.1)$$

Seismic waves are packages of elastic strain energy that propagate outwards from a seismic source. Except in the immediate vicinity of the source where the media is permanently displaced or deformed, the strains associated with the passage of a seismic pulse can be assumed to be elastic. On this assumption the propagation velocities of seismic pulses are determined by the elastic moduli and densities of the materials through which they pass (Kearey et al., 2002). So, elastic theory is used to explain seismic wave propagation and its moduli to describe the media properties. The spreading of these waves can be reproduced numerically and thus, their response can be computed at known detector locations. Seismic modelling uses seismic data recorded at that positions to obtain a subsurface image of a cross-section of the Earth. Its processing is commonly known as imaging, and is a sort of forward and inverse modelling.

Types of seismic waves

The passage of the wave through a medium produces a displacement and/or distortion transmitting the seismic energy in the form of harmonic motions in the particles. The physical properties of the rocks determine the velocity of propagation of the disturbance. The surface or locus that the pulse has reached at a particular time, and in which all particles vibrate with the same phase, is defined as wavefront. In an homogeneous

medium, the wavefront has a spherical shape (spherical wave) but at a far distances from the source is so flat that can be considered to be plane (plane wave). The direction perpendicular to the wavefront is called the seismic ray path. Several types of seismic waves can be identified depending on the motion of the particles and the direction of the seismic ray. There are two main groups of seismic waves, ones that travel through the medium as seismic body waves, and others over the free surface as seismic surface waves.

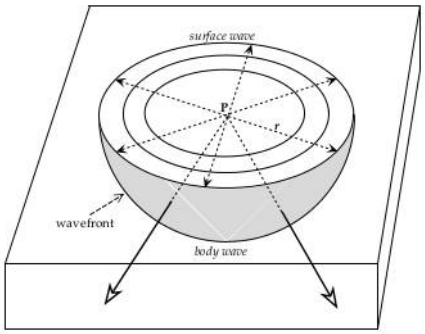

Figure 2.1: Propagation of a seismic disturbance from a point source P near the surface of a homogeneous medium; the disturbance travels as a body wave through the medium and as a surface wave along the free surface (Lowrie, 2007). Arrows correspond to seismic rays and the gray spheric surface represents a wavefront at a distance r from the point source P.

Body waves

Body waves can propagate through the internal volume of an elastic solid. According to the equation of motion and for a one-dimensional wave, a force ($\sigma_x A_x$) caused by the stress σ_x acting on the area A_x of a small volume element of mass $\rho dx A_x$ is given by

$$\rho dx A_x \frac{\partial^2 u}{\partial t^2} = dx A_x \frac{\partial \sigma_x}{\partial x} \quad (2.2)$$

where u is the displacement of the volume. Using the definition of elastic modulus (E), for a one-dimensional deformation $\sigma_x = E \frac{\partial u}{\partial x}$, gives the one-dimensional wave equation

$$\frac{\partial^2 u}{\partial t^2} = c^2 \frac{\partial_2 u}{\partial x^2} \quad (2.3)$$

where $c = \sqrt{\frac{E}{\rho}}$ is the propagation velocity of the wave, i.e. the distance traveled divided

by the time taken (Lowrie, 2007). Body waves are non-dispersive; that is, all frequency components travel through any material at the same velocity, determined only by the elastic moduli and density of the material. Body waves may be of two types depending on whether the vibration of the particles is parallel (compressional waves) or perpendicular (transverse waves) to the direction of propagation of the disturbance. Compressional (or longitudinal) waves are the fastest, primary or P-waves of earthquake seismology, and pass through a medium as a series of compressions and dilatations of uniaxial strains in the direction of wave travel (Fig. 2.2 a). In this thesis, the 2-D acoustic wave equation ($\frac{1}{c^2}\frac{\partial^2 u(x,y;t)}{\partial t^2} = \nabla^2 u(x,y;t)$) is used for the P-waves modelling. Transverse (or shear) waves propagate by a pure shear strain and travel more slowly than P-waves, so in earthquake seismology are also referred as secondary or S-waves. The particle displacement induced by S-waves can be polarized in the vertical (SV-wave) or horizontal (SH-wave) plane, i.e. oscillating up and down or side to side respectively but always at right angles (perpendicular) to the direction of wave propagation (Fig. 2.2 b). P-waves can propagate in solids, liquids and gases because all of which are compressible, whilst only solids allow shear and therefore S-waves propagation.

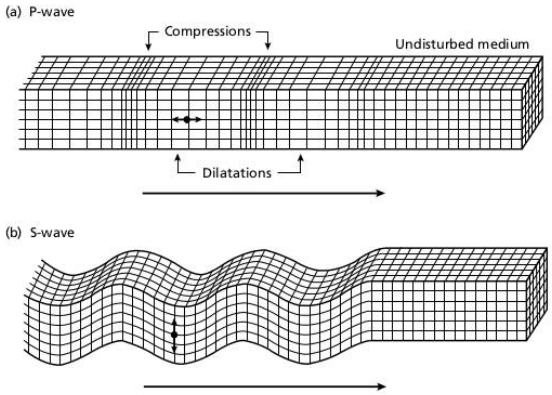

Figure 2.2: Elastic deformation and ground particle motions (small arrows represented at the black point) associated with the passage of body waves. Long arrows below the medium show the direction of propagation of the disturbance. (a) P-wave, in which the particle motion in the wavefront consists of a a combination of compressions and dilatations in the direction of wave propagation. (b) S-wave, in which the particle motion is perpendicular to the direction of propagation. (Kearey et al., 2002).

Surface waves

Only in a bounded elastic solid, surface waves are a kind of seismic waves that exist at the boundary of the propagation medium. There are two categories of seismic surface or L-waves, the Rayleigh (L_R) and the Love (L_Q) waves. The differences between them is the particle motion in their wavefronts. The particle motion originated by a Rayleigh wave can be described as a combination of the P- and SV- vibrations in the vertical plane (Fig. 2.3 a). The particles move in retrograde sense around an ellipse that has its major

axis vertical and minor axis in the direction of wave propagation. L_R -waves propagate almost at the same velocity as S-waves. Although it is a surface wave, the particles below the free surface are also displaced but with an amplitude that decreases exponentially with increasing depth. L_Q -waves are surface waves with horizontal particle motions and perpendicular to the direction of propagation (Fig. 2.3 b). L_Q -waves are originated from reflected SH-waves at supercritical angles (see section 2.2 "Reflection and Refraction (boundary effect)" below). They have a propagation velocity lower than the S-wave velocity in the underlying medium. L-waves are dispersive due to its dependence of velocity on wavelength. This dispersion is directly attributable to velocity variation with depth in the Earth's interior. Typically, the deeper penetrating long wavelengths travel with faster seismic velocities than the short wavelengths. As a result their waveform undergoing progressive change during propagation.

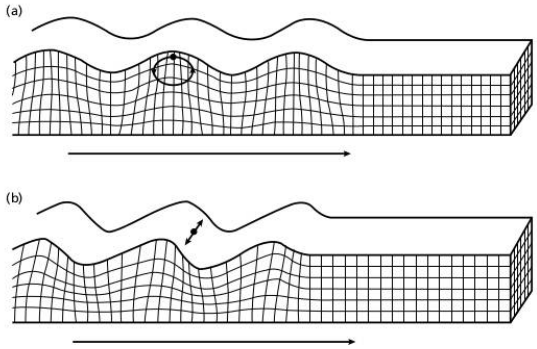

Figure 2.3: Elastic deformation and ground particle motions (small arrows represented at the black point) associated with the passage of surface waves. Long arrows below the medium show the direction of propagation of the disturbance. The deformation produced by the passage of the wave decreases with depth below the free surface. (a) Rayleigh or L_R -wave, in which the particle motion in the wavefront consists of a combination of P- and SV- vibrations in the vertical plane. The particles move in retrograde sense around an ellipse that has its major axis vertical and minor axis in the direction of wave propagation. (b) Love or L_Q -wave, in which the particle motion is horizontal and perpendicular to the direction of propagation. (Kearey et al., 2002).

2.2. Seismic wave propagation

The wave motion consists on a transmission of energy, with no transfer of mass, following a pattern that repeats in both time and space. This characteristic allows to describe the particle motion associated with the passage of a wave by means of the harmonic displacement about its fixed position. The displacement originated by a wave that travels in the positive x-direction can be written as

$$u = A\sin 2\pi\left(\frac{x}{\lambda}-\frac{t}{T}\right) = A\sin\left(kx-wt\right) = A\sin k\left(x-ct\right) \qquad (2.4)$$

where A is the amplitude, T the period, in which the amplitude of the disturbance is repeated at this regular time interval, and λ the wavelength, in which the disturbance is repeated along the direction of travel at this regular distance. Other wave parameters can be derived from the previous ones, such as the frequency ($f=\frac{1}{T}$), angular frequency ($w=2\pi f=\frac{2\pi}{T}$), wave number ($k=\frac{2\pi}{\lambda}$), and phase velocity ($c=\lambda f=\frac{w}{k}$). D'Alembert's principle demonstrates that any function of $(x\pm ct)$ that is itself continuous and that has continuous first and second derivatives is a solution of the one-dimensional wave equation. In the three dimensional case, the general solution to the wave equation for a particular time t is described by the wavefront or constant phase surface formed by the family of planes perpendicular to the direction of wave propagation, previously defined as the ray path of the wave. As the medium properties are not constant with position, neither the ray paths are straight lines nor the wavefronts are planar. Instead the wave can be expressed as a function of $(S(x,y,z)\pm c_0 t)$ where $S(x,y,z)$ is a function of position only and c_0 is a constant reference velocity that satisfies the wave equation (2.3) and gives the eikonal equation

$$\left(\frac{\partial S}{\partial x}\right)^2+\left(\frac{\partial S}{\partial y}\right)^2+\left(\frac{\partial S}{\partial z}\right)^2=\left(\frac{c_0}{c}\right)^2=\zeta^2 \qquad (2.5)$$

where ζ is known as refractive index of the medium (Lowrie, 2007). This equation describes the seismic wave propagation as wavefronts or ray paths, where the surfaces $S(x,y,z)$ represent the wavefronts and ($\zeta\frac{\partial S}{\partial x},\zeta\frac{\partial S}{\partial y},\zeta\frac{\partial S}{\partial z}$) the direction of the ray path.

As the disturbances are propagated farther distances, the seismic signal decreases. The intensity or energy density of a wave is the energy per unit of volume in the wavefront. On average is proportional to the square of its amplitude.

Attenuation of seismic waves

The attenuation is the effect referred to the reduction of the amplitudes of seismic waves with the distance traveled. The amplitude becomes smaller due to spherical spreading or geometric attenuation and imperfect elastic responses of the media. Regarding the geometric attenuation, as the energy is spread along enlarging wavefronts, its value per unit area becomes smaller. The decrease in intensity of body waves is proportional to $\frac{1}{r^2}$

while in surface waves to $\frac{1}{r}$, being r the distance of the wavefront from its source. Therefore, the amplitude attenuation of body and surface waves are proportional to $\frac{1}{r}$ and $\frac{1}{\sqrt{r}}$, respectively.

Another reason for attenuation is that rocks do not transmit all the seismic energy. Part of the energy is lost by scattering and some converted to heat. The absorption coefficient is an indicator of the deviation from perfect elastic media and expresses the proportion of energy lost during transmission through a distance equivalent to a complete wavelength. The absorption coefficient is inversely proportional to the wavelength of the signal (Lowrie, 2007). As a consequence, high frequencies are attenuated more rapidly than are lower frequencies. Thus, seismic records at longer times and farther distances have a higher content of low frequencies. Therefore, the frequency spectrum of a seismic signal changes continuously during the propagation due to the loss of the high frequencies, in which the ground acts as a low-pass filter.

Huygens' principle

The Huygens' principle describes the behaviour of wavefronts. The theory is based on geometrical constructions and permits the passage of a wave through a medium and across interfaces between adjacent media. It says that every point of a wavefront may be considered the source of secondary wavelets; the new wavefront is the tangential surface (or envelope) that propagate in all directions with a speed equal to the local waves propagation velocity (Fig. 2.4).

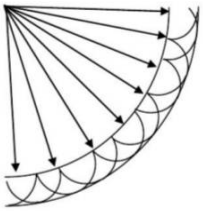

Figure 2.4: Huygens' principle (Gadallah et al., 2009). The points of the spherical wavefront defined by the seismic rays (arrows) are secondary sources originating new wavefronts (small spherical surfaces) which envelope is the new displaced wavefront.

Fermat's principle

The Fermat principle describes the behaviour of seismic ray paths. It selects from all the possible paths the one with the minimum travel-time (t) by searching for a connection between a specified source (s)-receiver (r) pair. Thus,

$$t = \int \frac{ds}{c_0} = minimum \qquad (2.6)$$

where ds is the element of distance along a ray path and c_0 the seismic velocity over ds.

Reflection and refraction (boundary effect)

When the seismic waves encounter the boundary between two layers of different seismic media properties some energy is reflected back to the surface and the rest is transmitted or refracted at the lower layer. The relative amplitudes of the transmitted and reflected waves depend on the acoustic impedance (Z) contrasts of the rocks in the media interface. This property is a function of density and seismic velocity of the media ($Z = \rho \cdot c_0$). The reflection coefficient (R) is the ratio of the amplitude of the reflected wave to the amplitude of the incident wave. The magnitude and polarity of the reflection coefficient depends on the difference between seismic impedances of the two media. In general, the smaller is the contrast in impedance of the rocks at the seismic boundary the lower is the energy reflected, i.e. the amplitude of the reflected wave. If R = 0 there is no contrast of acoustic impedance and all the incident energy is transmitted. If R = +1 or -1 all the energy is reflected back with the same or opposite polarity, as for example when an incident wave strikes the water free surface (Kearey et al., 2002). On the other hand, the transmission coefficient is the ratio of the amplitude transmitted to the incident amplitude. The sum of the reflected and transmitted coefficients must be equal to 1.

When the incident wave is oblique, the reflected and transmitted or refracted waves experience a change in the direction of propagation. The energy of a P-wave is partitioned between reflected and refracted P- and S- (or converted) waves (Fig. 2.5). When the incident wave is polarized as a SV-wave, a reflected and refracted P- and SV-waves will be originated at the geological interface. However, for an incident SH-wave no other polarizations or waves rather than SH will be generated at the boundary.

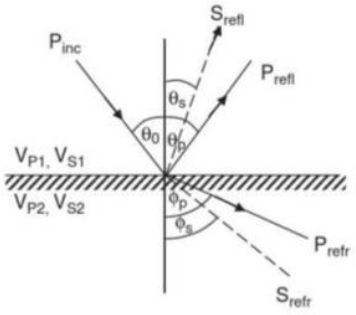

Figure 2.5: Reflected (P_{refl} and S_{refl}) and refracted (P_{refr} and S_{refr}) waves generated by an incident P-wave (P_{inc}) ray obliquely incident on an interface of acoustic impedance contrast ($v_{P2} > v_{S2} > v_{P1} > v_{S1}$, so according Snell's law $\Phi_p > \Phi_S > \theta_0 = \theta_p > \theta_S$). (Gadallah et al., 2009).

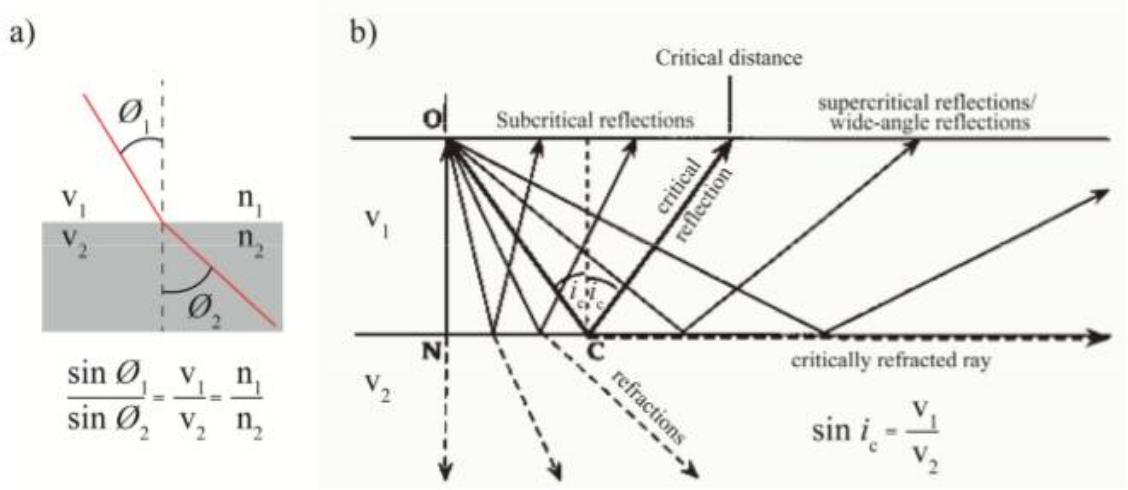

Figure 2.6: (a) Schematic representation and mathematical expression of the Snell's law. This relationship shows how an incident ray path (red line) with angle Φ_1 from a medium with velocity v_1 and refractive index n_1 to a lower medium with velocity v_2 and refractive index n_2 ; being $v_1 < v_2$, is transmitted with an angle Φ_2 through the lower medium. (b) Schematic image of the evolution of the reflections and refractions as the source-receiver distance increases. Point C corresponds to the position where the incident ray path of the seismic wave strikes the interface at a critical angle i_c and the waves critically refracts through the top of the lower layer. Reflections that occur after the critical distance are known as wide-angle reflections (Lowrie, 2007).

The laws of reflection and refraction of seismic waves at an interface can be derived using geometrical relations and applying Huygens' principle, i.e. using the explanation of the advance of the wavefronts which coincides with the tangent plane or envelope of the secondary wavelet (figure 3.53 and 3.54, Lowrie, 2007), or applying Fermat's principle, i.e. using the condition for the minimum travel-time (figure 3.56 and 3.57, Lowrie, 2007). The law of reflection says that the angle of reflection is equal to the angle of incidence, being that angles the ones formed between the normal to the interface and the respective rays. The law of refraction its equivalent to the so called Snell's law in optics. This mathematical expression relates the changes of direction of the ray paths of the seismic waves when they reach a geological discontinuity as a function of the media properties and the angle of incidence (Fig. 2.6 a). For a particular angle of incidence, when the lower media has a higher velocity than the upper one, the refracted ray is bent away from the normal. Otherwise, the refracted ray is bent back toward the normal. When the incident ray strikes the interface vertically with zero angle of incidence (normally incident ray), the reflected and transmitted rays are also vertical, so there is no change of direction. As the angle of incidence increases, the refracted ray changes the direction following the Snell's law. When the angle of refraction is 90º with the normal to the interface, the wave experiences a critical refraction. The ray that produces the critical refraction is incident to the boundary at the critical angle, i_c in Fig. 2.6 b, and is called

critical ray. At this and any greater angle of incidence, the energy passes up parallel to the boundary in the top of the lower layer with the faster velocity. As a result, critical refractions cause a perturbation in the upper media called head wave (Kearey et al., 2002). This disturbance travels through the upper media with the faster velocity and an oblique direction inclined at the critical angle. Furthermore, according to the law of reflection it is also produced a critical reflection. When the angle of incidence is larger than i_c , all the wave field bounces back entirely, in that case we have supercritical reflections or wide-angle reflections (Fig. 2.6 b). These waves can only be recorded when the source-receiver offset is equal or bigger than a certain critical distance, in which the ray path of the seismic wave has reached the geological boundary (point C in Fig. 2.6 b) with i_c . The reflections that are generated by an angle of incidence smaller than the critical are called subcritical reflections (Fig. 2.6 b).

Diffraction

Moreover, Huygens' principle can explain the diffraction effect by which a wave is bent around an obstacle or discontinuous surface that is located in its path (Fig. 2.7) (Lowrie, 2007). When the discontinuities have a radius of curvature shorter than the wavelength of incident waves, the previous reflection and refraction laws are not valid. Instead there is a radial scattering of the incident energy. The incident wavefront can penetrate into shadow zones because of the generation of new wavelets at the edge of the point obstacle or surface following Huygens' principle. As the angle of incidence increases with respect to the direction of travel of the incident wavefront, the intensity of the wave diffracted is weaker.

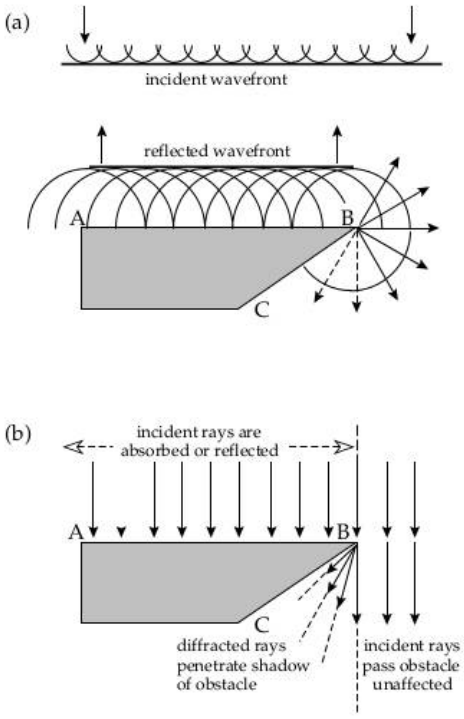

Figure 2.7: Explanation of diffraction at an edge with the aid of Huygens' principle. (a) The incident and reflected plane wavefronts are the envelopes to Huygens wavelets, which are able to carry the incident disturbance around a sharp corner. (b) The incident rays are absorbed, reflected or pass by the obstacle, but some rays related to the wavelets generated at the point of the obstruction are diffracted into its shadow (Lowrie, 2007).

2.3. Seismic exploration techniques

Seismic exploration is one of the most used and powerful geophysical technique to obtain rock properties (velocity, impedance, attenuation, anisotropy) that are fundamental to define lithology, as well as to generate images and models of the architecture of the Earth's interior. Seismic acquisition set ups consist of a source which releases energy into the Earth in the form of seismic waves, and a number of receivers that record the seismic

wave field that propagates through the medium. So, the set of observables consist of the seismic waveforms themselves or some of their attributes (travel times of seismic phases, amplitudes, envelope, reflectivity, etc.). Based on empirical results, the maximum depth that the seismic techniques can account for is 50-75% of the maximum experimental offset. The resolving depth is also influenced by signal-to-noise ratio depending on the source characteristics, the amplitude decay by geometrical spreading, attenuation effects and ambient noise.

Types of seismic systems

Depending on the acquisition set up, which marks the spatial distribution of seismic sources and receivers, two main different seismic exploration methods exist, namely near-vertical reflection, and refraction and wide-angle reflection (WAS) systems. While sources are generally very similar in the two systems (typically the main difference being the source energy), receivers are different, especially for marine acquisition systems. This is because whilst the near-vertical reflection system aims at obtaining laterally coherent images of the seismic impedance contrast at geologically boundaries, the WAS surveys aim at mapping rock properties from the characteristics of the seismic wave field. In the following section I present the main components, characteristics and differences of these two classes of seismic acquisition techniques for marine or land surveys.

Refraction and Wide-Angle reflection Seismics (WAS)

Modern wide-angle seismic experiments commonly consist of hundreds to thousands of shots, depending on source characteristics and marine or land recordings. Those shots are typically recorded at tens to hundreds of receivers. Modelling of these data provides information of the geometrical structure and physical properties of the subsurface. Below I describe the main characteristics of the elements that form the WAS set ups, especially focusing on offshore experiments. I first describe the sources and then the receivers, emphasizing their relative locations, deployment and recovering procedure depending on the recording device, and finally, the characteristics of the data collected.

· *Seismic sources*

Seismic sources generate waves that propagate through the medium and are reflected, transmitted or refracted at the geological boundaries that are characterized by impedance contrasts. Seismic sources can be classified into two main types based on their origin and cause. Passive sources are those generated by natural, or non-controlled, events. Examples are earthquakes (<20 Hz) or anthropogenic and natural sources of ambient noise, as commercial shipping (10 to 500 Hz), sea-surface agitation (500 Hz to 25 kHz) or thermal noise (>25 kHz) in the ocean (Hildebrand, JA., 2009). The main characteristics of most passive sources are their unknown location and origin time, and

additionally, such as for earthquake sources, the relatively low-frequency content. Conversely, active seismic sources are artificially generated, and their characteristics including location, time and energy, so that their frequency content, are partially controlled. The usage of active seismic sources is advantageous because their positions can be designed in strategic places to illuminate a particular target area, as the ones used in this work. Their main drawback is the limited capability of generating low-frequency signals (<4 Hz), the ones that penetrate deeper in the subsurface, due to the high power needed, and that their location is always at the earth's surface, whereas passive sources may be located deep in the subsurface and illuminate other targets.

The source design (number, size, power, spatial distribution and depth) and firing interval are parameters that must be defined according to the objective of study. The most common systems to generate controlled sources have been explosions and air guns (Fig. 2.8 a) for marine surveys and hammering a metal plate, using vibroseis trucks (Fig. 2.8 b), among others for land surveys. Explosive seismic sources are invasive methods with a potentially large environmental impact and have been falling out of use. Instead, for local land studies, seismic vibrators or sledge hammers can be employed because of their lower environmental impact.

(a)

(b)

Figure 2.8: Active seismic sources. (a) Seismic source showing an air gun cluster of the gun array installed on the starboard side of the RV Sarmiento de Gamboa during the TOPOMED (2011) cruise (from TOPOMED-GASSIS report, 2011). (b) Vibroses truck. For generating the seismic source, the truck hits the floor at a certain frequency (Dean, T. et al., 2013).

Focusing on offshore experiments, the most common source is the air gun (Fig. 2.9) because produces synchronized blasts of compressed air, which is cheap and readily available, and it has a limited impact on marine life that can be readily monitor with acoustic systems and marine mammal observers on survey ships. When the air gun

releases the air, it generates an acoustic pulse of energy, called pressure signature. The source ghost which is the integration of the primary energy pulse with the pulse reflected at the sea surface, and the bubble pulse caused by the expansion-collapse cycle of the air bubble (Landro and Amundsen, 2010) (Fig. 2.10) are characteristic features of the air gun signature. The pressure signature is described by two parameters, the primary pulse peak-to-peak amplitude or strength, that is the useful part of the signal, and its bubble period or peak-to-bubble ratio (Fig. 2.10). The bubble effect is caused by the pressure difference between the air bubble and the water. The bubble oscillates, with a period typically in the range of 10-100 ms, until stops due to frictional forces. If the cyclic motion of the bubble could ideally stops after the first expansion, the air gun signature would describe an ideal signal closer to a spike. The peak-to-bubble ratio is frequency dependent.

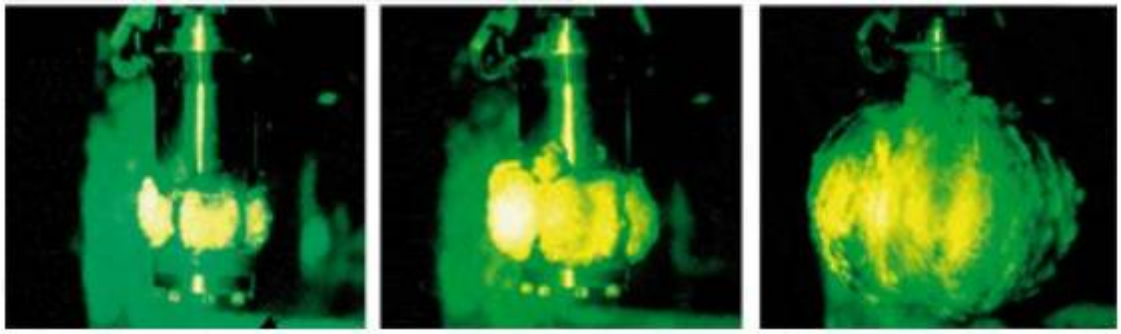

Figure 2.9: Single air gun after release the air. Pictures show the air bubble at 1 ms, 1.5 ms and 7 ms, respectively. (Langhammer, J., 1994).

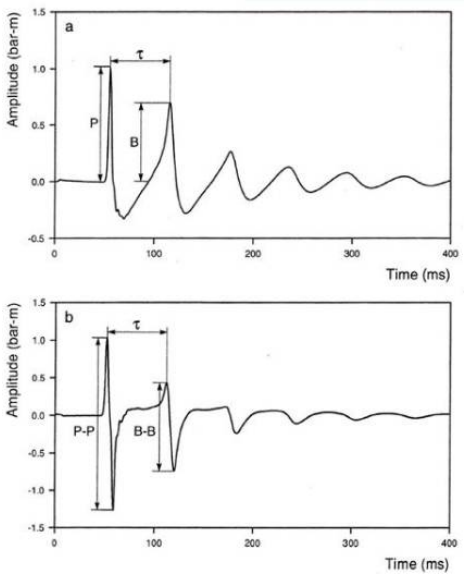

Figure 2.10: Pressure signature of the sound pulse of a single 40-in^3 air gun. The near-field signature (upper trace) shows the measurement of the released air producing a steep-fronted shock wave followed by several oscillations resulting from the repeated collapse and expansion of the air bubble. The signal strengths of the direct wave and the first bubble are P and B, respectively. The near-field peak-to-bubble ratio is PBR=P/B. The far-field signature (lower trace) shows the effect that the source ghost has on the near-field signature. The peak-to-peak amplitude P-P (the distance between the positive peak of the primary and negative peak of the ghost) is 2.3 bar-m. The far-field peak-to-bubble ratio is PBR=(P-P)/(B-B)=1.9. The bubble period is tau=60 ms (Langhammer, J., 1994).

The two parameters that characterize the pressure signature depend on air gun size, initial firing pressure, and depth. The dominant frequency of the bubble oscillation decreases with increasing gun volume, with increasing gun pressure, and with decreasing hydrostatic pressure, and thus, source depth (Landro and Amundsen, 2010). The depth of the source controls the interference of primary and ghost pulses. The effect of the source ghost on the useful frequency content of seismic data is substantial. The source spectrum of a shallow source presents its first destructive interference, zero amplitude value or ghost notch, at higher frequencies obtaining detailed information of the area. However, low amplitude values are recorded at low-frequency components meaning that the information is from the shallow part of the area. Contrary, when the source depth is increased also increases low-frequency content in the signal, allowing deeper targets to be characterized but decreases resolution. The bandwidth change occurs because the first ghost notch appears at lower frequencies but the amplitude of the useful frequency components is larger.

Academic seismic refraction studies can use individual air gun volumes up to 1600 in^3 (26,2 l). Usually, more than one air gun is used forming an array (Fig. 2.8 a) to create constructive interference of the acoustic signal (3-70 Hz) that maximize the energy of the pulse, and destructive interference that minimize the bubble effect. The motivation of using an air gun array is to produce pulse signatures closer to spikes, with a high-energy, low-frequency sound in the form of sharp, short-duration pulses. The total volume of an air gun array is the sum of the volumes of each gun in the array, and is typically in the range 3,000-8,000 in^3 (49.2-131.6 l). Cluster guns produce sound more efficiently than a single large gun with the same volume as the cluster. An example of the source signature and its corresponding amplitude spectrum for a 3,397-in^3 air gun are shown in Fig. 2.11. The notches represented are at frequencies 0 and 125 Hz. The amplitude is larger in the 20-100 Hz interval, but some energy will be present up to 150 Hz.

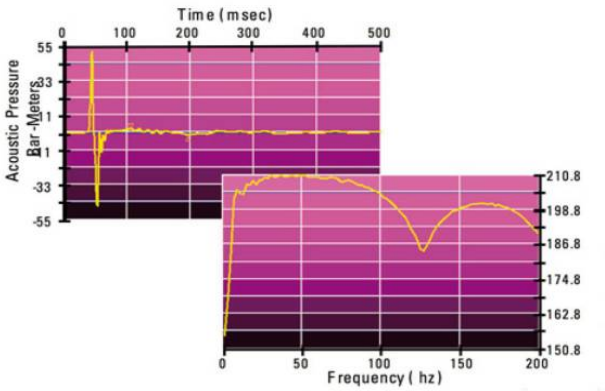

Figure 2.11: Source signature and amplitude spectrum for the 3,397-in^3 air gun array. The peak-to-peak amplitude is 102 bar-m. The source amplitude spectrum is normalized in dB relative to 1mPa/Hz at 1 m. A moderately sized air gun array will have a spectrum that peaks above 200 dB above this reference level. © WesternGeco

Academic WAS experiments are typically devised to recover the wave field that has penetrated in the deep layers of the Earth's crust and uppermost mantle. In order to retrieve information at a crustal scale, a powerful source is needed to generate a signal that contains lower frequencies. These frequencies are required because are the ones that suffer less the attenuation effects. As has been mentioned, one of the key factors to obtain the maximum possible of useful energy concentrated at the lowest frequency bandwidth is the depth of the source. The deeper the source location is, the cleaner is the wavefront that can be generated. For this reason, the marine sources are positioned beneath the sea surface at 10-20 m depth, deeper than most other set-ups. The shooting distance in WAS set-ups is also important and must be higher enough to avoid the wraparound noise produced from previous shots. The typical firing or shooting interval is 60-120 s, which corresponds to 150-300 m.

· *Seismic receivers*

A seismic receiver record, as a continuous temporal trace, the wave field that has been propagated through the medium at a certain position converting the motion or pressure variations to electricity. Receiver number and spacing are the important factors that define the lateral accuracy of the final result. The higher the number and lower the spacing is, the better the recorded wave field is mapped and thus also increases the accuracy that the subsurface might be constrained.

The seismograph was the first device for land applications to record seismic waves. Conventional seismic surveys on land use one geophone per receiver (Fig. 2.12 a) to detect mainly the ground motion in the vertical direction, but some of these devices can also record velocity, displacement and/or acceleration among others. The combination of three orthogonal geophones are typically used to collect 3-component seismic data. Marine surveys became more popular after the appearance of the hydrophone. Hydrophones, unlike geophones, are sensitive to changes in sound pressure rather than motion. On a WAS experiment, hydrophones are incorporated independently in Ocean Bottom stations.

Focusing on offshore systems, the Ocean Bottom Hydrophones (OBH) are the devices that collect the pressure variations of the media in one direction in a WAS experiment. 4-component seismic data can be recorded by stations that incorporate an hydrophone to three orthogonal oriented geophones. The most used receivers that record 4-component seismic data are called Ocean Bottom Seismometers (OBS) (Fig. 2.12 b). The stations are deployed on the seafloor by an expendable anchor. These sensors have the possibility to capture converted wave data, as shear wave (S-wave), as well as P-wave information, because they are located over a solid surface. When the experiment finishes, the devices are liberated from their anchors and float up to the sea surface, where they are tracked by acoustic signals, a flag, a satellite radio and a flashing light, and, finally recovered from the vessel consecutively.

In a WAS experiment, the receivers remain static at a fixed location (e.g. the seabed in marine experiments) and its relative distance can be arbitrarily large (e.g. up to few hundreds of km). Typical crustal-scale surveys have a receiver spacing of 5-15 km. Its distribution usually depends on the experiment logistics, local geology, seafloor depth and the number of available devices. The fact of having stationary sensors in a quieter environment makes the signal-noise ratio better than when other dynamic techniques are used. The typical geometrical configuration for WAS offshore experiments is shown in Fig. 2.13. As the receivers are static, the relative source-receiver distance is variable. In marine active surveys, the number of sources is much higher than receivers and the shot distribution is performed in a way that generates a wider diversity of ray paths from full azimuth range to obtain a better target illumination. The waves generated are reflected, transmitted or refracted through the medium. Different seismic arrivals can be recorded depending on the angle of incidence and the source-receiver distance.

(a)

(b)

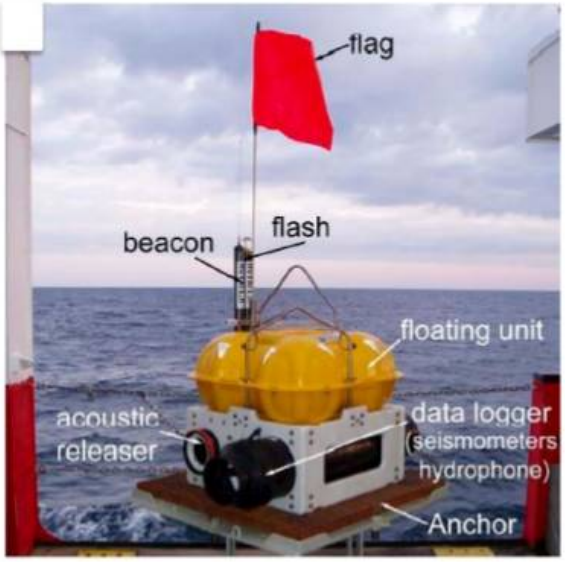

Figure 2.12: (a) Geophones. For recording, the nail-like end is introduced into the ground. Image from www.iongeo.com. (b) Ocean Bottom Seismometer from UTM-CSIC composed by the anchor, data logger (seismometers and hydrophone), acoustic release, float, flashing light, satellite radio and flag, (from Prada, 2014).

Recently, there have been the development of new acquisition devices that also include hydrophones and geophones as the Ocean Bottom Cables (OBC) and Ocean Bottom Nodes (OBN). The OBC has all the receivers connected by electrical wires that are deployed over the target study area to record and relay data to a seismic recording vessel (Fig. 2.14 a). OBC are limited to operate in shallow water depths environments of <2 km. Contrary, OBNs (Fig. 2.14 b) are similar to OBSs in the sense that they are independent receivers, but survey companies placed them on the seabed using Remotely Operated Vehicles. Industry experiments use a large number of OBNs to obtain high sampling data sets of the target areas often for monitoring purposes. The advantages of OBNs with respect to OBS/H stations are the precise knowledge of the receiver location, the large spatial density, which can be spaced around 100 m, and a much wider azimuth range.

However, its main drawbacks are seabed-related noise, low productivity and high costs, they are also limited to operate in relatively shallow water depths environments (3-3.5 km) and they are not suitable for many seafloors. The total number of sources and receivers and its spacing distance are parameters that must adapt to the objectives of the survey.

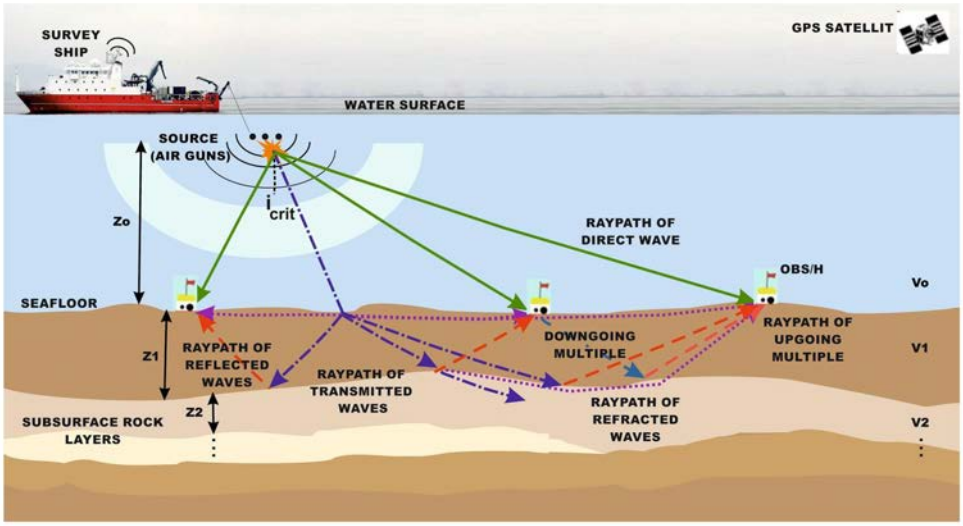

Figure 2.13: Schematic image of the geometrical configuration of a typical WAS experiment. The source (air guns) generates an acoustic pulse that is propagated through the medium which is shown with blue dashed-dotted ray paths, refracted and reflected at acoustic interfaces (i.e. seafloor and subsurface layers) and recorded by the OBS/H. Ray paths of refracted waves are represented as purple dotted lines, while reflected ray paths are drawn in red dashed lines. The ray path of the direct wave is represented with a green continuous line. The light blue and pink dashed lines correspond to the downgoing and upgoing multiple arrivals respectively. The positions of the survey ship is recorded during the whole experiment with a GPS.

(a) (b)

Figure 2.14: (a) OBC. 3-D active experiment formed by the shooting vessel and 4 cables distributed parallel to each other connected to the recording vessel. Image from Peakseismic. (b) Grid of OBN deployed using Remotely Operated Vehicles. Image from Sonardyne.

· *Data collected*

The kind of data recorded for an OBH is shown in Fig. 2.15 top. Each seismic trace is a continuous temporal signal that includes at different times the seismic events produced by the arrivals of the waves that bounces back at the subsurface discontinuities. In the sample record each trace is associated to their corresponding source-receiver offset, so the record section is constructed by juxtaposing the seismograms recorded at different offsets. Therefore, the seismic phases linked to the same event present lateral coherence on the records. Depending on the set up these record sections constitute a shot gather, or receiver gather. Fig. 2.15 top shows a receiver gather, so each seismic trace comes from the same receiver but different sources. The average shooting distance, i.e. the relative distance between consecutive traces, is 125 m in the example.

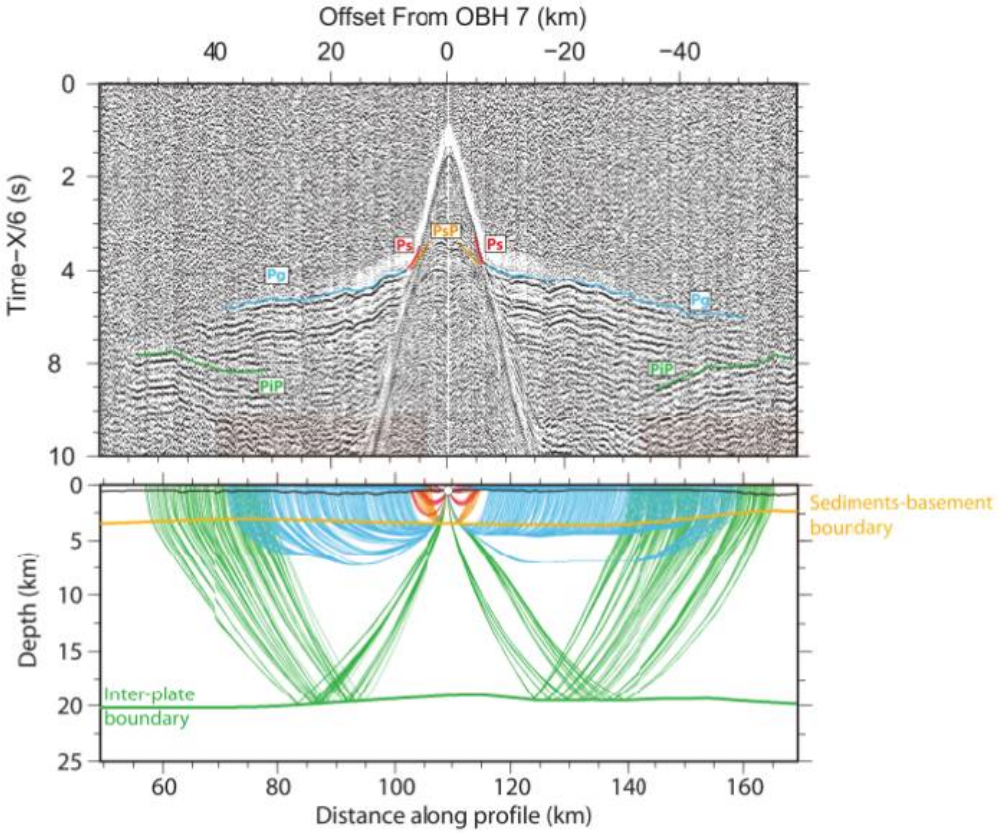

Figure 2.15: (top) Sample record section for OBH 7 from the trench-parallel profile NIC-125 acquired off-shore Nicaragua over the continental slope during R/V Maurice Ewing cruise EW00-05 in 2000 (Sallarès, et al., 2013). Colour contours mark the various seismic phases: refractions within the sedimentary layer (Ps) and the continental crust (Pg), and reflections from the top of the basement (PsP) and the interplate boundary (PiP). (bottom) 2-D section defined by profile NIC-125 displaying the ray paths associated to the travel-time picks from OBH 7. Rays were traced using TOMO2D for the final Vp and interface depth model presented in Sallarès, et al. (2013). The colour code is consistent with seismic phases indicated above. The thin black line represents the seafloor relief whereas the two reflecting interfaces are plotted as thick lines of the same colour as the corresponding reflected rays (Meléndez, A., 2014).

The main interest of the WAS data sets is in being able to identify and pick the arrival time of the seismic events (different colours in Fig. 2.15 top). Relatively straight lines of first arrivals with depth are shown at near offsets which correspond to the direct water wave. The time of the direct wave t_{dir} that travels through a media of velocity v_1 at distance Δ will be $t_{dir}=\Delta/v_1$. Moving towards farther offsets the refractions (Ps and Pg in Fig. 2.15) overcome the direct wave. The time of a refracted wave t_{refr} that travels through a media boundary of velocities v_1 and v_2 at distance Δ will be $t_{refr}=2h\cos(i_c)/v_1+\Delta/v_2$, where h is the depth of the first media and i_c is the critical angle. Refractions or diving waves are only dependent on the subsurface velocity distribution. Its local slope is proportional to the average propagation velocity of waves travelling down to a certain depth. The vertical scale in Fig. 2.15 top is reduced in time, so the refraction slope is not directly the real subsurface velocity. Most phases of interest appear as first arrivals after a certain critical distance. The critical distance is influenced by the velocity distribution of the media and the water column depth. Reflected arrivals appear later in time in the data as hyperbolas (PsP and PiP in Fig. 2.15). The near-offset reflections appear merged with the direct wave. The time of a reflected wave t_{refl} that travels through a media of velocity v_1 at distance Δ will be $t_{refl}=(2/v_1)\sqrt{(\Delta/2)^2+h^2}$. Reflected hyperbolas usually are deformed by the effect of geological relief, reflector's geometry and velocity heterogeneities. Analysis and interpretation of these seismic records may allow determination of subsurface layer thickness and velocities that can explain the travel times of the seismic phases (Fig. 2.15 bottom).

Multichanel (Near-vertical) Seismics Reflection (MCS)

The near-vertical multi-channel seismic (MCS) reflection experiments consist in several hundreds or thousands of shots recorded at typically several hundreds of receivers in a cable connected to the recording station (truck or ship). Dense data sets, and thus high redundancy and lateral resolution, are obtained using this acquisition geometry. Processing of MCS data provides detailed information of the geometrical structure of the subsurface. The main characteristics of the elements that form the near-vertical set ups, especially focusing on offshore experiments, are described below. Again, we first describe the sources, then the receivers, and finally, the characteristics of the data collected.

· *Seismic sources*

The systems to generate controlled sources on sea and land surveys are the same that the ones presented for WAS set ups. Again the objective of study defines the source design (number, size, power, spatial distribution and depth) and firing interval.

Focusing on offshore experiments, the array of air guns (Fig. 2.8 a) is also the most common source used to produce pulse signatures closer to spikes. The array of air guns in near-vertical reflection systems are submerged at a depths of 3-15 m below the sea surface and fired at constant distance interval (every ~10-20 s or 25-50 m) during the survey. The shot frequency of the source is one of the factors that determine the redundancy of data, and thus strongly impacts on the signal-to-noise ratio of the experiment. The gun pressure mostly used is 2000 psi (138 bar). The corresponding source spectrum to this kind of geometry configuration will have high frequencies obtaining high-resolution information mostly from the shallow part of the area, due to the low amplitude values recorded at low-frequency components. Thus, comparatively fine-scale details of the geological structures of the crust can be obtained after processing the seismic record.

As its name suggests, near-vertical reflection experiments are devised to recover the wave field that has traveled sub-vertically through the subsurface. The different characteristics of the radiated source signature depending on its direction is called directivity effect of a source. In order to propagate the wave field mostly downwards, the radiation pattern of a seismic source must be maximum for small angles from the vertical and attenuated for other directions of propagation.

· *Seismic receivers*

Conventional near-vertical seismic systems use as recording device a chain of equal spaced geophones on land surveys and hydrophones on sea, that is called cable or streamer (Fig. 2.16 a). The receivers are dynamic moving together with the truck or vessel preserving a fixed relative distance between them and the source. This receiver distribution jointly with a large number of active source points fired at a short distance makes possible the acquisition of a dense and high spatial resolution data set. Although the fact of having dynamic sensors increases the noise presence in the data, the repetition of the same media information in several receivers is very important to amplify the real signal, and thus improve the signal-to-noise ratio.

Focusing on offshore systems, the streamer is towed behind the vessel at few meters below the sea surface. A channel is formed by several hydrophones of the streamer, with their records usually summed before recording. The channels are typically equal spaced at a characteristic distance known as group interval, which for deep penetration MCS experiments is currently 12.5 m and for high-resolution 3.125 or 6.25 m. Other devices to stabilize, control and monitor the position of the streamer are the compasses to know the deviations of the streamer along all its length allowing to control its shape (Fig. 2.16 b), the birds that compensate for the deviations of the streamer depth during the survey (Fig. 2.16 c), and the tail-buoy that records with the Global Positioning System (GPS) the position of the end of the streamer (Fig. 2.16 d). The length and depth of the streamer, the group interval distance and the source configuration are parameters adapted to the target of the study.

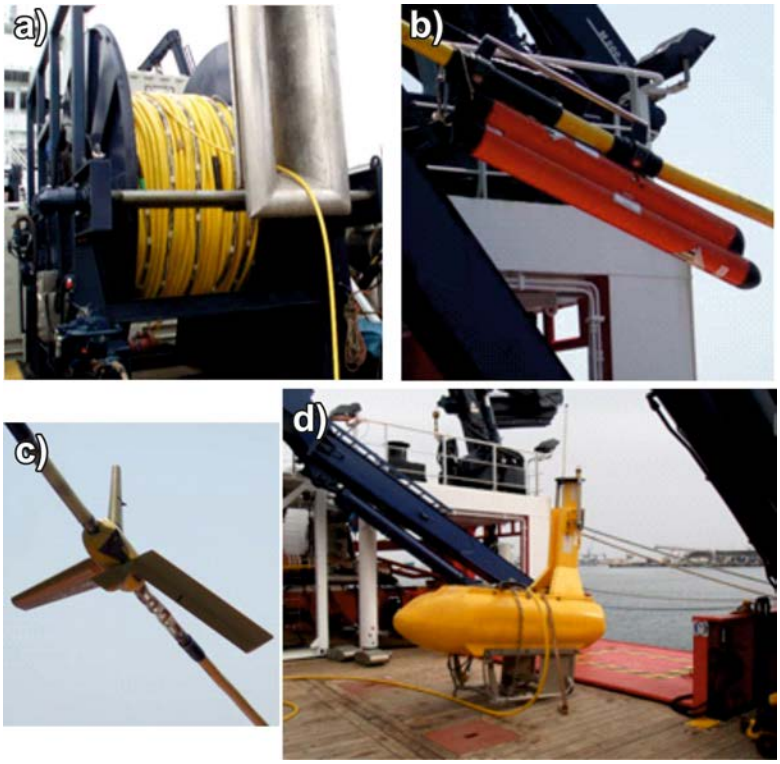

Figure 2.16: Elements of a MCS experiment, from Gómez de la Peña, 2017. (a). Streamer composed by the hydrophones. (b) Compass. (c) Bird. (d) Tail buoy.

MCS systems usually record the wave field that has been propagated vertically for short offsets, and hence reaching information of directly below the recording cable. The typical geometrical configuration for MCS offshore experiments is shown in Fig. 2.17. Using this geometry set up (Fig. 2.17), the reflected waves are mainly the ones registered by the hydrophones of the streamer. The reflection generated in the boundary of two consecutive layers with different acoustic impedance is larger as much higher is their acoustic contrast.

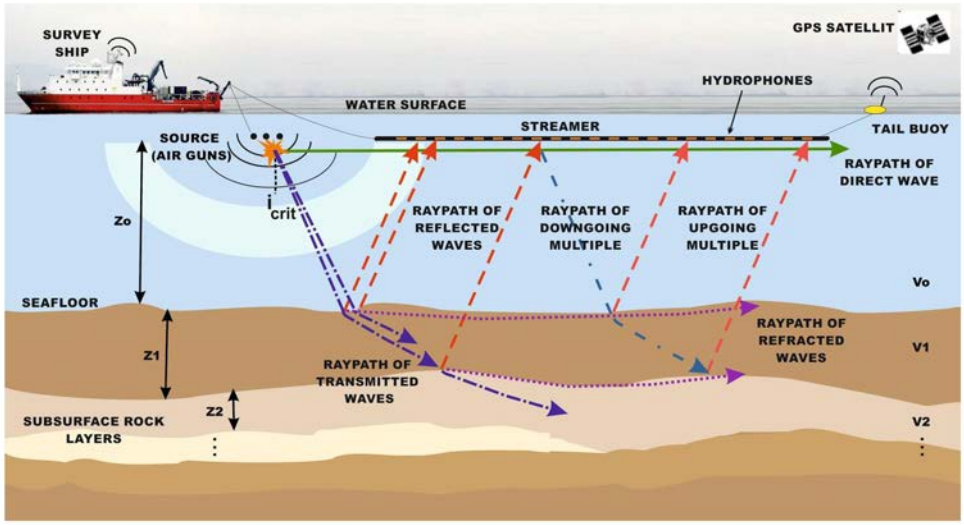

Figure 2.17: Schematic image of the geometrical configuration of a typical MCS experiment. The source (air guns) generates an acoustic pulse that is propagated through the medium which is shown with blue dashed-dotted ray paths, reflected at acoustic interfaces (i.e. seafloor and subsurface layers) which correspond to the red dashed ray paths and recorded by the receivers or hydrophones of the streamer. The ray path of the direct wave is represented with a green continuous line. The pink dashed lines correspond to upgoing multiple arrivals and they are also recorded in MCS set-ups. Ray paths of refracted waves are represented as purple dotted lines and their energy are usually not registered as first arrivals, so they appear masked within other seismic phases on the seismograms. The positions of the survey ship and tail-buoy are recorded during the whole experiment with a GPS.

· *Data collected*

An example of a synthetic streamer record is shown in Fig. 2.18. As in WAS records, each seismic trace is a continuous temporal signal that includes at different times the seismic events produced by the arrivals of the waves that bounces back at the subsurface acoustic boundaries. The seismogram is built according to the source-receiver offset of the traces. Figure 2.18 shows a shot gather, so each seismic trace comes from the same source but different channels. The average nominal receiver distance, i.e. the relative distance between consecutive traces, is 12.5 m. The first strong pulse corresponds to the arrival of the direct water wave. As in WAS travel-time diagrams, all the seismic phases linked to the same event present lateral coherence on the records. Therefore, the direct wave is shown as a straight line, because it reaches the receivers of the streamer travelling through the surface media following the minimum path, and the seismic phases that are reflected to the same acoustic interface form an hyperbolic shape. The first reflection is caused at the seafloor surface due to the large acoustic impedance contrast between the water column and the subsurface media. After a certain time the signal of multiple or secondary reflections appear in the travel-time diagram and mask the primary reflections.

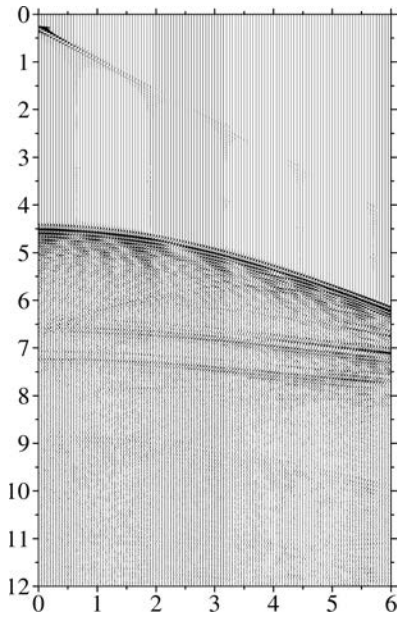

Figure 2.18: Streamer record section from a synthetic model. The vertical scale is in two-way travel-time (s) and the horizontal one is the relative offset distance (km) respect to the nearest receiver of the source.

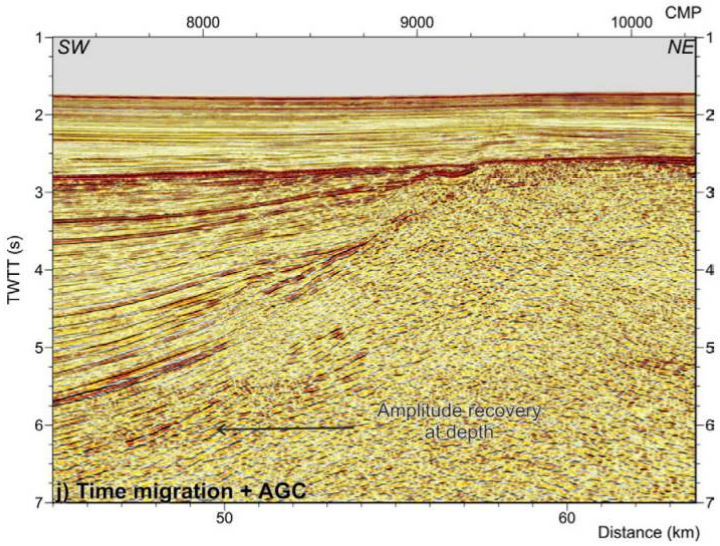

Figure 2.19: Final result of the processing flow of a seismic section of profile TM21 from Gómez de la Peña, 2017. Time migration with and automatic gain control applied. The automatic gain control allows recovering the amplitudes at depth. The result of the time domain processing flow is a high quality, clear and high-resolution image, in which sedimentary layers and tectonic structures can be satisfactorily identified and interpreted.

2.4. Seismic data processing and modelling

Seismic waves gather subsurface information on the physical properties of the Earth. After a seismic survey, the data collected is processed and/or modelled to extract this information and obtain a 2D cross-section or 3D volume of the image or map of subsurface properties.

Data processing converts field recordings into meaningful seismic sections that reveal and help delineating the structure of the subsurface. The reflectivity as an attribute of related seismic traces at the selected point of the reflector provides the migrated image needed for seismic stratigraphic interpretation. Seismic data, specially MCS data, are processed and combined to construct and image of the Earth's subsurface whose vertical axis is two-way travel-time (TWT) (Fig. 2.19). There is no unique data processing flow, instead optimal sequence and parameters for each step have to be found for each survey by means of testing.

On the other hand, as a seismic trace is one-dimensional, first modelling approaches were aimed at reproducing the subsurface properties at the recording location. The models obtained were based on a priori information extracted from well logs (Fig. 2.20). The impulse response (reflection coefficient) generated for each interface in the model is convolved with the source wavelet to calculate the synthetic seismogram. In the presence of lateral variations between different recording positions a two dimensional modelling is required to properly interpret the medium. Normal incidence ray tracing has been the most widely used method. Multiple calculations following a trial-and-error scheme in order to explore the model space was the first methodology to find a numerical model that explains the observations. Indirect interpretations involves four steps: 1) Construction of a reasonable model, 2) Computation of its response (forward modelling), 3) Comparison of computed with observed responses and 4) Alteration of model to improve correspondence of observed and calculated responses and return to step 2. The synthetic recordings are modified by changing the thickness, replacing or eliminating units to finally recreate the recorded ones. The earth model parameters that generate the model section are confined to some limits extracted from the local geological knowledge of the area. However, the forward modelling methods are not efficient and non-unique. Finally, three-dimensional modelling, which is the most appropriate due to the 3-D character of the data collected and earth modelled, is not commonly used because the high acquisition cost.

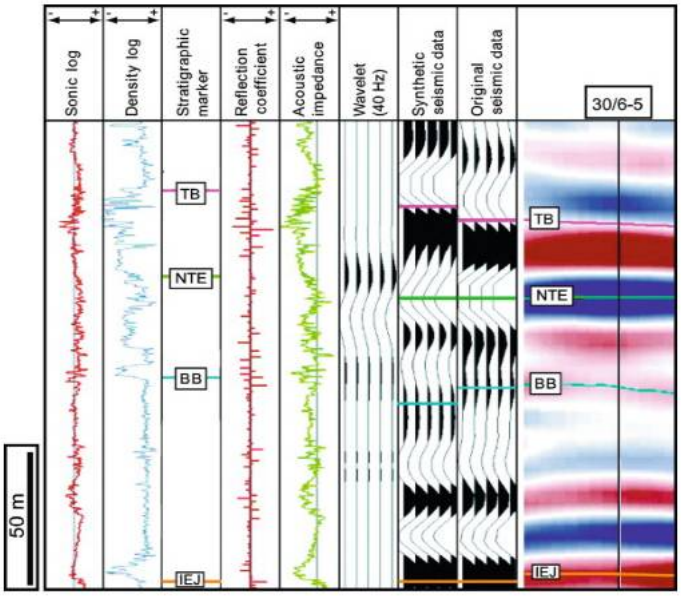

Figure 2.20: Well-to-seismic tie (Onajite, 2014).

Aside from forward modelling approaches, there is also the inverse modelling or inversion. The imaging process is typically a sort of forward and inverse modelling. Their major difference is that inversion tries to obtain a (geological) model of subsurface parameters that predicts the observed data, while forward modelling just simulates the data responses from a predefined model. Seismic tomography is a kind of inverse modelling. Earthquake seismology was the first in applying tomographic methods to produce a velocity model of the subsurface. It tries to fit the travel-time information of some pre-selected seismic phases.

There are two types of travel-time tomography depending on the seismic arrivals used as input: first arrival or reflection tomography. In reflection tomography (e.g. Bishop et al., 1985), it is required to define the geological interface or boundary in which the energy is reflected back. First arrival tomography involves refracted or transmitted waves that have travelled through the subsurface without reflection (e.g. Toomey et al., 1994). Long offset (compared to the subsurface target depth) or wide angle acquisition geometries are required to collect refracted energy as first arrivals. Furthermore, first arrival and reflection tomography can also be performed together in a joint travel-time tomography (e.g. Hobro et al., 2003; Korenaga et al., 2000). WAS systems are designed to provide a 2D/3D map of the subsurface by using mainly wide-angle refraction and reflection travel-time information. The Vp model is built to explain the seismic phases selected, and is then used to generate an image of the position of the reflecting horizons and Vp contrasts in the subsurface (Fig. 2.21).

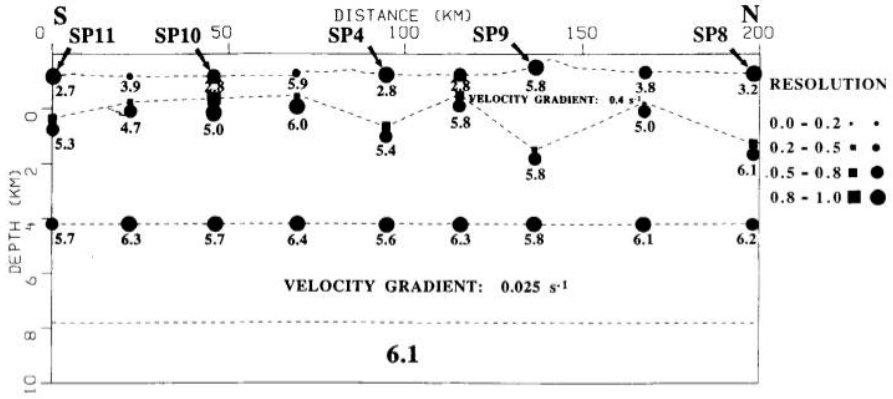

Figure 2.21: Final upper crustal Vp model for the north-south Nevada PASSCAL data. The five shot point locations are indicated. The dashed lines are layer boundaries. The Vp points are labelled in km/s and indicated by circles; the boundary nodes are indicated by squares. The size of the Vp and boundary nodes indicates their resolution. There is no Vp discontinuity across the boundary at 4.2 km depth. The vertical Vp gradient was fixed in the first and third layers according to the values indicated. The boundary at 7.8 km depth separates the upper and middle crust. (Zelt and Smith, 1992).

After determining the seismic travel times, a ray tracing modelling of the energy propagation through the medium is applied by solving equations to a velocity model. Chronologically, the most commonly applied ones are those defining analytical solutions to expand a wavefront (shooting or bending methods (Julian & Gubbins, 1977)), those calculating first-arrival wavefront travel times and associated ray paths solving by finite difference extrapolation method the eikonal equation (Vidale, 1988), and those using graph theory to expand a wavefront by finding the shortest path for all connections, with or without further ray bending refinements (Nakanishi & Yamaguchi, 1986; Moser, 1991; Moser et al. 1992; Toomey et al., 1994; Zhang et al., 1998; Korenaga et al., 2000; Van Avendonk et al., 2001) (Fig. 2.22).

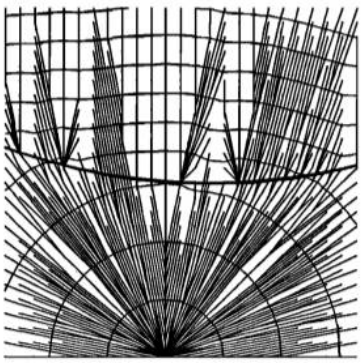

Figure 2.22: Two-dimensional 25x25 grid, covering a model with two horizontal layers with velocities 1.0 and 2.0, separated by a curved interface (heavy line). The shortest paths from one node at the bottom of the model are shown (thin lines), together with the isochrons (contours). (Moser et al., 1992).

Nowadays, seismic tomographic techniques have evolved and they can account for more wave attributes than the travel-time information alone. As an example, full-waveform tomography models the energy propagation of the whole wavefronts (e.g. Virieux and Operto, 2009; Davy et al., 2018) (Fig. 2.23). In the methodology part of this thesis appears a more detailed explanation on the travel-time tomography and the full-waveform inversion methods.

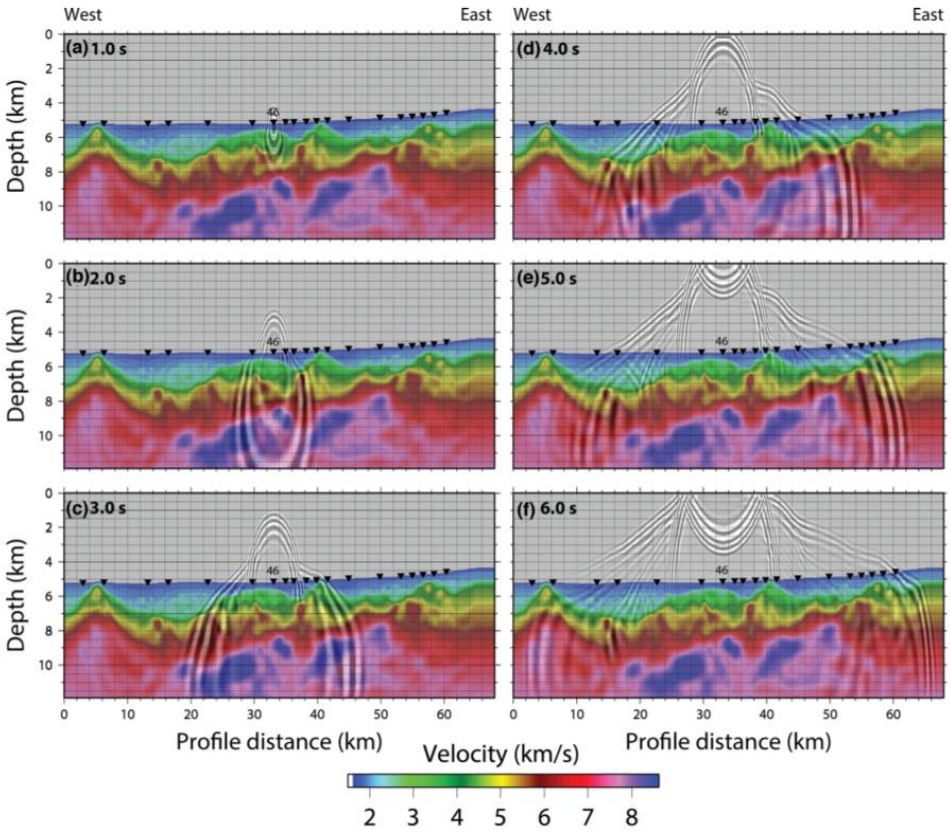

Figure 2.23: Propagation of a derived source wavelet through a Vp model, originating at OBS46, at discrete times: (a) 1.0 s, (b) 2.0 s, (c) 3.0 s, (d) 4.0 s, (e) 5.0 s and (f) 6.0 s. Black upturned triangles indicate the location of utilized instruments. Vertical exaggeration is 3.2. (Davy et al., 2018).

Long streamer MCS data are now being used to perform first arrival or waveform tomography (e.g. Delescluse et al., 2011). The increase of the streamer length allows to record refracted waves, so long-wavelength information, as first arrivals that are essential for building a model with the correct kinematics. However, the major problematic is the huge budget required to perform the seismic acquisition survey. An alternative to apply first arrival or waveform tomography to relatively short-offset MCS data is by using re-datuming techniques (e.g. Cho et al., 2016). The idea is to modify the recordings to highlight the refracted signal of the shallow subsurface. This re-datuming technique has been developed and applied in this thesis to synthetic and real MCS data, so that refracted waves can be identified as first arrivals and TTT can be conducted. For this, the first step of the proposed workflow consists on applying re-datuming techniques and they are presented in detail in Chapters 4, 7, and 10.

Part II

OBJECTIVES

From Small Things
(Big Things One Day Come)

(Bruce Springsteen)

Chapter 3. Specific objectives

The **general objective** of this thesis is to design, implement and test a combined data processing and modelling strategy to retrieve Vp models of the subsurface Earth structure with the highest possible resolution, using only limited-offset, relative high-frequency marine MCS streamer data as input. The purpose is having a new tool to improve the geological interpretations of the shallow subsurface structure based directly on Vp models, which provides more information on rock properties than seismic reflectivity alone. For this, we propose to use different tomographic methods and seismic imaging techniques and combine them wisely so that we can mitigate the drawbacks and enhance the potential of each of them.

This overall goal will be pursued by combining techniques based on MCS data re-datuming to recover refracted waves not visible in the original records, then do a travel-time tomography to obtain coarse initial Vp models, and finally full-waveform inversion to refine these models and extract the high-resolution features. The applicability of these techniques require the development and implementation of several original codes and adapting other existing ones to the particular characteristics of the problem. First, I will test the strategy and codes with synthetic data, then as final objective I will apply them to field records.

More in detail, the **specific objectives** to be met in this thesis are the following ones:

1.- Back-propagating marine MCS streamer data to a virtual datum in order to recover refracted waves from the seismic records. This includes:

1.1) Designing a re-datuming or downward continuation (DC) strategy (Berryhill, 1979, 1984).

Several methodologies have been proposed to reveal refraction signal by simulating another acquisition geometry (e.g. Arnulf et al., 2014, figure 2). The main challenge was to develop a robust and fucntional algorithm to DC the seismic records, easy to implement, and that can deal with spatial velocity variations in the water media and irregular datum surfaces, which usually coincide with the seafloor location. For this, here the designed re-datuming approach is based on the wave equation to extrapolate the recorded data to a virtual datum surface so that refractions can be retrieved as first arrivals. We have implemented DC following the steps proposed by Berryhill (1979, 1984) and the scheme of McMechan (1982, 1983). The overall goal of the DC algorithm is retrieving early arrivals, particularly the refractions that contain valuable information on the velocity of the media. These seismic arrivals are masked by the energetic water wave traveling directly between source and receivers in MCS systems. This issue is particularly acute for short offset MCS data and deep-water environments. So, modifying

the recordings to highlight the early arrivals is a key step to obtain accurate Vp models by mitigating the velocity-depth trade-off that is intrinsic to reflection tomography.

1.2) Implementing and testing the DC code.

The DC consists on back-propagating the seismograms from the original positions to generate virtual recordings in a new datum location. This is done by adapting a numerical solver previously developed at the Barcelona-CSI (23DAS, Dagnino et al., 2016). This code is based on a finite difference solution of the acoustic wave equation in time domain. The DC code will be tested by simulating streamer data of a typical marine seismic acquisition set up (both sources and receivers at sea level) generated in benchmark synthetic models that represent the Earth. The results can be validated by comparing the DC records with the ones simulated using the target model and the virtual streamer geometry set up with both sources and receivers located in the seafloor.

2.- Testing and implementing joint refraction and reflection travel-time inversion strategies combining downward continued and original MCS data.

2.1) Identifying and picking first arrivals in the DC MCS records and secondary (reflected) arrivals at the original MCS shotgathers.

This will be done in the shot gather domain using industry software (Claritas). The shot spacing for the travel-time picking will define the final model coverage and data redundancy.

2.2) Applying first arrival and/or joint refraction and reflection arrival TTT with the above-described first arrival data set and testing different regularization parameters to obtain a smooth version of the Vp model.

Our hypothesis is that coarse Vp models with the correct kinematics can be constructed by applying tomographic methods with the travel times of the first arrivals picked in the downward continued MCS data (e.g. Arnulf et al., 2011), especially when we combine this with travel times from reflected phases. Using these selected phases as input and the TOMO2D code (Korenaga et al., 2000), I will obtain a Vp model of the subsurface. I also will test the effects of different inversion parameters and tune them to get the best inversion result.

3.- Applying FWI to the MCS data using the TTT model as initial reference to add high-resolution details to the model.

I will perform FWI of the original MCS records using the code developed at Barcelona-CSI (Dagnino et al., 2014; Jimenez-Tejero et al., 2015), which uses the same finite difference solution of the acoustic wave equation in time domain, also used in the DC

step. To mitigate the inherent nonlinearity of waveform inversion by avoiding cycle skipping, we will use the Vp model obtained by either first arrival TTT (synthetic tests) or joint refraction and reflection TTT (real data set) as initial model for FWI. Finer structural details will be sequentially incorporated in the model following a hierarchical multi-scale inversion strategy.

4.- Applying the workflow developed and tested with synthetic data, to a real data set and interpret the obtained model.

I will use a field data acquired with a 6 km long streamer of 480 recording channels in the Alboran basin (TOPOMED-GASSIS experiment).

4.1) Applying downward continuation

I will select and preprocess the real MCS data set. Real data are affected by different sources of error that are difficult to simulate in synthetic data, such as noise, multiples and reverberations, source signature... A preprocessing step to increase the signal-to-noise ratio present in the recordings without affecting wave amplitudes at different frequencies will be designed.

4.2) Applying joint refraction and reflection travel-time inversion strategies to obtain a seismic Vp model.

I will identify, pick and incorporate the seismic phases corresponding to a major reflecting interface (e.g. top of the basement) together with the DC first arrivals into a common inversion scheme using TOMO2D. The goal is retrieving both Vp as well as the location and geometry of the reflector.

4.3) Applying FWI.

I will use the Vp model obtained by joint refraction and reflection travel-time inversion as initial model for FWI, applying the inversion scheme tested with synthetic data.

4.4) Checking the FWI model by combining it with the MCS data.

I will analyze the final model by comparing and combining it with the original MCS data. First, I will transform the 2-D Vp model in two-way time and compare it with the time-migrated seismic section. Then, I will also use the FWI model to pre-stack depth-migrate the MCS profile, and check whether energy is correctly focused at depth.

4.5) Geological interpretation of the results.

I will describe and interpret the subsurface structures shown in the FWI in terms of the regional geology and geodynamic setting.

Part III

METHODOLOGY

Born To Run

(Bruce Springsteen)

Chapter 4. Re-datuming method

Re-datuming techniques are typically used to remove the effects of irregular topography and complex overburden. In these conditions, the assumption of a vertical near-surface ray paths adopted for standard static corrections procedures is not valid. Thus, the seismic data needs to be improved by using a re-datuming procedure. The purpose is to transform the data measured at a certain surface to simulate data referenced to a new recording surface. Therefore, seismic data acquired by a virtual experiment carried out in a new surface can be generated from the original recordings. The application of this technique to MCS data in deep-water settings has deserved particular attention as a way to highlight the early refraction information hidden by near vertical reflections in the shot gathers. The idea is eliminating the effect of the water column, and thus retrieve the refracted phases as first arrivals in order to apply travel-time tomography techniques, by moving the experiment set-up to the seafloor surface (both sources and receivers).

In this chapter I present the mathematical formulation and procedure of the re-datuming method, also known as downward continuation (DC), that I have implemented during my PhD to achieve the above-mentioned goal. I have modified a forward solver code developed by other group members of the Barcelona-CSI (Dagnino et al., 2016) to back-propagate the data recordings and retrieve the virtual re-datumed wave field. The code used and the data sorting algorithms that I have developed are both parallelized using MPI standards in order to reduce computational time. In addition, due to the large number of traces involved in the calculation of one re-datumed trace, a multi-shooting strategy is also used to obtain the re-datumed wave field from a single back-propagation of all the traces that belong to the same gather. The application of this strategy allows to substantially reduce computational time and storage memory.

The description of the re-datuming method is presented in the next section. I first briefly introduce the basis of the wave equation datuming (WED) techniques. Then, the parameterization used for both model and acquisition geometry is presented. The model parameterization consists on the description of the physical properties by using a discrete representation of the medium. On the other hand, the acquisition geometry parameterization is the positioning of the original and virtual geometry set-ups on the discrete model. Next, I present the wave field extrapolation operator and the computational method used to back-propagate the data through the medium following a physical approximation. Finally, the steps of the re-datuming procedure are presented and illustrated. The multi-shooting strategy and the parallelization of the code are also described in additional sub-sections.

Wave equation datuming (downward continuation)

WED is a model-based re-datuming method that, as its name suggests, uses the wave equation to transform the original recordings into a data set measured in a different surface. The WED technique was first introduced by Berryhill (1979, 1984). WED consists on upward and downward continuing the recorded wave field through a medium defined between two arbitrarily-shaped surfaces. The Green's function computed from the medium model defined between those surfaces is used to build the wave propagation re-datuming operators. An overview of the different types of re-datuming methods, depending on its kernel formulation, is made by Schuster and Zhou (2006). Re-datuming of sources and receivers is applied as a two-step process over different group domains. Operating on a common source group of seismic traces is the first step to move the receivers from the acquisition surface to the new datum plane. In the second step, the datum plane of the sources is changed operating on a common receiver gather. The finite difference (FD) solution of the two-way acoustic wave equation in time domain is used here to extrapolate the data groups through the medium, using the 2/3D Acoustic Solver (23DAS) code developed at the Barcelona-CSI (Dagnino et al., 2016).

The most important characteristic of the WED formulated in this thesis is that it allows retrieving refracted seismic phases as first arrivals using the target Vp model between datums and the two-way wave equation (Mulder, 2005). Other re-datuming approaches, as Marchenko re-datuming, provide better estimates of the target reflected fields (Wapenaar et al., 2014; Vasconcelos et al., 2014; Wapenaar and Thorbecke, 2017) but under the assumption that the first arriving wave is the direct wave, without considering refracted waves.

The main advantage of WED using the FD approach is that, as a recursive method, local velocities can be used and, therefore, it can deal with lateral Vp variations within the water column and irregular datum surfaces, such as the seafloor. However, WED techniques need the target Vp model or a very good approximation to construct the re-datuming operators. Otherwise, amplitude and/or phase errors due to operator approximation can affect the wave field during the extrapolation. This method has no additional problems or inherent limitations aside from those associated with finite differencing, which can generally be overcome by the use of an accurate approximation of the reality. Its implementation is simple and it can also be easily extended to more complex approximations of the wave equation (i.e. elastic) and to more space-dimensions (3D) requiring only an appropriate modelling code.

The description of the DC parameterization and its procedure will be focused on the one used in this thesis. The flow diagram of the DC scheme used to change the datum of the recordings is shown in Figure 4.1.

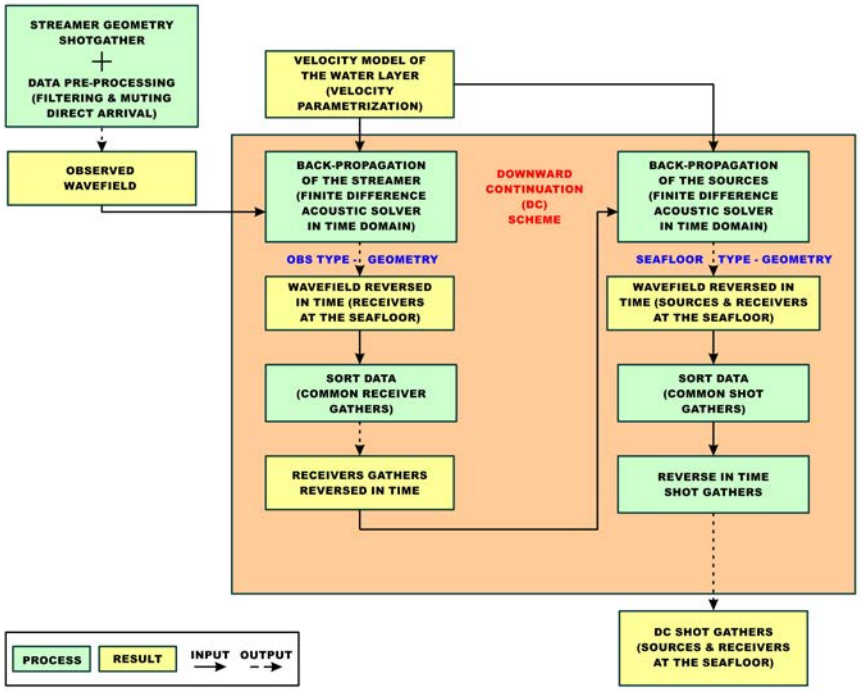

Figure 4.1: Flow diagram of the re-datuming method applied. The DC steps and data processes are represented in green boxes, whilst the obtained wave fields are in yellow.

4.1. Parameterization

This section describes the parameterization of the DC code that I have used, for both model and acquisition geometry. The parameterization characterizes the physical properties of the medium between two surfaces that coincide or include the two arbitrarily-shaped datums using a discrete representation. The accuracy of the result is influenced by the quality of the discrete approximation of the reality made. The acquisition geometry parameterization defines the positions of the original and virtual geometry configurations at its corresponding mesh nodes. The defined nomenclature will be useful for the ulterior re-datuming formulation.

Model parameterization

The DC code is formed by the 23DAS forward modelling solver that uses the FD scheme to solve the 2-D acoustic version of the wave equation in time domain. Its goal is to retrieve the acoustic pressure field of the media from a source response. The media is

represented by a 2-D Cartesian grid defined by the spatial coordinates of their nodes. The model has a regular parameterization in which nodal spacing is constant and equal for both horizontal and vertical directions. It can be interpolated by the code if a higher spatial resolution is required. The spatial resolution is limited to half the wavelength of the dominant frequency generated by the source. Thus, the nodal spacing of the mesh has to be able to reproduce the smallest wavelength to be resolved by the extrapolation process. Otherwise, the reconstructed wave field can be affected by aliasing effects, producing a decrease in the method resolution.

The Vp and density values are the physical variables that describe the media. Its values are defined at the mesh nodes for the discrete representation. In our case, and given that the medium of interest is water, the density values are fixed to 1 g/cm^3 in all the grid points. No restriction for Vp is imposed, so the model can have assigned a different value at each grid point without any further complication or additional computational cost. This media parameterization allows representing all the media variations, vertical and lateral, producing accurate results with moderate computational resources. Thus, homogeneous as well as heterogeneous media can be easily described with this model parameterization. However, if the Vp knowledge is inaccurate or erroneous, these errors would affect the result.

If the new recording surface does not coincide with the model boundary, the velocities of those nodes that are in between must be assigned with constant values. The objective is to avoid the insertion of spurious reflections from below the target recording surface that can interfere with the target wave field. Hence, those points must act as additional absorbing boundary nodes.

Parameterization of the acquisition system

All the array positions, original and virtual, have defined the sources and receivers at its corresponding grid points inside the model. The parameterization of the acquisition system consists on assigning sources and receivers to mesh nodes. In the same way, the seismograms are also represented by their source and receiver mesh positions. In the 2-D medium, spatial coordinates are denoted by (x, z), being "x" the horizontal coordinate and "z" the depth or vertical coordinate.

In the original experiment, so in the input data, the shot surface is defined as (x_s,z_s), where x_s and z_s represent the horizontal and depth positions of the sources respectively. Similarly, the recording surface is defined as (x_r,z_r), where x_r and z_r are the horizontal and depth positions of the receivers of the streamer, respectively. Thus, a shot gather is parameterized by the coordinates of one point in the shot surface and as many points as receivers are in the streamer, and a receiver gather by the coordinates of one point in the receiver surface and as many points as sources illuminate the receiver position.

The bathymetry surface is described as (x_{bat}, z_{bat}). The horizontal coordinates of the positions that are illuminated by the source downgoing wave field at the seafloor surface are denoted as x_d , while that propagating upwards from the seafloor as x_u . The definition of these coordinates will help to show the difference between the original wave field propagation and the simulated one, so the approximation of a continuous wave field using discrete and finite seismograms.

In the virtual experiment configuration, so in the output data, the horizontal source and receiver positions are the same as for the original experiment, so the same parameterization is used, x_s and x_r respectively. Because the shape of the final surface corresponds to the seafloor, the depth coordinates z_{bat} are also used for the definition of the depth positions of the downward continued geometry.

The coincidence between mesh nodes and the source-receiver positions are also important to get more accurate results and avoid interpolations. The approximate positions can also introduce round-off errors in the numerical computation of the pressure wave field. If the receiver position does not coincide with a mesh node, a bilinear interpolation to ensure continuity of the pressure wave field is used in the grid cell where it is located.

4.2. Wave field extrapolation

The wave field modelling technique aims at simulating the effects of the wave field propagation by carrying out a forward extrapolation. The forward extrapolation is done by convolution along the spatial axis. The Green's function defined through the wave equation, describes the wave propagation outward from a point source with spherical symmetry according to the Huygen's principle that every point on a wavefront can be regarded as the source of the subsequent wave. Moreover, the Snell's law, which defines the wave field behaviour crossing an interface, has to be fulfilled at all emergency angles. In 2-D seismic, the convolution (*) that describes the recorded wave field can be expressed as

$$S(x_s, z_s; t) * G(x_s, z_s; x_r, z_r; t) = u(x_r, z_r; t) \quad (4.1)$$

where *t* represents the time, *x* and *z* the previous defined spatial coordinates, *S* the source signal, *G* the Green's function that defines a forward wave field extrapolation process in a heterogeneous subsurface observed at (x_r, z_r) from a source at (x_s, z_s) and *u* is the seismic trace. Thus, in the forward problem calculation, the source signal and the wave equation that describe the Green's function are the two main components that characterize the extrapolation process. Additionally, as the propagation of the wave field is done through a finite medium, the forward modelling also requires the definition of boundary conditions.

The source function can be characterized mainly by its shape along the time and frequency content. The recorded seismograms contain the information of the medium in the source's frequency band. The optimal wave equation formulation depends on the type of data available and on the information to be retrieved. Here, we use the 2-D acoustic wave equation to describe the wave propagation through the media. It is well-justified in our case because our target re-datuming surface is the seafloor so the medium concerned is just the water column. Thus, transmission losses due to elastic effects as wave conversion, etc, are ignored.

The following 2-D acoustic differential equation,

$$\frac{1}{\kappa(x,z)}\frac{\partial^2 u(x,z;t)}{\partial t^2}+\nabla\cdot\left(\frac{1}{\rho(x,z)}\nabla u(x,z;t)\right)=s(x,z;t) \quad (4.2)$$

where x is the horizontal space coordinate, z the depth or vertical space coordinate, t the time, u the pressure wave field, s the source signal, κ the compressibility, and ρ the density of the medium, is implemented in a recursive and explicit FD scheme of the two-way wave equation in the space-time domain (Dagnino et al., 2016). The advantages of the two-way wave equation formulation are manifold. First, it can deal with events such as multiples and refractions, not only primaries (Mulder, 2005). Moreover, since no paraxial approximation is considered, it becomes more stable even in the presence of steep dips.

The FD methodology to integrate numerically the wave equation is the Runge-Kutta (RK) method of fourth order accuracy in time (Lambert, 1991). It is performed using three intermediate steps to weight the time integration and obtain the forth order precision in the time integration. Schematically,

$$\begin{aligned}
u^1 &= u^n \\
u^2 &= u^n+\alpha_2\,\delta t\,L(u^1) \\
u^3 &= u^n+\alpha_3\,\delta t\,L(u^2) \\
u^4 &= u^n+\alpha_4\,\delta t\,L(u^3)
\end{aligned} \quad (4.3)$$

where L represents the wave equation operator, u the field and α the RK coefficients for the intermediate steps, with $\alpha_2=\frac{1}{2}$, $\alpha_3=\frac{1}{2}$ and $\alpha_4=1$. Finally, the next field in the next step is weighted as

$$u^{n+1}=u^n+\delta t\left[\beta_1 L(u^1)+\beta_2 L(u^2)+\beta_3 L(u^3)+\beta_4 L(u^4)\right] \quad (4.4)$$

where β are the RK coefficients for the final step, with $\beta_1=0$, $\beta_2=\frac{1}{2}$, $\beta_3=\frac{1}{2}$ and

$\beta_4 = 1$. The stability condition for the time step (δt) used here is

$$\delta t > 1.25 \frac{\delta x}{max(v_p)} \quad (4.5)$$

where δx is the spatial step, v_p is the maximum velocity of the model. In order to optimize the numerical computation and avoid grid dispersion, the optimal time step is the largest value that fulfils the stability condition. The space derivatives are discretized using a staggered grid (Virieux, 1986) with a sixth-order Taylor expansion.

In the wave field extrapolation process, complex-frequency-shifted perfectly matched layers (CFS-PML) (Zhang and Shen, 2010) are defined as absorbing boundary conditions. These boundary conditions are more stable than the traditional perfectly matched layer (PML). While a damping term is the only variable of the PML, the CFS-PML has two extra terms to assure a better absorption. These additional CFS-PML parameters bend the waves that travel parallel to the boundary making easy its input at the added mesh nodes located outside the model boundaries. The number of added node layers must be large enough to assure the efficient mitigation of spurious events.

The forward modelling is also used to derive the inverse extrapolation operator. The objective of the inverse extrapolation is removing the effects of the wave field propagation by deconvolution along the spatial axis. WED methods have different types of inverse extrapolation operators derived for example from the Kirchhoff-summation approach (Berryhill, 1979, 1984; Bevc, 1997; Tegtmeier et al., 2008), the plane-wave method (Gazdag, 1978; Harding et al., 2007; Arnulf et al., 2014), or the FD approach (Claerbout, 1976; McMechan, 1982, 1983; Mo, 1997). A discussion of its different characteristics can be found in Berkhout (1981). The accuracy and efficiency of the result largely depends on the methodology associated to the operator calculation. The solution improves by the use of a higher-order scheme and a finer computational mesh, yet at the expense of increasing computational costs. The data sampling rates have also an influence on the expected resolution and required computational resources. Higher data sampling rates favour the definition of the wave field, avoiding aliasing effects and producing a better result, but at higher computational costs. Here, we use the FD approach because it is implemented in our solver code for the forward extrapolation of the wave field, and has the advantages explained in the previous section.

In this thesis, the inverse extrapolation follows the idea of the boundary value migration (BVM) scheme of McMechan (1982, 1983). Its FD reverse-time migration technique is based on the reversibility of the wave equation. It solves the inverse problem in the form of a boundary value problem. The migration is performed introducing backwards in time the data recordings at each corresponding grid position as a new boundary condition, whilst energy is transferred through the grid nodes that represent the medium following the wave equation. This technique is also used for the determination of source parameters. It is interesting to note that migration is actually done as a DC procedure.

Claerbout (1976) considers several definitions for the migration process. The main difference between McMechan (1982, 1983) work and the one presented here is that in our case this technique is used for the inverse extrapolation of wave fields in a new datum surface focusing progressively in time and space the arrivals contained in the recordings rather than migrating the time section according to an imaging principle. The simulation of the wave field recorded at a receiver located in our new datum is possible because the waves actually travelled through that medium, so you can extract this information by combining the entire set of traces that recorded one shot (Berryhill, 1984). The idea is based on the Huygen's principle which allows to consider as secondary sources the points of the new datum surface where the wave field has propagated through earlier in time. So, the new datum positions can be interpreted as secondary extended sources radiating energy simultaneously through time.

As in seismic modelling, the inverse extrapolation according to the BVM scheme is also described by the source, wave equation and boundary conditions used. The source function through time in this case is formed by the observed wave field. The wave field transferred from the seismogram to the 2-D model plane at each time step is taken as an equivalent source. The complete seismogram is used; thus no windowing or pre selection and arrival identification are needed. The usage of the entire trace avoids the extensive time-consuming user interaction of properly identify and isolate the reference event/s as is done in other techniques (e.g. Vrolijk et al., 2012). It must be keep in mind that prior to re-datuming it is convenient to improve the SNR ratio by (1) delete noisy channels, (2) apply some Butterworth filtering, and (3) mute direct arrival. The proper source spacing and optimal recording time step are the ones that avoid aliasing issues and grid dispersion, and reduce the effects caused by the discrete approximation of the wave field.

The inserted wave field is progressively expanded (Figure 4.2) according to the acoustic wave equation solved by the forward extrapolation scheme previously described. This process is the reverse of the forward propagation because the recorded traces acting as sources (upper seismograms in Figure 4.2) are introduced in the reverse time. This is because for a lossless medium, the wave equation is symmetric in time (reversible) and the Green's function is reciprocal. The idea is that reflectors exist in the Earth at places where the onset of the downgoing wave is time coincident with an upcoming wave (Claerbout, 1976). Thus, the target forward propagation of the wave field is compensated for the inverse extrapolation that sends the recorded energy back through the same paths but in the opposite direction. The progressive focusing in time and space of the wavefronts make it possible the recover the wave field at an earlier stage. Hence, the re-datumed wave field is directly imaged at the new surface depth along the extrapolation time.

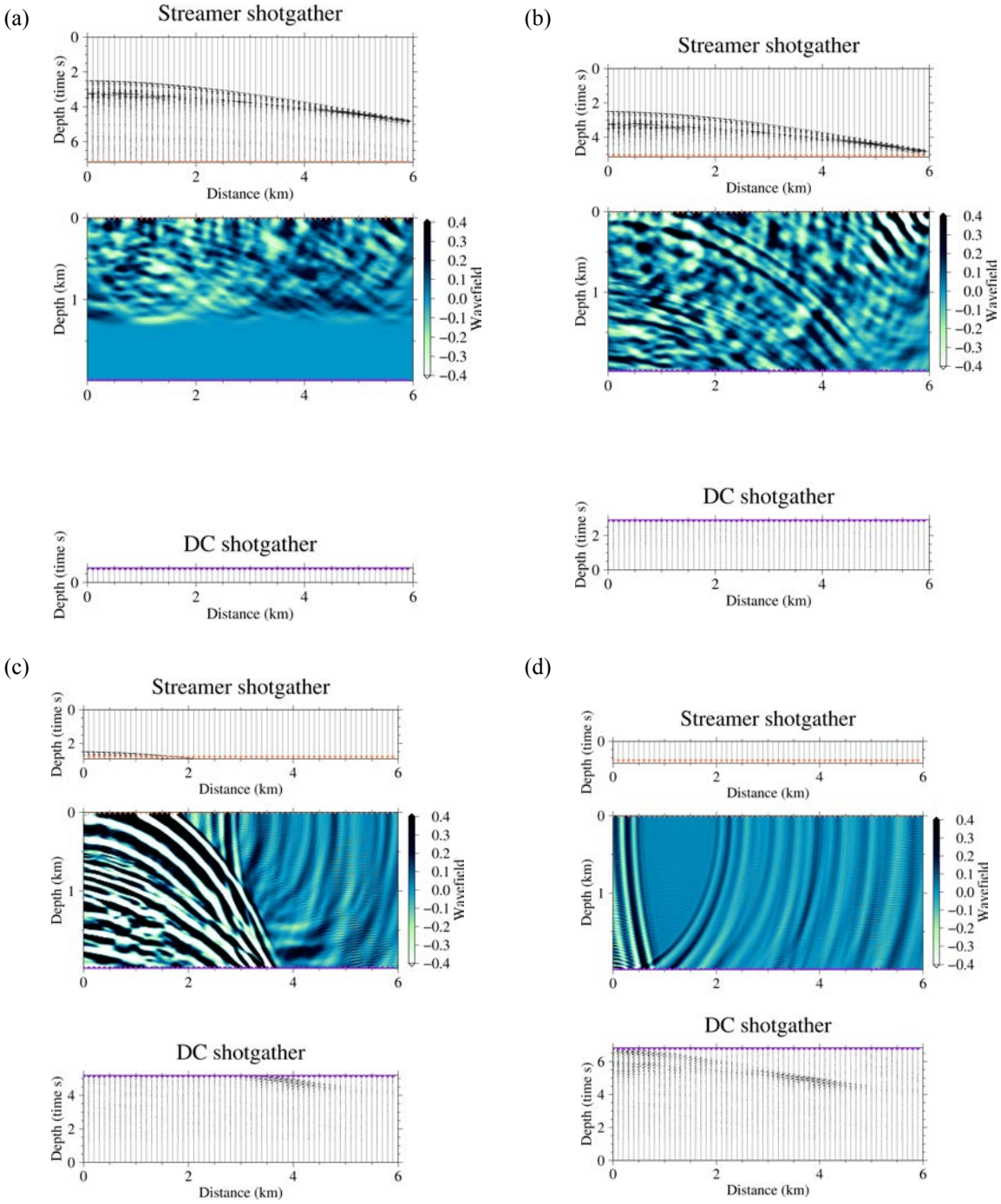

Figure 4.2: Snapshots from the wave field propagation in the water medium (Vp model) represented at successive times (a) 0,75 s, (b) 2.75 s, (c) 5.25 s, and (d) 6,75 s, together with the original or inserted shot gather (upper seismogram) send from the sea surface (orange triangles) and the resultant virtual shot gather (lower sesimogram) recorded at the seafloor (purple circles).

In the inverse extrapolation process, the absorbing boundary conditions (CFS-PML) are imposed to avoid spurious reflections in all model boundaries that may cause interference and mask the correct seismic phases. The only exception is the time-dependent boundary values associated with the equivalent sources.

The spatial and temporal resolution of the estimated traces at the virtual array positions depend on the sampling rate and on the maximum offset of the original recordings. One limitation that is inherent to the use of discrete field data for the reconstruction of the wave field is that only the wave contributions present in the recording points are considered, and thus only these ones can be used to reconstruct the virtual data in the new datum surface. Hence, only the energy that have the adequate emergent angle to reach the recording array is taken into account to perform the back-propagation. Obtaining the complete wave field in the new datum is therefore not possible with this technique. A better approximation of the target wave field, and thus a better result, would be achieved using denser and longer arrays. For sparse data sets, dispersion effects attenuate the high-frequency content and only the main phases and relatively low frequencies are simulated. Therefore, re-datumed arrivals would be less focused due to a larger amplitude loss and noise effects, but they would nevertheless be correctly located.

Another effect that can affect the result is the presence of artefacts such as diffraction tails located at the edges of the array and therefore where the observed wavefronts are truncated. These artefacts are due to the finite aperture of the recording system. Their effects are larger for small aperture set-ups (short offset acquisition systems), where they can interfere with the energy focusing in the new datum surface and mask the target arrivals. Moreover, the finite aperture of the acquisition array causes a non-uniform illumination of the wavefronts, which results in energy mitigation near the recording limits.

The resulting extrapolated wave field is also influenced by numerical dispersion, which attenuates high frequencies as it travels backwards in time through the medium. Thus, the spectrum of the frequency bandwidth of the data is reduced due to the Earth effect that acts as a filter (Berkhout, 1997a, 1997b). The frequency dispersion is advantageous on the reduction of high-frequency noise. During the back-propagation the noise of the recordings is separated from the original signal and as it is spatially incoherent is attenuated.

Moreover, the energy coming from the direct and surface waves is not included. In general, the amplitude of the result is also reduced due to the energy loss through the absorbing model boundaries during the inverse extrapolation process. Therefore, amplitude is not preserved as in other re-datuming approaches (Schuster and Zhou, 2006) and its attenuation factors are related to geometrical spreading and transmission losses.

As mentioned above, the equivalent source is based on sending back simultaneously the energy recorded at each time step. The process is repeated sequentially for all time steps.

The computational effort for the reconstruction of the wave field following this extrapolation scheme might be large depending on model dimensions and on the node size. The efficiency of this procedure that involves the wave field extrapolation of all the shot gathers is highly reduced by implementing multi-shooting (subsection 4.2.2.) and parallelization (subsection 4.3.) in the code.

4.2.1. Re-datuming procedure

Re-datuming can be considered as a data processing procedure (Barison et al., 2011). It has received a special attention as a powerful technique to remove the effects of a complex topography, interpolate data, remove the multiple... In marine settings, the effect of the wave propagation through the water media can be removed from the observed data changing the recording surface to a virtual one located at or close to the seafloor. The application of this technique becomes particularly relevant to apply first arrival travel-time tomography to streamer data in deep-water areas and short offset geometry set-ups. In this cases, refractions are hidden by the direct water wave and restricted to long offsets, normally beyond the length of the streamer (Cho et al., 2016; Arnulf et al., 2011, 2013, 2014) (Figure 4.3(b)). Note that refracted phases emerge after a critical distance, x_{crit} ,

$$x_{crit} = 2 \cdot z_0 \cdot tg\left(i_{\text{crit}_0}\right) \quad (4.6)$$

where z_0 is the depth of the layer and i_{crit_0} the critical angle, for which the refraction angle equals 90º, so $\sin\left(i_{\text{crit}_0}\right) = \frac{v_0}{v_1}$, where v_0 and v_1 are the velocities of consecutive layers. However, they overtake the direct wave and start appearing as first arrivals at a crossover distance, x_{cross} .

$$x_{\text{cross}} = 2 \cdot z_0 \frac{\sqrt{v_1 + v_0}}{\sqrt{v_1 - v_0}} \quad (4.7)$$

In Figure 4.3, the direct wave is represented by the green ray and it propagates with the velocity of the water column, v_0 =1.5 km/s. The total distance where refraction information is visible as first arrival phases (Δx) in the streamer data are expressed as,

$\Delta x = sl - x_{cross}$; when $sl - x_{cross} > 0$
$\Delta x = 0$; when $sl - x_{cross} < 0$

where sl represents the streamer length and it is typically smaller than the x_{cross} , so $\Delta x = 0$. Given a water column of 1 km depth and a subsurface velocity of v_1 =1.8 km/s,

the crossover distance (Eq. 4.7) is more than 6.6 km. For academic limited offset seismic acquisition systems, where the streamer length (sl) is 5 km, the identification of refracted phases as first arrivals is not possible, $\Delta x = 0$ km. However, for long-offset streamer set-ups, e.g. 10 km (sl), the distance with visible refractions as first arrival phases is $\Delta x = 10 - 6.6 = 3.4$ km.

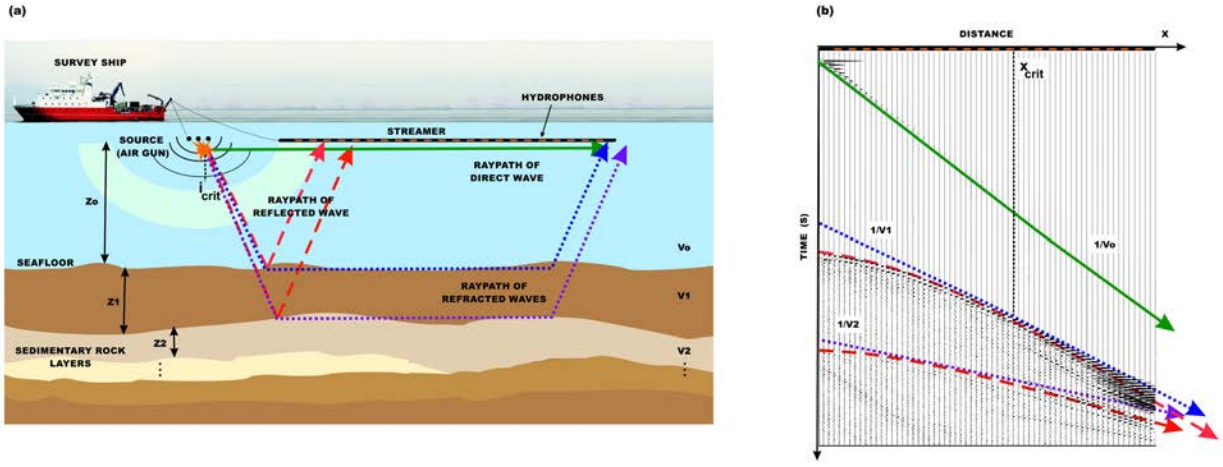

Figure 4.3: (a) Scheme of the ray trajectories corresponding to a streamer-type set-up and its geometric parameters, where $z_j \; j = 0,1,\ldots$ defines the depth of each layer, $v_j \; j = 0,1,\ldots$ its Vp and $i_{\text{crit}_j} \; j = 0,1,\ldots$ its critical angle. Green line is the direct water wave, blue and purple doted lines are refracted ray paths in different interfaces, and its corresponding reflected ray paths are the pink and red dashed lines respectively. (b) Shot gather diagram corresponding to the streamer-type geometry in (a). Refractions are not present as first arrival phases, so they cannot be identified and travel times cannot be used for Vp modelling.

In the streamer configuration (Figure 4.3), the recorded wave field in equation (4.1) has two contributions of the wave propagation through the water column that can be removed from the data by applying wave equation datuming. Following the matrix operator notation used by Berkhout (1981, 1997a, 1997b), the target two dimensional (2-D) wave field propagation from the sources to receivers is also formulated here by means of matrices but divided into three equations, each considering a different part of the total trajectory of the wave field, as

$$S^T(x_s, z_s; t) * G_d(x_s, z_s; x_d, z_{bat}; t) = u_d^T(x_d, z_{bat}; t) \quad (4.8a)$$

$$u_d^T(x_d, z_{bat}; t) * G_e(x_d, z_{bat}; x_u, z_{bat}; t) = u_u^T(x_u, z_{bat}; t) \quad (4.8b)$$

$$u_u^T(x_u, z_{bat}; t) * G_u(x_u, z_{bat}; x_r, z_r; t) = u^T(x_r, z_r; t) \quad (4.8c)$$

where equation (4.8a) corresponds to the downward propagation (G_d) from the source (S) surface (x_s, z_s) to the seafloor (x_d, z_{bat}) through the water column; equation (4.8b) describes the effects of the wave propagation through the Earth's subsurface (G_e) for an acquisition system deployed at the seafloor from an incoming wave field at (x_d, z_{bat}) to

an outcoming wave field at (x_u, z_{bat}), and (4.8c) represents the upward propagation (G_u) from the seafloor (x_u, z_{bat}) to the recording surface (x_r, z_r) through the water media; u_d^T , u_u^T , and u^T represent the pressure field expressed at its corresponding datum surface as a row vector, "*T*" being the transpose symbol. The G_d and G_u operators are equal only if sources and receivers are located at the same horizontal coordinates and thus the downward and upward vertical propagation follow the same path. In Figure 4.3(a) some ray paths are represented where their trajectories are formed by the previous contributions. The only exception is the energy that travels along the sea surface (green line). The previous equations consider only the contributions that have interaction with the new datum plane, and that would be present in the re-datumed data. The other pressure variations recorded in the seismograms are muted in a preprocessing step (removal of the direct wave) performed in the time-offset domain before the re-datuming procedure (Figure 4.1).

The re-datuming procedure aims at compensating for the effect of the wave propagation in equation (4.8a) and (4.8c) by performing an inverse extrapolation or back-propagation for each one (Figure 4.1). First, the downward continuation of the receivers from the recorded surface to the new datum is explained and illustrated. Second, the datum change of the sources to obtain the final geometry set-up. If the acquisition configuration is carried out in such a way that sources or receivers are at the target datum plane, then only one step is necessary in the re-datuming process. In this case, only the DC of the array that is not at the datum surface has to be performed. This situation can be found for example with WAS acquisition set-ups, where the receivers (OBS/N) are located at the seafloor, or when they are located inside an horizontal borehole (Bakulin & Calvert, 2006).

Downward continuation of the receivers

Transforming the seismograms recorded at the MCS streamer channels on the virtual ones that would be recorded if receivers were located at the seafloor is the objective of the first step of the DC code. The target configuration is equivalent to that of OBS experiments, so we refer to it as OBS-type geometry from here on (Figure 4.4). Because the receivers in the new configuration are located closer to the subsurface, refracted phases are recorded earlier in time than with the streamer-type geometry and they can be visible as first arrivals at shorter offsets, Figure 4.4(b). In Figure 4.4(a) I show the ray paths of Figure 4.3(a), but in this case excluding the upward contribution within the water column. The goal is compensating for the effect of equation (4.8c), so the upward propagation of the wave field through the water column between the seafloor and the recording surface. This is done by back-propagation of the preprocessed seismic traces that form each shot gather (reverse receiver wave field) (Figure 4.1), to extrapolate the wave field to the virtual receiver locations in the new datum surface.

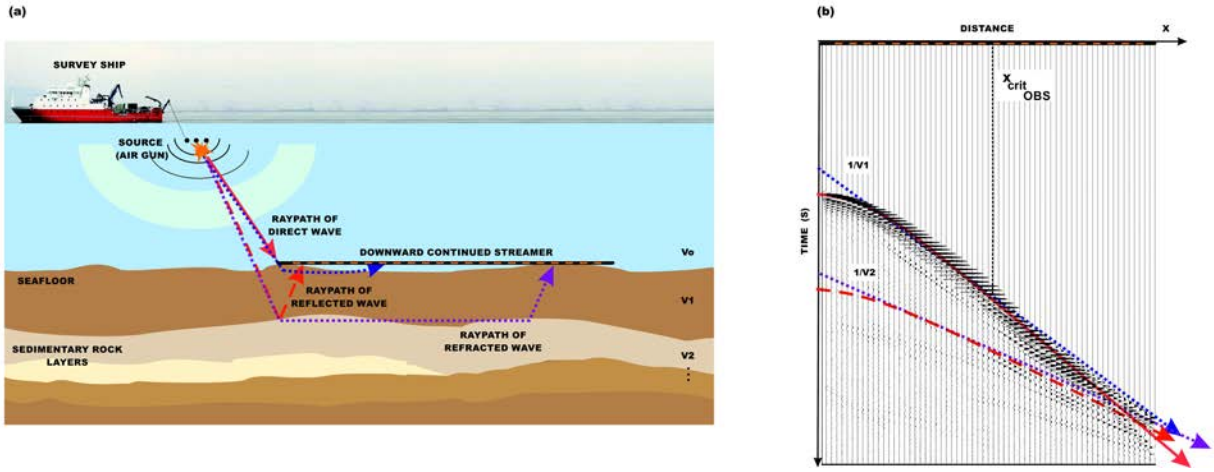

Figure 4.4: (a) Scheme of the ray trajectories corresponding to a OBS-type geometry. Pink line is the direct water wave, dotted blue and purple lines are refracted ray paths in different interfaces, and the dashed red line is a reflected ray path in the same interface as the dotted purple line. (b) Shot gather diagram corresponding to the OBS-type geometry in (a). Refractions emerge as first arrival phases at long offsets, so the travel-time information can be extracted and used for Vp modelling.

Each wavefront follows an independent path and propagates back towards its focal point. Before reaching the focal point, the wave field is recorded at the virtual datum surface, i.e. the seafloor. Therefore, in our inverse extrapolation, the re-datumed wave field can be expressed as

$$u^T\left(x_r,z_r;-t\right)*G_d\left(x_r,z_r;x_r,z_{bat};t\right)=u^T_{OBS}\left(x_r,z_{bat};-t\right) \quad (4.9)$$

where -t means reversed in time, and the downward operator (G_d)may not generally coincide with the one defined in equation (4.8a), which as is explained above depends on the path followed in the wave field propagation. However, as the forward propagation of the wave field has to follow the same path as the inverse extrapolation, then $G_d\left(x_r,z_r;x_r,z_{bat};t\right)=G^T_u\left(x_r,z_{bat};x_r,z_r;t\right)$ according to the principle of reciprocity. Reciprocity states that if source and receiver have identical directional characteristics, then interchanging the positions of sources and receivers yields the identical seismic trace (Berryhill, 1984).

$$S^T\left(x_s,z_s;t\right)*G_d\left(x_s,z_s;x_d,z_{bat};t\right)*G_e\left(x_d,z_{bat};x_u,z_{bat};t\right)=u^T_u\left(x_u,z_{bat};t\right) \quad (4.8a)\ \&\ (4.8b)$$

$$S^T\left(x_s,z_s;t\right)*G_d\left(x_s,z_s;x_d,z_{bat};t\right)*G_e\left(x_d,z_{bat};x_u,z_{bat};t\right)*G_d\left(x_r,z_r;x_r,z_{bat};t\right)=u^T_{OBS}\left(x_r,z_{bat};t\right) \quad (4.10)$$

The re-datumed field (u_{OBS}) is affected by the finite, discrete and single-sided illumination of the medium. Because the re-datumed field is built by using the recorded data, u_{OBS} is not identical to u_u . The medium inaccessibility from all sides is the major

limitation for the perfect focusing of the wave field.

After the first step of the re-datuming procedure, the direct water wave arrival disappears and refractions emerge as first arrivals at the critical distance. The critical distance for this configuration geometry is expressed as,

$$x_{crit_{OBS}} = z_0 \cdot tg\left(i_{\mathrm{crit}_0}\right) \quad (4.11)$$

In this case, the total distance where refraction information is visible as first arrival phases (Δx_1) in the OBS-type data is expressed as,

$$\Delta x_1 = sl - x_{crit_{OBS}} \text{ ; when } sl - x_{crit_{OBS}} > 0$$
$$\Delta x_1 = 0 \text{ ; when } sl - x_{crit_{OBS}} < 0$$

The relative gain of visible refractions in the recordings after downward continue the receivers (Δx_{r1}) is given by the absolute difference between critical and crossover distances, $\Delta x_{r1} = \Delta x_1 - \Delta x$.

Given the previous example, with a water column of 1 km depth and a subsurface velocity of v_1 =1.8 km/s, refractions emerge as first arrival phases from 1.5 km, $x_{crit_{OBS}}$ =1.5 km (Eq. 4.11). So, the visualization of refracted first arrival travel times along 3.5 km is possible using a streamer length of 5 km, where $\Delta x_1 = \Delta x_{r1} = 3.5$ km, as $\Delta x = 0$. For long-offset streamer set-ups, e.g. 10 km, refractions emerge as first arrival phases along $\Delta x_1 = 10 - 1.5 = 8.5$ km, having a relative gain of visible refractions as first arrivals with the receivers on the seafloor of $\Delta x_{r1} = 8.5 - 3.4 = 5.1$ km.

Downward continuation of the sources

The objective of the second step of the DC code is to retrieve the wave field recorded by the virtual acquisition system with both sources and receivers located at the datum level, the seafloor in our case. The target configuration is referred here to as Seafloor-type geometry, Fig. 4.5. Given that sources and receivers are both located just at the seafloor, the refracted and subsurface head phases emerge now as first arrivals from zero offset (Fig. 4.5b). In Fig. 4.5a I show the subsurface ray paths also shown in Fig. 4.4a, but in Fig. 4.5a without the downward propagation of the wave field through the water column between the shot surface and the seafloor. The goal is this case is compensating for the effect of equation (4.8a), so a back-propagation of the sources (Fig. 4.1) to extrapolate the wave field and change its datum plane is necessary to transform the seismic data to the final geometry set-up.

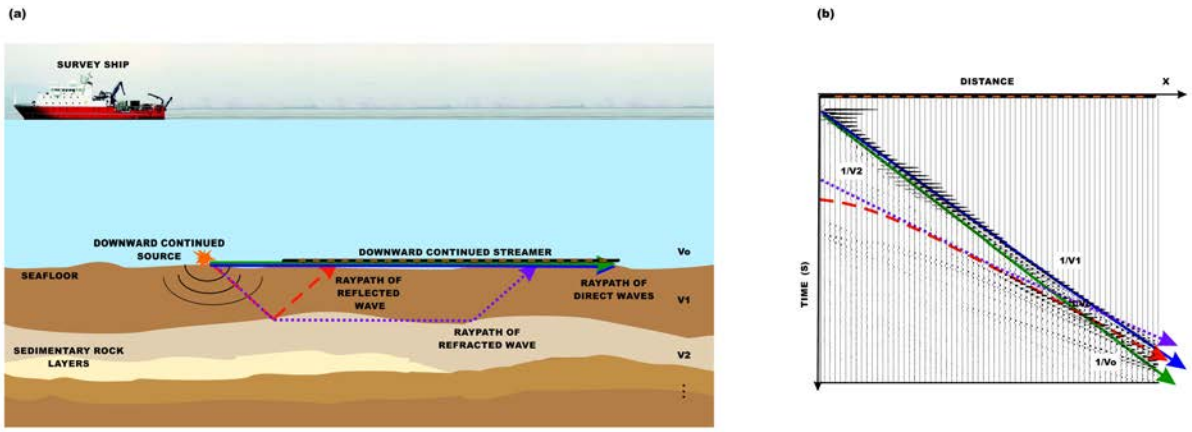

Figure 4.5: (a) Scheme of the ray trajectories corresponding to a Seafloor-type geometry. Green line is the direct water wave, blue line is the head wave that travels through the seafloor interface, dotted purple and red dashed lines are respectively the refracted and reflected ray paths of an interface of the subsurface. (b) Shot gather diagram corresponding to the Seafloor -type geometry in (a). Refractions emerge as first arrival phases from zero offset so that arrival times can be now picked and used for Vp modelling.

As in the previous case, the reverse-time propagation of the downward source wave field can be expressed as

$$u_d^T\left(x_d, z_{bat}; -t\right) * G_u\left(x_d, z_{bat}; x_s, z_s; t\right) = S^T\left(x_s, z_s; -t\right) \quad (4.12)$$

where the determination of source parameters (S) can be done through the inverse extrapolation of the downward propagated wave field (u_d). Therefore, equation (4.12) focus the wave field recorded at the seafloor (x_d, z_{bat}) to its source point position/s at the sea surface (x_s, z_s). Given that our goal is changing the datum plane of the sources instead of the one defined by the incoming wave field (u_d) at (x_d, z_{bat}), the seismic traces have to be sorted in common receiver gathers. The rearrangement of the data is possible because the sources and receivers satisfy the reciprocity principle, as a consequence $G_d\left(x_s, z_s; x_d, z_{bat}; t\right) = G_u^T\left(x_d, z_{bat}; x_s, z_s; t\right)$. So, the pressure field u_{OBS} can be formulated as

$$G_e^T\left(x_r, z_{bat}; x_d, z_{bat}; t\right) * G_u^T\left(x_d, z_{bat}; x_s, z_s; t\right) * S\left(x_s, z_s; t\right) = u_{OBS}\left(x_r, z_{bat}; t\right) \quad (4.13)$$

Once the traces are rearranged into common receiver gathers, the second DC step can be applied to extrapolate the wave field to the seafloor surface. In this case, the seismic traces that form each receiver gather are introduced backwards in time (reverse source wave field) at its corresponding time step and its target seafloor grid positions inside the medium as a new boundary condition. The focusing wave field is emitted from the seafloor to the shot surface, as in equation (4.12), in order to compensate for the effect of the downward wave field propagation through the water column by an upward

propagation. Therefore, in the reverse extrapolation, the re-datumed wave field (u_r) can be expressed by

$$G_d^T(x_s,z_s;x_s,z_{bat};t)*u_{OBS}(x_r,z_{bat};-t)= \quad (4.14)$$
$$G_d^T(x_s,z_s;x_s,z_{bat};t)*G_e^T(x_r,z_{bat};x_d,z_{bat};-t)*G_u^T(x_d,z_{bat};x_s,z_s;-t)*S(x_s,z_s;-t)=u_r(x_r,z_{bat};-t)$$

where *r* denotes re-datumed, *-t* means reversed in time and the downward operator (G_d^T) here coincide with $G_u(x_s,z_{bat};x_s,z_s;t)$. Finally, the seismic traces have to be shifted in time and reorganized back into shot gathers in order to recover the data in the original domain. The final virtually recorded wave field with sources and receivers located at the seafloor can be expressed as

$$S^T(x_s,z_s;t)*G_e(x_s,z_{bat};x_r,z_{bat};t)=u_r^T(x_r,z_{bat};t) \quad (4.15)$$

Again, because the re-datumed wave field (u_r) is built by using finite, discrete and single-sided recordings, it is not the pressure wave field (u_u) that would be recorded by performing the experiment with the virtual geometry set-up, described in equation (4.8b).

After all the re-datuming procedure, the total distance where refraction information is visible as first arrival phases (Δx_2) in the Seafloor-type data is equal to the streamer length, $\Delta x_2 = sl$. Thus, subsurface Vp information from zero offset is obtained.

The minimum recording time (t_{rec}) of the data required for all the re-datuming procedure to reproduce data covering the whole streamer length with subsurface information can be approximated as

$$t_{rec} \geq \frac{sl}{v_1} + 2 \cdot z_0 \cdot \frac{\sqrt{v_1^2 - v_0^2}}{v_0 \cdot v_1} \quad (4.16)$$

where the first term ($\frac{sl}{v_1}$) defines the travel-time that is necessary to record the subsurface head waves at the maximum offset distance in the Seafloor-type geometry, whilst the second ($2 \cdot z_0 \cdot \frac{\sqrt{v_1^2 - v_0^2}}{v_0 \cdot v_1}$) represents the two-way travel-time through the water column. If the physical parameters of the previous example are taken to define the medium, then for a streamer length of 5 km a $t_{rec} \geq 3.5$ s is required, whilst a streamer length of 10 km needs a $t_{rec} \geq 6.3$ s.

4.2.2. Multi-shooting strategy

All the wave field extrapolations are performed in the 23DAS code by forward modelling through a known Vp field. In this case, the computational time involved to solve the forward propagation depends on the model and data parameterization. The computational complexity rapidly increases with a finer mesh and dense data sets. Typically, the computational cost increases proportionally to the number of input traces used in the forward calculation, as it does the accuracy of the output result. However, according to the BVM scheme in which all the traces that form a gather are introduced simultaneously along the time at the 2-D model, only one extrapolation is enough to change the datum surface of one gather independently of the number of traces that it contains.

In order to reconstruct the wave field from all the information in the time samples of the seismic traces and transform it along the time during the same back-propagation, the DC solver incorporates a multi-shooting strategy. It considers all the traces that belong to the same gather as an extended simultaneous source (Figure 4.2). In comparison to the calculation of each re-datumed trace alone, the multi-shooting strategy computes all the traces in the new recording surface at once, increasing the signal-to-noise ratio and making the process more efficient both in memory usage and computational time. Contrary to standard static corrections, this strategy enables to account for all emergent angles (fulfilling the Snell's law) of all the traces simultaneously by applying just one propagation for each seismic gather. Thus, the multi-shooting strategy increases the efficiency of the re-datuming procedure.

The usage of all the recording information is advantageous because it overcomes the need to specify and pre-select certain reference phases, avoiding the time-consuming user interaction. Contrary to other data-mapping approaches (Tegtmeier et al., 2008; Pila et al., 2014), the knowledge of the Vp values below the new datum surface is not required with this method because no calculation of the focusing reflection points are needed. Once the wave energy is recorded in the new datum positions, it can be absorbed in order to avoid artefacts coming from below. Consequently, it is unnecessary the building of a locus or focus surface (bases Kirchhoff migration, (Vidale, 1988)). So, using the multi-shooting strategy, the specular reflection paths for all the source-receiver pairs are automatically obtained at any incident angle without any surface-consistency assumption. The back-propagation of the entire field following the two-way wave equation scheme retrieves multiples and refractions contained in the recordings without additional computational cost.

Although the multi-shooting strategy reduces the necessary computational resources, a considerable cost is required to perform the extrapolations of the re-datuming procedure. The total number of extrapolations is the sum of the total number of shot and receiver gathers of the acquisition experiment. In order to reduce the computational time parallelization (subsection 4.3.) has been implemented.

4.3. Parallelization

All the algorithms in the DC code are parallelized using OpenMPI standards (Dagnino et al., 2014, 2016). Most computing time is consumed solving the inverse extrapolation and writing the output data set. These processes are solved simultaneously and independently for all the Central Processing Units (CPUs) . For each re-datuming step in which the multi-shooting strategy is used, each CPU computes at least one extrapolation, and at most the result from dividing all gathers among the available CPUs. Once the gather is transformed, a new gather is sent to the CPU and the process is repeated until all the data is re-datumed into the new surface.

Not only the solver is parallelized, also the arrangement of the seismic traces in different gather domains. Reading and writing the correct seismic traces of each gather to properly sorting out the data is a time-consuming procedure. Again, as the algorithms perform with a MPI extension, the executing time is smaller. In this case, each CPU would at least build one gather in the target domain, and at most the result of dividing the number of target total gathers between the number of available CPUs. Once the gather is formed, a new one is passed to the CPU until all the data are sorted in the new domain.

Therefore, the computational time in the DC code will depend on the total number of extrapolations per CPU and the total number of gathers that must be built per CPU.

Chapter 5. Seismic tomographic methods

Seismic tomography methods are one of the most powerful geophysical techniques to retrieve physical properties of the media. The exploration of strategies to obtain high-resolution Vp models from MCS data constitutes the overarching goal of my work. Specifically, in this chapter I describe the mathematical formulation of the two seismic tomographic methods that I have used during my PhD, the TTT and the FWI. In both cases, I have used codes developed and implemented by other group members of the Barcelona-CSI. Understanding the fundamentals and the implicit characteristics of these techniques is essential to design an appropriate modelling strategy. In particular, combining the robustness of TTT and the accuracy of FWI is crucial to extract high-resolution information of the physical properties of the subsurface.

The description of the two tomographic methods is presented in two different sections. After a brief introduction, the common characteristics for all inverse methods are presented for each case. These include, the model parameterization, which is the description of the physical properties by using a discrete representation. The forward problem, which is the numerical simulation of the wave propagation through a medium following a physical approximation. Finally, the inverse problem is the numerical procedure to obtain the model of physical parameters (Vp, Vs, etc.) that better explains the acquired data by iteratively updating an initial model. Additional sub-sections are dedicated to the FWI code in order to explain ways to stabilize the inverse problem, as using pre-conditioners (Dagnino et al., 2014) or multi-scaling strategies (Bunks et al., 1995).

Concerning TTT I will focus the description on the code that I have used, which is a version of TOMO2D (Korenaga et al., 2000) that was modified at Barcelona-CSI to allow using MCS data. The code allows for joint inversion of travel times from first arrivals and secondary phases (reflections). The main modifications by our group have been to extend the program to 3D (Meléndez et al., 2015) and to adapt it to all sorts of acquisition geometries. As an example, having sources and receivers on the water column, which is essential when one has to deal with streamer data, becomes possible with this code.

On the other hand, the FWI algorithm used has been fully developed and implemented in the Barcelona-CSI (Dagnino et al., 2014, 2016). The code solves the 2D acoustic version of the wave equation in time domain by using a FD scheme.

5.1. Travel-time tomography

TTT is a widely used method to build subsurface velocity models and reflecting interface geometries by minimizing the differences between the forward calculated and the

observed travel times of some predefined seismic phases in the seismogram. Refractions, or first arrivals, carry direct information on the the large and intermediate wavelength velocity information of the media -First Arrival Tomography- (Toomey et al., 1994), whereas the reflected arrivals have indirect information on both velocity as well as the location and geometry of reflecting boundaries -Reflection Tomography- (Bishop et al., 1985). A ray tracing technique is used to solve the forward problem in order to calculate both travel times and ray paths through a reference model. Then a linearised, iterative inverse problem is set to minimize the travel-time differences by changing the model according to some regularization constrains.

The main strengths and advantages of TTT in comparison to other seismic inversion methods are their robustness, moderately non-linear behaviour and low computational cost, whereas its main drawback, is its limited resolution. In particular, it is commonly accepted that the limit of resolution of ray-based TTT methods is close to the size of the first Fresnel zone,

$$\sqrt{\lambda \cdot L/2} \quad (5.1)$$

where λ is the source wavelength and L the source-receiver propagation distance. For typical seismic acquisition systems, where L≈10 km and λ ≈10 m the theoretical resolution is around 1 km. It is widely accepted that TTT provide appropriate models to be used as starting models for higher resolution techniques.

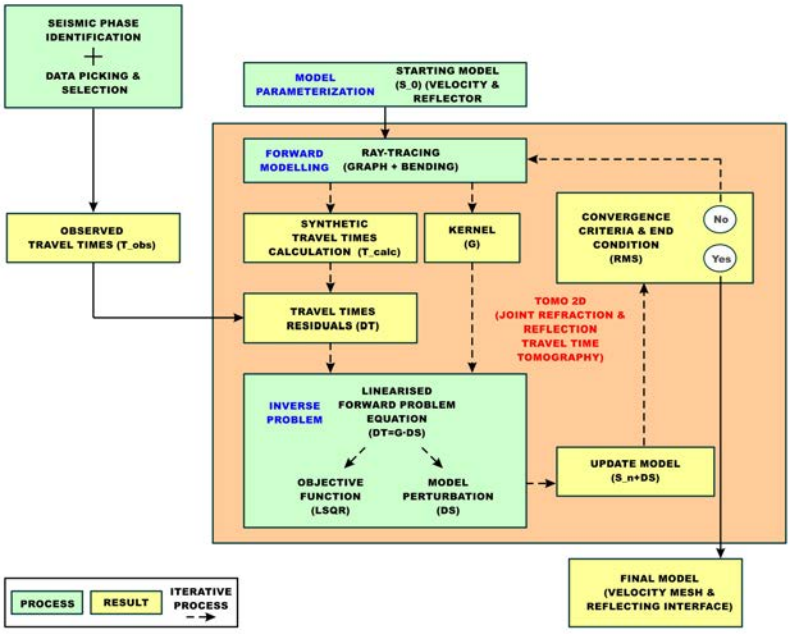

Figure 5.1: Flow diagram of the joint refraction and reflection travel-time inversion method applied with TOMO2D. The three common points for all the inverse methods are written in blue.

The description of the different parts of the modelling and inversion procedure will be focused on the solution proposed by the TTT code used in this thesis. The flow diagram of the Barcelona-CSI modified version of TOMO2D, which includes the three main parts above-mentioned (model parameterization, forward modelling, and inverse problem), is shown in Fig. 5.1.

5.1.1. Model parameterization

TOMO2D code is a joint refraction and reflection travel-time inversion algorithm. Thus, its goal is to retrieve a subsurface Vp model together with the location and geometry of the reflecting interfaces. For the 2-D TTT, the Vp models are represented by a 2-D Cartesian grid defined by the spatial coordinates of their nodes, whereas reflecting boundaries are represented by linear segments defined by the spatial coordinates of a 1-D node mesh. TOMO2D follows Toomey et al. (1994) model parameterization based on Moser (1991) ray tracing. Toomey et al. (1994) used a sheared grid representation in which nodal spacing is not necessary to be constant both horizontal and vertical directions. This media parameterization allows to easily adapting the mesh to the irregular media variations obtaining accurate results with moderate computational resources. In addition, reflector and velocity nodal spacing are independent each other allowing a free updating of the floating reflector without forcing adjacent velocity changes. The nodal spacing of the mesh influences the coarseness of the resultant velocity variations. Increasing the number of mesh nodes (so decreasing the nodal distance) in this case do not always ensure a better model resolution because it is limited by the amplitude of the first Fresnel zone. The coincidence between mesh nodes and the source-receiver positions are also important to get accurate results.

In TOMO2D code, the Vp (or Vs) values or the depth location of the reflecting discontinuities are the variables that are defined at the mesh nodes for the discrete representation of the media. To assure the continuity of the velocity field and depth interface geometry a bilinear interpolation is used in each parallelogram-shaped grid cell (equation 1 and figure 2 of Van Avendonk et al., 1998). The velocity is estimated below a 1D boundary that typically corresponds to the bathymetry or topography, above which constant velocity values (for either water or air) are imposed. The new modification makes reliable trace the rays from the bathymetry to the sea surface and backwards assuming a constant water velocity through nodes (Begović et al., 2017).

To avoid issues related to multiple reflector inversion, TOMO2D is prepared to deal with the location and geometry of only one reflector at a time. It is possible to invert more than one reflecting interface and their associated velocity changes following a data-driven strategy called “layer-stripping” (Meléndez et al., 2015) where they are inverted sequentially, one by one.

5.1.2. Forward problem

There is a bunch of different techniques to calculate ray paths and travel times. The accuracy and efficiency of the results largely depends on the methodology used in the forward calculation. The basic principles applied in all of them for forward travel-time calculation are the Huygens' principle, the Fermat principle, the Snell's law and the wavefront marching method.

In the case of TOMO2D the methodology applied to solve the forward model is the graph-theoretical method followed by a ray-bending refinement. Similar ray tracing techniques have been used by Papazachos and Nolet (1997) or Van Avendonk et al. (1998), because these kind of hybrid approaches become more efficient in terms of computational resources for a typical experiment configuration (figure 5 of Korenaga et al., 2000; figure 5 of Van Avendonk et al., 2001).

Graph method

Graph theory and shortest paths are present in many network science applications. Its utility to link a path using a discrete mesh represented as a set of nodes with a weight function assigned to each connection arc has made possible the expansion of a wavefront in a network as a Huygens' principle application (Dijkstra, 1959). In addition, Fermat principle is satisfied when the shortest path is extracted.

In the seismic travel-time case the graph solution is a set of first arrival travel times and corresponding polygonal ray paths following Fermat's principle by using as a nodal distance the travel times (Nakanishi and Yamaguchi, 1986) obtained from the velocity mesh nodes connections (figure 1 and 2 Moser et al. 1992, Fig. 2.22). The first arrival which has the minimum travel-time is the one with the shortest path. So, the graph method finds the first arrival travel-time by tracing ray paths from a source node to their surrounding mesh nodes until the receiver position is reached by the shortest path (Dijkstra, 1959; Moser, 1991). The number of available connections for each node is predefined according to the order of a forward star (FS) structure (Zhang and Toksöz, 1998; Van Avendonket al., 2001) (Fig. 5.2).

Numerous seismic travel-time tomography studies using the graph method can be found on the literature (Moser et al. 1992; Toomey et al., 1994; Zhang and Toksöz, 1998; Korenaga et al., 2000; Van Avendonket al., 2001). The first introducing the ray tracing by using a regular nodal mesh in a parametrized media was Moser (1991). Toomey et al. (1994) was the first one using graph method to a sheared grid. The calculation of later arrivals such as reflection phases can be formulated as a two-step application of the graph method (Moser, 1991; Zhang et al., 1998), first to find the shortest path from the source to the depth interface and then, following Huygens' principle, from the previous reflecting node acting as a source to the receiver. One graph solution can be associated to the downward and the other to the upward propagations. In the reflected ray tracing case,

only the mesh nodes between the sources and the depth interface are taken into account. The ray paths from sources and receivers located on the water column characteristics of the streamer geometry set-up can be obtained with the adapted version of the code (Begović et al., 2017). Sources and receivers located inside the water layer are connected to seafloor nodes by straight paths that cross the layer with the minimum travel-time following Fermat's principle in order to complete the entire ray trajectories. The ray tracing of the water layer multiples or particularly the Multiple – Seafloor Reflection Interference can also be solved (Meléndez et al. 2013). Recently, Meléndez et al. (2014) adapted the graph method for 3D ray tracing in the 3D version of TOMO2D, named TOMO3D.

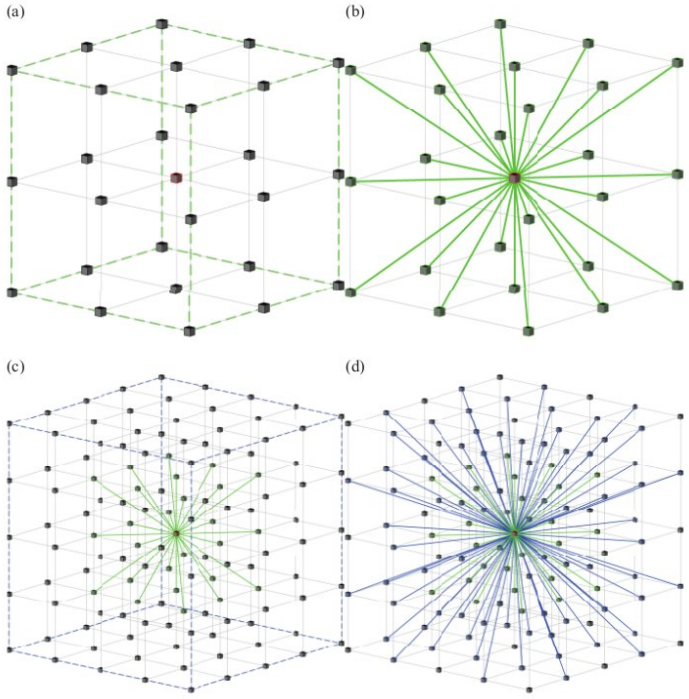

Figure 5.2: FS construction on sample portions of 3-D velocity mesh. The origin node is marked in red. (a) FS of (1,1,1). Connections are restricted to the nodes within the limits indicated by the green dashed lines. (b) Candidate path segments for (a). (c) and (d) idem as (a) and (b) for a FS of (2,2,2). This includes all previous connections plus those marked in blue. A higher-order FS increases the trade-off angles, whoch increases accuracy as well as computational time. Note that the FS in (c) and (d) only considers nodes that yoeld candidate ray path directions not present in the FS in (a) and (b), (Meléndez, 2014).

TOMO2D graph formulation follows Moser (1991) algorithm based on Dijkstra (1959) scheme. The fundamentals of the graph method formulation can be found in Moser (1991) or Meléndez (2014, Fig 4.3). The graph method efficiency is directly related with the number of mesh nodes and ray path calculations of different source – receiver pairs. All the possible ray paths combinations from the origin nodes to all available neighboring nodes in the mesh have to be built to actually get the shortest path. Therefore, the cost of computing a single ray path is equivalent to that of building all possible ray paths from a

given node. Thus, taking advantage of the reciprocity principle meaning that sources or receivers can be treated equally as origin nodes in a graph problem, we use as origin nodes those being less numerous for a given acquisition setting (receivers in the case of wide-angle seismics).

The accuracy of ray path tracing is directly related to the order of the FS, which restricts and determines the search direction of all possible ray paths, and by the nodal spacing of the mesh that influences the local coarseness of the seismic rays. These two sources of ray path and travel-time inaccuracies are independent (Moser, 1991; Zhang and Toksöz, 1998). Therefore, independently of the grid size, the rays of a graph solution usually are polygonal paths that tend to zig-zag causing travel-time overestimations. This happens especially when the number of node connections in the graph template or FS is small and then the possible candidate connections is kept to the immediate neighbor nodes. To improve the convergence of ray path directions more azimuthal and incidence angles have to be included adding in the FS structure additional connections to more distant nodes. Optimal order of the FS and nodal spacing depends on the complexity of the velocity model, increasing the graph accuracy in the presence of strong velocity gradients. Detailed ray trajectories can be obtained using higher order FS and a fine mesh. However, the computational complexity rapidly increases with higher FS degree and finer mesh (Moser, 1991; figure 4 of Cheng and House, 1996). In the case of TOMO2D the originally coarse graph solution is subsequently refined by applying a ray-bending technique instead of using a higher-order FS and a finer mesh. In fact, the existing trade-off between the accuracy of the initial ray path guess and computational burden saved during the graph calculation is usually solved by using a coarse mesh and a lower order FS. Although the resulting polygonal ray paths does not match the real trajectories at all, they are usually rough but good initial guesses to be subsequently refined. The ray-bending technique of TOMO2D applied to refine the graph solution is described below.

Ray bending method

The ray bending method improves and finds the locations of successive points on a ray taking some initial estimate trajectory. In TOMO2D code the ray-bending procedure is the one developed by Moser et al. (1992a). The algorithm refines the discrete polygonal initial guesses or estimates to produce continuous and realistic ray paths that minimize the travel-time as a functional of the ray curve between its source-receiver pairs ($t_S^R(\gamma)$) (Meléndez et al., 2014, Fig 4.5). Starting ray paths are perturbed until they satisfy the minimum travel-time criterion.

$$t_S^R(\gamma) = \int \frac{d\Gamma}{v} \; -> Min \qquad (5.2)$$

where the ray paths crossing through a velocity field (v) were discretized and

parameterized by the arc length (Γ). The sequence of grid nodes that define the initial trajectories are employed as control points to parametrize the rays as beta splines (Appendix A of Moser et al., 1992a). A beta-spline is a curve of connected segments each built using a small number of consecutive control points that are averaged with polynomial weights (for additional information see Appendix A of Moser et al., 1992a and/or Meléndez, 2014). The travel-time is minimized using the conjugate gradient method. The gradient of the travel-time function along a beta-spline curve with respect to one support point is calculated using its formal differentiation expression (Appendix B of Moser et al., 1992a).

The main drawback of the ray bending technique is its dependence on the initial guess. When starting ray paths are far from the true solution, the resulting trajectories acquired will have a slow convergence and may not correspond to the global minimal travel-time path.

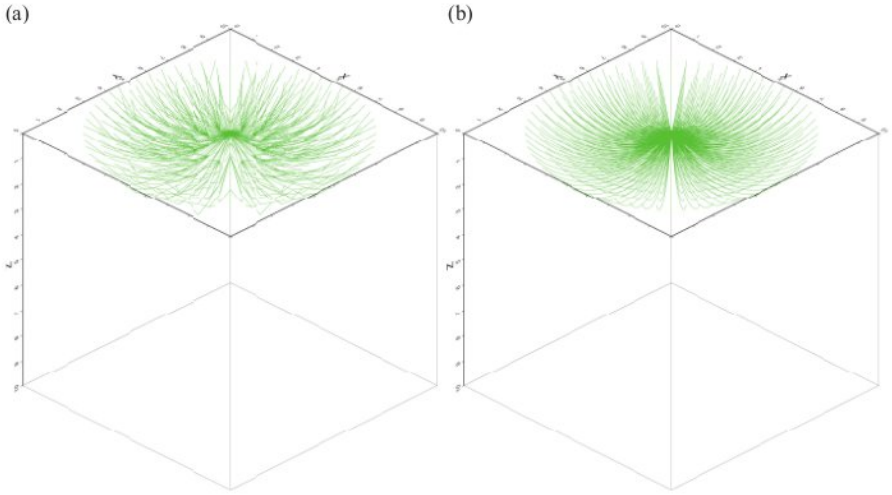

Figure 5.3: Sample polygonal paths (a) and the corresponding ray trajectories after bending (b) for refractions calculated with TOMO3D. Polygonal paths are obtained with the graph method and then used to build initial guess paths for the bending method, which produces the refined ray trajectories, (Meléndez, 2014).

The combination of the robustness of graph method and the accuracy of bending refinement is considered to be one of the best strategies to solve the forward problem in travel-time tomography (Moser et al. 1992a; Van Avendonk et al., 1998; Van Avendonk et al., 2001). This hybrid approach allows mitigating the convergence problems of the bending method guaranteeing the global minimal travel-time paths providing as initial guesses the shortest travel-time trajectories of the graph method (Fig. 5.3).

Although a coarse mesh and a lower order FS are usually chosen for the graph calculation, they must ensure that the number of points on the resultant rays is large enough for the beta-spline curve to accommodate the variations in the velocity field.

Having poor graph solutions make the hybrid approach less efficient due to a slow ray-bending method (Van Avendonk et al., 2001). However, in comparison to the use of graph method alone, this hybrid strategy obtains a better fitting seismic rays with the same computational effort or drastically reduces its computational cost for the same accuracy. Synthetic examples show in many studies (Korenaga et al., 2000; Meléndez et al., 2014) the improvement of this hybrid strategy against the usage of just one method.

5.1.3. Inverse problem

Given a velocity model and the acquisition set-up, the travel times along the calculated ray paths obtained by solving the forward problem (see previous section) must be compared with the observed ones. The travel-time differences are called residuals. In the inverse problem the velocity and interface depth and geometry models are changed to fit the travel times and corresponding ray paths, therefore minimizing residuals. The relationship between travel-time and model parameter perturbations is non-linear. However, it can be and is often linearized for small parameter perturbations. Then this relation is commonly iteratively inverted using gradient-based minimization strategies.

In the case of TOMO2D, a well-known and widely-used conjugate gradient-type method to solve sparse systems of linear equations (i.e. the Least Square Root (LSQR) algorithm by Paige and Saunders (1982)) is employed to minimize the travel-time residuals by least squares. This method is numerically more stable than the conventional conjugate gradients method. The matrix inversion is regularized by applying a number of smoothing and damping constraints. The final inversion results are a velocity and interface depth models that fit the observed refracted and reflected arrival travel times within a predefined degree of accuracy.

Linearized forward problem equation

Taking a Cartesian initial 2D subsurface slowness (u=1/v where v is wave velocity, either Vp or Vs) and reflector depth (z) models, the travel-time residuals (δt_i) can be defined as the path integration of parameter perturbations (δs) along the whole ray paths (Γ_i) in a reference model, for the refraction can be expressed as

$$\delta t_i = \int_{\Gamma_i} \delta s_u \, d\Gamma \qquad (5.3)$$

and for the reflections as

$$\delta t_j = \int_{\Gamma_j} \delta s_u \, d\Gamma + \frac{\partial t}{\partial z}\Big|_{x=x_j} \delta s_z(x_j) \qquad (5.4)$$

where x_j represents the reflecting point of the jth ray path. The linearised approximation of the forward problem equation that links the residual travel times, $\delta t = t_{obs} - t_{calc}$, with any small model perturbation, δs , in each parametrized cell "k" of the discretized medium is defined as

$$\delta t_j = \sum_k g_{jk} \delta s_k \quad (5.4)$$

Using a matrix notation, the computation of the residual travel times vector can be formulated as,

$$\delta t = G \cdot \delta s \quad (5.5)$$

where the model perturbation vector is $\delta s = \left(\delta s_u, \delta s_z \right)$ and G is called sensitivity kernel or Fréchet derivative matrix, which contains the partial derivative of the travel-time residuals with respect to the parameters of interest (v and/or z).

In the seismic travel-time case the sensitivity kernels correspond to the segment length variations of a reference ray path. This matrix is built by using Eqs. (5.3) and (5.4). The size of G is equal to the number of observed travel times multiplied by the number of model parameters. G matrix has two parts. One corresponding to the velocity contribution coming from the refracted and reflected arrivals, G_u and the other to reflector depth parameters that is influenced just by the reflections, G_z . The depth sensitivity kernel for a reflecting point position is as follows (Bishop et al., 1985),

$$\frac{\partial t}{\partial z}\Big|_{x=x_j} = \frac{2 \cdot \cos\theta \cdot \cos\beta}{v_{x_j}} \quad (5.6)$$

where θ is the incident angle upon reflection, β is the slope of a reference reflector, and v_{x_j} the velocity at the reflecting point. There is an inherent trade-off between depth of an interface and velocity above it in the reflected travel times information. This ambiguity becomes an additional cause of non-uniqueness in the inverse solution. For a given perturbation scale, different models can fit the reflected travel times giving equally valid solutions in areas poorly covered by refractions. Those models become identical from a data resolution point of view. For this reason, a depth-kernel weighting parameter, w, is introduced in order to adjust the relative weighting of depth sensitivity with respect to velocity sensitivity in the Fréchet matrix. Results obtained using different values of w reflect the degree of the inherent velocity-depth ambiguity for reflection travel-time inversion. Besides, it also helps to avoid singularity in Eq. (5.5). It is important to note that this parameter controls the weighting of depth relative to velocity perturbations not between reflected over refracted travel times. Larger (smaller) depth vs. velocity sensitivity is obtained by increasing (decreasing) the weighting parameter value, producing larger (smaller) depth perturbations with smaller (larger) velocity changes.

Covariance matrices are used to normalize all the data, C_d , and model parameters, C_s , (Korenaga et al., 2000). The data covariance matrix includes the uncertainty in the travel-time observations. Thus, possible artefacts in the result caused by wrong travel times are minimized. Since no correlation in data errors is assumed, it is a diagonal matrix whose elements are each an estimate of the variance in an arrival time observation.

$$\delta t' = C_d^{-1/2} \delta t \quad (5.7)$$

The model scaling matrix, C_s , acts as a penalty function applied to the perturbational model. It is used to preserve the prior knowledge incorporated on the starting model. Normalization of model parameters by the initial model is important for a good distribution of the perturbation throughout the model and thereby reduce possible solution bias. It is a diagonal matrix whose elements are each a square of a model parameter.

$$\delta s' = C_s^{-1/2} \delta s \quad (5.8)$$

To be consistent the sensitivity matrix has to be also normalized by the covariance matrices, as

$$G' = C_d^{-1/2} G C_s^{-1/2} \quad (5.9)$$

The following expressions are normalized by the covariance matrices as shown in Eqs. (5.7), (5.8) and (5.9), but the prime sign will be omitted to facilitate the notation.

Regularization constraints

The higher number of model parameters with respect to the number of available data make the use of regularization constraints essential to reduce convergence issues. In order to get an inversion that follows a stable and proper evolution towards the correct solution, the changes introduced to the model should not be abrupt. Besides, if prior information is available from other studies, then it can be interesting to preserve it to obtain a reliable result. All of these aspects that helps to stabilize the inversion procedure are reflected in the regularization constraints.

In the case of TOMO2D the smoothness constraints for both velocity, v, and depth, d, perturbations are introduced using predefined correlation lengths. Because of the large variation in crustal slowness with depth and in order to reduce computational cost, independent 1-D smoothing constraints for slowness perturbation, one for each direction, horizontal L_H and vertical L_V , are chosen against the usage of a dense 2-D matrix. The smoothing constraint for a model parameter perturbation is built following Toomey et al., (1994). A 1-D correlation length for depth perturbation, L_z , is also introduced to Eq.

(5.5). Additionally, as the Fréchet matrix is normalized by the model scaling matrix, the same normalization is also applied to the smoothing matrices. In order to control the relative importance of the smoothing constraints with respect to the data resolution, the λ factor is defined independently for both velocity and depth components. Structures will not be well defined if the smoothing dominates the inversion, whereas artefacts can appear for short correlation lengths. There is no specific rule that determines the proper smoothing parameters. The selection is defined by the user mainly depending on the characteristics of the studied area and acquisition geometry. A convenient way to proceed is to carry out several tests and select the appropriate regularization parameters based on the misfit and model evolution the one that allows a better exploration of the model space according to the expected resolution. Similar correlation lengths for depth and slowness perturbation are recommended if the velocity-depth ambiguity has to be estimated.

If independent additional a priori information of the medium is available, it can be incorporated a jumping strategy (Toomey et al., 1994) based on introducing damping matrices, D, for velocity and depth nodes. Also a factor to control the strength of the damping constraint, α, one for each model parameter component is added. Damping constraints can be assigned for all mesh nodes and maintained during the inversion process to preserve some a priori model knowledge. This strategy is useful when some part of the model does not have to change (because it is well known) while the rest must change. On the other hand, an automatic damping strategy can be applied when no a priori information is available. The model parameter perturbation contribution of the surrounding cells for each mesh node are taken into account to build damping matrices (Van Avendonk et al., 1998). Again, to be consistent with the normalization applied to the Fréchet matrix, the damping matrices are also scaled by the corresponding initial model parameter value. Damping weights are automatically calculated by the secant and bisection method to keep the average perturbation within user-defined limits. In this case, damping constraints are convenient to avoid instability problems when large model parameter perturbations are necessary to update the model, typically during the first iterations of the inversion. The automatic damping strategy is recommended over a manual fixed damping constraints unless no inversion stability can be achieved or no true model features can be kept from the data set contribution.

So, all the mentioned regularization parameters define the linear system to be inverted using the LSQR algorithm as

$$\begin{bmatrix} dt \\ 0 \\ 0 \\ 0 \\ 0 \\ 0 \end{bmatrix} = \begin{bmatrix} G_u & wG_z \\ \lambda_u L_{Hu} & 0 \\ \lambda_u L_{Vu} & 0 \\ 0 & w\lambda_z L_z \\ \alpha_u D_u & 0 \\ 0 & w\alpha_z D_z \end{bmatrix} \begin{bmatrix} \delta s_u \\ \frac{1}{w}\delta s_z \end{bmatrix} \qquad (5.10)$$

When a target solution is far from a starting model and travel-time residuals are large, the inversion is repeated without these outliers and adding damping constraints to stabilize it. The discarded data are incorporated in the subsequent iterations. Final model has to explain all data set so the number of outliers should be limited at the end of the inversion. However, several factors make sometimes impossible fit all data correctly, as hand-picking errors, 3D effects or a non-valid linear approximation of the reality (Toomey et al., 1994).

The ray tracing technique is the most time consuming step of seismic travel-time tomography (Zhang and Toksöz, 1998) and must be solved at each iteration. The computational time involved to solve the inverse equation (5.10) is over an order of magnitude less than the one needed for the ray tracing calculation. Contrary to TOMO3D (Meléndez et al., 2015), there is no parallelization in TOMO2D, so the time spent in the inversion is conditioned by the number of travel-time residual calculations and its sensitivity kernels. The efficiency of the inversion process is directly related to the amount of data, the model parametrisation and the regularisation constraints.

Least-squares system

Direct inversion of equation (5.10) is not feasible because it requires too many computational resources. Consequently, and as explained above, to obtain the model parameter perturbation δs needed to update the n-th model,

$$s_{n+1} = s_n + \delta s \quad (5.11)$$

TOMO2D uses as iterative matrix solver the LSQR algorithm of Paige and Saunders (1982), which is based on a more stable variant of the conjugate gradients method. It provides the minimum-norm solution of an objective function expressed as

$$OF = \| G \cdot \delta s - dt \|^2 + \lambda^2 \| \quad \quad \quad \| \quad \quad \quad \| + \alpha^2 \| \quad \quad \quad \| \quad (5.12)$$

During the first iterations, the larger perturbations will be applied to the initial model. At the end of the inversion process, since the result is close to the target solution, the perturbations tend to be smaller. Reduce the magnitude of the perturbation applied in the last iterations is important to avoid artefacts. Thus, a post-inversion smoothing after each iteration is introduced (Korenaga et al., 2000).

At the end, systematic exploration of a large set of parameters or a hierarchical multi-scale strategy for smoothing constraints to obtain the correct inversion result is the usual way to proceed.

5.2. Adjoint-state full-waveform inversion

Adjoint-state FWI is a pseudo-automatic data-fitting technique that potentially allows extracting high-resolution and high-accuracy models of the rocks elastic properties. This is done by iteratively minimizing the differences between the forward calculated and the observed waveforms or some wave attribute measurable in the seismograms (Lailly, 1983; Tarantola, 1984). As TTT and most deterministic inverse approaches, it is constituted by a forward and an inverse problem. The forward one solves the wave propagation through a reference model in order to calculate their corresponding seismograms. Then a linearized, iterative inverse problem is set to minimize the trace differences by changing the model according to some optimization constraints. Different schemes and applications of FWI using synthetic and/or field data to provide high-resolution models of Vp and Vs velocities, density (ρ), anisotropy, and/or attenuation can be found in the bibliography (e.g. Fichtner et al., 2013; Dagnino et al., 2014; Warner et al., 2014).

In our case, the input data of the FWI algorithm are the shot gathers recorded in a seismic survey (observed or field data). Those seismograms contain the information of the subsurface to be extracted. As in most inverse methods, FWI requires a starting point, i.e. a reference or initial model. In general, a suitable initial model can be obtained using other techniques such as TTT. This initial model is introduced in the code by using an optimal parameterization that depends on the source used, the experimental set-up, and the target of the study. Once we have defined the model, the wave propagation algorithm simulates the synthetic shot gathers, Fig. 5.4. After some data preprocessing or preconditioning, the code calculates the misfit between synthetic and observed shot gathers. There are several numerical norms to measure the misfit (e.g. Jiménez Tejero et al., 2015). If the misfit is larger than a cut-off value, then the inverse problem will find where and how the model has to be changed to reduce it. The inverse problem is solved by calculating the gradient of the misfit function applying the adjoint method. The gradient is the error derivative with respect to all the possible perturbations that one can make to any model node. In this way, the gradient will describe the perturbations that will decrease the error. The gradients of the FWI objective function are part of an optimization set-up to find the search direction and inverting an unknown Vp model. The model is updated with the resultant perturbation. This process is repeated iteratively until a stopping criterion is fulfilled and, at that point the final model is reached, Fig. 5.4.

The main advantage of FWI is its high-resolution, which theoretically is comparable to that of depth-migrated seismic images. For typical seismic acquisition systems, the expected resolution is around a half the propagation wavelength (λ). Despite its potential, FWI suffers from a number of issues that makes it challenging to be applied to most types of field data. Its main drawbacks are the non-linear behaviour and the high computational cost. In particular, high-performance computing systems an parallel computing are needed to solve the forward and inverse problem. FWI is not yet a particularly robust and stable technology because of the limited accuracy of the initial

model, the lack of low frequencies in the field data, the presence of noise, and the approximate modelling of the wave-physics complexity (Warner et al., 2014). Additionally it is difficult to assess the quality of the results (Shah et al., 2012). It is commonly accepted that the solution is strongly dependent on the initial model selected. So, building a good initial model is essential to overcome the non-linearity of the problem and to obtain geologically sound results, in particular for relative high-frequency data sets. As FWI is a local inversion scheme and seismic data are oscillatory, the fitting of the up and downs of two signals which are out of phase (Fig. 5.5), i.e., with a phase-shift higher than half the wavelength, so data that are cycle-skipped, causes that the inversion ends up with a final erroneous Vp model. More specifically, to avoid cycle skipping effects and achieve a successful FWI it is required initial models that allow reproducing seismograms differing by less than half a period from the recorded ones (see Fig. 5.5, and Figure 7 in Virieux and Operto (2009) for an illustration) (Shah et al., 2012; Guasch & Warner, 2014; Jiménez Tejero et al., 2015). As a consequence, FWI might demand human interaction in terms of model set-up, constraints, and data preconditioning.

The code used in this thesis is based on the time domain FD acoustic solver of Dagnino et al. (2014; 2016), which has been developed by Barcelona-CSI group members. The flow diagram of the code, which includes the three main parts mentioned at the beginning of the chapter (model parameterization, forward modelling, and inverse problem) is shown in Fig. 5.4.

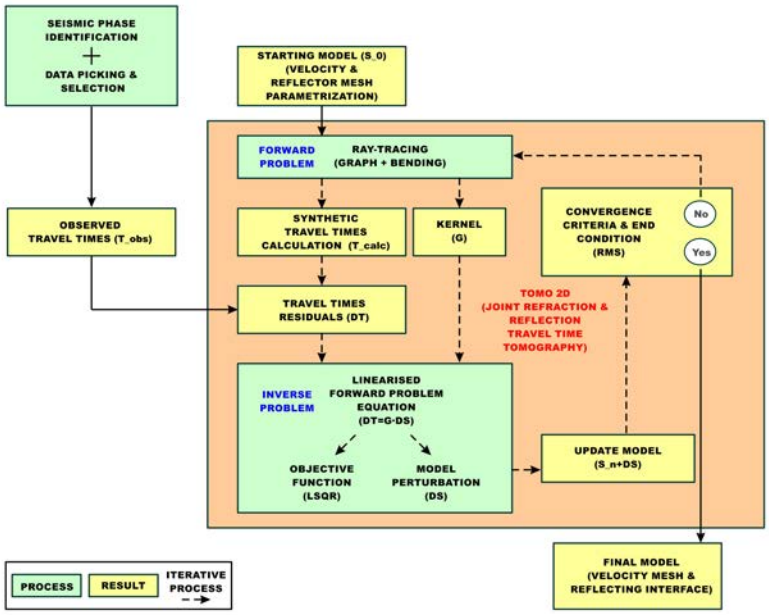

Figure 5.4: Flow diagram of the adjoint-state FWI method applied with Barcelona-CSI code. The three common points for all the inverse methods are written in blue.

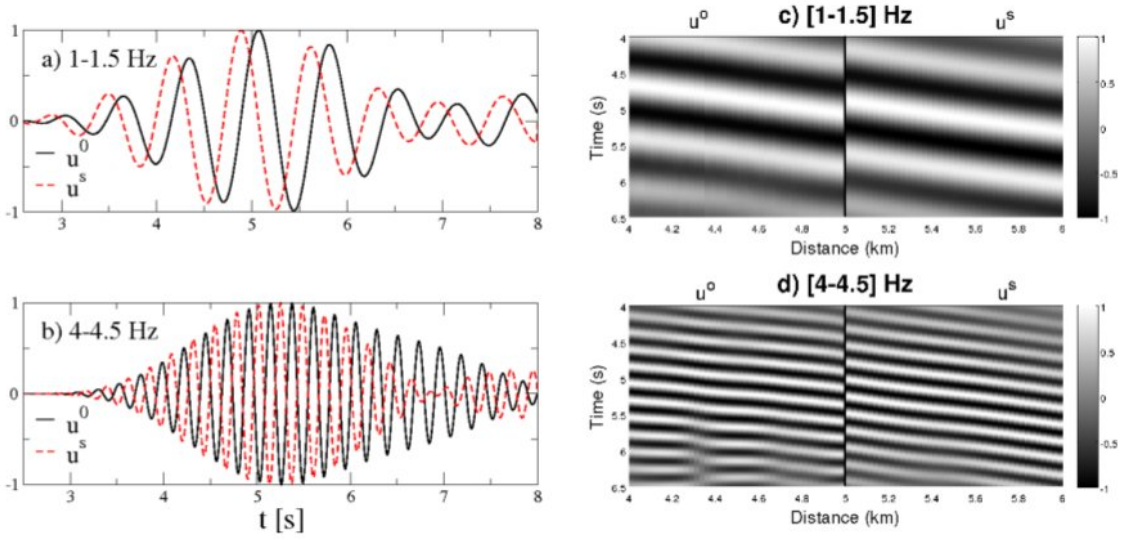

Figure 5.5: Comparison of the amount of cycle-skipping obtained between true and synthetic data for the filters [1–1.5] Hz and [4–4.5] Hz and for the first shot located at 1 km. (a,b) Comparison of traces for the receiver placed at 5 km distance. (c,d) True and synthetic shot gather compared at 5 km distance. The synthetic trace is built using as initial model the homogeneous vertical gradient Vp (Fig. 2a), [Jiménez Tejero et al., 2015].

5.2.1. Model parameterization

The goal of applying the adjoint-state FWI in this thesis is to retrieve a high-resolution Vp model of the media that explains the acoustic pressure field recorded in a particular survey. The physical parameter (Vp) of the media is represented by a regular mesh and is defined at the spatial coordinates of their nodes (see Figure 1 in Pratt et al. (1998) for an illustration). The model parameterization used in the FWI code is equal to the one explained in Chapter 4, because the numerical solver of the DC is the same. Basically, the media is represented by a 2-D Cartesian mesh. The space is discretized over the computational domain with a staggered grid (Virieux, 1986) with a sixth-order approximation and a uniform grid size in both x and z direction. The algorithm also contains the option of interpolate the mesh to obtain higher spatial resolution. The coincidence between modelling mesh nodes and the source-receiver positions are also important to get accurate results, but is not a mandatory requirement.

The physical variables that describe the media are Vp and density (ρ). The values are defined at the mesh nodes for the discrete representation. In our case, the ρ values are calculated using the Vp model and the Nafe-Drake (Ludwig) experimental relationship (Mavko et al., 1998) in all the grid points.

In this case, the model parametrization allows representing vertical as well as lateral media variations producing accurate results. Alternatively more sophisticated

parameterizations such as spectral elements or finite elements (Marfurt, 1984) can be applied in FWI but they are much more demanding from a computational perspective.

5.2.2. Forward modelling

The simulation of the data in the reference model is the first step of all inverse codes, $u=G(m)$, where G is a non-linear operator that relates the seismic data u and the parameters m described in a given reference model. Although the basic principles to calculate the forward problem in FWI are the same as in TTT, i.e. the Huygens' principle, Snell's law..., the main difference with the TTT method is that the FWI solves the wave equation simulating the full seismic wave field rather than the ray trajectories alone. So, the wave equation is the one that will describe the physics of the propagation through the media. Depending on the target of study we can add complexity to the equation to simulate the spatio-temporal evolution with higher reliability. Forms of the wave equation are the acoustic, elastic, visco-elastic, etc. Depending on the version of the wave equation used, different models of parameters should be set, for example Vp and ρ in the acoustic case, or Vp, Vs and ρ in the elastic case, etc. In the extreme situation of the fully anisotropic elastic case, 21 elastic moduli should be constrained to characterize the media. An anisotropic solver will be one that takes into account the different propagation Vp of the waves in the media depending on the direction followed. Using an isotropic solver to an anisotropic media will introduce errors for example in the depth positioning of the layers of the subsurface. In conclusion, the equation chosen must faithfully resolve the properties that one wants to fit.

In the case of Dagnino et al. (2016) algorithm, the forward problem is calculated using the simplest wave equation to concentrate on Vp changes alone. This solver is the same that is used to extrapolate the DC wave field, so considering the 2-D acoustic differential equation in the time domain expressed in the form that appears at Eq. (4.2). The properties of the subsurface to be quantified are embedded in the κ and ρ of Eq. (4.2). The input data are the pressure field recorded by the receivers. The expression of Eq. (4.2) must be verified at the nodes of the numerical grid. So, not only the Vp model and wave fields are discretized, but also the approximations of the spatial and temporal derivatives. The wave equation is usually discretized in the time and frequency domains using the FD method (Virieux, 1986). The algorithm of Dagnino et al. (2016) is implemented in a recursive and explicit FD scheme to approximate numerically the two-way wave equation in the space-time domain. Thus, the value of the wave field at a time step (n+1) at a spatial position is inferred from the value of the wave fields at previous time steps. We use the non-viscous expression and inhomogeneous form, because no symmetries are considered.

Figure 5.6 displays several snapshots from the forward wave field captured at different time steps superimposed on the Vp model that represents the media and the acquisition geometry of the experiment (red star and purple circles). The forward solver generates the

source signal and the pressure field is propagated through the media along time. Next to the wave propagation is displayed up to each time step the pressure wave field recorded at the receiver positions, i.e. the shot gather or shot record. The snapshots show the first wavefront and the result of its interactions with the boundaries of structures with different media properties. The wave propagation part is very important because it represents the 95% of the computational time.

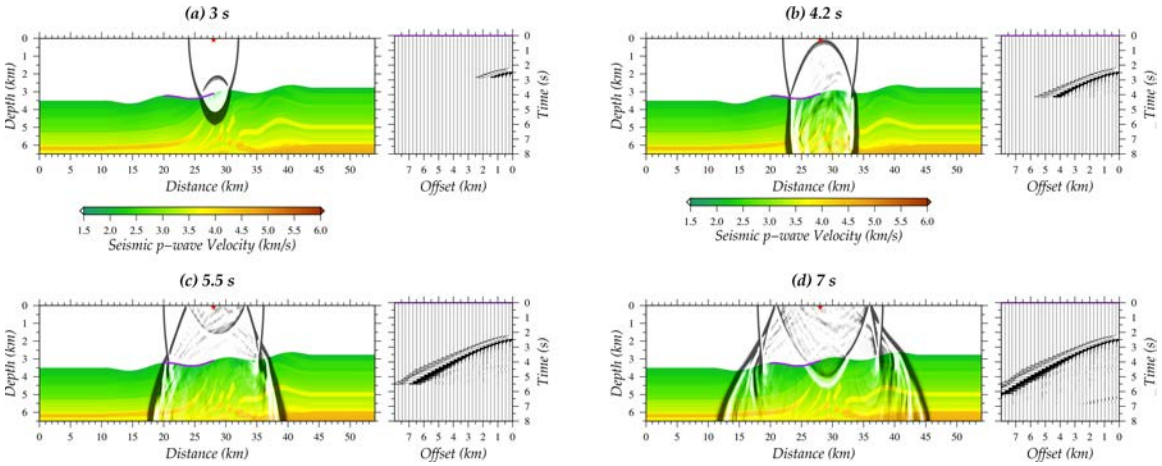

Figure 5.6: Snapshots from the wave field simulation in the medium (Vp model) represented at successive times (a) 3 s, (b) 4.2 s, (c) 5.5 s, and (d) 7 s, next to the resultant numerical seismograms recorded at the seafloor (purple circles). Only 4 seismic traces each km are plotted, so 1/10 traces. Red star marks the source position.

The precision of the forward solver plays a key role on the accuracy of the result. The numerical algorithm of Dagnino et al. (2016) uses the RK method of fourth order in time (Lambert, 1991) and a sixth-order approximation in space of the discretized FD derivatives. As a reminder from Chapter 4, RK method of fourth-order employs the extrapolated output as input for the next extrapolation step (recursively) plus four weighted average increments.

The code includes a CFS-PML (Zhang and Shen, 2010) as boundary conditions to eliminate numerical reflections and a free surface at the top of the model that represents the water/air discontinuity. The absorbing boundary conditions avoid spurious reflections in the model boundaries that may cause interference and mask the correct seismic phases. Thus, they ensure that almost all the energy passing out of the model does not bounce back into it.

In our code, the wave field for the seismic experiments only can be excited by an active (impulsive) source, which is a function of space and time. We use a Ricker wavelet with different central frequencies depending on the experiment. The optimal temporal step (dt) to solve the forward problem fulfils the usual Courant-Friedrich-Lewy stability condition to avoid instabilities in the PML (Dagnino et al., 2014). So, the number of time samples

(nt) to solve the forward problem corresponds to the total recording time inverted (t) divided by the time step, nt=t/dt.

5.2.3. Inverse problem

The inverse problem is the next step to reach an updated model closer to the target one. In FWI, for a given Vp model and acquisition set-up, the seismic records obtained by solving the forward problem (see previous section) must be compared with the observed ones. The differences between those wave fields are quantified for each source-receiver pair of the seismic survey to obtain the misfit or objective function. The goal of the inversion is to find the model parameters, in our case the Vp, that minimizes the misfit function. The relationship between the pressure wave field and model parameter perturbations is non-linear. Thereby, the problem is set for small parameter perturbations. Then, the model is updated in a search direction in which the misfit is reduced. Those model changes follow the gradient of the misfit versus the model parameter to be inverted.

However, fitting the whole seismogram makes the inverse problem very ill-posed, being complicated to obtain a final model with the target characterization of the media. The search of the global minimum or true or target solution is hindered by local minimum, which obstruct the proper evolution of the model by applying another perturbation that partially minimizes the misfit. As FWI is a local inversion scheme, to prevent cycle skipping the matrix inversion is usually regularized by applying a number of gradient-based smoothing and data preconditioning constraints. Dagnino et al. (2016) algorithm has implemented both preconditionings to guide the inversion.

Objective function

The goal of the inversion is to find the parameters m , in our case the bulk modulus κ or V_P ($V_p = \sqrt{\frac{\kappa}{\rho}}$), defined at each node of the numerical mesh that minimize the discrepancy, misfit or objective function (χ) between some predefined waveform attributes of the observed (u^o) and synthetic (u^s) seismic traces at each iteration (Jiménez Tejero et al., 2015). The objective function is used to quantify the data residuals calculating the data-fitting for each source-receiver pair over the time (in the time domain) or frequencies (in the frequency domain).

Several objective functions have been proposed (second column in Fig. 5.7) based on the waveform attribute extracted from the seismic traces (first column in Fig. 5.7). The most simple and widely used waveform attribute in the inverse methods is the observed signal itself (Fig. 5.7 a). Other attributes are the envelope (Fig. 5.7 c), the energy that is

accumulated in the waveform during the time, the phase of the wave (Fig. 5.7 d) and the cross-correlation time between the two traces (Fig. 5.7 e). Depending on the norm used to evaluate the residuals we have different misfit functions, such as L1- ($\chi_{L1}=\int |u^s-u^o|dt$), Euclidean- or L2-norm ($\chi_{L2}=\int (u^s-u^o)^2 dt$), cross-correlation-based (CC) (Luo & Schuster, 1991a) or phase- ($\chi_{phase}=\int (\theta^s-\theta^o)^2 dt$) and envelope-misfit functions (Bozdag, 2011; Fichtner, 2008). All of them have been developed and successfully applied to the FWI algorithm showing different advantages and drawbacks or limitations (Jiménez Tejero et al., 2015).

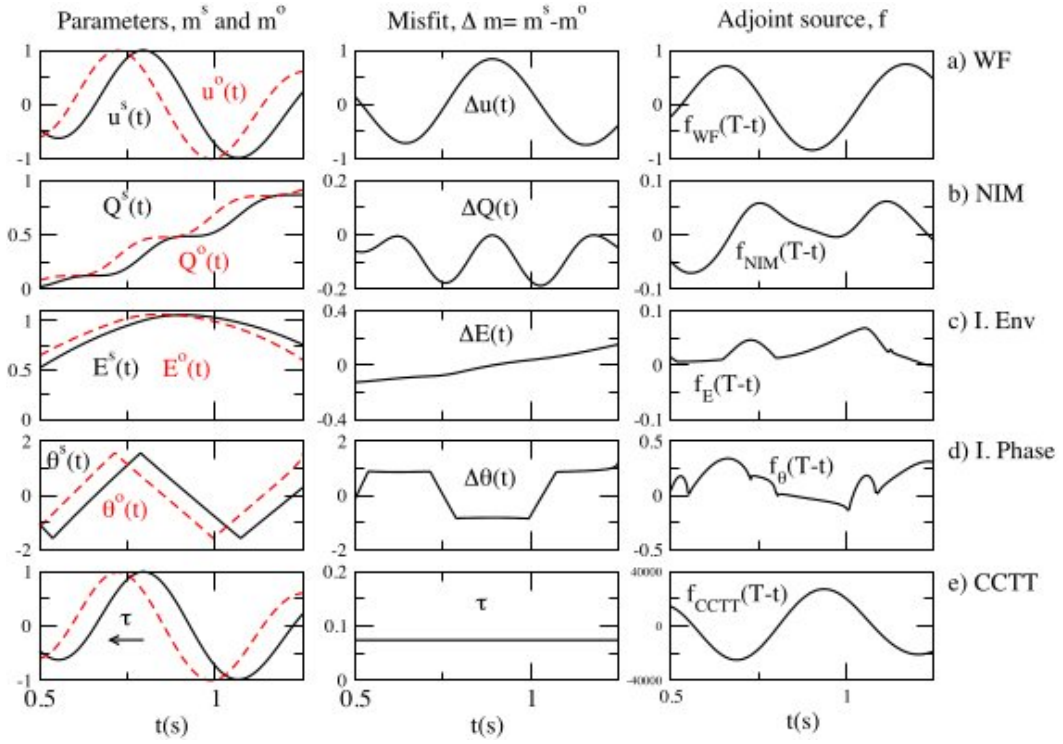

Figure 5.7: In the first column, we show the synthetic (solid black line) and true (dashed red line) wave attributes that can be extracted from the waveform. The second and third columns show the resultant misfit and adjoint sources. The results are shown for the different objective functions in time domain, from top to bottom: (a) Waveform, (b) Non-Integration Method (NIM), (c) Instantaneous Envelope, (d) Instantaneous Phase and (e) Cross-Correlation Travel Time (CCTT). Figure extracted from Jiménez Tejero et al., 2015.

Recent studies found that when data lack low frequencies, the functions which do not include amplitude information work better (Jiménez Tejero et al., 2015). That is because many non-linear effects arise from amplitudes differences between two traces. The best objective function has to be robust and provide accurate results. In Fig. 5.8 is shown the efficiency of the misfit functions in terms of robustness and resolution as a function of input data frequency content.

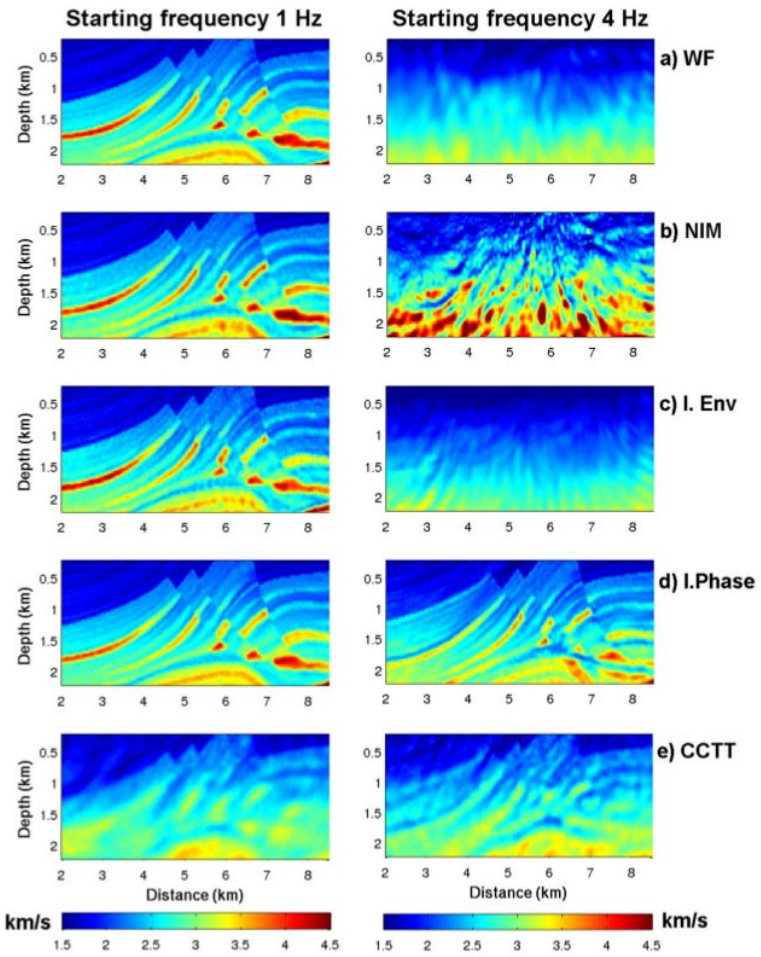

Figure 5.8: Inversion results with and without low-frequency content; the first column with a frequency content of 1 Hz and the second column with 4 Hz. The results are shown for the central area of the Marmousi model, from top to bottom: (a) Waveform, (b) NIM, (c) I. Envelope, (d) I. Phase and (e) CCTT functions. Figure extracted from Jiménez Tejero et al., 2015.

In this work I have focused on the classical L2-waveform objective function (χ) that is built as the least-squares norm of the corresponding misfit (Tarantola, 1984) for a source as follows,

$$\chi_{WF} = \sum_{r,t} \frac{\left(u^s(x_r,t) - c_r u^o(x_r,t)\right)^2}{2} \qquad (5.13)$$

where x_r is the receiver position, t the time and c_r the calibration term. The calibration term is calculated independently for each source-receiver as in Dagnino et al. (2016), but fixing the sea bottom reflection instead of the direct water wave. This term allows correcting source signature changes due to an irregular bathymetry and the

inhomogeneous source directivity. The wave field of each shot gather was resampled to fit on the FD grid. The synthetic data (u^s) for the misfit calculation are simulated solving the forward problem previously explained in an initial model and its updates.

The sensitivity kernels for the different parameters are computed using the L2-norm. It has the advantage of being easy to implement and manipulate mathematically (Tarantola, 2004). It compares the data point by point, so using information from all arrivals at all frequencies and incorporating both phases and amplitudes, such a norm is very sensitive to small perturbations in the measurements, being able to introduce high-resolution details, but at the same time is also highly non-linear and noise dependent. The classical L2-norm is strongly affected by amplitude changes, which might not always properly map into model changes (Kormann et al., 2016).

A data preprocessing and/or preconditioning (see section 5.2.4.) is applied before the calculation of the residuals to reduce modelling issues related with the numerical approximation. For example, the acoustic 2-D forward modelling code compensates the actual 3-D amplitude decay of the field data multiplying the observations by $\sqrt{t}$ (Hicks et al., 2001; Dagnino et al., 2016). Another issue to have in mind when comparing field and synthetic data is that noise is not modelled by the acoustic code, so the signal-to-noise ratio (SNR) of the field data must be high to avoid artefacts. Moreover, the energy of the shots is normalized dividing it by the total source energy to overcome problems due to elastic effects. The ρ model of the subsurface used for the inversion also affects the reflectivity part of the data set, so it is important to interpret the reflectors not only as Vp contrasts. In our case, it is updated after the inversion of each frequency band using the Vp model obtained at the previous iteration and the Nafe-Drake (Ludwig) experimental relationship (Mavko et al., 1998).

Adjoint method and source

The following step consists on updating the model in the direction where the misfit decreases. For this purpose, we calculate the gradient of the misfit function with respect to the model parameters, $\nabla_m \chi = \nabla_u \chi \nabla_m u$, where $\nabla_m u$ are the sensitivity kernels to be computed for each observable, u , with respect to each model parameter to be inverted, m (Tarantola, 1984; Fichtner et al., 2006; Virieux and Operto, 2009). The sensitivity kernels correspond to the kernel of the Born integral that relates the model parameter perturbation, δm_n , to the wave field perturbations, δu_n . More information can be found in Appendix 1 of Tarantola (1984). So, in the acoustic algorithm the sensitivity kernels will be the partial derivative of the pressure field with respect to κ or Vp, ρ and the source. The calculation of theses derivatives implies a huge computational cost. Instead, the Fréchet derivative matrix in the FWI scheme that links the model parameter perturbation to the wave field perturbation is computed following the adjoint-state method proposed by Lailly (1983) and Tarantola (1984). In this case, the calculation of

the gradient relies on the cross-correlations of the forward and adjoint wave field for all source-receiver pairs without calculating explicitly the partial derivatives or Fréchet derivatives.

For a model to be updated, κ_n in the acoustic case, and for a given source point x_s, the adjoint wave field is obtained back-propagating (i.e. reversely in time) the wave field generated by the residuals in time and radiated in-phase from each receiver position, x_r. The residuals represent the part of the signal which is not explained by the current model (i.e., the differences between the simulated and measured wave fields at a receiver position). So, the adjoint wave field constitutes the missing diffracted field that is needed to obtain null data residuals (Gauthier et al., 1986). The adjoint source is calculated as $f(x_r,t)=-\nabla_{u^s}\chi$, and it is specific of the misfit function selected (third column in Fig. 5.7). In our case, we use the waveform adjoint source that is expressed as $f_{WF}(x_r,t)=-(u^s(x_r,t\text{-}T)-u^o(x_r,t\text{-}T))$. The wave propagation algorithm has implemented the backwards reconstruction of the wave field from the model boundaries to calculate the kernels.

Gradient calculation

In first order minimization schemes such as the one used here, the goal is to calculate the gradient and reduce it to zero. The gradient of the objective function with respect to the model, $\nabla_\kappa\chi$ in the acoustic case Eq. (5.14), is computed by convolution of the forward propagated wave field of the source term and the adjoint or back-propagated wave field of the residuals from the receiver location (Tarantola, 1984).

$$\nabla_\kappa\chi=\sum\frac{1}{\kappa(x,z)}\int\frac{\partial u(x,z)}{\partial t}\frac{\partial f(x,z)}{\partial t} \quad (5.14)$$

Figure 5.9 shows an example of how the gradient is obtained along time. The target model has a rectangular shaped Vp anomaly of 4 km/s embedded at an offset distance of 2-4 km and at 1 km depth over a background Vp of 2 km/s. The correlation or product along time of the direct and adjoint wave fields for all the source-receivers pairs gives the gradient, as is expressed in Eq. (5.14). Initial model is an homogeneous model of 2 km/s, therefore the gradient points towards the position of the missing high-Vp anomaly (pannel d in Fig. 5.9) where the changes must be applied.

In our adjoint-state FWI code, both forward and adjoint propagations are performed using the same FD acoustic solver (section 5.2.2.). To avoid that the gradient points toward a local minimum, the FWI code has implemented a gradient-based preconditioning that concentrates model updates in the regions where the gradient is more reliable (section 5.2.4.). Specific details on the gradient preconditioning techniques applied can be found in Dagnino et al. (2014; 2016).

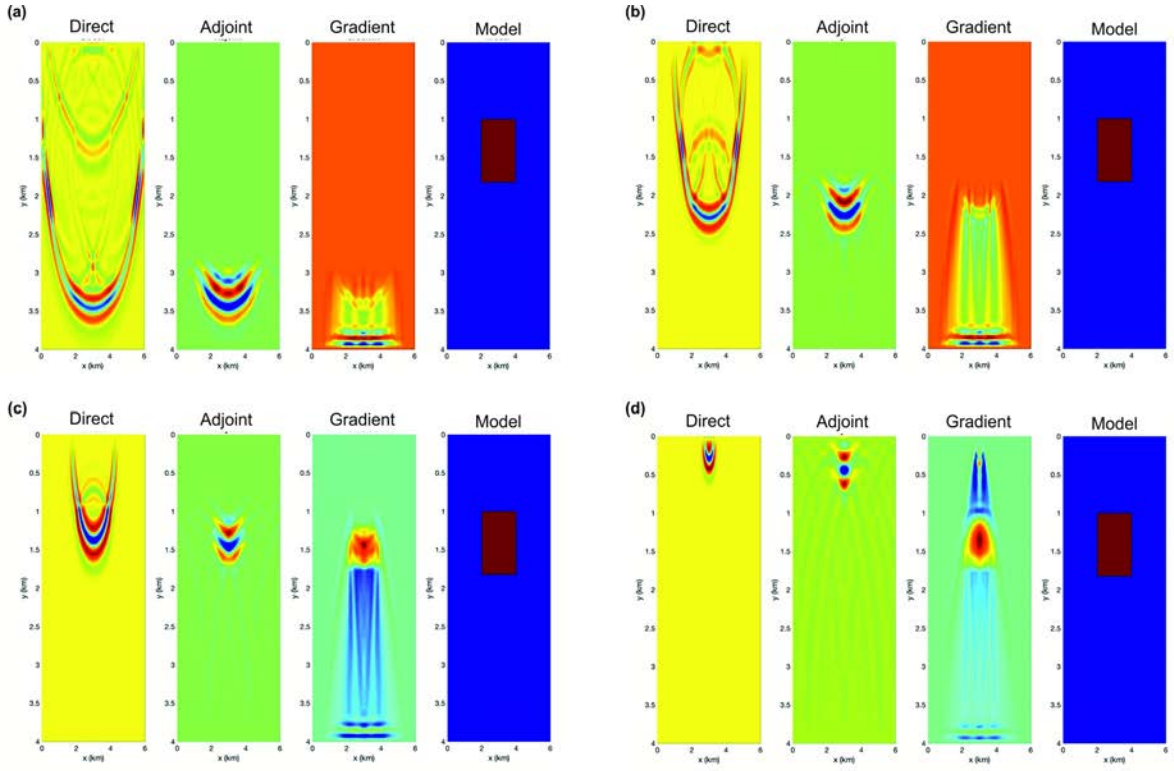

Figure 5.9: Direct wave field, adjoint wave field, gradient and target model at different time steps, (a) 0,3 s, (b) 0,6 s, (c) 0,9 s and (d) 1,2 s. Direct wave field is plotted reversed in time instead of the adjoint wave field for a better illustration. Initial model is an homogeneous media of 2 km/s, same as target model but without the red rectangular anomaly of 4 km/s. Gradient in pannel (d) clearly shows the area where there is a different Vp, so where to apply changes in the initial model. Figure from D. Dagnino (personal communication).

Optimization, search direction and model update

The last step of the inversion process is the optimization of the problem. It consists on finding the direction in the model-space in which the value of the misfit function locally decreases, p_i .

There are different optimization methods implemented in the algorithm to find the search direction and model perturbation, such as the steepest descent (SD), non-linear conjugate gradients (NLCG) and Limited-memory Broyden - Flecher - Goldfarb - Shanno (l-BFGS). In first order minimization schemes, such as in the SD and NLCG, the search direction is defined in each iteration using the gradient. The SD method has the advantage that it is particularly low sensitive to noise. The step used to find the direction in the model space where the misfit function locally decreases, is just the opposite of the gradient in the SD approach, $p_i = -\nabla_m \chi_i$.

The NCG approach with Polak-Ribière criterion is also widely used as search algorithm (Grippo & Lucidi, 1997; Nocedal & Wright, 2006). In this case, the direction at the iteration i, p_i, is a linear combination of the gradient at iteration i, $\nabla_m \chi_i$, and the direction at iteration i-1, p_{i-1}.

$$p_i = \nabla_m \chi_i + \beta_i p_{i-1} \quad (5.15)$$

The parameter β_i is commonly calculated using the Polak-Ribière criterion which provides a direction reset automatically,

$$\beta_i = \frac{\nabla_m \chi_i (\nabla_m \chi_i - \nabla_m \chi_{i-1})}{||\nabla_m \chi_i||^2} \quad (5.16)$$

Finally, the l-BFGS (Nocedal, 1980) is formulated as $p_i = -H^{-1}[\chi_i]\nabla_m \chi_i$, where H is the Hessian matrix. The H matrix is the second order Taylor expansion of the objective function near the solution. The inverse of the Hessian is used to weight the gradient. In the l-BFGS method, the p_i is iteratively approximated using Quasi-Newton methods without explicitly computing H.

In the FWI algorithm, we use a normalized search direction. Then, the optimal step length (α_i) is determined by imposing $\alpha_i = min_{c>0} \chi(m_i + cp_i)$, where m_i and p_i are the model and the search direction at the ith iteration. The final step is obtained after acquire the minimum of a polynomial approximation over three steps calculation in the search direction of the misfit function (see Figure 1in Vigh et al., (2009) for an illustration). In the framework of the Born approximation, the model can be updated as $m_{i+1} = m_i + \alpha_i p_i$.

Figure 5.10 shows for the SD (left panels) and l-BFGS (right panels) optimization algorithms how the misfit or error value decreases along the iterations (top panels) and the trajectory of the misfit evolution along the iterations in the model perturbation space (bottom panels) to finally end up to the global minimum (central point). The goal of the inverse problem is to reduce the misfit iteratively. Consequently, the calculated seismograms are each time closer to the recordings. This means that the model should also be each time a better approximation of the target media.

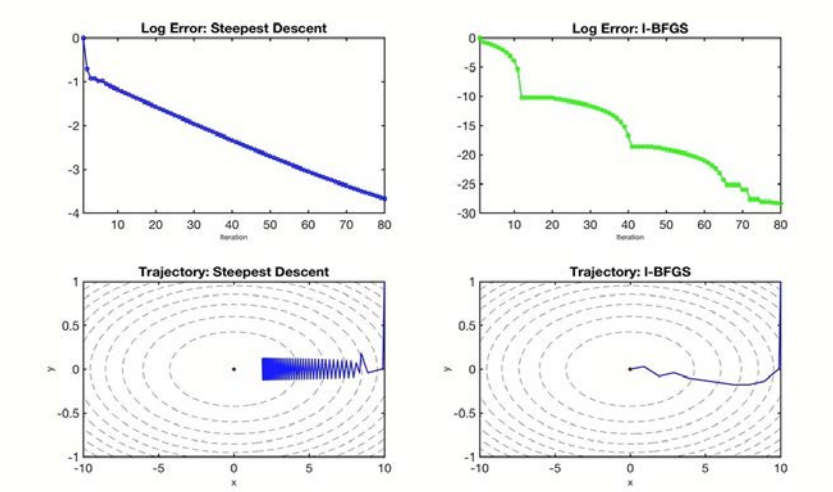

Figure 5.10: Reduction of the misfit function for the SD (left panels) and l-BFGS (right panels) optimization algorithms. Top panels show the decreasing of the error or misfit value along the iterations. Lower panels show the trajectory of the misfit evolution along the iterations in the model perturbation space to reach the global minimum (central point). Figure from D. Dagnino (personal communication).

Stopping criterion and convergence

The inverse process is repeated iteratively until a pre-defined stopping criterion is fulfilled. There are many stopping criterion, such as a data misfit cut-off, a maximum number of iteration allowed, etc. The main objective of these constrains is to reduce computational costs. In our code, the stopping criterion during the inversion are (1) the Arminjo rule (Nocedal and Stephen, 2006) when changes are < 0.01, (2) setting a maximum number of iterations per frequency step and (3) setting a maximum number of calculations in the optimization process. Overall, a trade-off between computational efficiency and quality of the image must be found (Virieux and Operto, 2009).

Theoretically, the model that better explains the input data set must be obtained after the inversion. However, it usually happens that the algorithm does not converge and it stops because the search direction is trapped into a local minimum. Because local optimization does not prevent convergence of the misfit function toward local minimum, it is a challenge defining a minimization criterion that mitigates the sensitivity of FWI especially to amplitude errors. The maximum cause of non-linearity is when the initial model is far from the target solution (it is not kinematically correct) (Virieux and Operto, 2009) and the data are insufficient to resolve subsurface structures for that range of wavelengths. This is often the case in the conventional short-streamer reflection seismic data, which typically have high-frequency data that do not allow the reconstruction of large and intermediate wavenumbers (Jannane et al., 1989). Low frequencies of the data and the wide apertures help resolve the intermediate and large wavenumbers of the medium (Virieux and Operto, 2009; Brossier et al., 2014). Therefore, having a good

initial Vp model that properly reproduces the lowest usable signal frequency in the data set is essential to prevent cycle skipping artefacts and obtain “a true” solution that is close to the target model. Figure 1 of Shah et al. (2012) illustrates the importance of the accuracy of the initial model used and detects the cycle skipping problematic with plots of phase difference between the observed and calculated data at the lowest usable frequency present in the field data.

Developing mathematical or modelling strategies to build an adequate initial model for L2-FWI without *a priori* information of the subsurface is necessary to make the method robust. The misfit function is a strongly non-quadratic function of the parameters describing the background velocities, so when data are cycle-skipped the misfit function saturates (Jannane et al., 1989). Consequently, practical FWI schemes invert early arrivals before late, low frequencies before high, and phases before amplitudes. The so called multi-scale approach (Bunks et al., 1995), where different frequency bands are inverted sequentially, from low to high, is now followed in almost all FWI schemes (Shipp and Singh, 2002; Dagnino et al., 2014, 2016; Jiménez Tejero et al., 2015; Kormann et al., 2016). In particular a low-pass Butterworth filter is applied to the data, so that let solve different frequency bands of the same data at each external iteration, restricting the inversion in a limited bandwidth (Fig. 5.11). The inversion jumps to the next frequency band when the algorithm does not satisfy one of the previous restrictions or stopping criterion. Therefore, it consists on repeating all the iterative inverse process for different frequency bands using as initial model the one obtained in the previous step. Implementing this strategy reduces the risk of falling into local minimum because the objective function is smoothed when the data are filtered. Details or high-wavenumber information are incorporated progressively into the model in successive iterations.

In order to make the problem better-posed, we can also apply some mathematical algorithms (Métivier et al., 2016) or strategies focused on changing or combining different objective functions (see fig. 15 of Jiménez Tejero et al., 2015; Kormann et al., 2016) and/or inversion techniques (Delescluse et al., 2011). That is to say, finding a way to calculate the misfit by using a numerical technique or strategy more robust in front of the cycle skipping problem that cope with missing long-wavenumber features on the initial models. The strongest concern for the algorithm is fitting the phases correctly (Métivier et al., 2016). As reported by Jiménez Tejero et al. (2015), CC functional is able to provide good background models, but lack in resolution, so Kormann et al. (2016) embedded this approach with the classical L2-norm in the same global FWI package to retrieve the short-wavelength features in a semi-automatized and stable procedure. In this thesis, we use the resultant model of applying the TTT technique to generate the data for the first iteration of the FWI.

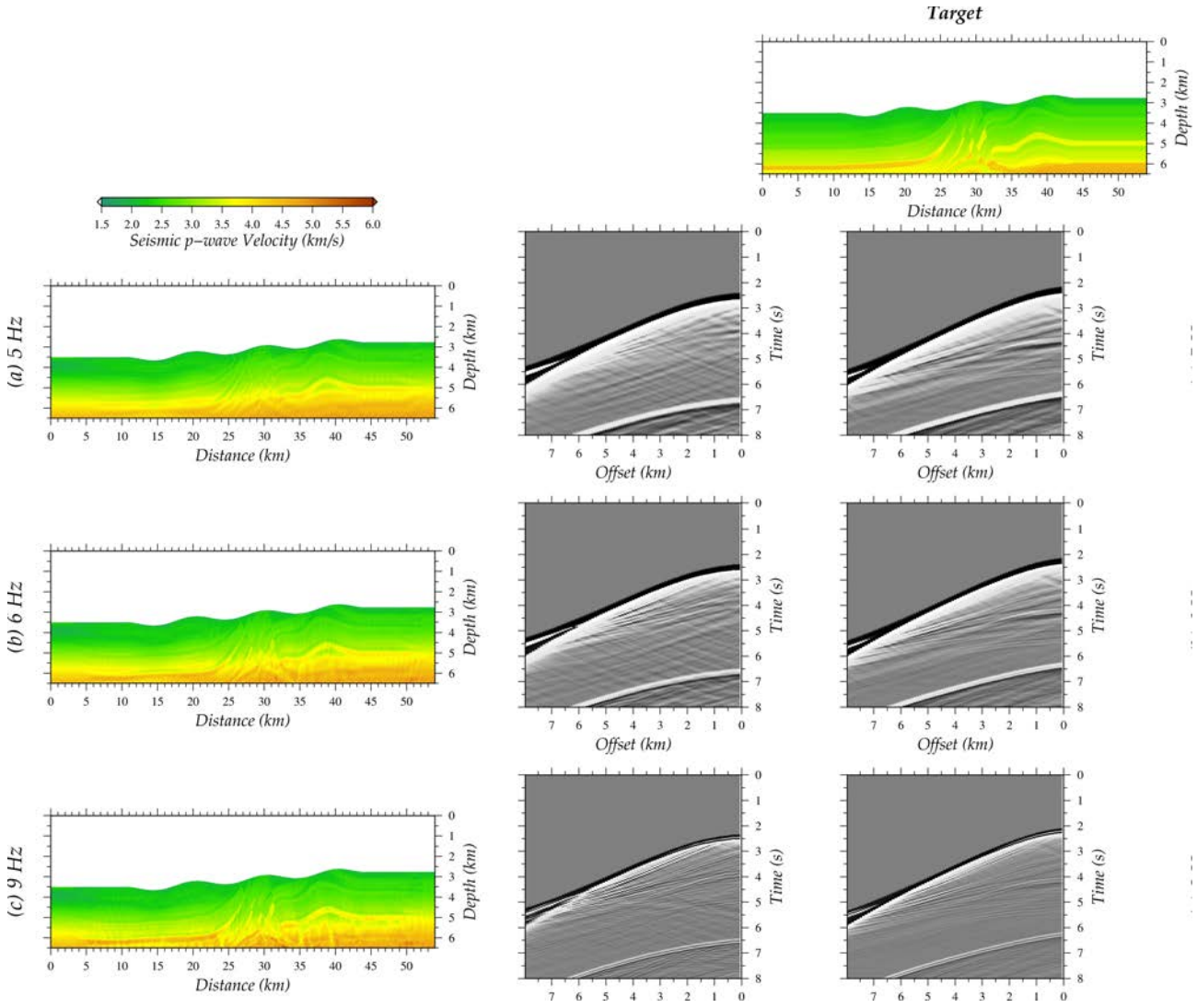

Figure 5.11: Model and data evolution along the multi-scale FWI. Target (right panels) and resultant (middle panels) data after the inversion of (a) 5 Hz, (b) 6 Hz, and (c) 9 Hz in a multi-scale strategy. After the inversion of each frequency band data present more arrivals, so detailed information of the media is added at each step. In the same way, model (left panels) is gaining in resolution each time that a new subset of data are fitted, i.e. after the inversion of a higher frequency band.

5.2.4. Gradient preconditioning

The usage of regularization or preconditioning constraints is essential to reduce convergence issues in the FWI, caused by the high-number of model parameters and quantity of data to fit (Dagnino et al., 2014). There are mainly two types of preconditioning, one based on the data and the other on the model. Its goal is to stabilize the inversion procedure and conduct it to the proper evolution towards the correct solution. In the case of the model-based preconditioning, the changes introduced to the

model should not be abrupt. This aspect will be reflected in the insertion of smoothing constraints or filters to reduce artefacts or errors in the gradient coming from wrong low-wavenumber information in the initial model, an imperfect source or noise in the data. In Dagnino et al. (2016) code, a 2-D low-pass zero-phase Butterworth filter is defined as smoothing regularization operator to balance the gradient and thus reduce its sensitivity to the presence of 'spikes'. In the case of the data-based preconditioning, they are focused on fitting or highlight a particular part of the seismograms. Then, only the data selected by this time-window is contained in the objective function and inverted. This purpose requires to identify the target phases of each trace and then select the size of the window and the weighting applied. A bandwidth filter can be implemented to achieve an appropriate time-window.

As it was mentioned, the preconditioning is also applied to compensate the effects of the real wave propagation that are not included in the forward simulation, such as the amplitude loss at depth, viscoelasticity or 3-D effects. Some weighting parameters can be introduced in the gradient or the source signature to correct these issues.

Finally, we perform and apply a data preconditioning to optimize the introduction of the reflected information between the first arrival, typically the seafloor reflection, and its multiple with a specific type of data-windowing. We identify the first arrival travel-time by using a maximum kurtosis and k-statistics criterion (Saragiotis et al., 2002) in a time-window that is centered in the seafloor reflection. The travel-time of the seafloor reflection is calculated approximately using a water Vp of 1.5 km/s, the seafloor depth and the source-receiver offset distance. When the first arrival is not found, for example due to a noisy channel, or the difference between the synthetic and observed first arrivals is bigger than a half a period of the inverted frequency, then the trace is set to zero. On the other hand, the trace value is set to zero before the first arrival travel-time, and after that it is balanced by a function defined as $\sqrt{t}$ to compensate the amplitude decrease with depth. Finally, the trace is also set to zero after the travel-time of the first multiple. Therefore, the gradient calculation is focused on introducing to the model detailed information of the data set coming from the near-vertical reflections.

5.2.5. Parallelization

The adjoint-state FWI code used here of Dagnino et al. (2014, 2016) is written in Fortran 99 with the exception of some libraries that are programmed using C language. The algorithm is parallelized to decrease the computational time and increase its functionality. The parallelization consists of distributing sources over different processors. So, the multiple forward and adjoint-propagations responsible for the most of the run time in the inversion are distributed among the available computational resources. Depending on the number of available CPUs, each one takes care of one propagation or more. As an example, if you have 1000 shots and 1000 cores then each core is in charge of calculating only one shot. However, if the number of cores is less than shots, for example 500, each

core is responsible of two propagations. Sources are assigned in the form of MPI processes. The code is automatic, so a new shot is generated in each core sequentially until all of them are simulated. The global Fréchet derivative matrix is calculated from the gradient and misfit of the whole data set, so the communication between CPUs is needed at these steps.

Aside from possible numerical dispersion problems, this formulation gives very efficient results in terms of computational resources required, fast propagation and easy implementation of different acquisition geometries.

Part IV

RESULTS

“A l'aigua pura,
No hi ha peixos”

Chapter 6. Synthetic models

This section presents the synthetic tests made to test the proposed workflow. The first one represents a canonical, checkerboard-like media, whilst the second is the Marmousi-2 model (Martin et al., 2006), a more realistic and complex one commonly used as a benchmark by both industry and academia. The description of the acquisition geometry is presented for each model, jointly with the methods used to simulate the corresponding data set.

The objective of the synthetic study is to prove that the subsurface Vp can be successfully retrieved using an appropriate modelling strategy of MCS streamer data. The obtained results are also compared with the reference subsurface structure to evaluate the accuracy of the Vp retrieval in the different parts of the models.

6.1. Checkerboard model

The first Vp model is the one presented in Fig. 6.1. It includes checkerboard-like Vp anomalies superimposed on a background vertical Vp gradient. The model is ~ 9.5 km long x 3 km deep. A horizontal seafloor is located below 1 km deep of constant Vp water layer. The water Vp value is set to 1.5 km/s. The background Vp gradient is built following the linear function of depth $v(z)=1.5+1.25\cdot z$ (km/s), going from 1.5 km/s at the seafloor to 4 km/s at the bottom of the model. Given that the resolving power decreases with depth, the Vp anomalies superimposed are bigger and have larger Vp contrasts in the deeper part than in the shallower one. Thus, the checkerboard anomalies dimensions are 1.5 km wide x 0.75 km deep in the shallowest 0.75 km below the seafloor, whereas at deeper levels the dimensions are 2.25 km wide x 1.25 km deep. The box anomalies have an amplitude of ±10% with respect to the background Vp in the shallow part, and of ±15% in the deeper part. So, the anomaly pattern is described by

positive anomaly:

$$v(x,z)=v(z)+0.10\cdot v(z);\quad z<0.75(km)$$
$$3\cdot(n-1)\le x<3\cdot(n-1/2)\le 9.575(km);\quad n=1,\ldots,4 \qquad (6.1a)$$

negative anomaly:

$$v(x,z)=v(z)-0.10\cdot v(z);\quad z<0.75(km)$$
$$3\cdot(n-1/2)\le x<3\cdot n(km);\quad n=1,\ldots,3 \qquad (6.1b)$$

positive anomaly:

$$v(x,z)=v(z)+0.15\cdot v(z);\quad z\ge 0.75(km)$$
$$4.5\cdot(n-1)\le x<4.5\cdot(n-1/2)\le 9.575(km);\quad n=1,\ldots,3 \qquad (6.1c)$$

positive anomaly:

$$v(x,z)=v(z)-0.15\cdot v(z);\quad z\ge 0.75(km)$$
$$4.5\cdot(n-1/2)\le x<4.5\cdot n(km);\quad n=1,2 \qquad (6.1d)$$

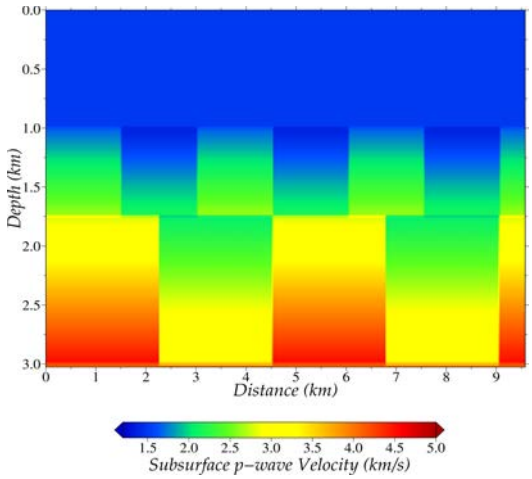

Figure 6.1: The target 2-D checkerboard Vp model, which includes a 1 km deep water layer lying above a checkerboard-type model, with larger-size anomalies in the deeper than in the upper part; superimposed on top of a vertical Vp gradient. The color scale represents Vp in km/s.

Acquisition geometry

The geometry set up for the checkerboard model simulates a 5 km long streamer. The streamer is composed of 100 hydrophones (channels), separated 50 m from each other. The source is located 75 m ahead of the first channel. A total of 45 shots spaced 100 m, starting at 5075 m from the left boundary, are used to simulate the synthetic experiment. The vessel moves towards the right. The acquisition geometry set up is summarized in Table 6.1.

Parameters of the checkerboard model	**Values**
Dimensions of the area	~ 9.5 x 3 km
Number of active channels	100
Distance between channels	50 m
Total streamer length	4950 m
Streamer depth	25 m
Distance source - 1st channel	75 m
Maximum offset	5025 m
Common Midpoint (CMP) distance	25 m
Number of shots	45
Shot distance	100 m
Source depth	25 m

Table 6.1: Relevant acquisition parameters that characterize the simulated geometry for the checkerboard test (Vp model in fig. 6.1).

The initial MCS streamer configuration has the sources and receivers located at a depth of 25 m. However, this depth can be modified using the DC technique that is described in Chapter 4.

Velocity parameterization and forward modelling parameters for the simulation of the data set

A regular nodal mesh is chosen to represent the Vp field. The nodal distance is 12.5 m both vertically and laterally, resulting in a uniform grid of 768 x 244 nodes. The main forward parameters used to generate the data set in the checkerboard model with the geometry configuration shown in Table 6.1 are included in Table 6.2.

Forward parameters	**Values**
Node spacing	12.5 m
Model dimensions (# nodes)	768 x 244
Source signature	Ricker wavelet
Central frequency of the source	8 Hz
Trace length	8 s
# trace points	5798
Sample rate	1.4 ms
Forward star order (x,z) (node connections)	(5,5)

Table 6.2: Model parameterization and relevant forward parameters used to solve the forward problem (wave propagation, ray tracing and travel-time calculation) for the checkerboard test.

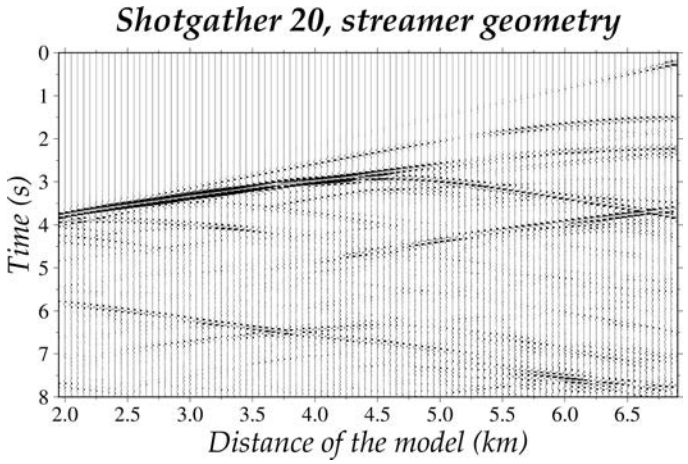

Figure 6.2: Shot gather simulated with the acquisition geometry of Table 6.1 and using the forward parameters and the 2-D checkerboard Vp model parameterization of Table 6.2. The shot is located at a distance of 6.975 km along model.

The shot gathers were simulated with the acquisition geometry of Table 6.1 using the 23DAS solver (Dagnino et al., 2016), the forward parameters, and the 2-D checkerboard Vp model parameterization of Table 6.2 (see Fig. 6.2). The first arrival travel times and corresponding ray paths were computed using the forward solver that is described in section 5.1.2. The forward travel-time solver corresponds to a modified version of the tt_forward subroutine of TOMO2D (Begović et al., 2017).

6.2. Marmousi-2 model

The second synthetic model chosen is a modified version of Marmousi-2 benchmark model (Martin et al., 2006). Marmousi-2 was created by the Institut Français du Pétrole, and it was based upon geology from the North Quenguela Trough in the Quanza Basin of Angola. The intricate geological system together with the stratigraphic features generate a complex distribution of Vp anomalies and discontinuities that require advanced processing techniques to obtain a correct tomographic image. This model has become the most widely used industrial and academic benchmark to test seismic processing and inversion algorithms and even today is routinely used in many works.

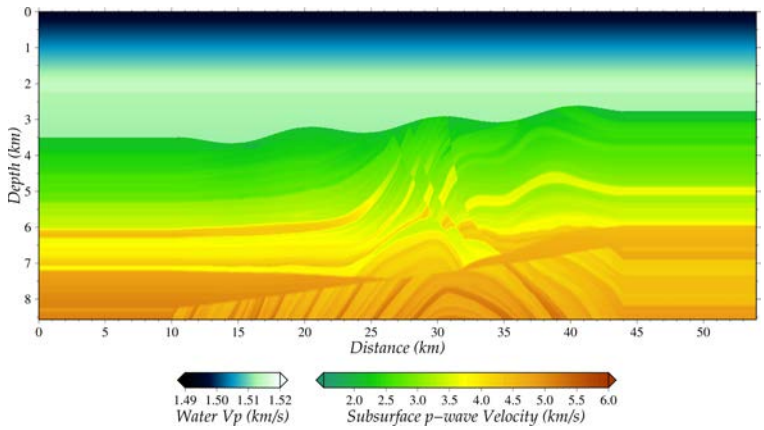

Figure 6.3: The target 2-D Marmousi-2 Vp model. Vertical and horizontal distances have been re-scaled from the original Marmousi-2 benchmark model. A laterally stretching in both extremes was also applied to assure full coverage of the target geological structures in the inversion. We have modified the shallow part of the original model so that we include a complex bathymetry that is covered by a realistically heterogeneous water column.

The Vp model has been modified by applying a smoothing and a laterally stretching of 10 km in both edges to assure the entire recovery of the central area, which is the target of our test. The model dimensions have been re-scaled to simulate a realistic experimental setting. Thus, the final model size together with the water layer is ~ 54 km wide x 9 km deep (Fig. 6.3).

In this case, two different Vp models have been considered for the water layer. The first water model is set to an homogeneous Vp value of 1.5 km/s, whilst the second is the one

with realistic Vp variations reflecting the seawater heterogeneity according to oceanographic measures (e.g. Dagnino et al., 2016). The water Vp has the following function of depth

$$\begin{aligned} v(z) &= 1.515 - 0.01 \cdot z \qquad z < 2 \\ v(z) &= 1.495 \qquad 2 < z < 2.25 \\ v(z) &= 1.495 + 0.0006 \cdot z \qquad z > 2.25 \end{aligned} \tag{6.2}$$

Where the velocity v is in km/s and the depth z in km. One of the goals is testing the influence of the water layer heterogeneity on the DC and inversion results. Additionally, in this case the seafloor is not flat, but it is a sloping wavy surface resulting in an irregular bathymetry that reflects a more realistic and complex case. The seafloor has a dip angle of 2.4%, and a sinusoidal perturbation as a function of horizontal distance $z(x) = A \cdot \sin\left(2\pi\upsilon + \frac{\pi}{2}\right)$, where A = 0.15 km (amplitude of the perturbation) and $\upsilon = 10^{-7}$ km (frequency of the perturbation), has been added on top of it. This perturbation frequency generates seamount-like features in the seafloor.

Acquisition geometry

The geometry set up for the Marmousi-2 model simulates a 8 km long streamer. The streamer is composed of 320 channels, separated 25 m each. The source is located 50 m in front of the first channel. A total of 920 shots spaced 50 m were considered starting at 8025 m from the left boundary to simulate the synthetic experiment. The vessel moves towards the right. The acquisition geometry set up is summarized in Table 6.3.

Parameters of the checkerboard model	**Values**
Dimensions of the area	~ 54 x 9 km
Number of active channels	320
Distance between channels	25 m
Total streamer length	7975 m
Streamer depth	25 m
Distance source - 1st channel	50 m
Maximum offset	8025 m
CMP distance	12.5 m
Number of shots	920
Shot distance	50 m
Source depth	25 m

Table 6.3. Relevant survey parameters that characterize the acquisition geometry for the Marmousi-2 test.

Velocity parameterization and forward modelling parameters for the simulation of the data set

A regular nodal mesh is chosen to represent the Vp field. The nodal distance is 12.5 m both vertically and laterally, resulting in a uniform grid of 4321 x 688 nodes. The main forward parameters used to generate the data set in the Marmousi-2 model with the geometry configuration shown in Table 6.3 are included in Table 6.4.

Forward parameters	**Values**
Node spacing	12.5 m
Model dimensions (# nodes)	4321 x 688
Source signature	Ricker wavelet
Central frequency of the source	10 Hz
Trace length	8 s
# trace points	4501
Sample rate	~ 1.8 ms
Forward star order (x,z) (node connexions)	(5,5)

Table 6.4. Model parameterization and relevant forward parameters used to solve the forward problem (wave propagation, ray tracing and travel-time calculation) for the checkerboard test.

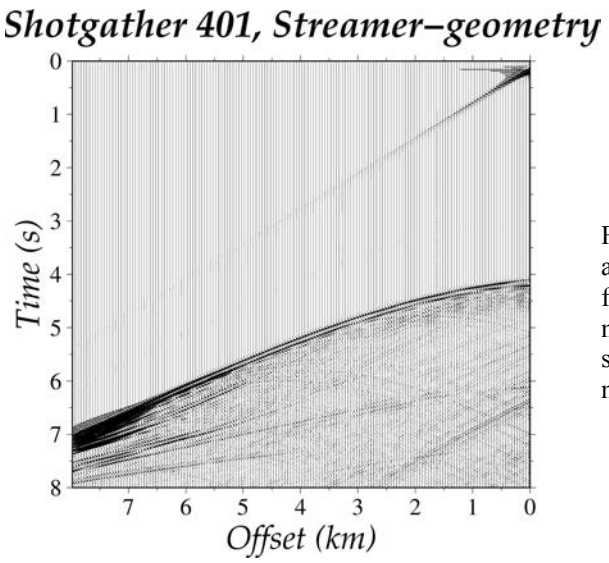

Figure 6.4: Shot gather simulated with the acquisition geometry of Table 6.3 and using the forward parameters and the Marmousi-2 Vp model parameterization of Table 6.4. The source is located at a distance of 28 km along model.

The shot gathers were simulated with the acquisition geometry of Table 6.3 using the 23DAS FD solver (Dagnino et al., 2016), the forward parameters, and the Marmousi-2 Vp model parameterization of Table 6.4 (see Fig. 6.4). The first arrival travel times and corresponding ray paths were computed using the forward solver that is described in section 5.1.2. The forward travel-time solver corresponds to a modified version of the tt_forward subroutine of TOMO2D (Begović et al., 2017).

Chapter 7. Synthetic downward continuation results

Seismic record sections include a combination of reflected and refracted phases among others. These phases are often masked by one another. As it is shown in the simulated MCS seismic records in Figs. 6.2, and 6.4, the direct arrival and the seafloor reflection mask the later arrivals of the refracted phases throughout most of the record section. The main target of the DC methodology explored and applied in this thesis consists on moving the experiment set up to a virtual surface, which in our case is the seafloor (seafloor-type geometry), in order to remove the water column's effect and highlight the subsurface Vp information contained in the first arrivals or early refractions. Different WED approaches have problems with the irregular datum surface and/or heterogeneous subsurface Vp media (Cho et al., 2016). The objective of this section is to prove that the first arrival travel-time information of the MCS streamer data can be successfully simulated at the seafloor using the 23DAS code (Dagnino et al., 2016) and the methodology explained in the previous Chapter 4 for arbitrarily complex media.

In this chapter, we first describe the data set preprocessing. Then, we show the results obtained by applying the first and second DC steps for the two synthetic models presented in Chapter 6. The parameters describing the back-propagation, i.e. the model parameterization and the geometry set ups for each DC step, are summarized in tables. To analyse the accuracy of the method we compare the results with data simulated using the target subsurface model and the corresponding virtual geometry for each DC step. Finally, we discuss the advantages and limitations of the method.

Data set preprocessing

Prior to re-datuming, the streamer shot gathers generated in Chapter 6 are preprocessed. In these synthetic tests, the only preprocessing step consists of muting the direct arrival. There are two main reasons to remove the direct arrival of the input data set. First, because this energy has no valuable information of the subsurface properties. The other reason is that this energy is not recorded in a seafloor-type geometry, which is the one to be simulated by the DC. To remove this energy, we simulate the direct arrival using the 23DAS code (Dagnino et al., 2016) and the water Vp model, and then the result is subtracted from the shot gathers.

7.1. Checkerboard test

The objective of this synthetic study is to apply the DC methodology in a simple case to show that it works in basic conditions. Therefore, the DC is performed through an

homogeneous or constant Vp water layer to extrapolate the wave field at an horizontal flat datum surface. So, Vp media is set to 1.5 km/s and has a total surface of ~ 9.5 km length x 1 km depth. Under this conditions, given a water column of 1 km depth and a subsurface Vp on average of ~ 1.8 km/s, the crossover distance (Eq. 4.7) is more than ~ 6.6 km. As the streamer length is 5 km refractions can not be identified as first arrivals.

OBS acquisition-type shot gathers

Here we show the first step of the DC that consists on moving the streamer (i.e. the receivers) from the sea level to the seafloor surface. To do so, each preprocessed shot gather is used as a source, so it is propagated backward in time through the water layer. Therefore, as each shot gather has in this test 100 traces, then each back-propagation will have 100 sources that are shot simultaneously. This is done by applying a multi-shooting technique (section 4.2.2). This wave field is recorded by 100 receivers, i.e. the virtual streamer, located at the seafloor. The acquisition geometry set up for the back-propagation of the streamer to the seafloor is summarized in Table 7.1.

Parameters for the back-propagation of the streamer	**Values**
Dimensions of the area	~ 9.5 x 1 km
Node spacing	12.5 m
Model dimensions (# nodes)	768 x 82
Number of sources	100
Number of receivers	100
Distance between sources	50 m
Distance between receivers	50 m
Source depth	25 m
Receivers depth	987.5 m
Number of shot gathers (files to back-propagate)	45

Table 7.1: Relevant survey parameters for the back-propagation of the streamer for the checkerboard test.

Fig. 7.1 a shows the resultant wave field in the correct time after the back-propagation of receiver records for a shot located at a distance of 6.975 km along the model (see section 6.1 Fig. 6.2). Fig. 7.1 b shows the simulated seismic wave field that is generated with the source at the sea surface and the streamer at the seafloor (i.e. the OBS-type acquisition setting) and using the checkerboard model (Fig. 6.1). The wavefronts of most seismic events are imaged in Fig. 7.1 a. Aside from wave amplitude, differences arise from the direct arrival that travels through the water column, which is the strong event in Fig. 7.1 b that masks the signal below it, as for example at 5 km offset distance where this energetic arrival is clearly observed at ~ 3.5 s. Because of this high-amplitude event, the image is

displayed using less gain and reflections are less clear in Fig. 7.1 b. Another difference is the appearance of hyperbolic wavefronts with positive slopes in Fig. 7.1 a that are seen before the first arrival. This energy is a product of the extrapolation process.

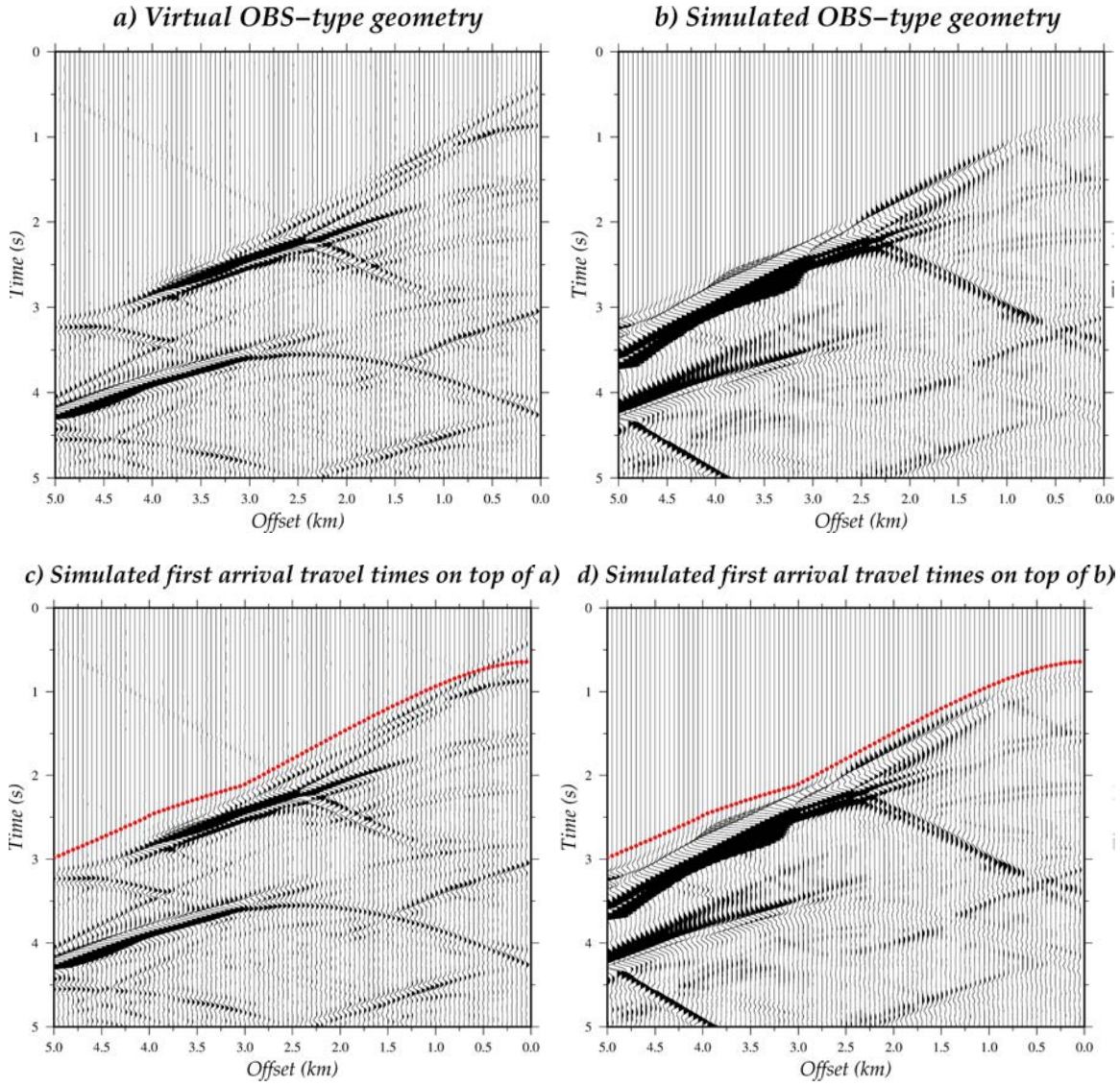

Figure 7.1: a) Seismic data obtained after the first DC step simulating a virtual OBS-type geometry. b) Simulated seismic data generated using the checkerboard model and the OBS-type geometry. Lower panels c)- d) show shots a)-b) together with first arrivals (red dots) calculated using TOMO2D, the checkerboard model and the OBS-type geometry.

A number of refractions that were obscured in the original recordings (see section 6.1, Fig. 6.2) can now be observed. The relative gain of visible refractions in the recordings after downward continuing the receivers (see section 4.2.1) is Δx_{rl} of 2 km (from kilometer 3 to 5).

Seafloor acquisition-type shot gathers

The second step of the DC consists on moving the shots or sources from the sea level to the seafloor surface for the checkerboard model. To do so, each OBS-type shot gather is re-sorted into receiver gathers and it is propagated backwards in time through the water layer (Fig. 7.2 a) as a source. Therefore, as a receiver gather can be illuminated in this test by a maximum of 45 shots (i.e. the maximum fold is 45), then each back-propagation will have 45 sources that are shot at the same time by applying the multi-shooting technique (section 4.2.2). This wave field is recorded by 45 receivers, i.e. the number of sources, located at the sea surface. The acquisition geometry set up for the back-propagation of the sources to the seafloor is summarized in Table 7.2.

Parameters for the back-propagation of the sources	**Values**
Dimensions of the area	~ 9.5 x 1 km
Node spacing	12.5 m
Model dimensions (# nodes)	768 x 82
Number of sources	45
Number of receivers	45
Distance between sources	100 m
Distance between receivers	100 m
Source depth	987.5 m
Receivers depth	25 m
Number of receiver-gathers (files to back-propagate)	188

Table 7.2: Relevant survey parameters for the back-propagation of the sources for the checkerboard test.

Fig. 7.2 a shows the wave field reversed in time used as input for the second back-propagation for a receiver located at a distance of ~ 5 km along the model. Fig. 7.2 b shows the output or resultant wave field reversed in time after the back-propagation of the receiver gather shown in Fig. 7.2 a. Then, the data is re-sorted in the original domain and corrected in time. Figs. 7.3 a, and c show the final DC result and Figs. 7.3 b, and d the simulated seismic wave field for the same shot as in Fig. 7.1, located at a distance of 6.975 km along the model. In this case, both source and streamer are at the seafloor. Again, most seismic events are displayed in Fig. 7.3 a. Wave amplitudes from the final DC shot (Fig. 7.3 a) are much lower than the simulated ones (Fig. 7.3 b) because of the energy lost during the two back-propagations. Aside from wave amplitudes, differences arise again from the direct arrival and the sea surface reflection, both present only in Fig. 7.3 b. As the water and the shallow subsurface velocities are similar, the direct wave that travels through the water column and the one that travels trough the subsurface have almost the same slope and appear superimposed as first arrivals in the first 2.5 km of offset distance in the seismic record. On the other hand, the sea surface reflection is

located at ~ 1.5 s at zero offset in Fig. 7.3 b. As in the previous case, energy that arises due to the extrapolation process is seen before the first arrival in Fig. 7.3 a. This energy is more evident here than after the first DC step. This fact may be due to a possible source aliasing because of the high-distance set as source spacing in the experiment.

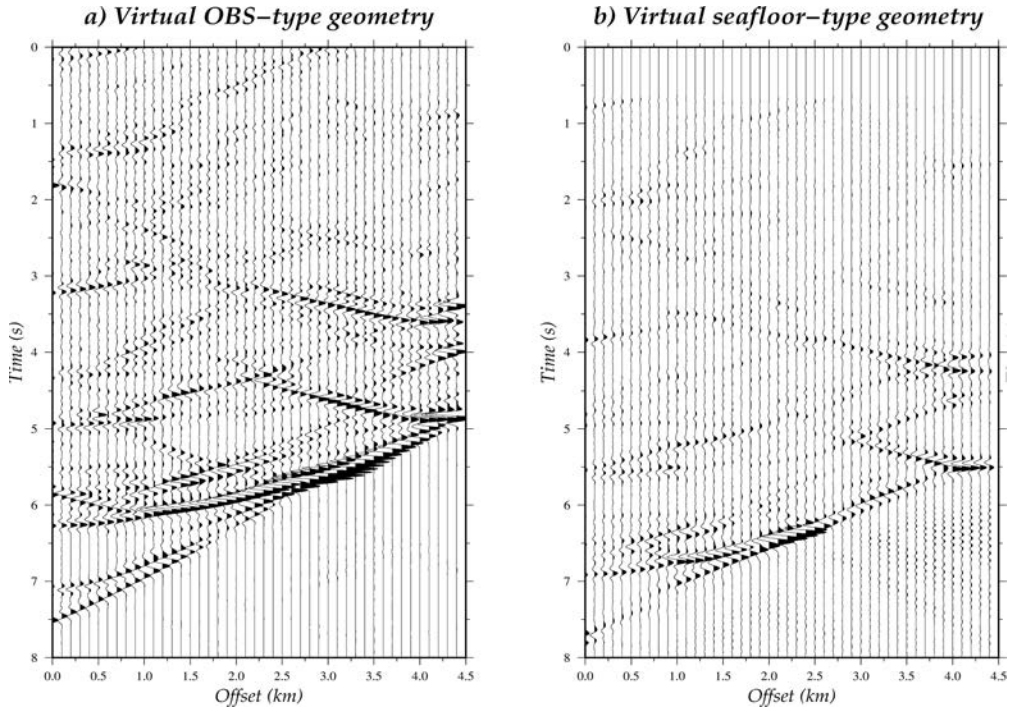

Figure 7.2: a) Receiver gather from the data obtained after the first DC step (reversed in time). This seismic wave field is used as input for the second DC step. b) Receiver gather obtained after the second DC step simulating a virtual seafloor-type geometry (reversed in time).

As it can be observed in Fig. 7.3, early refractions from shallow subsurface that were obscured in the original recordings (see section 6.1, Fig. 6.2) can now be observed. The arrival times simulated and plotted as red dots in Figs. 7.3 c, and d correspond to those seen from DC data within ±0.13 ms on average (Fig. 7.3 c). Thus, Fig. 7.3 c demonstrates that first arrival travel times are not significantly affected by the DC. The fact that both sources and receivers are located at the seafloor, make that first arrivals can now be tracked from zero offset up to the maximum offset, which corresponds to the streamer length. However, first arrivals are more difficult to identify at long offsets, because of amplitude attenuation.

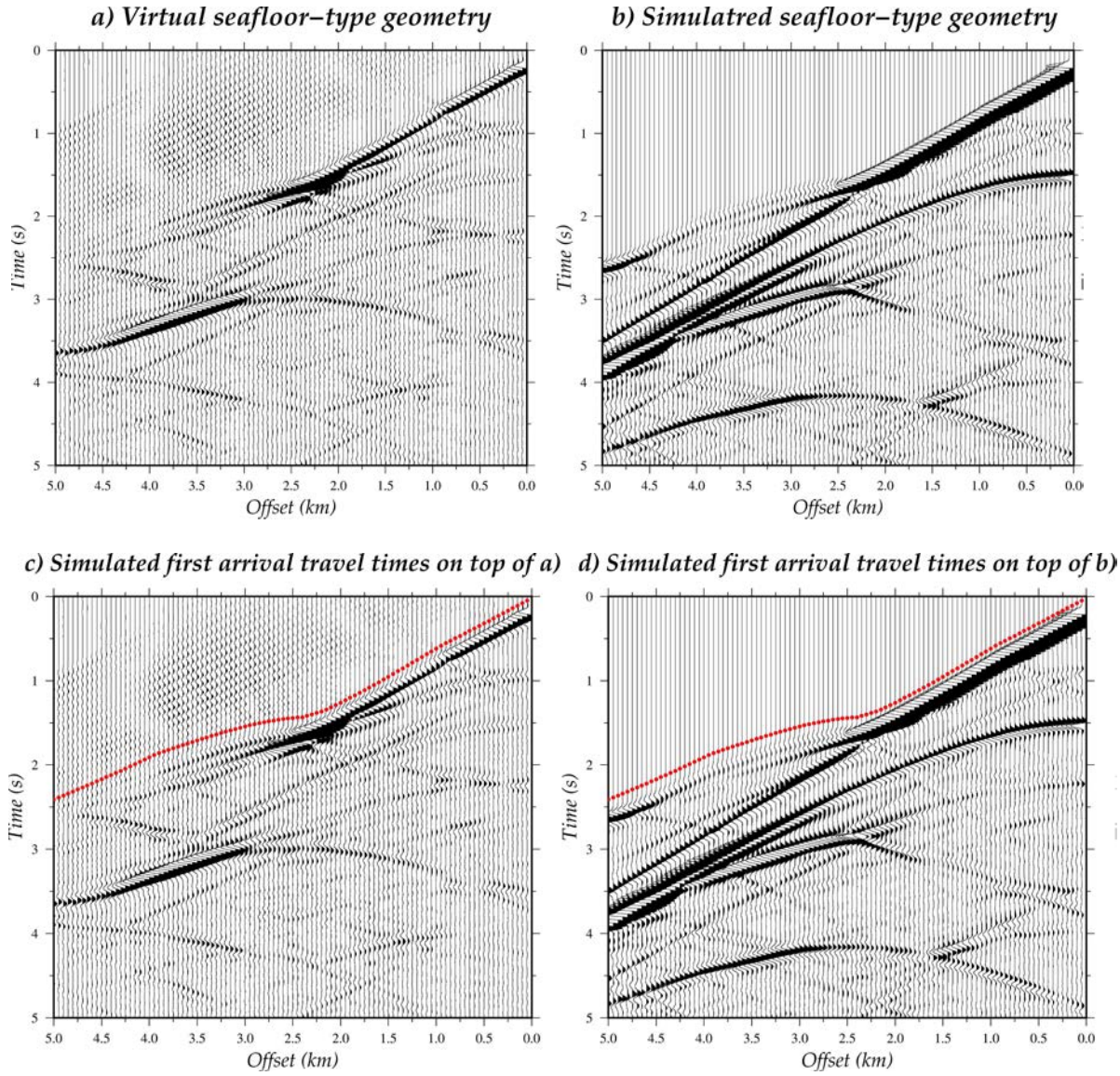

Figure 7.3: a) Seismic data obtained after the second DC step simulating a virtual seafloor-type geometry. b) Simulated seismic data generated using the checkerboard model and the seafloor-type geometry. Lower panels c)- d) show shots a)-b) together with first arrivals (red dots) calculated using TOMO2D, the checkerboard model and the seafloor-type geometry.

7.2. Marmousi-2 test

In this section, the DC process is tested for a more complex synthetic case, which is the Marmousi-2 model presented in section 6.2. As explained in Chapter 6, the Vp distribution is based on the geological characteristics of a real area, and the introduction of a non-uniform water Vp and irregular shaped seafloor, and therefore datum surface,

makes it more challenging for DC. The effect of using constant versus variable water Vp in the DC results is also discussed.

In this case, the water Vp model has a total surface of ~ 54 km length x 4 km depth. For this model, given an average datum surface of 3.1 km depth and a subsurface Vp of ~ 2.2 km/s, the crossover distance (Eq. 4.7) is more than ~ 14 km. As the streamer length is 8 km, refractions can not be identified as first arrivals.

OBS acquisition-type shot gathers

In this test each preprocessed shot gather has 320 traces that act now as sources. The back-propagated wave field is recorded by 320 receivers, i.e. the virtual streamer, located at the rough seafloor. The acquisition geometry set up for the back-propagation of the streamer to the seafloor is summarized in Table 7.3.

Parameters for the back-propagation of the streamer	**Values**
Dimensions of the area	~ 54 x 4 km
Node spacing	12.5 m
Model dimensions (# nodes)	4321 x 82
Number of sources	320
Number of receivers	320
Distance between sources	25 m
Distance between receivers	25 m
Source depth	25 m
Receivers depth	Seafloor topography
Number of shots (files to back-propagate)	920

Table 7.3: Relevant survey parameters for the back-propagation of the streamer for the Marmousi-2 test.

Fig. 7.4 a shows the resultant wave field in the correct time after the first back-propagation for a shot located at a distance of 28.025 km along the model (see section 6.2 Fig. 6.4). Fig. 7.4 b shows the simulated seismic wave field that is generated with the source at the sea surface and the streamer at the seafloor (i.e. the OBS-type acquisition setting) for the Marmousi-2 model. The wavefronts of most seismic events are imaged in Figs. 7.4 a, and c but they appear more curved than in Figs. 7.4 b, and d. In Figs. 7.4 a, and c, the direct water wave that travels from the source at sea surface to the seafloor, is added for a better comparison with Fig. 7.4 b, and d. Again due to the extrapolation, hyperbolic wavefronts with positive slopes appear before the first arrival in Fig. 7.4 a, and c. The strongest one is located at ~ 1.5 s at zero offset. It arises from the water reflection in the streamer recording, which after the first DC step becomes a one-way

travel-time event. Another difference is that no signal is recorded after ~ 5.7 s (with the exception of the direct water wave introduced a posteriori) because of the time (~ 2 s) needed for the wave field that act as a source to travel from the sea level to the seafloor surface (~ 3.1 km).

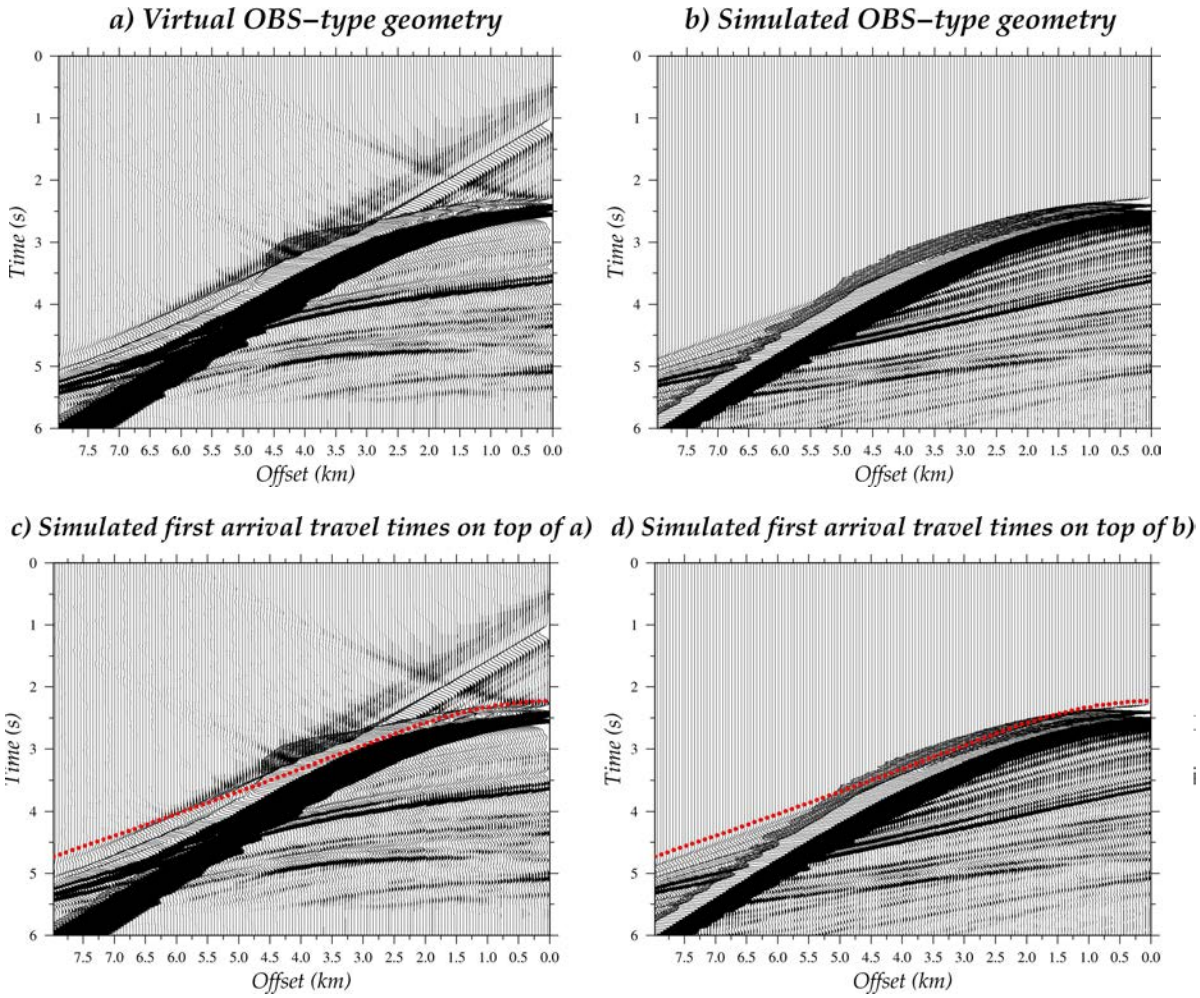

Figure 7.4: a) Seismic data obtained after the first DC step simulating a virtual OBS-type geometry. b) Simulated seismic data generated using the Marmousi-2 model and the OBS-type geometry. Lower panels c)- d) show shots a)-b) together with first arrivals (red dots) calculated using TOMO2D, the Marmousi-2 model and the OBS-type geometry.

The relative gain of visible early refractions (see section 4.2.1, Δx_{rl}) observed with the OBS-type geometry is of ~ 3.4 km (from kilometer 4.6 to 8). The first arrivals at far offsets are in Figs. 7.4 a, and c affected by attenuation effects and appear less focused due to the finite nature of the seismic record used as equivalent source.

Seafloor acquisition-type shot gathers

In this section the previous results (Fig. 7.4 a) are sorted into receiver gathers and send backwards in time as equivalent sources (second step of the DC) through the Marmousi-2 water column model to move the shots or sources at the seafloor surface. As a receiver gather can be illuminated in this test by a maximum of 920 shots, then each back-propagation will have 920 sources that are shot at the same time by applying the multi-shooting technique (section 4.2.2). Traces that correspond to shots that are out of the receiver fold are set to zero. The wave field is recorded by 920 receivers, i.e. the number of sources, located at the sea surface. The acquisition geometry set up for the back-propagation of the sources to the seafloor is summarized in Table 7.4.

Parameters for the back-propagation of the sources	**Values**
Dimensions of the area	~ 54 x 4 km
Node spacing	12.5 m
Model dimensions (# nodes)	4321 x 320
Number of sources	920
Number of receivers	920
Distance between sources	50 m
Distance between receivers	50 m
Source depth	Seafloor topography
Receivers depth	25 m
Number of receiver-gathers (files to back-propagate)	2158

Table 7.4: Relevant survey parameters for the back-propagation of the sources for the Marmousi-2 test.

Fig. 7.5 a shows the shot imaged in the previous section (Fig. 7.4) but after the whole DC process simulating a seafloor-type acquisition setting. As a way of comparison, Fig. 7.5 b displays the simulated shot gather located at the same position and seafloor-type geometry but generated using the Marmousi-2 model. Fig. 7.5 a is plotted using more gain because of the energy lost during the two back-propagations. It is not straightforward to correlate the wavefronts in Fig. 7.5 a with the ones in Fig. 7.5 b. A clear difference is that the energy is less focused in Figs. 7.5 a, and c, so wavefronts are not as well defined as in Figs. 7.5 b, and d. The water wave displayed in Fig. 7.5 b is not seen in Fig. 7.5 a. Again, energy that arises before the first arrivals from the extrapolation process is seen in Fig. 7.5 a. First arrivals in Fig. 7.5 a have higher amplitude as compared with later arrivals. Early refractions (red dots in Figs. 7.5 c, and d) from the shallow subsurface that were obscured in the original recordings (see section 6.2 Fig. 6.4) can now be observed. The arrival times correspond to those observed in the simulated data within ±0.17 ms. At far offsets, the presence of slightly upward diffraction tails in Figs. 7.5 c and a higher amplitude attenuation hinder the identification of the first

arrivals. Moreover, truncation of the recordings also in time makes even more difficult the identification of first arrivals at far offsets. In this case, the minimum recording time (Eq. 4.16 section 4.2.1) is of $t_{rec} \sim 6.7$ s for a 3.1 km depth (z_0) at an average water (v_0), and subsurface velocities (v_1) of 1.5 and 2 km/s respectively at 8 km offset distance. Therefore, as total recoding time is of 8 s, at the maximum offset distance the wave field recovered by the DC process is approximately of 1 s after the first arrival.

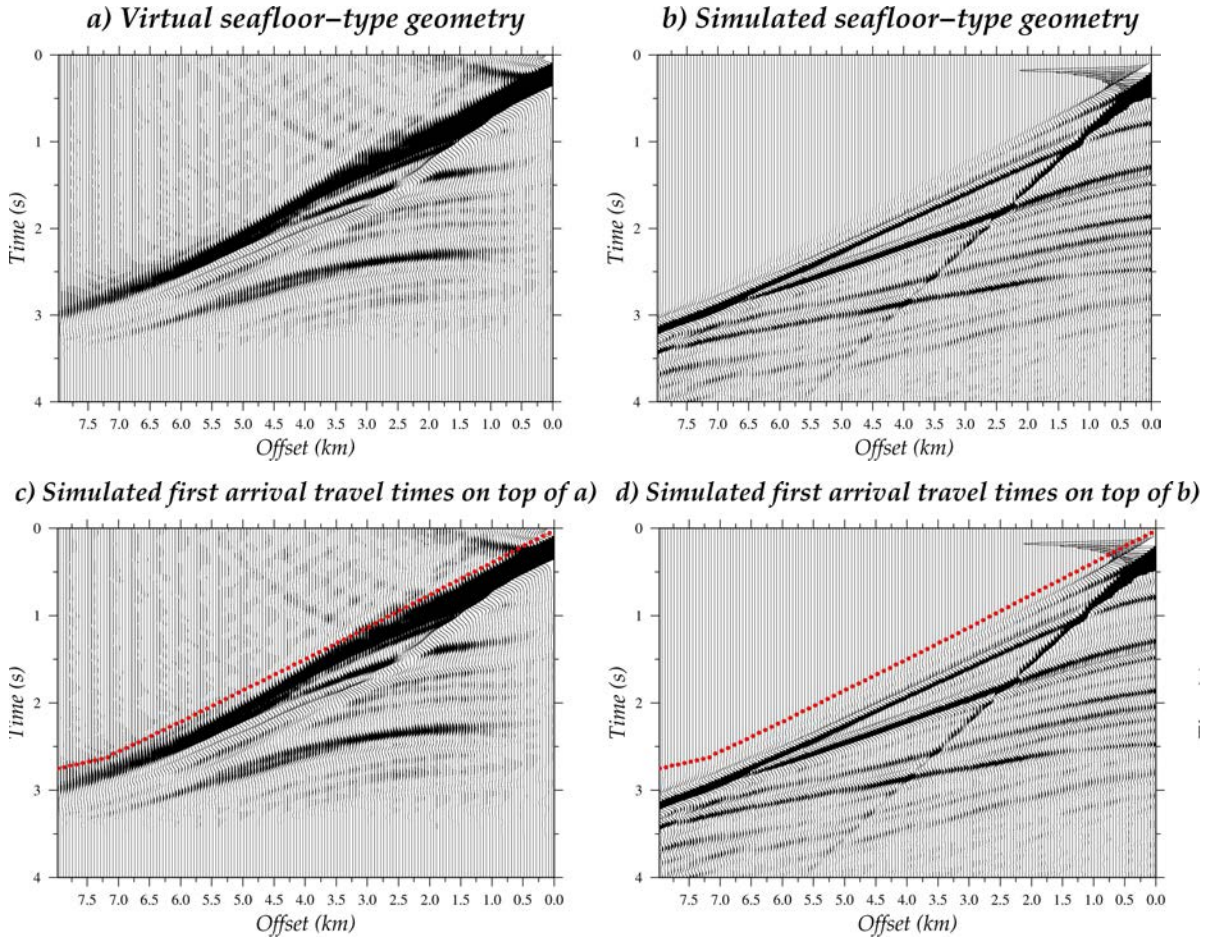

Figure 7.5: a) Seismic data obtained after the second DC step simulating a virtual seafloor-type geometry. b) Simulated seismic data generated using the checkerboard model and the seafloor-type geometry. Lower panels c)- d) show shots a)-b) together with first arrivals (red dots) calculated using TOMO2D, the Marmousi-2 model and the seafloor-type geometry.

Downward continuation in a constant water velocity media

Here, the back-propagation is performed using a constant water Vp model set to 1.5 km/s, instead of the one defined in section 6.2, whose mean value in depth is 1.515 km/s. The input data is formed by the same preprocessed shot gathers used in the previous test. The

following analysis is focused on first arrival travel-time misfits caused by Vp changes in the water column.

Fig. 7.6 shows the ray paths or trajectories for the first arrival phases corresponding to the first shot located at a distance of 8.075 km with a OBS-type geometry and using the Marmousi-2 Vp model with the variable water Vp (a), and the constant Vp one (b). No significant differences are observed between the ray trajectories in Fig. 7.6 a, and b. Just in Fig. 7.6 b rays concentrate to follow the exact same trajectories, and small gaps appear. However, Vp variations are too faint to produce important changes in the ray trajectories. As in both cases first arrivals follow almost the same paths, travel-time misfits are very small (see Fig. 7.7). Fig. 7.7 shows the distribution of travel-time misfits in the form of a histogram. Travel-time misfits from 1.5 up to 3.5 ms are obtained by using TOMO2D. Travel-time misfits are therefore smaller than 3-3.5 ms, which is less than the picking uncertainty.

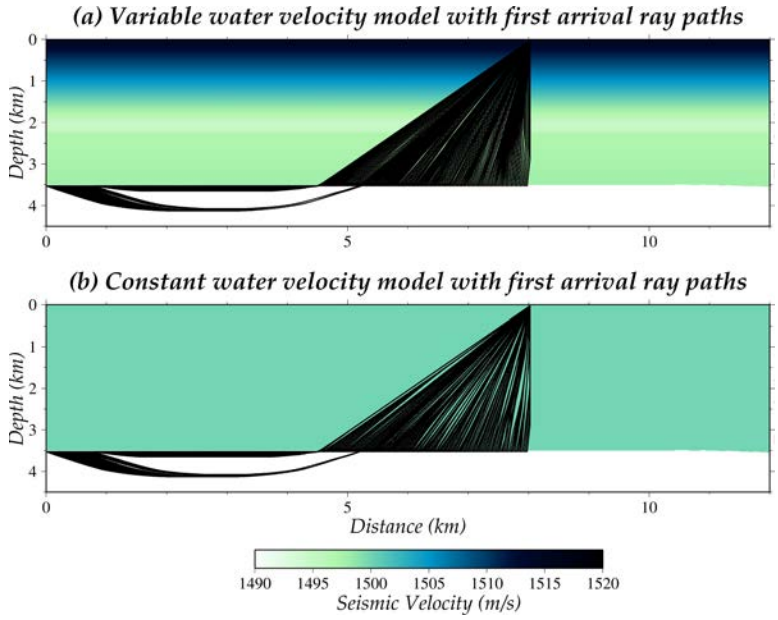

Figure 7.6: First arrival ray paths for the first shot located at a distance of 8.075 km with a OBS-type geometry and using the Marmousi-2 Vp model with its variable water Vp (a) and a constant one set to 1.5 km/s (b).

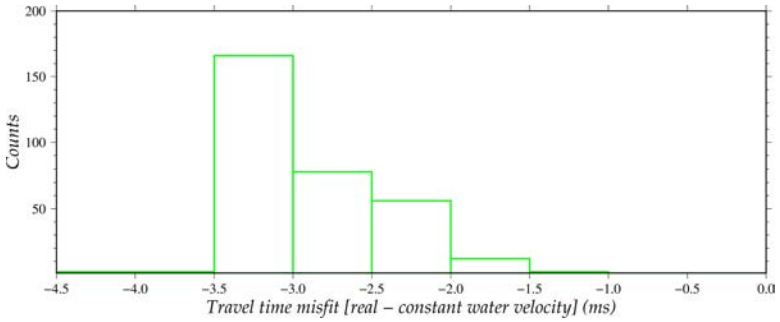

Figure 7.7: Histogram of travel-time misfits obtained with the variable and constant water Vp models for the first shot located at a distance of 8.075 km.

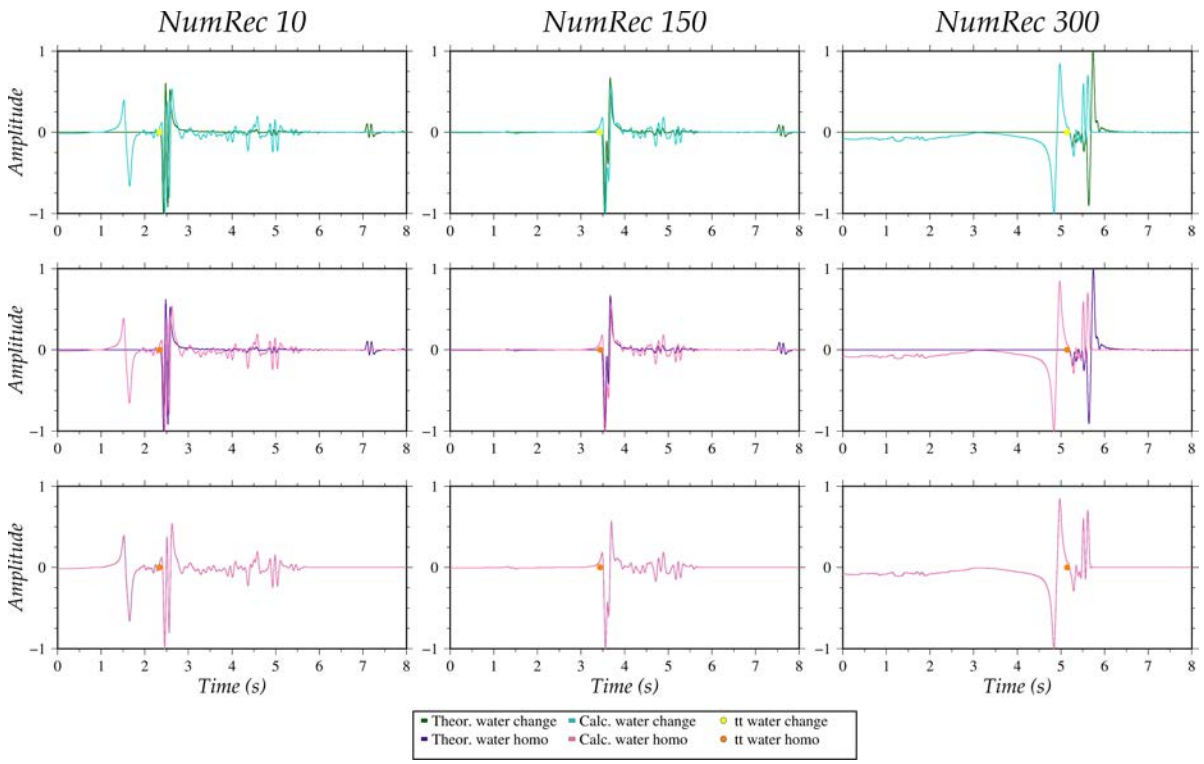

Figure 7.8: Upper panels show pressure recordings calculated (calc.) or obtained after the first DC step (blue lines), the theoretical (theor.) or simulated recordings generated with the OBS-type geometry (green lines), and the first arrivals travel times (tt) calculated using TOMO2D (yellow dots) for the variable water Vp (water change). Seismograms are calculated at traces number 10, 150 and 300 of the first shot gather, located at a distance of 28.025 km. Middle panels show the same results for a constant or homogeneous (homo.) water Vp of 1.5 km/s, including pressure recordings after first step (pink lines), theor. or simulated seismograms with the OBS-type geometry (purpule lines), and first arrivals tt calculated using TOMO2D (orange dots). Lower panels show a comparison of the previous pressure recordings obtained after the first DC step calculated for the variable (blue lines) and constant (pink lines) water Vp, and first arrivals tt calculated using TOMO2D for the variable (yellow dots) and constant (orange dots) water Vp. All trace amplitudes are normalized.

Shot gathers have no visible differences due to the small range of Vp variations in the water column (1490-1520 m/s). Upper panels in Fig. 7.8 show the results under ideal conditions in which the water Vp model is perfectly known. Blue traces are equivalent to the ones plotted in Fig. 7.4 a and the green ones in Fig. 7.4 b but for a different shot gather. Aside from wave amplitudes, which are normalized in each trace, seismic events in the simulated traces have the same waveform characteristics as the ones recorded after the first DC step. However, blue traces have noise caused by the extrapolation process, i.e. the first high-amplitude event that arise from the water reflection (see discussion Fig. 7.4 a) at receiver number 10 or the diffraction tails displayed at receiver 300. Moreover, no signal is recorded after ~ 5.7 s because of the time (~ 2.3 s) needed for the source or input wave field to travel from the sea level to the seafloor surface (3.5 km). Aside from these effects, first arrival travel times calculated with TOMO2D (yellow dots) match with

the first real events of the seismic traces. Middle panels in Fig. 7.8 show the same results and characteristics as the upper panels but they are calculated using a constant water Vp of 1.5 km/s instead of the one described in section 6.2. Finally, lower panels in Fig. 7.8 display the comparison between the upper and middle pannels for results after the first DC step and first arrival travel times, calculated using the correct variable (blue lines and yellow dots) and homogeneous (pink lines and orange dots) water Vp models. Results for the correct variable water Vp are masked by the ones obtained from the homogeneous water Vp. According to the results shown in Fig. 7.7, misfits are of a few ms, so they can not be appreciated in the plots of the lower panels.

Therefore, no significant differences in the wave field and travel times are introduced due to the water Vp model used for the back-propagation in this case. Given that the water Vp model does not change laterally, first and second DC step results will present similar trace time shifts, i.e. order of ms. Therefore, results are equivalent for the second DC step.

7.3. Discussion

This section presents the application of the DC technique to streamer (i.e., MCS) data for two synthetic experiments. Different seafloor geometries that define the new virtual surface (i.e., the new datum) and different water Vp models are checked to test the effects on the results.

The usage of the DC process to change the geometry set up from the sea level to the seafloor surface works very well. The main advantages of using DC through the water column are the acoustic behavior of this medium making adequate the usage of an acoustic solver for the back-propagations, that water Vp is almost constant, and it can be very well-constrained (~ 1.5 km/s) in depth with oceanographic instruments.

Most seismic phases are observed in both the virtual shot gathers after the DC as well as in the simulated data with the virtual acquisition geometry (Figs. 7.1, 7.3, 7.4, and 7.5). Although wave amplitudes are not preserved, the first arrival travel times are correctly retrieved (Figs. 7.1 c, 7.3 c, 7.4 c, 7.5 c, and 7.8). As the re-datuming surface is at the seafloor, they can be identified from zero offset allowing to recover shallow subsurface information. However, first arrivals are not always evident or easy to track. On one hand, at near offsets the energy collapses instead of a point to a wider area (Figs. 7.3 a, and 7.5 a). On the other hand, at far offsets the wavefronts are affected by the presence of diffraction tails (Figs. 7.3 a, 7.5 a, and 7.8). The fact that the complete wave field is not used in the DC process, but just finite and discrete recordings, can introduce artefacts in the record sections. Aliasing effects can also appear if sources and receivers are too spaced (Figs. 7.2 b, and 7.3 a). Moreover, especially in deep water environments, the total recording time of the input or streamer shot gathers must be long enough to reproduce

virtual data covering the whole offset distance or streamer length with subsurface information (Fig. 7.5 c).

In contrast of the acquisition geometry parameters, the shape of the new datum level or seafloor does not affect or modify the DC result. The only important parameter of the new virtual surface is its position in depth. Furthermore, the differences between using a variable or constant water Vp are also negligible (Fig. 7.8) even if the Vp is not exactly the average of the water column Vp. Small differences are observed between the virtual shot gathers obtained by using the correct variable or a constant water Vp model for the back-propagation (Fig. 7.8) when their first arrival travel-time misfits are also minimal (Fig. 7.7).

In view of the results, as the synthetic DC first arrivals match with the calculated travel times from TOMO2D for almost all offsets (Figs. 7.1 c, 7.3 c, 7.4 c, and 7.5 c), these phases likely contain the correct Vp information of the shallow subsurface.

Chapter 8. Synthetic travel-time tomography results

In this chapter, we present results obtained by applying first arrival TTT to DC data (Chapter 7) for the two synthetic models described in Chapter 6. These include the canonical, chessboard-type model presented in section 6.1, and the Marmousi-2 model presented in section 6.2. The objective is to prove that kinetically accurate background macro-Vp models can be successfully retrieved using the emergent early arrivals in the DC shot gathers. The tests are also designed to analyse the coverage and resolving potential of the TTT method for a seafloor acquisition-type data configuration.

The updated version of TOMO2D code explained in the methodological section is applied to obtain the Vp structure of the subsurface. Initial models have no a priori information on the model structure and properties, to demonstrate that robust Vp models can be retrieved from the DC picks alone. A series of inversion parameters have been tested, but I only present here the ones providing the best result in terms of accuracy.

8.1. Checkerboard test

In this case, the target model is the one shown in Fig. 6.1. The input data set, the model parameterization and the inversion parameters used in the TTT are presented before the results.

Data set and experimental coverage

The acquisition geometry used to generate the data set is the one displayed in Table 6.1, with the exception of the experimental depth. As DC shot gathers are used for this test the depth of the survey will be at the seafloor surface rather than the sea level surface. The forward parameters and model parameterization employed to compute the DC input data set are the same as the ones presented in Table 6.2.

Figure 8.1 shows the first arrival ray paths for this survey, which in turn illustrates the model coverage. The travel-times of these rays are the ones to be used in the inversion. The right part is the best covered zone because the vessel moves in that direction. It must be noted that the areas with poor coverage will not be correctly inverted, so the model will be strongly conditioned by the regularization constraints. The coverage and number of crossing rays strongly decrease with depth, especially in the low-Vp zones. The shallowest areas are better covered and hence better resolved than the deeper ones. As I only use first arrival travel times, low-Vp anomalies tend to be avoided by rays. A data set consisting of 4,500 first arrival picks is obtained from this source-receiver

configuration. Figure 8.2 displays the first arrivals picks plotted on top of a DC shot gather (red dots), together with the associated ray paths.

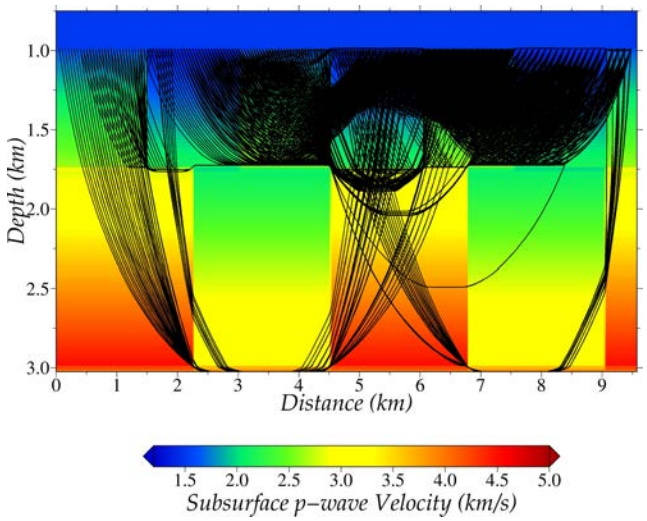

Figure 8.1: First arrival ray paths for all the source- receiver pairs of the DC data set, which are re-datumed at the seafloor. The model will be better resolved in the good covered areas than in the poorly covered ones.

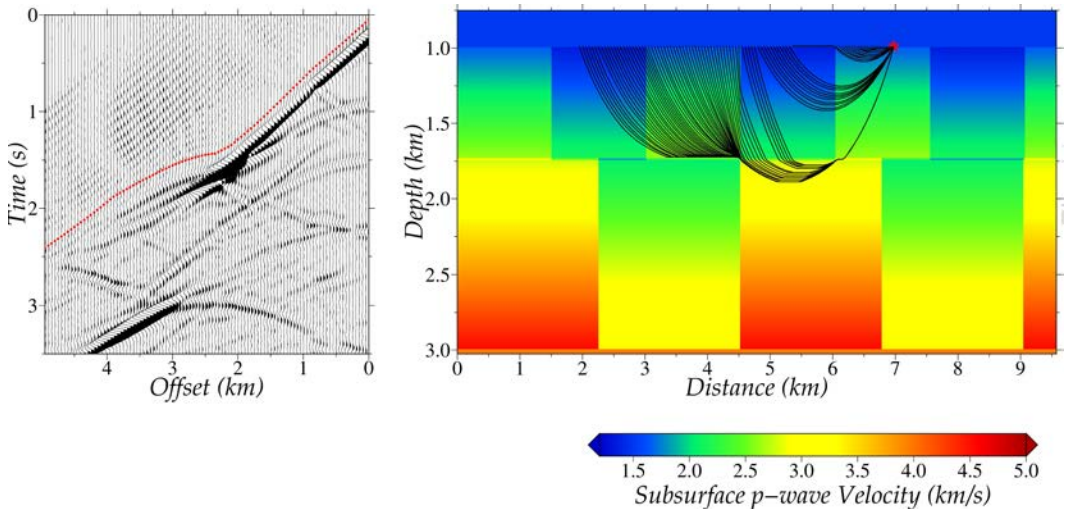

Figure 8.2: First arrival picks are plotted as red dots on top of the DC shot gather (previously presented in Fig. 7.3), together with the associated ray paths on the target model. Red star marks the source position at a distance of 6.975 km along profile. Only one trace every 100 m is shown in the DC shot gather (so 1/2 of the total).

Description of the velocity model parameterization and inversion parameters

TTT is performed in a regular mesh. The nodal distance is 12.5 m both vertically and laterally, resulting in a uniform grid of 768 x 244 nodes. As a first simple test, the same

characteristics are used to parameterize the Vp model and compute the forward part of the inverse method.

As it usually occurs with tomographic models, the system to be inverted is underdetermined, meaning than the number of unknowns (187,392 Vp nodes) is larger than the number of equations (4,500 rays/travel times). Besides, parallel ray paths correspond to linearly dependent equations so that they do not allow to uniquely resolve the involved parameters. Thus, regularisation constraints are required to reduce the number of independent variables and stabilize the inversion.

The inversion parameters used in the next section as well as the Vp model parameterization are included in Table 8.1.

Parameters	**Values**
Node spacing	12.5 m
Model dimensions (# nodes)	768 x 244
FS order (x,z) (node connexions)	(5,5)
Eliminate data outliers with chi values greater than	15
Tolerance level to terminate inversion	0.001
Number of iterations	10
Velocity smoothing parameter (λ_u)	100
Top velocity correlation lengths (x,z) (km) (L_{Htop} , L_{Vtop})	(0.1,0.1)
Bottom velocity correlation lengths (x,z) (km) (L_{Hbot} , L_{Vbot})	(0.5,0.25)

Table 8.1: Relevant inversion parameters used to solve the forward problem (ray tracing and travel-time calculation) and the inverse problem (Vp model and travel-time misfits) for the checkerboard test. Correlation lengths for the Vp model are set at the top and bottom nodes of the Vp grid and interpolated for the rest of the nodes in between. The increase with depth reflects the decrease in resolution from top to bottom of the model.

First arrival travel-time inversion

In the checkerboard test, the initial Vp model is a laterally homogeneous model with a vertical increasing Vp gradient that follows the function $v(z)=1.5+0.85\cdot z$ (km/s), going from 1.5 km/s at the seafloor to 3.2 km/s at the maximum depth, Fig. 8.3 a. Therefore, the background gradient differs from the target one so that we can consider that it does not contain a priori information. As is shown in Fig. 8.3 b, the Vp distribution obtained follows the overall trends of the target Vp model, although it does not reproduce the sharp geometry and the correct amplitude of the anomalies. The differences between the initial, target, and the inverted models are shown in Figs. 8.3 d, e, and f. The

maximum Vp misfit in the shallowest anomalies and the deeper central anomaly are around ±0.2 km/s. As expected, the larger differences concentrate in the sharp Vp contrasts, and in the poorly covered areas, especially in the deepest parts and in both edges of the model. Figure 8.4 displays three 1-D vertical Vp profiles that reflect the improvement of the TTT result versus the initial model compared with the target one. The correct trend or low-wavenumber information in the shallow part is successfully recovered after the TTT inversion; however there are significant discrepancies at depth. The location of the 1-D profiles are marked by pink dashed lines in Fig. 8.3 a.

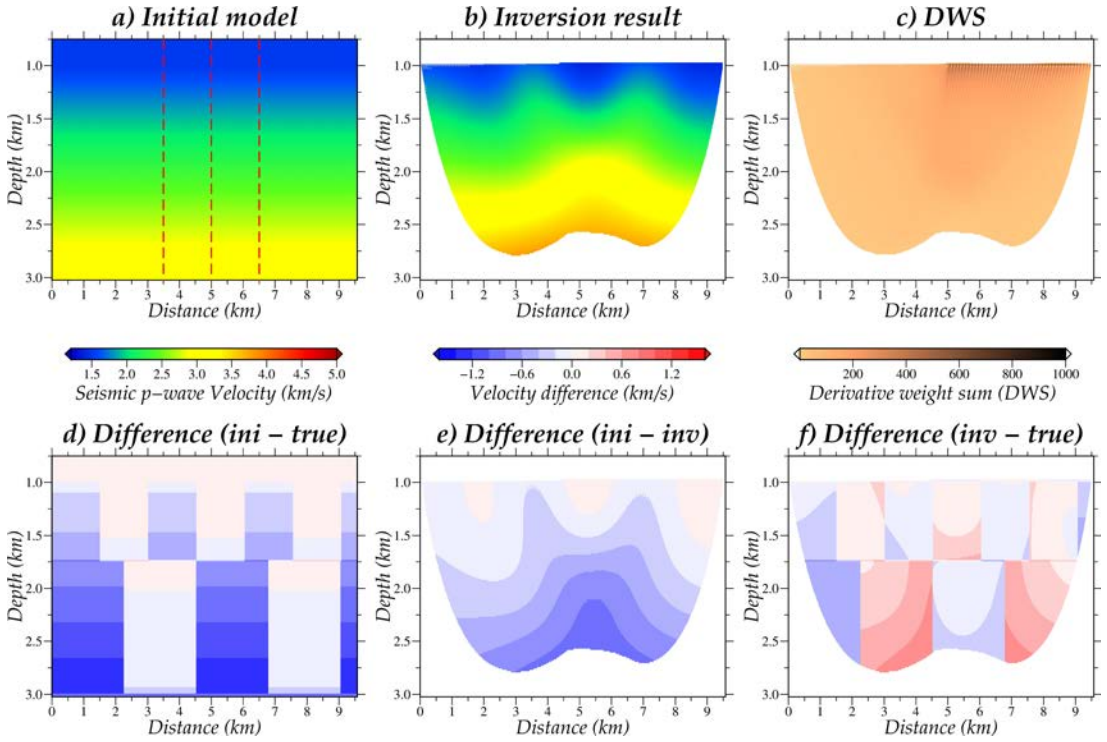

Figure 8.3: 2-D Vp model obtained by TTT for the checkerboard model. (a) Initial Vp model, characterized by a laterally homogeneous model with a vertical Vp gradient. (b) Inverted Vp model obtained by TTT using the first arrivals of the DC MCS data (Fig. 8.1). (c) DWS, which reflects ray density (Toomey et al., 1994). Uncovered areas (DWS=0) are masked. Vp difference between: (d) initial and target model, (e) initial and inverted result, and (f) inverted result and target model.

The derivative weight sum (DWS, Fig. 8.3 c) is the sum of ray lengths within a given cell (Toomey et al., 1994), and can be expressed as follows:

$$DWS\left(\alpha_i\right)=\sum \frac{\partial t_k}{\partial \alpha_i}$$

Where the α_i represents the model value at the i-th parametric node and t is the travel-time which is summed over all possible seismic ray paths (n), so it is a measure of ray

density. It is influenced by the geometry set-ups and the subsurface Vp distribution. Thus, the DWS has a low-ray density in the edges and deeper areas of the model. As expected, DWS is larger beneath the source locations. Only the areas where the DWS is not zero are considered and plotted in Figs. 8.3 b, e, f, and 8.4.

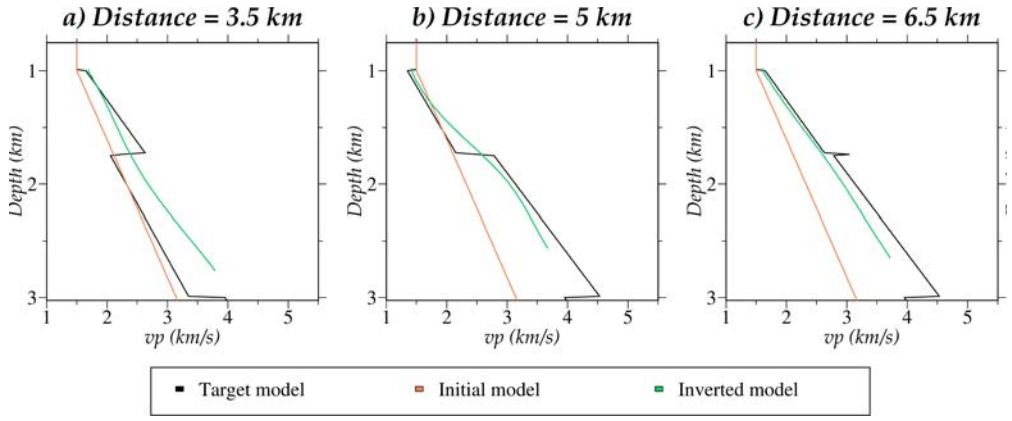

Figure 8.4: 1-D Vp/depth profiles extracted from the target, initial, and TTT inverted models in Figs. 6.1, 8.3 a, and b respectively, at distances of (a) 3.5 km, (b) 5 km and (c) 6.5 km along the model. The locations correspond to dashed lines in Fig. 8.3 a. Black lines indicate the target model, orange lines the initial model, and green lines correspond to the inversion results. Uncovered areas (DWS=0) are masked.

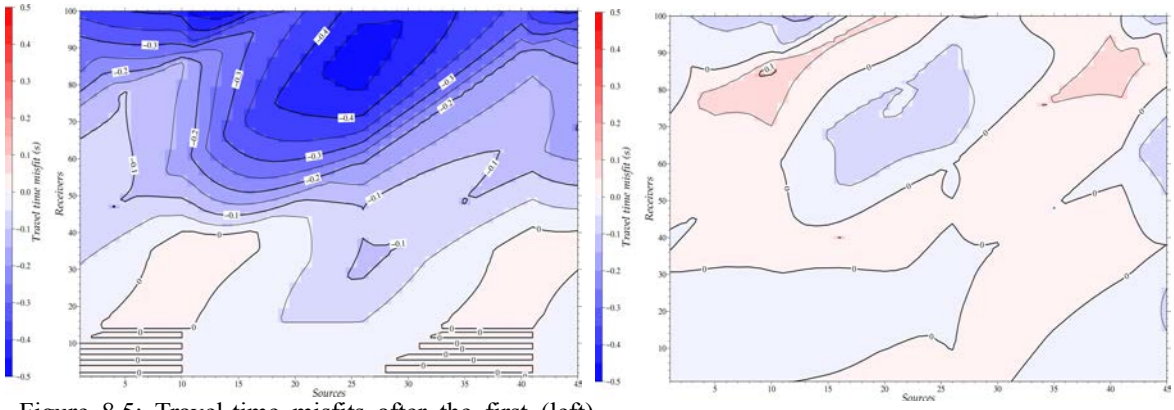

Figure 8.5: Travel-time misfits after the first (left) and final (right) inversion step for each source-receiver pair along the profile. The colour scale shows misfit and the contour interval is 0.1 s.

The first arrival travel-time residuals as a function of source-receiver distance positions for the first and last iterations are displayed in Fig. 8.5. Residual travel times are larger for the longer offsets because they correspond to the longest rays reaching the deeper levels, where Vp uncertainty is larger. Residuals are negative on average because average Vp in the initial model is lower than that of the target model. Residuals larger than -0.4 s caused by the central deep high-Vp anomaly are reduced to less than -0.1 s after the inversion. It is noteworthy that the largest residuals coincide with the location of the largest differences between initial and target model and between inverted and target

model (Figs. 8.3 d, and f respectively). Figure 8.6 shows the distribution of travel-time residuals for the first and last iterations in the form of a histogram. The root mean square (RMS) residual is of ~ 0.2 s in the first iteration and ~ 0.03 s in the final one, reflecting the improvement of the Vp model and the corresponding travel-time fitting after the inversion.

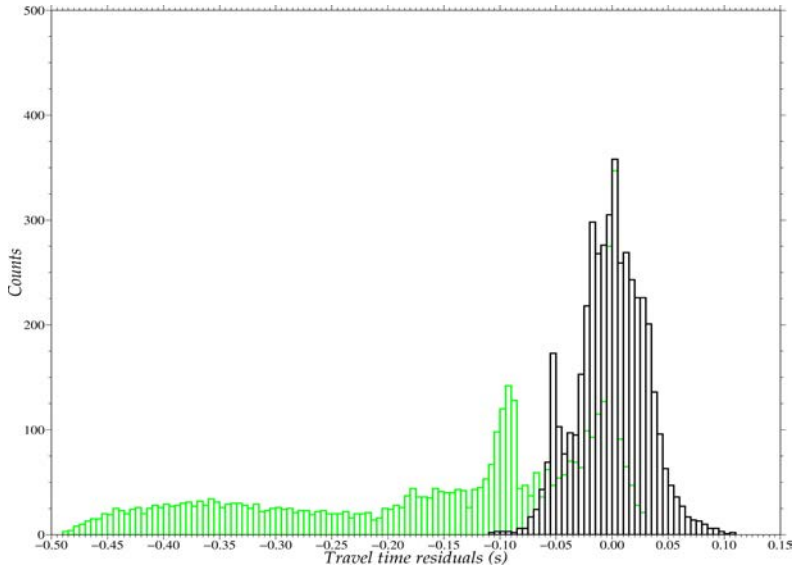

Figure 8.6: Histogram of travel-time residuals obtained with the initial (green) and final (black) models.

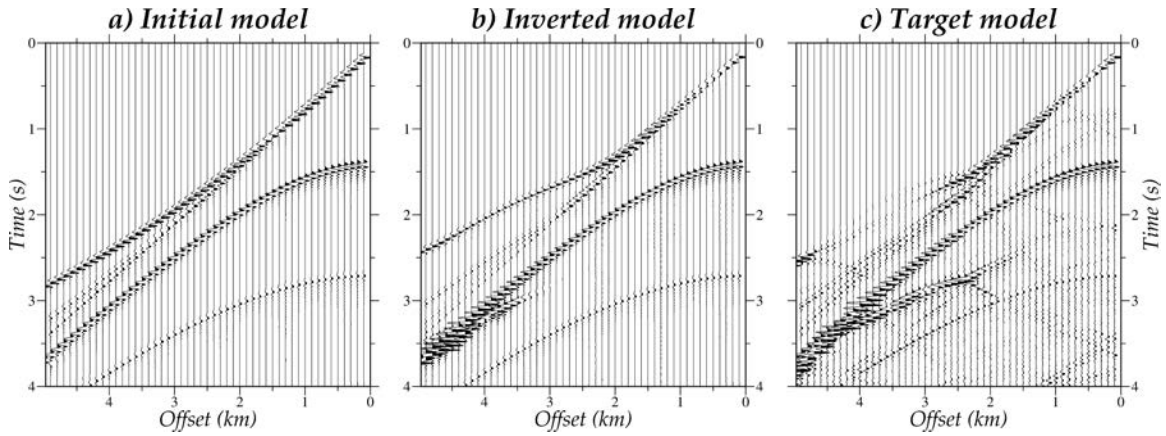

Figure 8.7: Virtual DC shot gathers generated using the FD solver (Dagnino et al., 2014) and the initial gradient (a), TTT inverted result (b), and target (c) models in Figs. 8.3 a, b, and 6.1 respectively. The shot gather location is indicated in Fig. 8.2. Only one trace every 100 m is shown (so 1/2 of the total).

Figure 8.7 shows virtual, DC shot gathers generated using the FD solver (Dagnino et al., 2014) and the initial, inverted, and target models, respectively. The comparison between the different shot gathers clearly shows the fit improvement in the data domain. The shot gather simulated with the TTT inversion result (Fig. 8.7 b) shows many of the features

displayed in the data simulated with the target one (Fig. 8.7 c), in contrast to what is observed in that generated with the initial gradient model (Fig. 8.7 a), which is wrong even in the first arrival travel-times. A time shift of approximately 0.5 s at 5km offset distance is observed between the first arrival shown in Figs. 8.7 a, and c. Aside from wave amplitudes, the main difference between the data generated with the inverted and target models are the reflected waves at the sharp boundaries between the different blocks, which cannot be recovered using first arrivals alone. Figure 8.8 shows a detailed comparison of the phase differences between the record sections displayed in Fig. 8.7. The top panels in Figs. 8.8 a, and b show differences between the data generated with the initial and target models; whereas the bottom panels Figs. 8.8 c, and d show differences between those generated with the inverted and target ones. In both cases, data are filtered between 4-4.5 Hz, which is typically the lowest available frequency in conventional MCS recordings. The key observation is that seismograms for the initial and target models are cycle-skipped for the early arrivals (Fig. 8.8 a), whereas those of the inverted and target models are not cycle-skipped (Fig. 8.8 c). This is also observed in the combined record sections as a function of offset displayed in Figs. 8.8 b, and d, respectively. As it is discussed in Chapter 5, the fact that the data are cycle-skipped for the initial model but not for the inverted one has profound implications concerning their appropriateness to be used as initial models in full-waveform inversion.

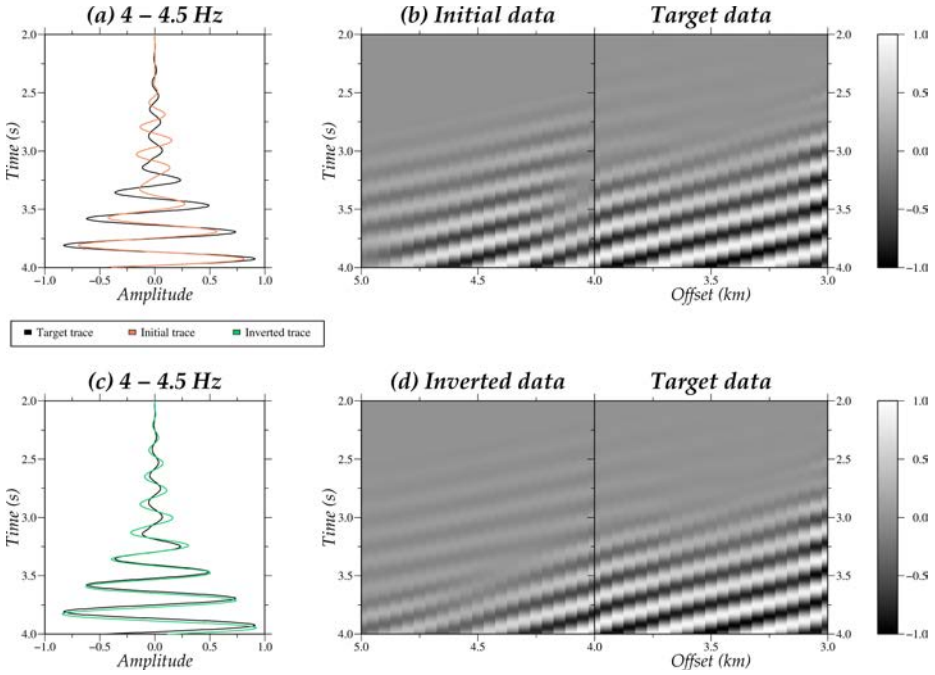

Figure 8.8: Comparison of phase differences between the record sections displayed in Fig. 8.7. The top panels (a) and (b) show differences between the data generated with the initial and target models, whereas the bottom panels (c) and (d) show differences between those generated with the inverted and target ones. The left panels (a) and (c) show a receiver trace extracted from the right panels (b) and (d) respectively, at an offset distance of 4 km. Black lines indicate the target receiver traces, orange line is the initial one, and green line correspond to the inversion result. In all the panels data are filtered between 4 - 4.5 Hz and normalized to its maximum amplitude value.

8.2. Marmousi-2 test

In this case, the target model is the one shown in figure Fig. 6.3. The input data set, the model parameterization and the inversion parameters used in the TTT are presented before the results.

Data set and experimental coverage

The acquisition geometry used to generate the data set is the one displayed in Table 6.3, with the exception of the experimental depth. As in the previous synthetic test, the depth of the experiment is the one corresponding to the virtual acquisition set-up, so in this case a rough seafloor surface. The forward parameters and model parameterization employed to compute the DC input data set are the same as the ones in Table 6.4.

In this case, the input data set is decimated in order to decrease the computational burden. One shot gather every 2.4 km (so 1/48th of the total) have been used, because it is approximately the size of the first Fresnel zone (Eq. 5.1), so that the limit of resolution that can be achieved using a ray-based tomography scheme. According to additional tests, increasing the number of picks does not change the inversion result.

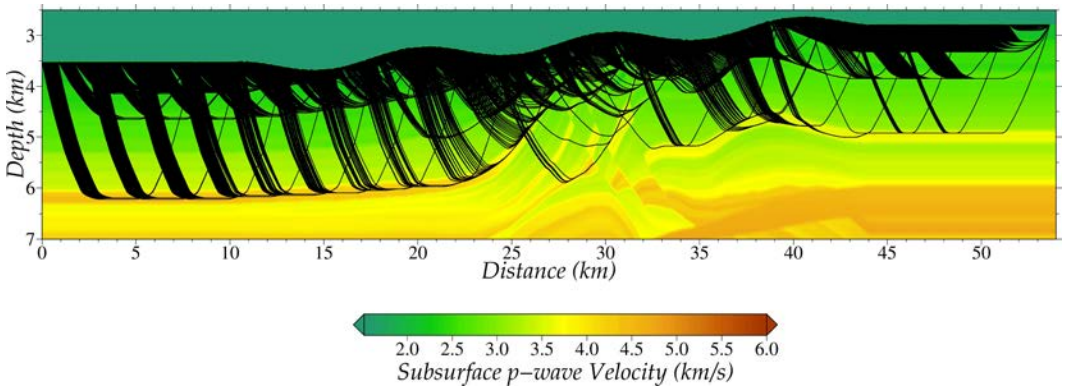

Figure 8.9: First arrival ray paths for all the source- receiver pairs of the DC data set, which are re-datumed at the seafloor. The inversion results will be better in the good covered areas that in the poorly covered ones.

Figure 8.9 illustrates the first arrival ray paths for this acquisition set-up. As in the previous case, and as a result of the re-datumed data set configuration, the rays concentrate in the shallow part. The maximum depth that is achieved for this model and survey configuration is around 2.5 km below the seafloor. The vertical Vp gradient in the upper part of the model is weak, so that rays cannot penetrate deep into the model. Deeper ray trajectories are limited to some interfaces marked by Vp contrasts. A total of 6,400 first arrival picks are retrieved from this reduced source-receiver configuration.

Figure 8.10 shows the first arrivals picks plotted on top of the DC shot gather (red dots), together with its associated ray paths on the target model.

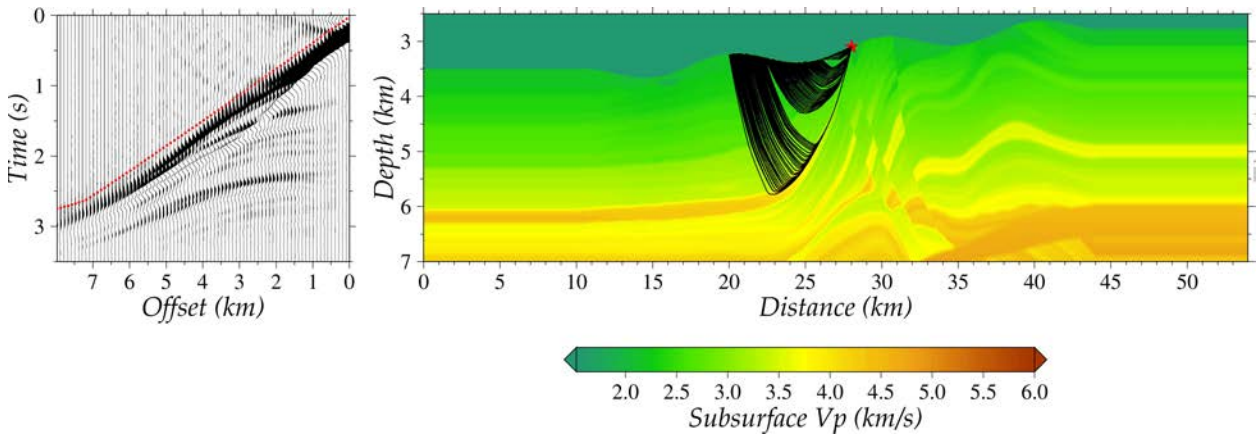

Figure 8.10: First arrival picks are plotted as red dots on top of the DC shot gather (previously presented in Fig. 7.5), together with the associated ray paths on the target model. Red star marks the virtual source position at 28.025 km along the profile and at a depth of 3.1 km. Only one trace every 100 m is shown in the downward continued shot gather (so 1/4 of the total).

Description of the velocity model parameterization and inversion parameters

TTT is performed in a regular mesh. In order to reduce the computational burden and increase the efficiency of the inversion, the nodal spacing is 25 m in both dimensions, resulting in a grid of 2160 x 344 nodes.

As in the previous case, the system to be inverted is underdetermined, meaning than the number of unknowns (743,040 Vp nodes) is 100-fold larger than the number of equations (6,400 rays/travel times). Thus, regularisation constraints are also required to reduce the number of independent variables and stabilize the inversion.

The inversion parameters used in the next section jointly with the Vp model parameterization are included in Table 8.2.

Parameters	Values
Node spacing	25 m
Model dimensions (# nodes)	2160 x 344
Forward star order (x,z) (node connexions)	(5,5)
Eliminate data outliers with chi values greater than	15
Tolerance level to terminate inversion	0.001
Number of iterations	10
Velocity smoothing parameter (λ_u)	75
Top velocity correlation lengths (x,z) (km) (L_{Htop} , L_{Vtop})	(0.6,0.05)
Bottom velocity correlation lengths (x,z) (km) (L_{Hbot} , L_{Vbot})	(3.,0.5)

Table 8.2: Relevant inversion parameters used to solve the forward problem (ray tracing and travel-time calculation) and the inverse problem (Vp model and travel-time misfits) for the Marmousi-2 test. Correlation lengths for the Vp model are set at the top and bottom nodes of the Vp grid and interpolated for the rest of the nodes in between. The increase with depth reflects the decrease in resolution from top to bottom of the model.

First arrival travel-time inversion

In the Marmousi-2 test, the initial Vp model is a laterally homogeneous model with a vertically increasing Vp gradient that follows the function $v(z)=1.06+0.575\cdot z$ (km/s), Fig. 8.11 a. Therefore, the background gradient differs from the target one (Fig. 8.11 d) so that we can consider that it does not contain a priori information. As it is shown in Fig. 8.11 b, the Vp distribution obtained follows the overall Vp trends of the target model, so that a thick lower Vp layer is retrieved in the left side. However, the inverted model does not reproduce the sharp geometry and properties of the faults, reservoirs and sand layers. The differences between initial, target, and inverted models are shown in Figs. 8.11 d, e, and f. The Vp misfit in Fig. 8.11 f is around ±0.2 km/s in the shallower 1.5 km below the seafloor. Deeper than 1.5 km below the seafloor, misfits are higher, reaching ±0.6 km/s. As expected, the largest differences concentrate around the sharp Vp contrasts, and in the poorly covered areas, especially in the deepest parts and in both edges of the model. Figure 8.12 displays three 1-D vertical Vp profiles that reflect the improvement of the inverted versus the initial model in comparison with the target one. The initial Vp is clearly higher than the target one. The correct trend or low-wavenumber information in the shallow part is successfully recovered after the TTT inversion; however there are significant discrepancies at depth. The location of the 1-D profiles are marked by pink dashed lines in Fig. 8.11 a.

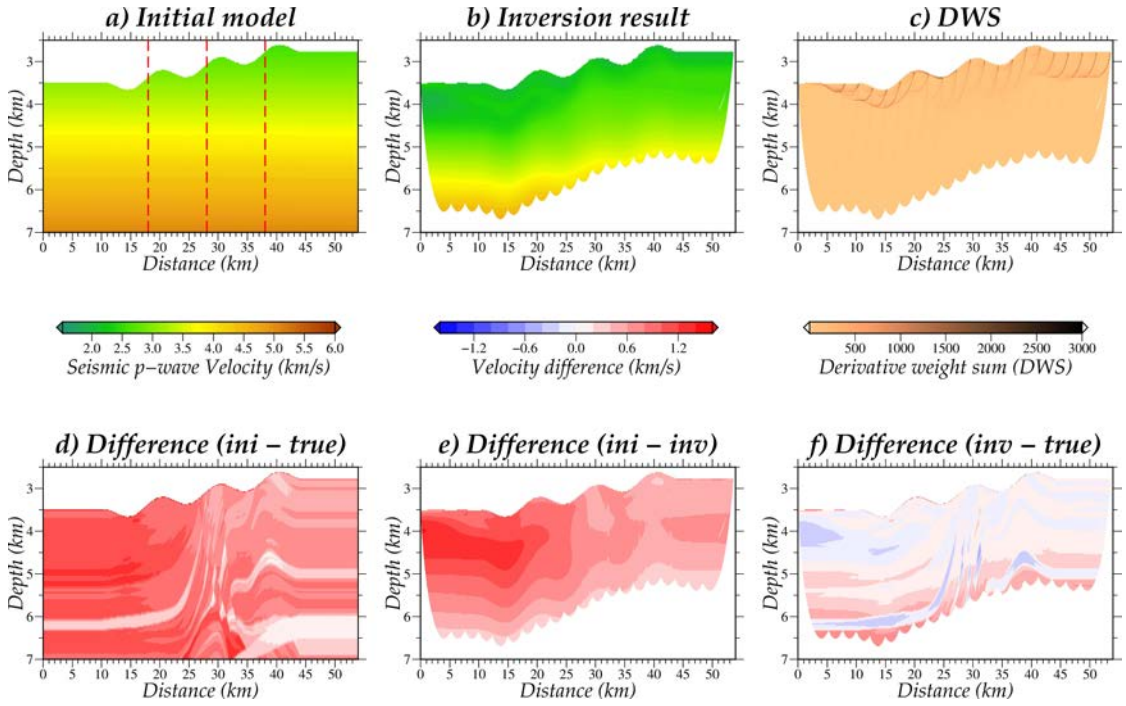

Figure 8.11: 2-D Vp model obtained by TTT for the Marmousi-2 model. (a) Initial Vp model, characterized by a laterally homogeneous model with a vertical Vp gradient. (b) Inversion result obtained by TTT using the first arrivals of the DC MCS data (Fig. 8.9). (c) DWS. Uncovered areas (DWS=0) are masked. Vp difference between: (d) initial and target model, (e) initial and inversion result, and (f) inversion result and target model.

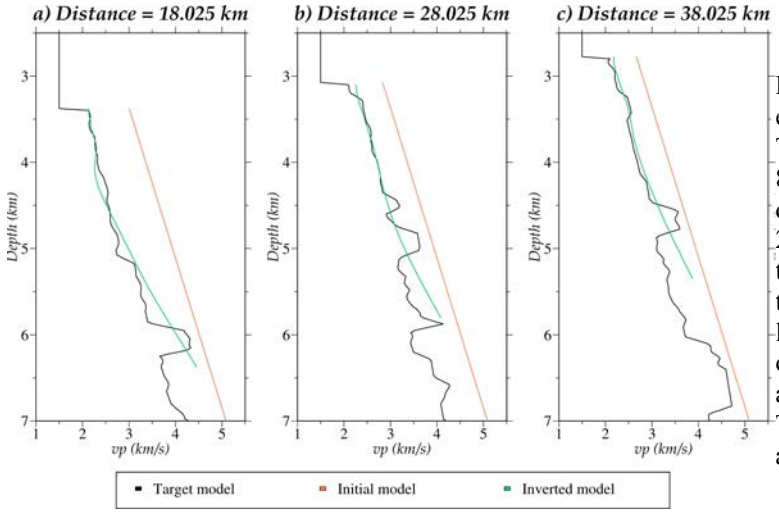

Figure 8.12: 1-D Vp/depth profiles extracted from the target, initial, and TTT inversion models in Figs. 6.3, 8.11 a, and b respectively, at distances of (a) 18.025 km, (b) 28.025 km and (c) 38.025 km along the model. The locations correspond to dashed lines in Fig. 8.11 a. Black lines indicate the target model, orange lines are the initial model, and green lines correspond to the TTT inversion result. Uncovered areas (DWS=0) are masked.

As in the previous case, the DWS (Fig. 8.11 c) displays a low-ray path distribution in the edges and deeper areas. As expected, the DWS is greater beneath the source locations. Only the areas where the DWS is not zero are considered and plotted in Figs. 8.11 b, e, f, and 8.12.

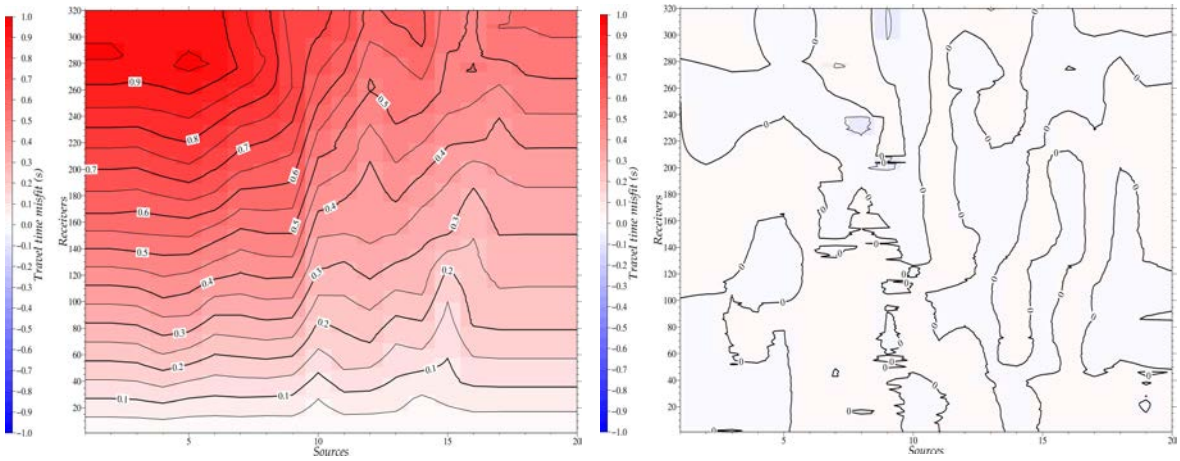

Figure 8.13: Travel-time misfits after the first (left) and final (right) inversion step for each source-receiver pair along the profile. The colour scale shows misfit and the contour interval is 0.1 s.

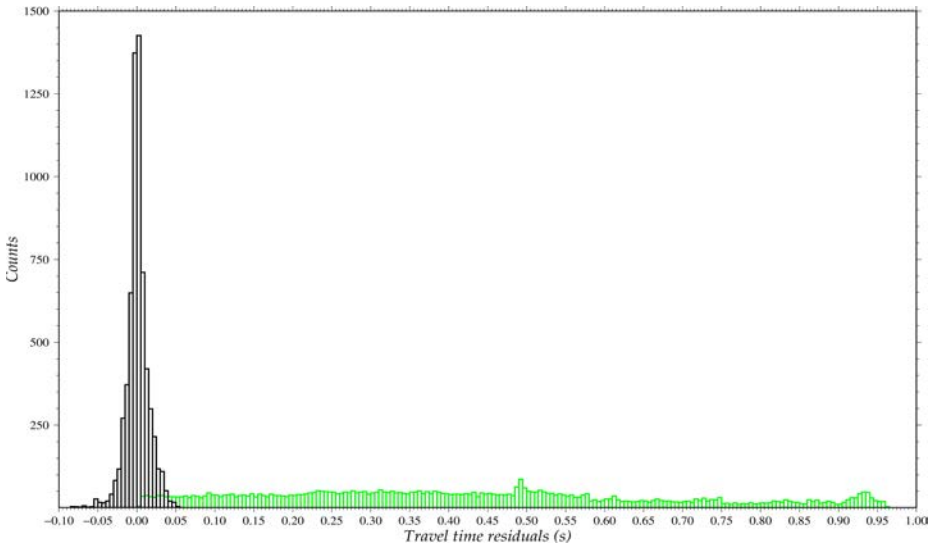

Figure 8.14: Histogram of travel-time residuals obtained with the initial (green) and final (black) models.

The first arrival travel-time residuals as a function of source-receiver distance positions for the first and last iterations are displayed in Fig. 8.13. As expected, residual travel times are larger for the longer offsets because they correspond to longer rays reaching the deeper levels, where Vp uncertainty is larger. Residuals are positive because the velocities present in the initial model are higher than those in the target model. Large residuals, higher than 0.9 s, caused by the left thick low-Vp layer are reduced to zero after the inversion. It is noteworthy that the largest residuals coincide with the location of the largest differences between initial and target model and between inverted and target model (Figs. 8.11 d, and f, respectively). Figure 8.14 shows the distribution of travel-time residuals for the first and last iterations in the form of a histogram. The RMS residual is

of ~ 0.49 s in the first iteration and ~ 0.01 s in the final one, reflecting the improvement of the Vp model and the corresponding travel-time fitting after the inversion.

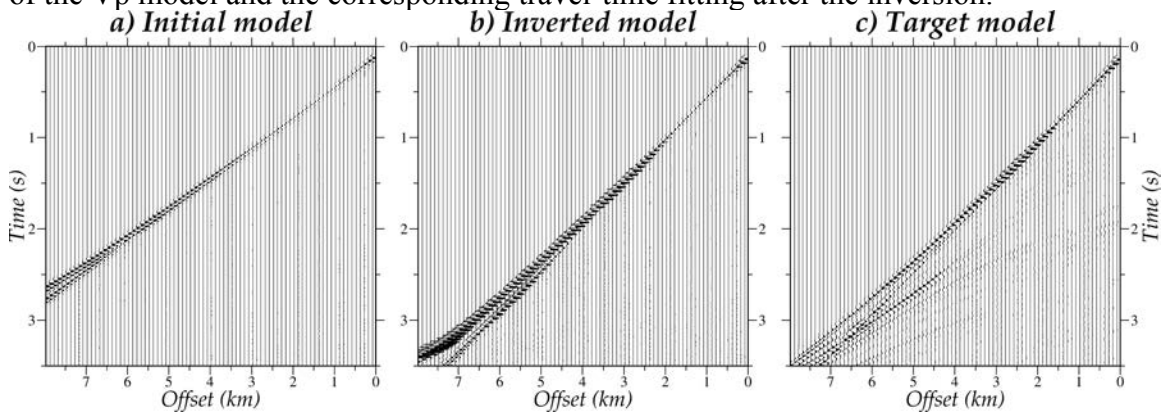

Figure 8.15: Virtual DC shot gathers generated using the FD (Dagnino et al., 2014) and the initial gradient (a), TTT inversion result (b), and target (c) model shown in Figs. 8.11 a, b, and 6.3, respectively. The shot gather location is the same previously presented in Fig. 8.10. Only one trace every 100 m is shown (so 1/4 of the total).

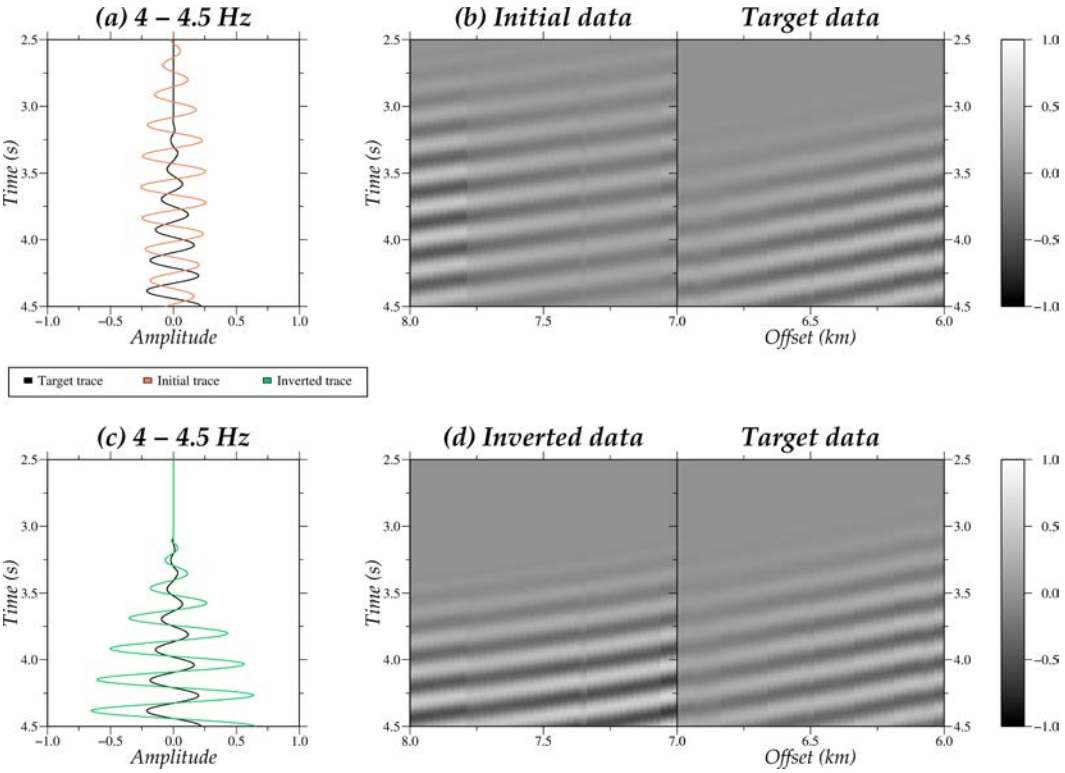

Figure 8.16: Comparison of the phase differences between the record sections displayed in Fig. 8.15. The top panels (a) and (b) show differences between the data generated with the initial and target models, whereas the bottom panels (c) and (d) show differences between those generated with the inverted and target ones. The left panels (a) and (c) show a receiver trace extracted from the right panels (b) and (d)

respectively, at an offset distance of 7 km. Black lines indicate the target receiver traces, orange line is the initial one, and green line correspond to the inversion result. In all the panels data are filtered between 4 - 4.5 Hz and normalized to its maximum amplitude value.

Figure 8.15 shows virtual DC shot gathers generated using the FD solver (Dagnino et al., 2014) and the initial gradient (Fig. 8.15 a), TTT inverted result (Fig. 8.15 b) and target model (Fig. 8.15 c), respectively. As in the checkerboard test, the comparison between the different shot gathers clearly shows the fit improvement in the data domain. The shot gathers simulated with the initial gradient (Fig. 8.15 a) and the target model (Fig. 8.15 c) show a time shift of approximately 0.75 s at 8 km offset distance. In contrast, the shot gathers simulated with the inversion result (Fig. 8.15 b) and the target model (Fig. 8.15 c) present the same first arrival travel times, which corresponds to the property that is fitted by the TTT method. The wave amplitudes and the reflections are the main difference between Figs. 8.15 b, and c. Clear reflections are not shown in Fig. 8.15 b because we have not introduced reflected travel-times in the inversion. Therefore, Figs. 8.15 a, and b are shot gathers without reflections because they have been simulated using the Vp models in Figs. 8.11 a, and b, which are gradients that do not present sharp discontinuities. Including reflected travel-times will help to improve the data domain, and thus the Vp model. Figure 8.16 shows a comparison of the phase differences between the record sections displayed in Fig. 8.15. The top panels Figs. 8.16 a, and b show differences between the data generated with the initial (Fig. 8.15 a) and target (Fig. 8.15 c) models; whereas the bottom panels Figs. 8.16 c, and d show differences between those generated with the TTT inversion result (Fig. 8.15 b) and target (Fig. 8.15 c) ones. In both cases data are filtered between 4-4.5 Hz. Data are clearly cycle-skipped and first arrivals are very different in the upper panels (Figs. 8.16 a, and b). As an example, in Fig. 8.16 a the first arrival at 7 km offset distance is displayed at around 3.2 s in the target shot gather, whereas is before 2.5 s in the initial shot gather (Fig. 8.16 a). In contrast, Fig. 8.16 c shows that the first arrival travel-time in the seismogram obtained using the TTT result matches with the target one. Moreover, the phase of both seismic traces is also coincident along time (Fig. 8.16 d).

8.3. Discussion

This section is devoted to perform first arrival travel-time inversion of the DC streamer shot gathers, and to analyse the obtained results for two synthetic models. The main issue to perform TTT with streamer data is its intrinsically short-offset, which makes it difficult to identify refractions as first arrivals. The DC process is necessary to retrieve the Vp information from the first arrival travel times, or early refractions, on the virtual shot gathers. Otherwise, refractions are not visible in the shot gathers with the experimental set-ups described in Chapter 6 (Figs. 6.2 and 6.4). As the wave field is propagated to a virtual surface that coincides with the seafloor, early refractions emerge from zero offset. The maximum experimental offset available is limited by the streamer length. Given the positive depth Vp gradient of the medium, the source-receiver distance is a key factor that determines the maximum depth that can be reached by the turning rays, which as a

rule of thumb is 50-75% the offset distance, as it is shown in Figs. 8.1 and 8.9. Using the seafloor as virtual surface we have refraction information in the DC shot gathers all over the offset range or streamer length (Figs. 8.2 and 8.10). Moreover, the stronger the gradient is, the deeper is the area covered by rays for the same offset. An additional advantage of MCS records is data redundancy, which allows to have a high horizontal resolution at the shallow levels. Thus, the result in the upper part of the model is very well-constrained in the inversion allowing to retrieve shallow Vp details (Figs. 8.3 b and 8.11 b). This fact is advantageous compared to wide-angle data inversions in which upper velocities are typically very conditioned by the smoothness regularization constraints.

The reduction of the travel-time residuals between initial and final TTT inversion result is significant (Figs. 8.6 and 8.14) for all the offset distances (see Figs. 8.5 and 8.13). This fact is also reflected in the Vp models and its differences (see Figs. 8.3 d-f and 8.11 d-f). Small Vp differences are imaged just between target and final TTT inversion result confirming that after the inversion the correct background gradient is recovered. Therefore, the test results confirms that the DC process helps retrieving first arrival travel times from the seafloor virtual geometry efficiently and accurately enough to obtain kinematically correct background Vp models.

In the ray-covered area, the largest travel-time residuals or Vp differences concentrate in the parts of the model that have strong Vp contrasts. It is not possible to recover accurately sharp Vp changes using TTT and first arrival information alone. To image a Vp contrast, reflections coming from that discontinuity must be included in the inversion. On the other hand, large differences are also displayed in the areas with low DWS or ray density, particularly in the corners and deeper parts of the model (see Figs. 8.3 and 8.11).

Last but not least, the shot gathers simulated using the final TTT inversion results are close to the target ones (see Figs 8.7 and 8.15). Again, major differences concentrate in the vicinity of sharp Vp variations. However, the final TTT shot gathers show a huge improvement in the data domain, displaying smaller residuals. Initial and target shot gathers display larger time shifts as offset increases. Finally, the key point is that the shot gathers simulated using the final TTT inversion results are not cycle-skipped with respect to the target model ones at the lowest available frequency recorded in field data sets (see Figs. 8.8 and 8.16), which is essential and a necessary requirement to perform FWI.

Chapter 9. Synthetic full-waveform inversion results

This chapter is devoted to perform FWI of the original MCS data or streamer shot gathers to analyse the results for the two synthetic models presented in Chapter 6. The objective is to prove that if data lack low frequencies (> 4 Hz), FWI converges successfully only providing kinematically accurate initial models, such as the ones obtained using TTT from first arrivals of DC shot gathers. Therefore, TTT models shown in Chapter 8 are used here as initial ones for several tests.

The FWI code explained in the methodological section (5.2) is applied to obtain the Vp structure of the subsurface. A series of inversion parameters have been tested, but I only present here the ones providing the best result in terms of accuracy.

9.1. Checkerboard test

A total of 45 shot gathers (4,500 seismograms) with no preprocessing are used as input data set for the inversion (see Table 6.1, and 6.2 of section 6.1 for more specifications in the acquisition geometry and forward parameters). We start the multi-scale FWI applying a band-pass Butterworth filter of 4 – 4.5 Hz. A frequency step of 0.5 Hz is set until reach a maximum frequency up to 9.5 Hz. A total of 11 different frequency bands in the multi-scaling strategy are inverted with a maximum of 20 iterations per frequency band. The size of the space grid is constant and set to 12.5 m, resulting in a uniform grid of 768 x 244 nodes. The L2-norm is the one used to calculate the misfit function and the SD method as search direction algorithm.

Full-waveform inversion using TTT as initial model

We perform FWI of the original streamer shot gathers using as initial model the TTT Vp result in Fig. 8.3 b. Figure 9.1 a shows the initial Vp differences as percentages between the TTT and the target model. On the other hand, Fig. 9.1 b shows the final Vp differences in % between the FWI and the target model. At the initial stage, as has been explained in section 8.1, the larger discrepancies are imaged in the deepest parts and in both edges of the model because only few rays constrain these areas. Moreover, large Vp differences concentrate at the anomaly boundaries due to the impossibility of TTT method to recover strong Vp changes without reflections. In contrast, once FWI is performed, the Vp differences are negligible in the central part of the model. Aside from the anomalies in the left part, initial difference of (20,30) % at the low-Vp checkerboard anomalies, and of (-5,-10) % at the high-Vp checkerboard anomalies seen at the deepest parts in Fig. 9.1 a, are of (0,10) %, and (-2,2) % in Fig. 9.1 b after the FWI. Although the

edges of the rectangular shaped anomalies are blurred, the Vp contrasts are now very well recovered together with the internal Vp gradient. This fact is due to the integration of the whole information of the seismic records in the inversion. On the left side large discrepancies of approximately (-25,-30) % are obtained. This area is the worse retrieved because it is illuminated by few receiver traces located at far offsets. In contrary, due to the vessel movement towards the right, the right part of the model is the best covered (larger data redundancy) so the better retrieved.

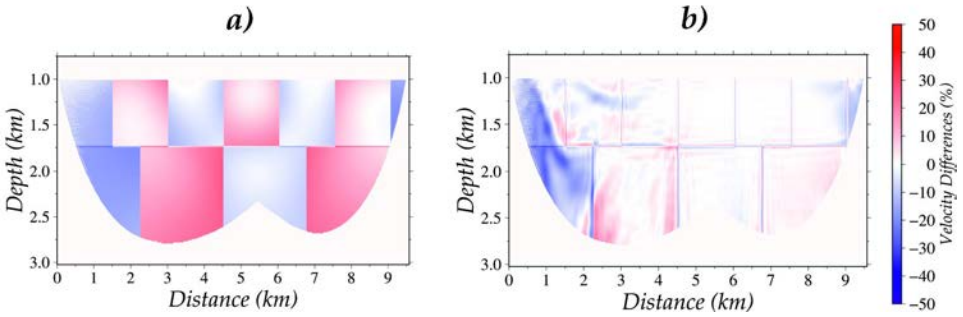

Figure 9.1: Vp difference between on one hand, (a) TTT model (Fig. 8.3 b) and checkerboard model (Fig. 6.1), and, on the other hand, (b) FWI result obtained using the previous TTT model as initial one, and checkerboard model (Fig. 6.1). Vp differences are expressed as percentages. Uncovered areas (DWS=0) are masked to only see the regions where low-frequency information is recovered by the TTT.

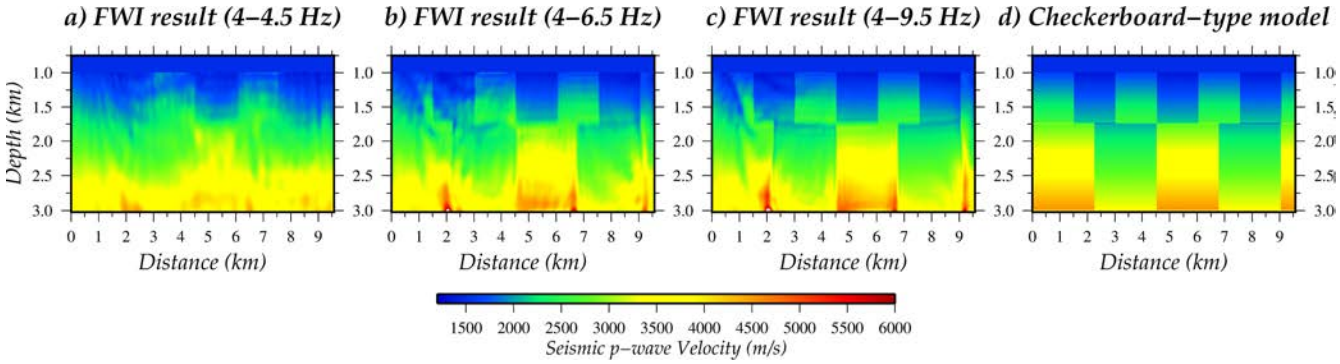

Figure 9.2: Vp models retrieved after the first (a), fifth (b) and eleventh or final (c) stages of the multi-scale strategy applied in the FWI. Band-pass frequencies of the multi-scaling applied to data are written within parentheses. (d) Target or checkerboard-type model (Fig. 6.1).

The improvement of the Vp model tanks to multi-scale FWI is clearly shown in Fig. 9.2. Figure 9.2 displays the Vp models obtained after first (a), fifth (b), and eleventh or final (c) stages of the multi-scale strategy applied in the FWI. After inverting the first frequency band (i.e. 4-4.5 Hz), the definition of the shape and internal gradients of the upper anomalies are considerably improved (Fig. 9.2 a). In contrast, the deeper part is not modified. After several multi-scale stages the details of the Vp model increase (Fig. 9.2 b). The boundary between upper and lower anomalies and its internal Vp gradients are

now well-defined. Finally, Fig. 9.2 c shows an almost perfect match with Fig. 9.2 d except for the zone close to the left edge (Fig. 9.1 b), and higher than target velocities at the lower anomaly boundaries. Figure 9.3 displays three 1-D vertical Vp profiles that reflect the Vp improvement of the FWI result versus the initial TTT model compared with the reference one at these positions. The orange lines (FWI resultant model) coincide with the black lines (checkerboard model) along all profiles, while green lines (TTT resultant model) only reproduce the overall trends. Therefore, high-wavenumber information is successfully retrieved after the FWI inversion using TTT as initial model. Only areas where there is ray coverage are plotted, so the deeper Vp discrepancies (Fig. 9.2 c) are not seen in Fig. 9.3. The locations of the 1-D profiles are the same as in Chapter 8 marked by pink dashed lines in Fig. 8.3 a.

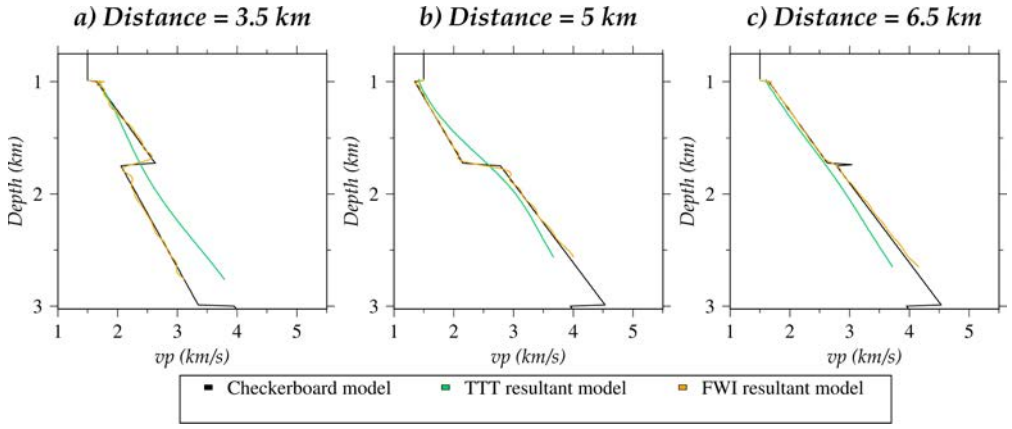

Figure 9.3: 1-D Vp/depth profiles extracted from the checkerboard model (black lines), initial model or TTT inverted result (green lines) and final FWI result (orange lines) in Figs. 9.2. d, 8.3 b, and 9.2 c respectively, at distances of (a) 3.5 km, (b) 5 km and (c) 6.5 km along the model. The locations correspond to dashed lines in Fig. 8.3 a. Uncovered areas (DWS=0) are masked.

Figure 9.4 shows streamer shot gathers generated using the FD solver (Dagnino et al., 2014) and the initial (TTT) (a), final FWI (b), and checkerboard (c) models, respectively. The shot gather simulated with the TTT (Fig. 9.4 a) shows only few events, mainly the first arrivals, in the correct position in time and space. The largest initial residuals are observed after the first arrivals at offsets of 2.5-4 km (Fig. 9.4 d). Data domain is clearly improved after FWI (Figs. 9.4 b, and e), in which reflections are introduced in the seismic records (Fig. 9.4 b). The final wave field imaged in Fig. 9.4 b coincides with the target wave field (Fig. 9.4 c). The initial wave field residuals (Fig. 9.4 d) almost disappear after FWI (Fig. 9.4 e). This fact evidences that the Vp model retrieved using FWI (Fig. 9.2 c) accurately reproduces the target data (Fig. 9.4 c). Figure 9.4 f shows the seismic signals properly reconstructed after FWI, so blue traces coincide with black traces, contrarily to orange traces from the initial wave field (Fig. 9.4 a), which do not contain most reflected events. In the initial wave field there is no signal after a certain time, such as in Fig. 9.4 f after 3.0 and 3.5 s in which orange traces are straight at zero amplitude for receivers 1 and 80. Largest initial reflection difference is obtained between 3.0-3.5 s for receiver 80

(Fig. 9.4 f). It is produced by a small phase misfit of an energetic reflection. In Fig. 9.4 f is displayed the seafloor reflection as first arrival in its correct travel-time, for both initial and final seismic traces, although amplitudes and phases of some latter events are only correctly obtained by FWI. The fitting of the up and downs in the receiver traces using FWI allows the detailed reconstruction of the final Vp model.

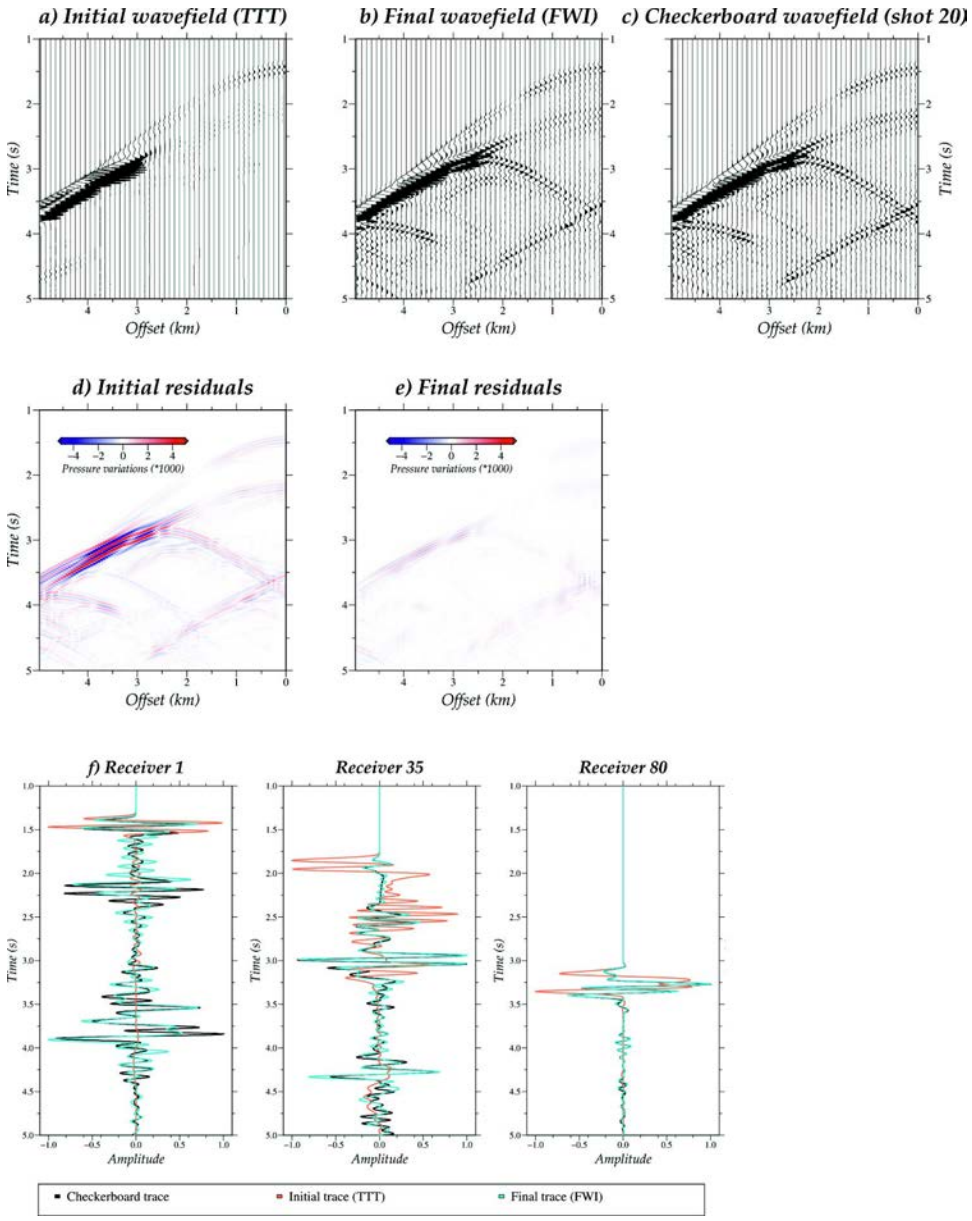

Figure 9.4: Streamer shot gathers simulated using the (a) initial (TTT), (b) final (FWI) and (c) checkerboard Vp models presented in Fig. 8.3 b, Fig. 9.2 c, and Fig. 9.2 d respectively, and the FD solver of the FWI algorithm. Only one trace every 100 m is plotted (so ½ of the total). Initial (d) and final (e) residuals are displayed for a better comparison of the results. The location of the streamer is at a distance of ~2 to 7 km along profile. (f) Comparison of the initial (orange; cf. a), final (blue; cf. b) and checkerboard (black; cf. c) seismic traces for receivers 1, 35 and 80.

The misfit reduction for FWI along the different steps of the multi-scale strategy is shown in Fig. 9.5. Misfit is reduced after the whole inversion by a factor of 290. The jumps in which the misfit increases are due to the change of inverting frequency band. Misfit increases because of the introduction of high-frequency content or new detailed information that has to be fit. The total RMS decreases from 0.1 to 0.07.

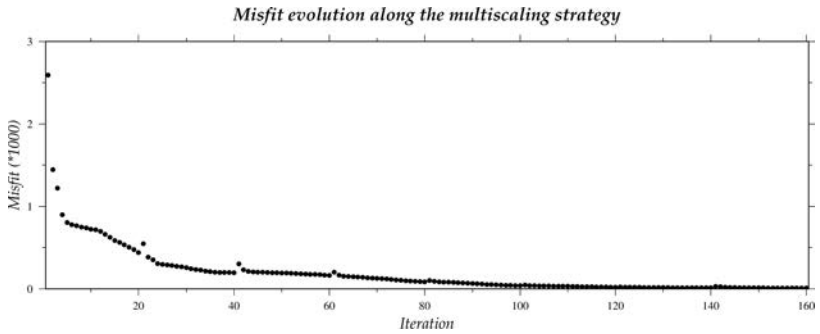

Figure 9.5: FWI misfit decrease along the iterations. The jumps where misfit increases are due to the inversion of next multi-scaling frequency band.

Full-waveform inversion using a gradient-based initial model

The objective of this section is to illustrate the problems of performing FWI using data lacking low frequencies and an initial model that is far from the target one. For this reason, the same previous inversion parameters, data and inversion approach are used in this test, being the only difference the initial model. The initial model is the same background gradient with no a priori information used as initial for the TTT, see section 8.1 Fig. 8.3 a.

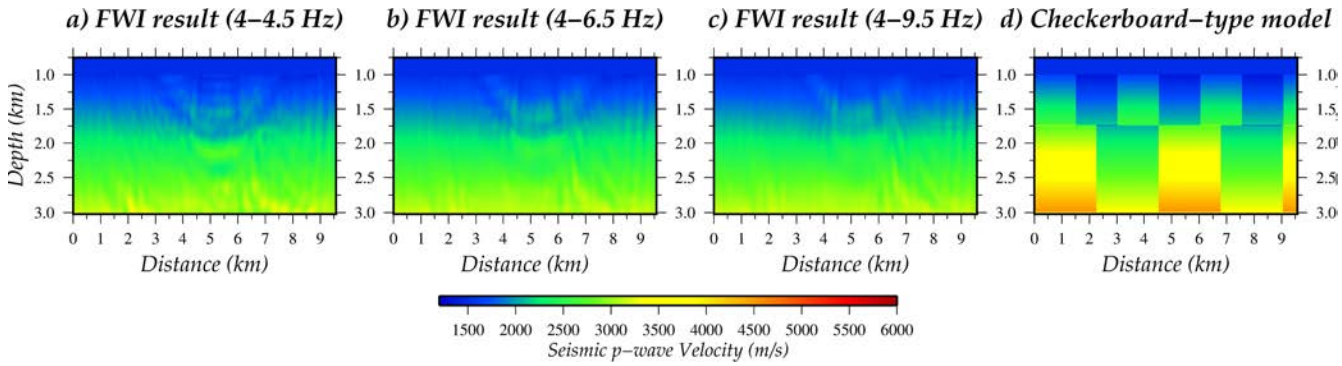

Figure 9.6: Vp models retrieved after the first (a), fifth (b) and eleventh or final (c) stages of the multi-scale strategy applied in the FWI. Band-pass frequencies of the multi-scaling applied to data are written within parentheses. (d) Target or checkerboard model (Fig. 6.1).

Figure 9.6 shows the Vp models obtained after several multi-scale stages of the FWI. During the inversion only the shallowest central anomaly at 4.5 – 6 km offset distance is recovered. However, neither the boundaries nor the internal gradient are perfectly reconstructed. The other parts of the model are almost not modified. Final model (Fig. 9.6 c) is very similar to the initial model, and thus far from the target one (Fig. 9.6 d).

The misfit variation in the different FWI steps is shown in Fig. 9.7. Misfit decreases up to ~ 500 after the whole inversion, far from zero. Again, the jumps in which the misfit increases are due to the inversion of next multi-scaling frequency band. The total RMS is of approximately 0.15 along all the multi-scale FWI. It is clearly seen in Fig. 9.6, and 9.7 that the inversion has fallen into a local minimum. Therefore, in this situation the FWI is not capable to find the proper model change to reach the global minimum, and retrieve a solution that is close to the target model.

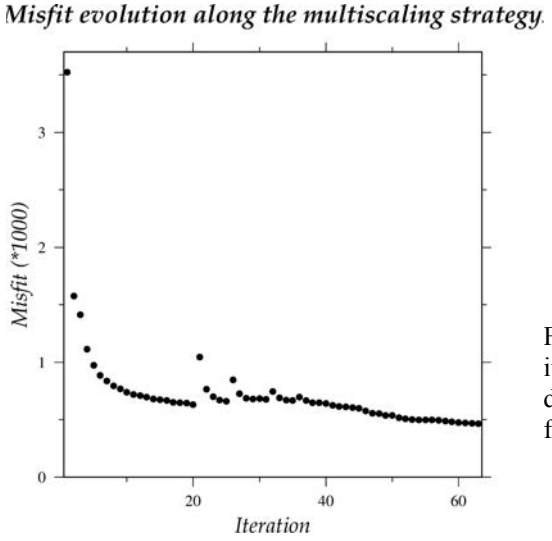

Figure 9.7: FWI misfit evolution along the iterations. The jumps where misfit increases are due to the inversion of next multi-scaling frequency band.

9.2. Marmousi-2 test

In this case, the input data set for the FWI is constituted by a total of 920 shot gathers (294,400 seismograms) with no preprocessing. Table 6.3, and 6.4 of section 6.2 include all the details of the acquisition geometry and the parameters for the forward propagation. As in the previous synthetic test, we start the multi-scale FWI by applying a band-pass Butterworth filter of 4 – 4.5 Hz. A frequency step of 0.5 Hz is set to reach a maximum frequency up to 11.5 Hz. A total of 15 different frequency bands in the multi-scaling strategy are inverted within a maximum threshold of 20 iterations. The size of the space grid is constant and set to 25 m, resulting in a uniform grid of 2160 x 344 nodes. The L2-norm is the one used to calculate the misfit function and the SD method as search direction algorithm.

Full-waveform inversion

As in the checkerboard test, we apply FWI using two different initial Vp models. First, the model obtained through TTT (Fig. 9.8 a) and, second, the gradient-based model used as initial model for the TTT (Fig. 9.8 d). Figures 9.8 b, and e, show the resulting Vp models after the multi-scale FWI. Figure 9.8 b displays the same Vp distribution as the Marmousi-2 model (Fig. 9.8 c). Detailed structures, such as the central three major faults, reservoirs and thin sand layers characterized by Vp differences of low-magnitude, are imaged in the Vp model obtained using FWI. As in the checkerboard model, differences concentrate in the less covered or constrained areas, the deeper parts and both edges of the model. The right edge of the model until ~ 5 km along profile is crossed by few rays, so this area is poorly constrained by TTT and consequently also after FWI. Thus, the inversion results (Figs. 9.8 b, and e) display the same velocities as those shown in their respective initial models (Figs. 9.8 a, and d). Again, due to the vessel movement towards the right, left area is the worse retrieved because is illuminated by few receiver traces located at far offsets. As usual, the increase with depth reflects a decrease in resolution of the result. Finally, the velocities in Fig. 9.8 b coincide along almost all the model, so the subsurface structure and properties are accurately retrieved by FWI starting from the TTT model (Fig. 9.8 a).

However, FWI fails (Fig. 9.8 e) with the linear gradient-based initial model (Fig. 9.8 d) . In this case, the resultant Vp gradient is slightly closer to Marmousi-2 than the initial one, although the model is plenty of artefacts and none of the previous mentioned geological structures can be identified. In summary, this test confirms that successful FWI requires a kinematically correct initial model. If it is not the case, data are cycle-skipped (Fig. 8.16 in chapter 8) and FWI fails (Fig. 9.8 e).

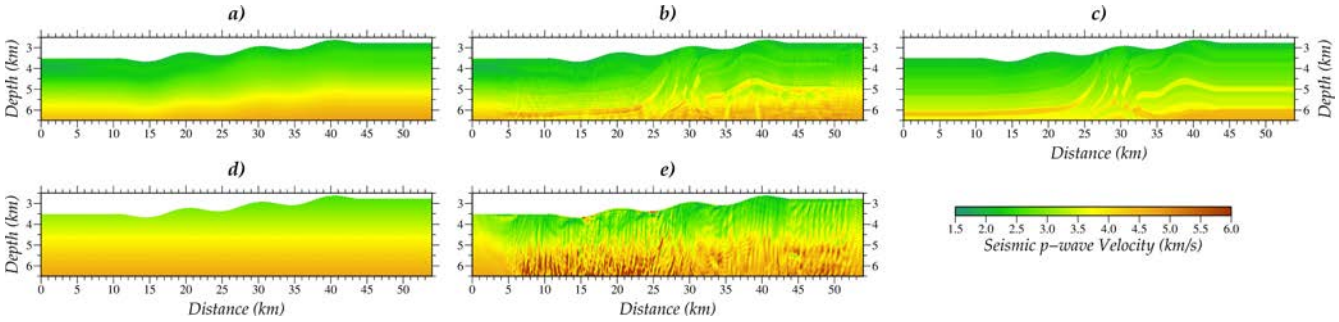

Figure 9.8: Initial, FWI resultant and target Vp models. Initial models for multi-scale FWI are the TTT (a) and a gradient-based (d) models. Final Vp models retrieved after performing multi-scale FWI using the TTT (b) and the gradient-based (e) models as initial ones. Right panel (c) corresponds to the Marmousi-2 or target model (Fig. 6.3).

Figure 9.9 displays at three different model distances the 1-D vertical Vp profiles that reflect the Vp improvement of the FWI result versus the initial TTT model compared with the Marmousi-2 or target model. The orange lines (FWI resultant model) retrieve the

up and downs of the black lines (Marmousi-2 model) along most profiles, while green lines (TTT resultant model) just reproduce the background trends. Therefore, high-wavenumber information is successfully retrieved after the FWI inversion using TTT as initial model at these locations. The locations of the 1-D profiles are the same as in chapter 8 marked by pink dashed lines in Fig. 8.11 a.

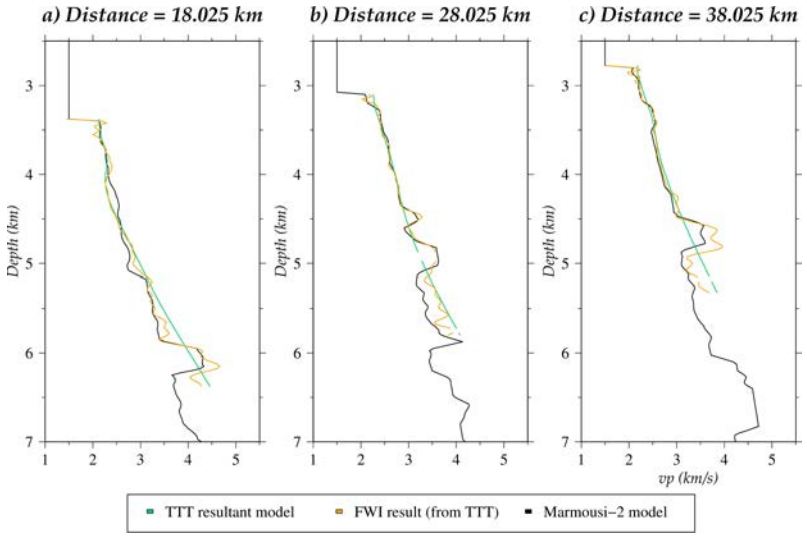

Figure 9.9: 1-D Vp/depth profiles extracted from the Marmousi-2 model (black lines), initial model for FWI, i.e. TTT result (green lines), and final FWI result (orange lines) in Fig. 9.8 c, a, and b respectively, at distances of (a) 18.025 km, (b) 28.025 km and (c) 38.025 km along the model. The locations correspond to dashed lines in Figure 8.11 a. Uncovered areas (DWS=0) are masked.

Upper panels in Fig. 9.10 (a-c) show streamer shot gathers generated using the FD solver (Dagnino et al., 2014) with the initial (TTT result) (a), final FWI (b), and Marmousi-2 (c) models, respectively. Only the first arrival corresponding to the reflection at the seafloor is imaged in the shot gather simulated with the TTT result (Fig. 9.10 a). Figure 9.10 b shows seismic events after the first arrivals recovered from the FWI technique. Target or Marmousi-2 shot gather is plotted in Fig. 9.10 c to compare and show the fit before and after the FWI in the data domain. Initial (Fig. 9.10 d) and final (Fig. 9.10 e) residuals are also displayed for a better visualization of the mismatches. Pressure variations in Fig. 9.10 d, and f, are originated due to small time shifts, the absence of reflections and/or differences in wave amplitudes. Data misfits close to the seafloor reflection are numerical artefacts arising in the sharp Vp contrast between water and subsurface. Figure 9.10 e shows smaller differences than Fig. 9.10 d at the first arrivals as well as at later seismic events. Main but low residuals are observed at far offsets approximately after 7 km. In general, FWI has reduced the residuals introducing and correcting the arrivals of the initial seismic wave fields or shot gathers, which means that the final Vp model retrieved using the FWI (Fig. 9.8 b) can explain properly the target data (Fig. 9.10 c). Figure 9.10 f shows the comparison of seismic traces obtained after FWI for the Marmousi-2 model, so blue traces coincide with black traces, in contrast to orange traces that present a small positive time shift, slightly different wave amplitudes and lack of some reflection events. A large amplitude misfit is obtained after 7 s for receiver 300 in Fig. 9.10 f. In contrast, seismic traces simulated with the FWI Vp model (blue traces in Fig. 9.10 f) display most of the seismic events with only few and small amplitude and phase differences at the end

of the recordings and far offsets.

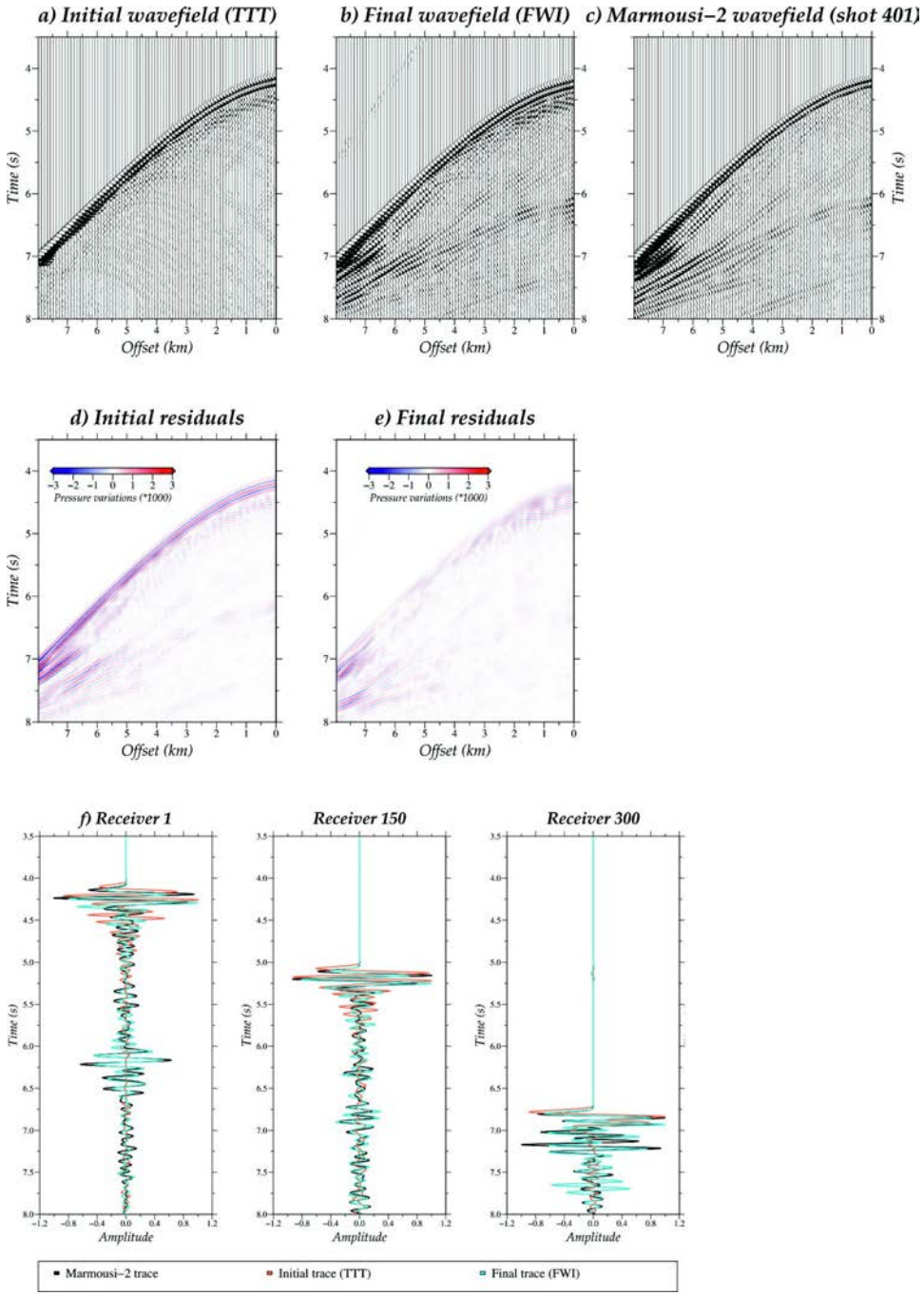

Figure 9.10: Streamer seismograms for shot 401 simulated using the (a) initial (TTT), (b), final (FWI), and (c) Marmousi-2 Vp models presented in Figure 9.8 a, b, and c respectively, and the FD solver of the FWI algorithm. Only one trace every 100 m is plotted, so ¼ of the total. Initial (d) and final (e) residuals are displayed for a better comparison of the results. The location of the streamer is at a distance of ~20 to 28 km along profile. (f) Comparison of the initial (orange; cf. a), final (blue; cf. b) and Marmousi-2 (black; cf. c) seismic traces for receivers 1, 150 and 300.

The misfit reduction for FWI along the different steps of the multi-scale strategy is shown in Fig. 9.11. Misfit is reduced after the whole inversion and it is stabilized almost to zero. The misfit increases when a new multi-scaling frequency band is inverted due to the introduction of high-frequency content or new detailed information to be fit.

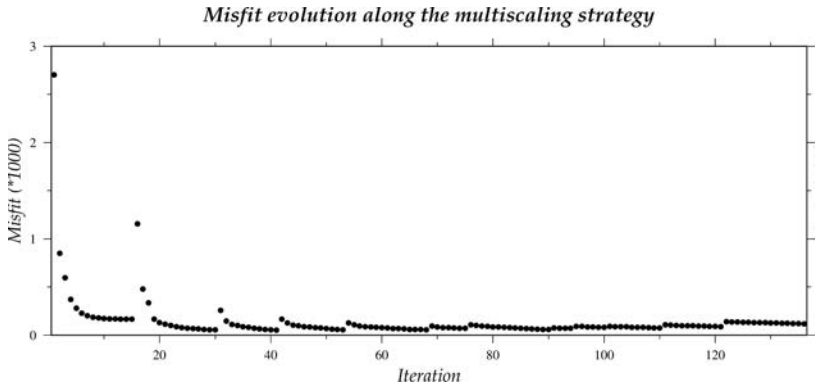

Figure 9.11:FWI misfit decrease along the iterations. The jumps where misfit increases are due to the inversion of next multi-scaling frequency band.

9.3. Discussion

This section presents the last step of the processing/modelling workflow proposed in this thesis, which is the application of FWI. Here, FWI is performed from the original streamer (i.e., MCS) data for two synthetic models, the checkerboard and Marmousi-2 models (Chapter 6). On one hand, the recovery of the vertical Vp profiles and specifically the Vp contrasts at the edge of the anomalies is a challenging task for FWI (and for inverse methods in general). On the other hand, Marmousi-2 presents a detailled and complex Vp distribution that is located in a deep-water environment and below an irregular seafloor surface, which is trying to simulate a more realistic case in a geologically complex area.

The main problem regarding FWI is its intrinsic non-linear behaviour, which makes difficult to calculate the proper model changes that lead towards the correct solution. As a consequence the problem is very sensitive and conditioned by the selection of the initial model. It has to be close enough to the target one to avoid cycle skipping at the lowest available frequency. Under optimal conditions, FWI allows fitting most of the seismic events of the seismic records (Figs. 9.4, and 9.10) and thus, obtaining a high-resolution model of the subsurface in which the structure and properties (Vp) are characterized in detail (Figs. 9.1 b, 9.2 c, and 9.8 b). Otherwise, when the initial model is far from the target one (Figs. 8.3 a, and 9.8 d) and initial data are cycle-skipped (Figs. 8.8, and 8.16), FWI is unable to reach the final solution and gets stuck at a local minimum that changes the model in a wrong direction causing the appearance of artefacts (Figs. 9.6 c and 9.8 e).

It has been proved that TTT models (Figs. 8.3 b, and 9.8 a) obtained from DC first arrivals are good enough to properly perform FWI (Figs 9.1 b, 9.2 c, and 9.8 b). Thus, TTT models have the correct background information (low-frequency content in the data) necessary to reach a successful FWI using them as initial ones. Most of the differences between FWI resultant and target models are concentrated in areas where the initial model is not well constrained and with lower data coverage, as in the left side and deepest areas (Figs. 9.1 b, 9.2 c, and 9.8).

Since the whole information of the seismic records is integrated in the inversion, FWI retrieves features at all offsets and depths. This is the reason why the subsurface is imaged more accurately than using other techniques such as TTT. In particular, in the streamer shots the FWI mainly introduces information on the reflections that are absent in the initial records (simulated using TTT or gradient-based models) (Figs. 9.4 a, and 9.10 a). The wave field generated using the final FWI model (Fig. 9.4 b, and 9.10 b) and its corresponding target seismic record (Figs. 9.4 c, and 9.10 c) match for all offsets and times (Figs. 9.4 e, and 9.10 e) when initial model is kinematically correct, so initial data are not cycle-skypped with the target one (Figs. 8.8, and 8.16). Under this situation, FWI is capable of decreasing the wave field misfit to almost zero (Figs. 9.5, and 9.11) and thus, accurately retrieve the events shown in the target seismic records. Therefore, under these conditions it is possible to retrieve an accurate Vp model of the subsurface that explains the data set. The key point is that, even if the shot gathers lack of low-frequency content, the TTT model obtained with the DC first arrivals are good, and kinematically correct to avoid cycle skipping, which is an essential and a necessary requirement to perform FWI retrieving a reliable and detailed Vp model of the subsurface.

Chapter 10. Application to a field data set

Here we show the results obtained after applying each step of the modelling strategy described in the previous sections to a field data set acquired in the Alboran Sea (see Fig. 10.1). We work under the premise that we have no a priori information on the structure and properties of the subsurface, so the goal is to recover all the possible information on the Vp model from the MCS data alone. The DC result of the streamer recordings to make the early refractions visible as first arrivals is shown first. Then, a macro-velocity model is obtained by joint refraction and reflection TTT, which is then used as initial model to perform FWI starting at ~ 6 Hz, the lowest usable signal frequency in the data set. Finally, we perform a pre-stack depth migration (PSDM) of the recorded data using the 2-D Vp models obtained by TTT and by FWI.

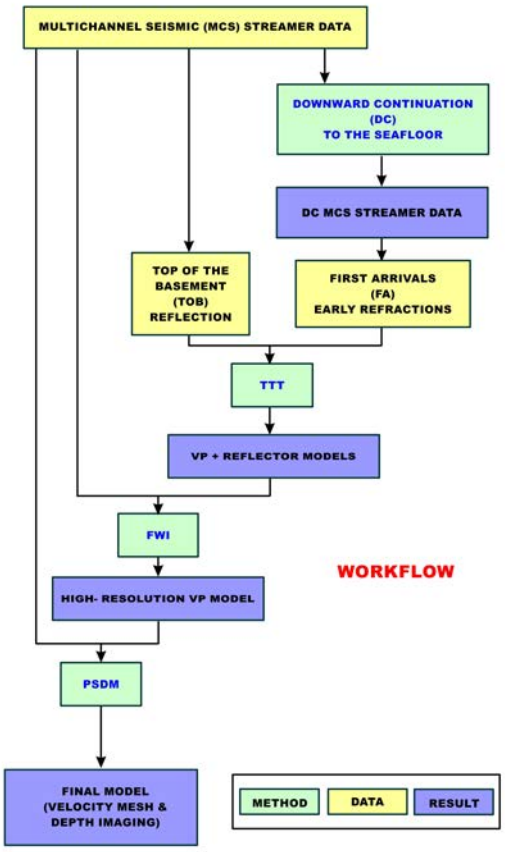

Figure 10.1: General scheme of the workflow. We build the Vp model sequentially, from long to short wavenumbers, taking advantage of all the information contained in our data. We apply the different techniques referred to in the text (DC, TTT, FWI, and PSDM) to obtain a high-resolution image of the subsurface.

10.1. Study area and data set

The field data used to test the described approach correspond to an experiment conducted in the Alboran Sea (SE Iberia), a complex basin located in the westernmost Mediterranean, Fig. 10.2 (Booth Rea et al., 2007; 2018). The target of this survey was to image the structure and properties of the sediment units and the nature of the uppermost basement.

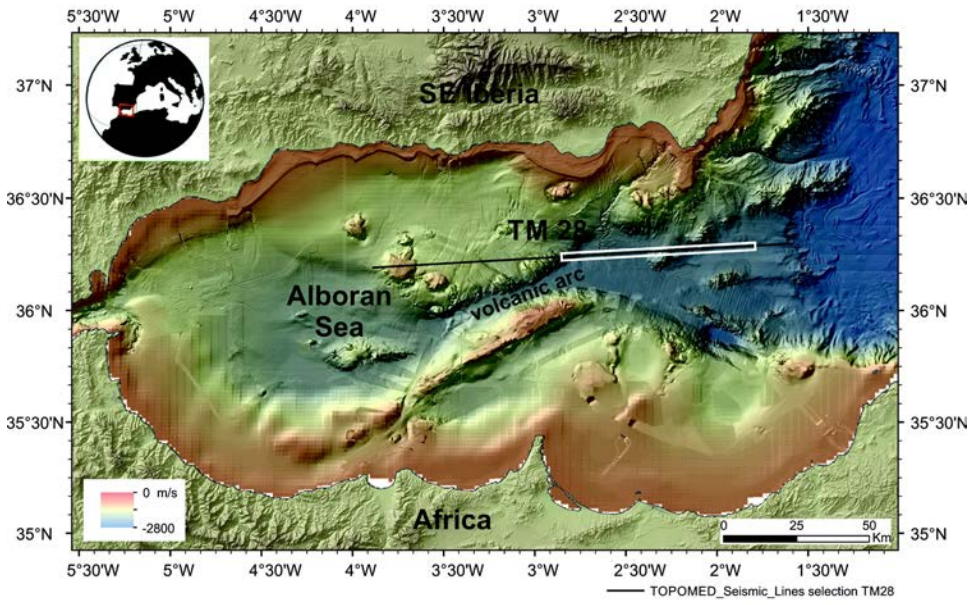

Figure 10.2: Relief map of the study area (Ballesteros et al., 2008; Gràcia et al., 2012, Gómez de la Peña et al., 2016). The field data used in the test correspond to the white box along the TM28 profile.

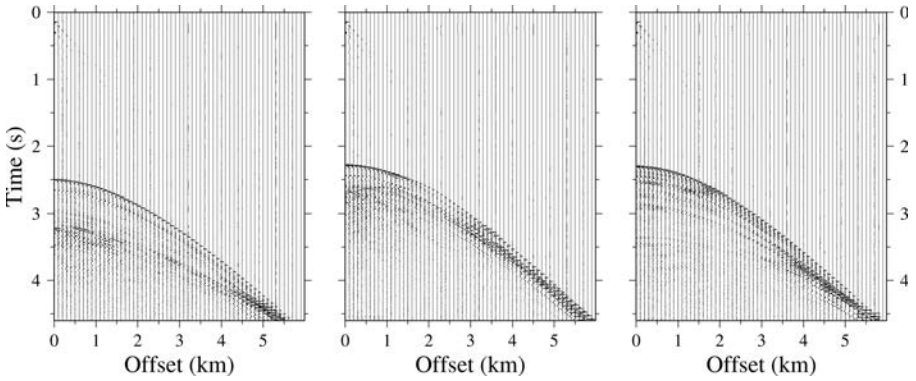

Figure 10.3: Decimated example of the field data set; only 10 traces in each kilometer are plotted (so 0.2 of the total) for clarity. From left to right, shot locations are at 171.1, 138.7 and 112.5 km along the profile.

Acquisition geometry (TOPOMED experiment) – Data quality and preprocessing

The seismic records used in this study were collected in 2011 on board Spanish R/V *Sarmiento de Gamboa*, as part of the TOPOMED cruise. We selected an 80 km long section of the TM28 profile that crosses the central and deepest part of the basin, across a volcanic arc (Gómez-de-la-Peña et al., 2018), to test the approach. The input data consist of series of seismograms (traces) recorded with a 6 km long streamer (Fig. 10.3). The

streamer has 480 channels with a group interval of 12.5 m. The length of the trace record used is 8 s and the time sampling is 2 ms. In total, we use 1517 air guns shots with an average spacing of 50 m. The source power was 4,600 c.i., producing a central frequency of ~ 20 Hz. The system was towed at a depth of 10 m, and the nearest-offset distance was 203.7 m. The early arrivals in the streamer recordings are dominated by the shallow near-vertical sediment reflections, as can be seen in Fig. 10.3. Hence, data preconditioning is essential to identify first arrivals and make the data set appropriate for TTT. Before starting our processing and modelling workflow, we apply a 2-D band-pass minimum-phase Butterworth filter to the data set for swell noise removal. The low cut and high cut of the band-pass filter are 2 and 60 Hz respectively.

10.2. Downward continuation results

In order to parameterize and build the heterogeneous water velocity model of the media required for the back-propagations, we used the information of two in-situ oceanographic measurements of water properties obtained with expendable bathy-thermographic (XBT) probes. In this case, grid size in both the x and z direction is 12.5 m to perform DC. Moreover, the new virtual positions are the seafloor relief itself extracted from bathymetric data.

So, we compute the data re-datuming by wave equation DC of the streamer recordings to the seafloor surface. Fig. 10.4 shows the result after the first step of the DC for three shot gathers derived using the full wave field of each shot and a heterogeneous water layer model built as explained above. We image the wavefronts of all the seismic events recorded in the streamer traces reconstructed by the solver after its back-propagation to the virtual receiver positions in the correct reversed time (i.e. the OBS-type acquisition setting). In this way, we recover several first arrivals that were obscured in the original recordings. However, the main first arrival along the recordings is still the seafloor reflection.

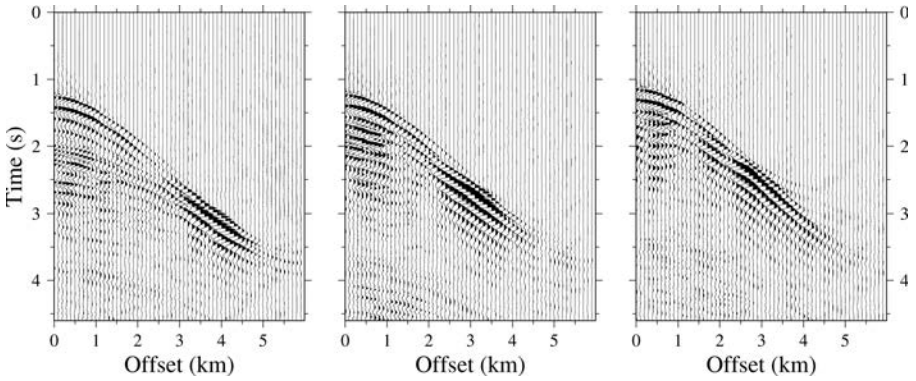

Figure 10.4: Seismic data obtained after the first DC step of the streamer shots recorded in the TOPOMED cruise. The wave fields are displayed for every fifth trace (so 10 traces each kilometre, 0.2 of the total). From a) to c), shot locations are at 171.1, 138.7, and 112.5 km along the profile.

In the second step, we re-sort the virtual "OBS-type" wave field in receiver gathers, and then, the data from all shot gathers are combined to construct the final virtual shot gather. Figure 10.5 shows the final result for the three shot gathers also shown in Fig. 10.4. The DC has collapsed the seafloor reflection toward a single point at zero offset, so refractions from shallow subsurface can now be identified and tracked as first arrivals from zero offset. First arrivals are more difficult to identify at long offsets because of amplitude attenuation and the presence of diffraction tails. Lower panels in Fig. 10.5 show the first arrivals used as input for the TTT (blue dots).

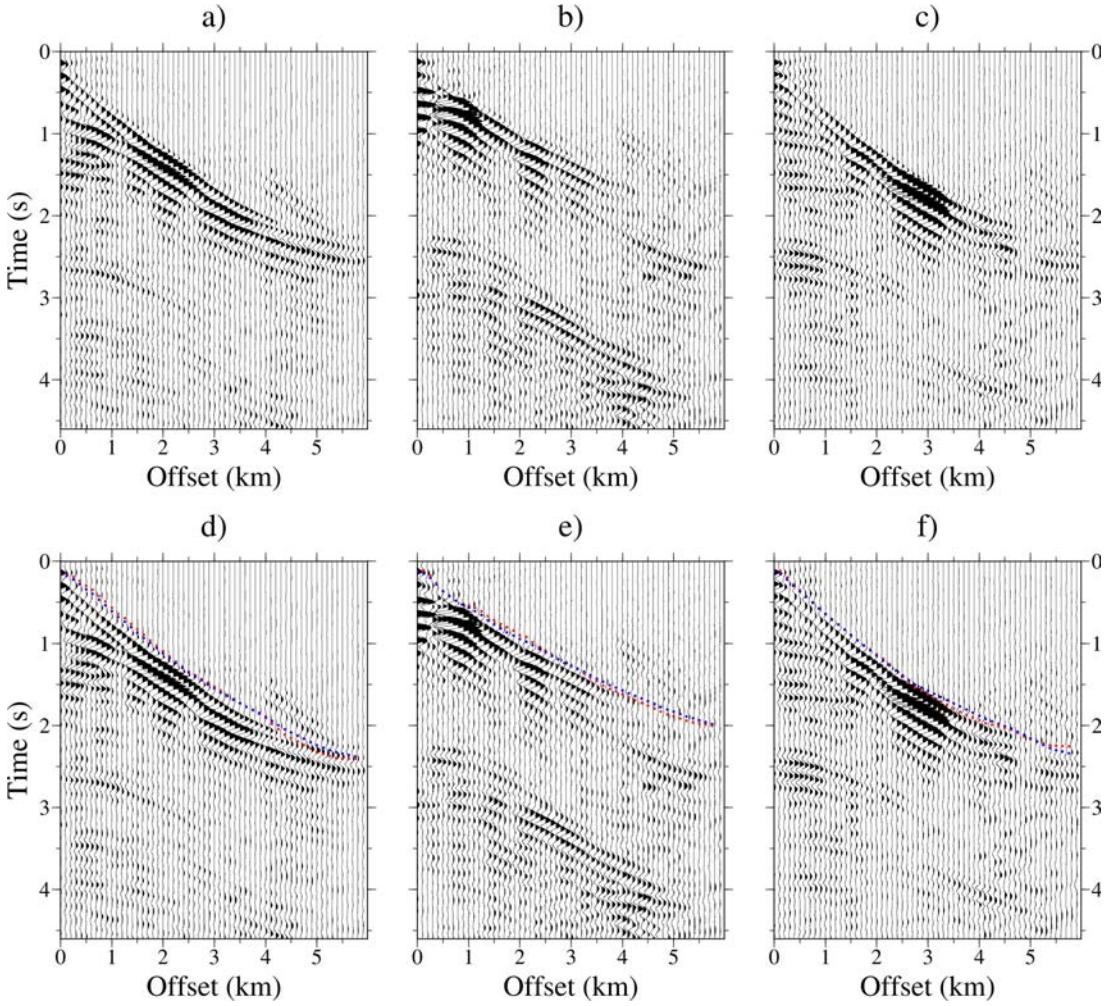

Figure 10.5: Seismic data obtained from the DC of the streamer shots recorded in the TOPOMED cruise. Only 10 traces each kilometre are plotted (so 0.2 of the total) for clarity. From left to right, shot locations are at 171.1, 138.7, and 112.5 km along the profile. Lower panels show shots a)-c) together with first arrivals used as input for the TTT (blue dots) and the first arrivals simulated with the TTT model (red squares).

10.3. Joint refraction and reflection travel-time tomography results

This section presents the macro-velocity model by joint refraction and reflection travel time tomography. We work under the premise that we have no a priori information on the structure and properties of the subsurface. The inversion parameters used in the TTT are shown in Table 10.1. A two-dimensional slowness (inverse of velocity) model is parameterized in our TTT study as a regular mesh beneath the seafloor relief. The area considered in the inversion has a total surface of ~ 82.5 km long x 5 km deep, under ~ 1.1 – 1.9 km of water depth. Velocities in the water layer are fixed to be 1.5 km/s. A 1-D floating reflector boundary is defined along the profile and updated independently of the velocity nodes. The node spacing for the TTT inversion is constant and equal of 25 m for both horizontal and vertical directions. We invert some predefined seismic phases on the seismogram, particularly the first arrivals from the DC recordings and one reflection from the original MCS data. All the seismic phases were picked manually using the software "Globe Claritas". We do not use the entire data set to reduce the computational burden, but all receivers are used to ensure data redundancy. The selected reflection corresponds to the top of the basement (TOB), which is a clear event (e.g. see Fig. 10.6). Reflection travel times are picked from MCS common midpoint gathers where it is a bright continuous reflection, which is also interpreted at the same time in a fully processed stacked image (Fig. 10.6). Reference picking uncertainty to calculate chi-squared value is set to ±35 ms. The source and receiver positions were projected to a straight line defined between first and last shots, preserving their offset distance. Correlation lengths for the velocity model are set at the top and bottom nodes of the grid and are linearly interpolated for the intermediate nodes. The velocity gradient is stronger in the vertical direction, so the vertical correlation lengths are selected to be shorter than the ones defined in the horizontal direction. Our inversion process follows the layer-stripping strategy as described in Meléndez et al. (2015). In the first step, the initial TOB depth model is a flat boundary located at 2.25 km depth, and the initial Vp model follows the linear function of depth from the seafloor $V_P(z)(km/s) = 1.61+0.72 \cdot z$ (km), increasing from 1.61 km/s at the seafloor to 4.13 km/s at a depth of 3.5 km below the seafloor (Fig. 10.7 a). In the second inversion step we use the inverted TOB from the first step (Fig. 10.7 b) as initial TOB depth model and the same data set and inversion parameters. Regarding the Vp model, we build a new initial model that is equal to the Vp model above the TOB obtained in the first step, whereas below it Vp is defined as $Vp(z)(km/s) = V_{TOB}+(z-z_{TOB}) \cdot (V_{Zf}-V_{TOB})/(z_f - z_{TOB})$ (km), varying from 3.6 km/s at the TOB interface (V_{TOB}) to 6 km/s (V_{Zf}) at a depth of 8.6 km below the seafloor (z_f) (Fig. 10.7 c). The goal of the layer-stripping strategy is to recover the sharp velocity contrast at the sediment-basement reflecting boundary, which might otherwise appear as a smooth velocity gradient, contributing also to the improvement of the deepest part of the model.

Inversion parameters	**Values**
Grid dimension (long x deep)	82.5 x 5 km
Range of water layer depth	1.1-1.9 km
Node spacing (dx = dz)	25 m
Number of DC shot gathers picked	121
Distance between DC shots picked	~500 m
Maximum experimental offset	~6 km
Total of first arrival travel times	58,080
Total of reflected travel times	56,920
FS order (x,z) (node connections)	(7,7)
Eliminate data outliers with chi values	> 15
Tolerance level to terminate inversion	0.001
Number of iterations	10
Velocity smoothing parameter (λ_v)	75
Depth smoothing parameter (λ_z)	10
Average velocity perturbation limit (%)	15
Average depth perturbation limit (%)	15
Top velocity smoothing correlation lengths (x,z) (L_{Htop} , L_{Vtop})	(0.6,0.05) (km)
Bottom velocity smoothing correlation lengths (x,z) (L_{Hbot} , L_{Vbot})	(3,0.5) (km)
Horizontal smoothing correlation length for the reflector (x) (L_z)	1.5 km

Table 10.1: Relevant inversion parameters used in the travel-time tomographic inversion.

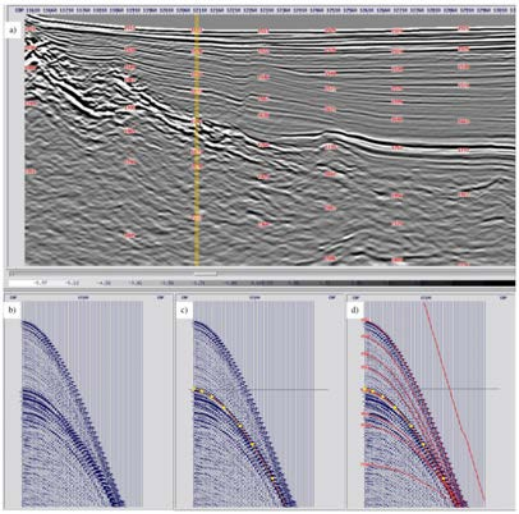

Figure 10.6: Reflector picking procedure. Processed stack image of a section of the seismic profile (a) showing the location of the CMP gather that is plotted with (c), (d) and without (b) the TOB reflection travel times (yellow circles) used as input for the TTT. The TOB is a bright continuous reflection on CMP gathers. The arrow in (a) and horizontal line in (c), (d) indicate the position of the TOB reflection in the stack image and CMP gathers. Red lines in (d) correspond to velocity parabolas that are used as a velocity control during the reflector picking.

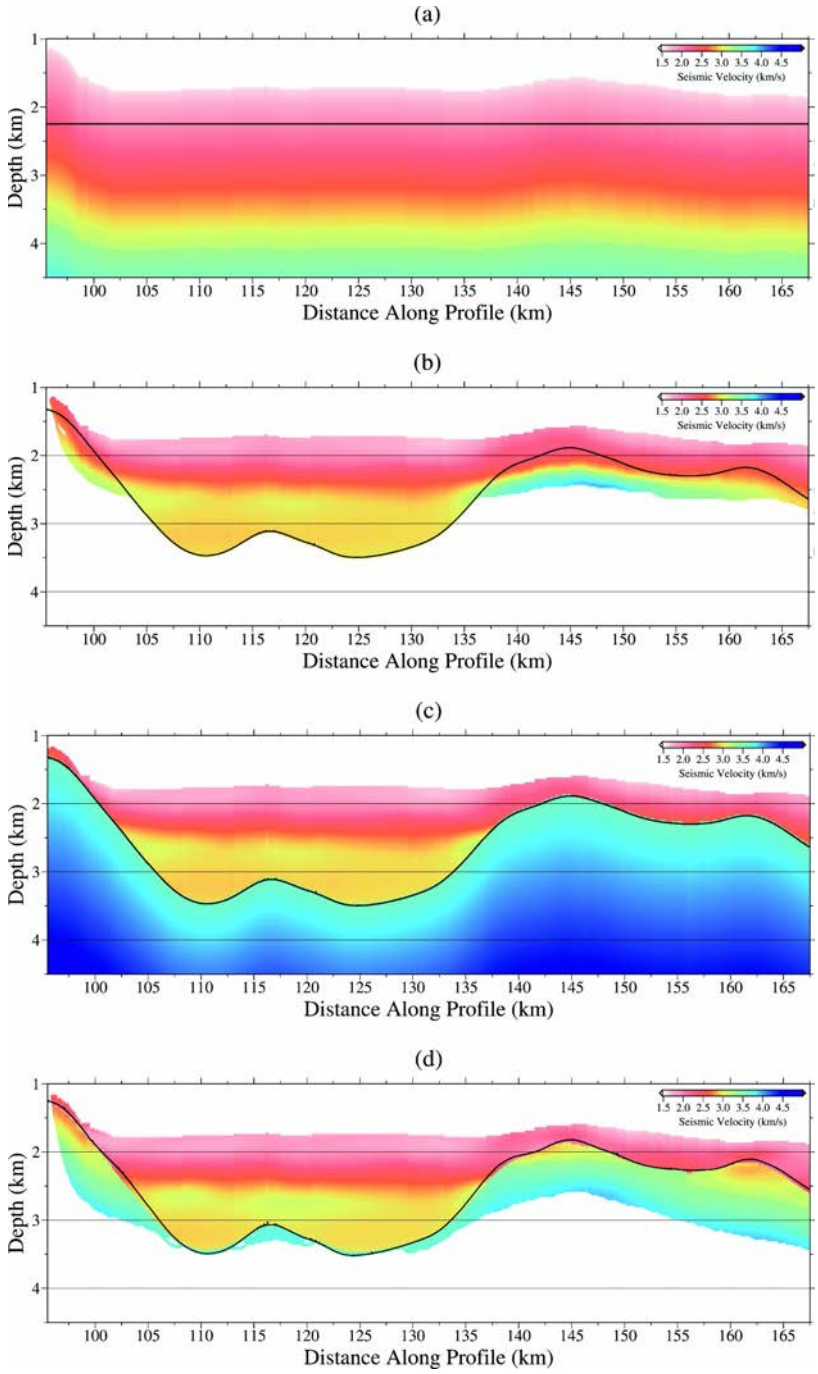

Figure 10.7: (a) Initial Vp and TOB models for the first inversion step. (b) Inverted Vp and TOB models after the first inversion step using (a) as initial ones. (c) Initial Vp and TOB models for the second inversion step (d) Inverted Vp and TOB models after the second and final inversion step using (c) as initial ones. Both inversion steps use the same inversion parameters in Table 10.1, and the data set is made up of the first arrivals of the DC shot gathers and the reflected phase of the TOB discontinuity identified in the original streamer records. Only the ray-covered areas of the model, where the derivative weight sum (DWS) is not zero, are plotted. The thick black line corresponds to the location of the TOB.

Description of the final TTT velocity model

The final macro-velocity model is presented in Fig. 10.7 d. The joint refraction and reflection TTT allows recovering the long-wavelength geometry of the sharp sediment-basement boundary. The ray coverage of the model inversion is quantified by the DWS (Toomey et al., 1994) (Figs. 10.7, and 10.8), which is influenced by the geometry of the experiment and the subsurface velocity distribution. Thus, ray coverage decreases to the edges of the model and with depth, and it is denser beneath the source locations. The model is well constrained in the central part that is covered by both refractions and reflections, whereas the lateral areas mapped only by reflections are subject to a higher degree of velocity-depth ambiguity. In the central area, the overall trend is an increase in velocity with depth, from ~ 1.6 km/s at the seafloor to ~4.0 km/s at the bottom. The results display a high-velocity anomaly (>3.5 km/s) located at ~ 115 km along profile and ~ 3 km depth. Slower velocities are obtained at shallower depths below the TOB. The velocity contrast that accurately follows the geometry of the TOB is delimiting steeply dipping discontinuities. As an example, we show that on the left-hand side of the profile in Fig. 10.7 d the basement is located just below the seafloor (~ 200 m with respect to the seafloor), whereas ~15 km further along the profile the basement position is at a depth of ~ 3.5 km. On the other side, the geometry of the TOB is gently wavy around an average depth of 2 km. The TOB boundary marks strong velocity changes with an average jump of ~ 0.5 km/s between sediment and basement velocities (>2.7 km/s).

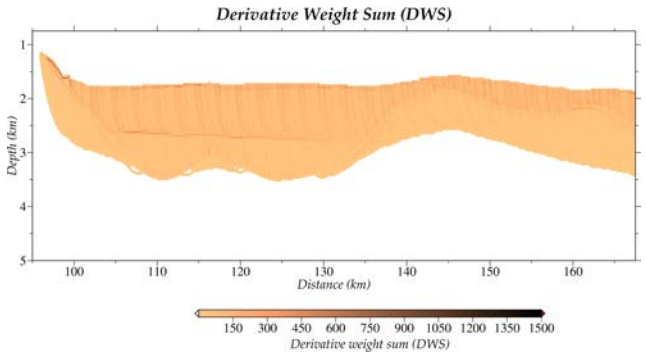

Figure 10.8: DWS of the final inversion result.

Figure 10.9 shows histograms of travel-time residuals for three data groups after the first and last iterations of the two inversion steps of the layer-stripping strategy. The distribution of data misfit with the initial model (red lines) are asymmetric and wide for both refractions and reflections. After the first inversion step (orange lines), the distributions are symmetric and narrower, with the highest pick around zero. At the initial stage of the second inversion step of the layer stripping (green lines), an increase in positive travel-time residuals is shown with respect to the distribution after the first step (orange lines) due to the insertion of higher velocities below the TOB to recover the sharp velocity contrast. Thus, the distributions (green lines) are slightly asymmetric and wider

than after the first step of the layer stripping (orange lines). The final distributions of travel-time residuals (blue lines) are narrower than the previous ones and approach to a Gaussian centred at zero with the largest counts. This fact evidences the improvement of the velocity model, and therefore the corresponding travel-time fitting during the inversion. Lower panels d)-f) in Fig. 10.5 d show the first arrivals for three DC shot gathers used as input for the TTT (blue dots) and the first arrivals recovered after TTT (red squares). The iterative inversion process shows a good convergence with RMS residual travel times of ~ 20 ms (Fig. 10.7 d), which is of the order of the picking uncertainty ($\chi^2 \approx 1$). Note that the initial RMS before the inversion is ~ 420 ms (Fig. 10.7 a).

To assess the reliability of the inversion results, we convert the velocity and TOB models to TWT and superimpose the results on top of the time-migrated image (TMI) (Fig. 10.10). The figure shows that the TTT Vp and TOB geometry models are consistent with the MCS image. Both the velocity contrasts and the depth of the TOB coincide with a strong reflectivity band displayed at the TMI. The good match validates our travel-time picks, given that neither the interpolation of the reflected picks or the inclusion of the far-offset first arrival DC travel times introduce substantial artefacts or errors in the model. However, the TTT model lacks resolution compared to the time-migrated image. It does not reproduce the sharp geometry and changes in amplitude of the anomalies in detail, such as the highs and lows of the TOB, the faults at the flanks, or the sediment layering seen in the TMI.

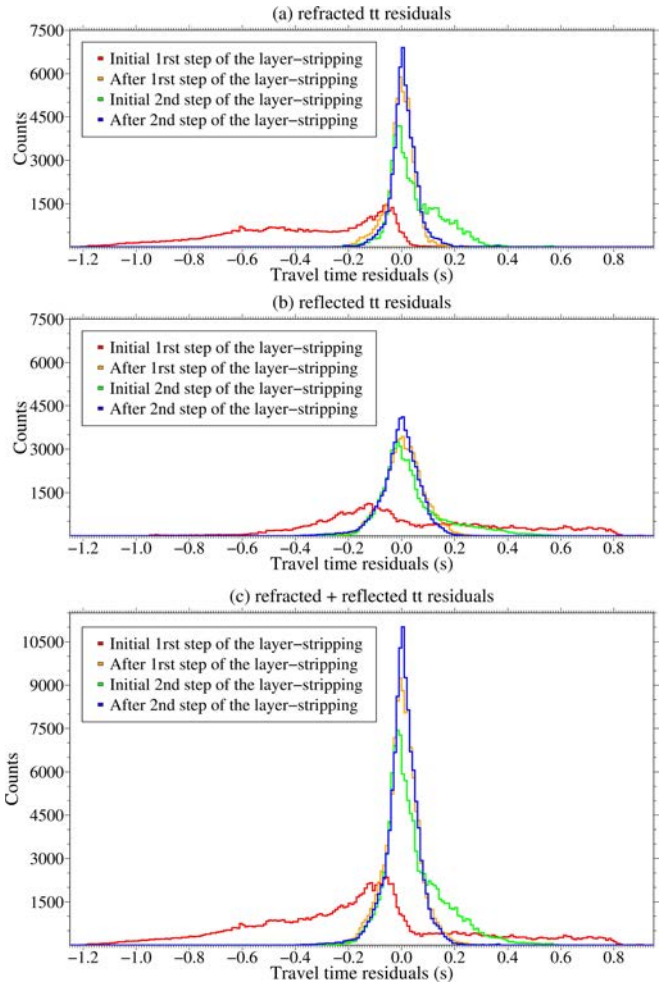

Figure 10.9. Histogram of travel-time residuals. Panel (a) shows only the residuals of the refractions obtained with the initial (red), after the first inversion step (orange), initial for the second inversion step (green), and final (blue) models. Panel (b) shows only the residuals of the reflections obtained with the initial (red), after the first inversion step (orange), initial for the second inversion step (green), and final (blue) models. Panel (c) shows the residuals of both phases (refractions and reflections) for the initial (red), after the first inversion step (orange), initial for the second inversion step (green), and final (blue) models.

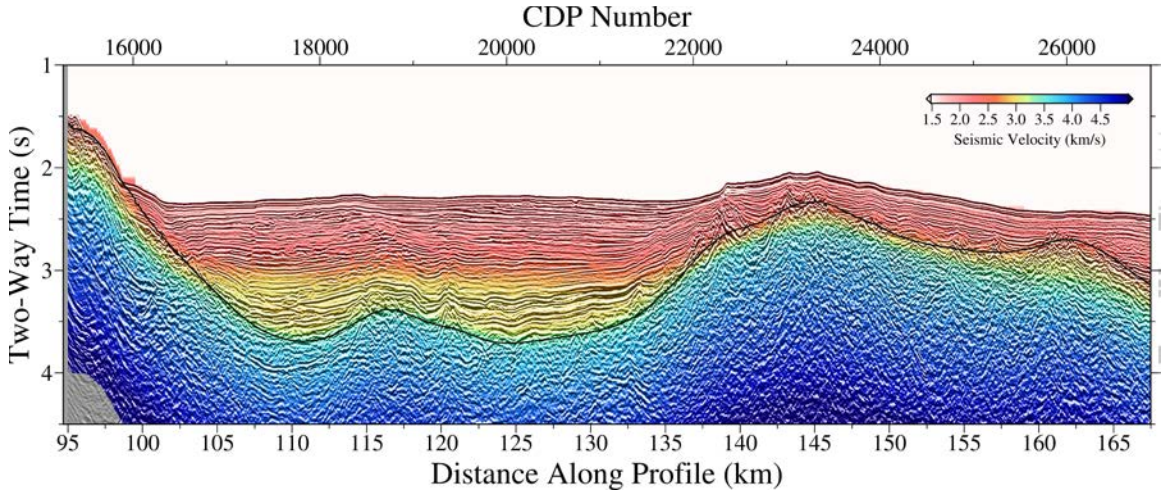

Figure 10.10: Two-way time-transformed Vp and TOB models obtained after the joint DC refraction and streamer reflection TTT are shown superimposed on the time-migrated MCS image.

10.4. Full-waveform inversion results

After TTT, we perform FWI of the original streamer shot gathers starting from a smoothed version of the TTT Vp model of Fig. 10.7 d. A total of 1,512 shot gathers (>720,000 seismograms) are used for the inversion. The length of the traces is 4.6 s. In order to reduce computational costs, we invert sequentially four different sets of 378 shot gathers for each frequency band. Source and receiver positions are also projected to a straight line defined between first and last shots, preserving its offset distance. As in TTT, no decimation is applied to receiver sampling.

We apply a data preconditioning to emphasize reflections between the first arrival, typically the seafloor reflection, and its first multiple, using data windowing. We define a time window centred at the seafloor reflection. We identify this phase by using a maximum kurtosis and k statistics criterion (Saragiotis et al., 2002). We estimate the travel-time of the seafloor reflection using a water velocity of 1.5 km/s, the seafloor depth, and the source-receiver offset distance. When the first arrival is not found, for example due to a noisy channel, or the observed and simulated seismograms are cycle-skipped for the inverted frequency, then the trace is eliminated. The trace value is set to zero before the first arrival travel time, and after that it is balanced by a function defined as $\sqrt{t}$ to compensate for the amplitude decrease at depth. Finally, the trace is also set to zero after the travel time of the first multiple. Therefore, the gradient calculation focuses on information of the data set coming from the near-vertical reflections. Additionally, when the absolute difference between the maximum amplitudes of a field and its corresponding synthetic traces is higher than 3 times the maximum amplitude of the

synthetic trace, it is considered to be a noisy channel and the trace is eliminated. Another issue to consider when comparing synthetic and field data is having a high SNR, so each trace is stacked with its two neighbours at frequencies lower than 8 Hz.

We start the multi-scale FWI at 6 Hz. The maximum frequency inverted is up to 16 Hz. A frequency step of 0.5 Hz is applied at the beginning and 1 Hz at the final stages of the multi-scaling inversion. A total of 14 different frequencies in the multi-scaling strategy are inverted. The size of the space grid for the inversion ($dx < \lambda_{inv}/5$) depends on the frequency step and the minimum velocity of the model, being smaller at high frequencies. The minimum and maximum velocities were constrained as gradient preconditioning and set at 1.4 and 5.0 km/s.

Characterization and assessment of the final FWI velocity model

Figure 10.11 displays the final FWI velocity model. This model has higher resolution than the TTT one (Fig. 10.7 d), showing velocity contrasts of intermediate and short wavelength and a number of geologically meaningful structures that cannot be identified in the TTT model. The improvement due to the higher inverted frequencies is clearest in the shallow part of the model. The velocity contour of ~ 3.25 km/s, which corresponds to the sediment-basement boundary, is better focused and detailed highs and lows are recovered. Thus, in the right-hand side of the profile the velocity variations reproduce the TOB geometry accurately. Dipping low-velocity features are shown with high resolution. The velocity differences between these anomalies and the surrounding media are 0.5-1.0 km/s at ~ 2.25 km of depth between 137 km and 165 km along the profile. The sedimentary package shows velocities from ~ 1.7 km/s near the seafloor increasing to ~3.0 km/s just above the basement. The blue colour found in the deeper parts of the model corresponds to high velocities of more consolidated rocks. However, there are areas where the high velocities are shallower than in others, due to the action of normal faults, as in the left edge of the model.

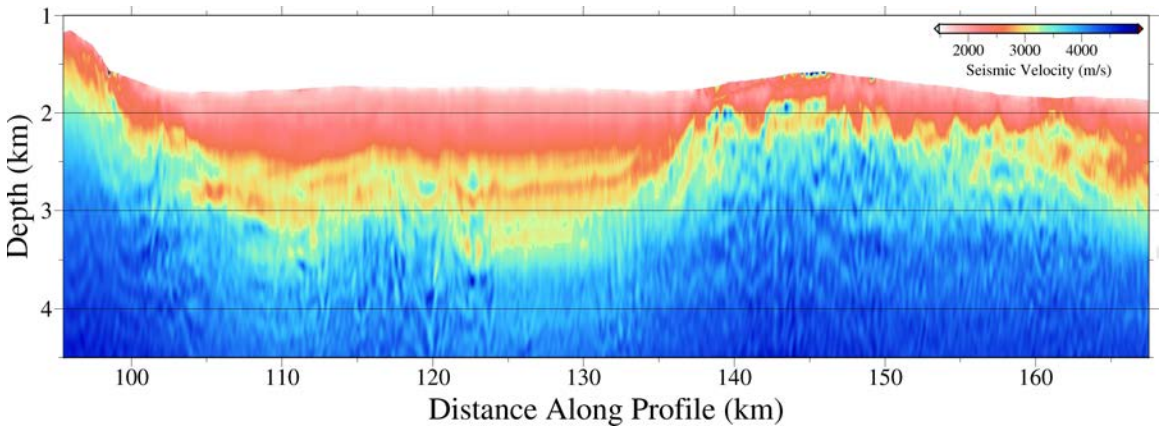

Figure 10.11: Final velocity model after the FWI using Fig. 10.7 d as initial model.

A basin from 95 km to 137 km distance is displayed between two sloping faults. In addition, a ~ 25 km long, 200-300 m thick, high-velocity layer (~ 3 km/s) is clearly imaged embedded within the sedimentary package. Below, there is a dome-shaped structure resembling a volcano cone at ~ 2.6 km depth. The key point is that all these features have been imaged with a streamer of only 6 km thanks to the workflow followed here (Fig. 10.1).

To show the model improvement in the data domain, in Fig. 10.12 we compare a recorded shot gather (Fig. 10.12 c) and a synthetic one generated with the FD solver (Dagnino et al., 2014) using the initial TTT and final FWI velocity models. In contrast with the synthetic data generated with the TTT model (Fig. 10.12 a), the shot gather generated with the FWI velocity model (Fig. 10.12 b) presents some near-vertical reflections. Thus, the seismogram simulated with the final model shows a larger number of seismic events compared to the initial one, which only recovered the first arrival phases and the TOB reflection from the TTT. The data-driven preconditioning of the FWI strategy targeted the energy corresponding to the near-vertical reflections. Therefore, in that region final residuals (Fig. 10.12 e) are smaller than initial ones (Fig. 10.12 d), but are larger around the seafloor reflection. Again, in Fig. 10.12 f aside from wave amplitudes, the main difference between the data generated with the TTT model (orange line) and the target (black line) seismogram is the presence of reflected waves. A better fit between the final (blue line) and field data set (black line) is obtained, except for the effects that are not modelled, such as 3D diffractions or the arrivals not included in the data-based preconditioning.

The misfit reduction for three steps of the multi-scale strategy is shown in Fig. 10.13. Normalized least-squared misfit is reduced after the whole inversion, and the final residual approaches to zero typically after five iterations.

As in the case of the TTT model, we have converted the FWI Vp model to TWT and we have superimposed it to the TMI (Fig. 10.14). Velocity contrasts present a remarkable match with the reflectors of high amplitude of the TMI. The geometry of the TOB interface reflector, for example, is recovered with great detail. Here, velocity differences are of short wavelength, so many of the details that were previously not displayed can now be properly identified (Fig. 10.16 a).

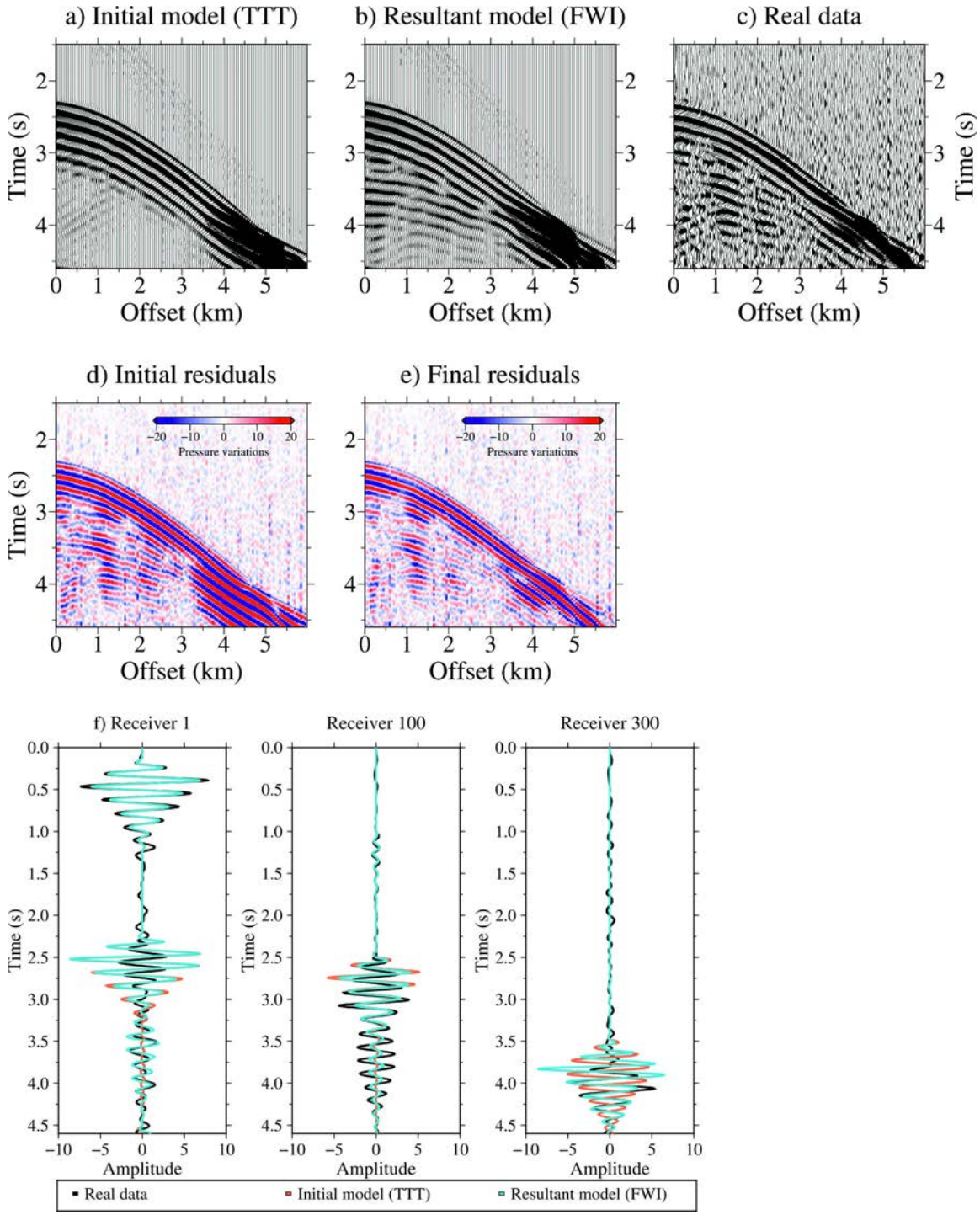

Figure 10.12: Streamer synthetic seismograms, which are computed using the initial (a) and final (b) velocity models presented in Fig. 10.7 d and Fig. 10.11 and the FD solver of the FWI algorithm, together with the real data (c). Only every fourth trace at 50 m is plotted. The location of the streamer is at a distance of ~101 to 107 km along the profile. Initial (d) and final (e) residuals are displayed for a better comparison of the results, as well as (f) initial (orange, cf. a), final (blue, cf. b) and observed (black, cf. c) seismic traces for receivers 1, 100, and 300.

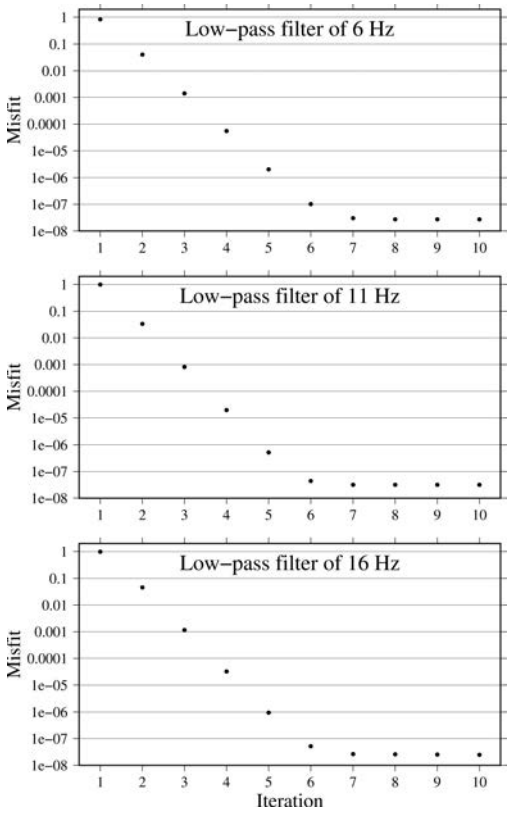

Figure 10.13: Misfit decrease plotted on a log axis along the iterations. The upper panel corresponds to the misfit reduction of the seismic information contained in the first multi-scaling step (low-pass filter of 6 Hz), the middle one for an intermediate step (low-pass filter of 11 Hz), and the lower panel for the final frequency band inverted (low-pass filter of 16 Hz).

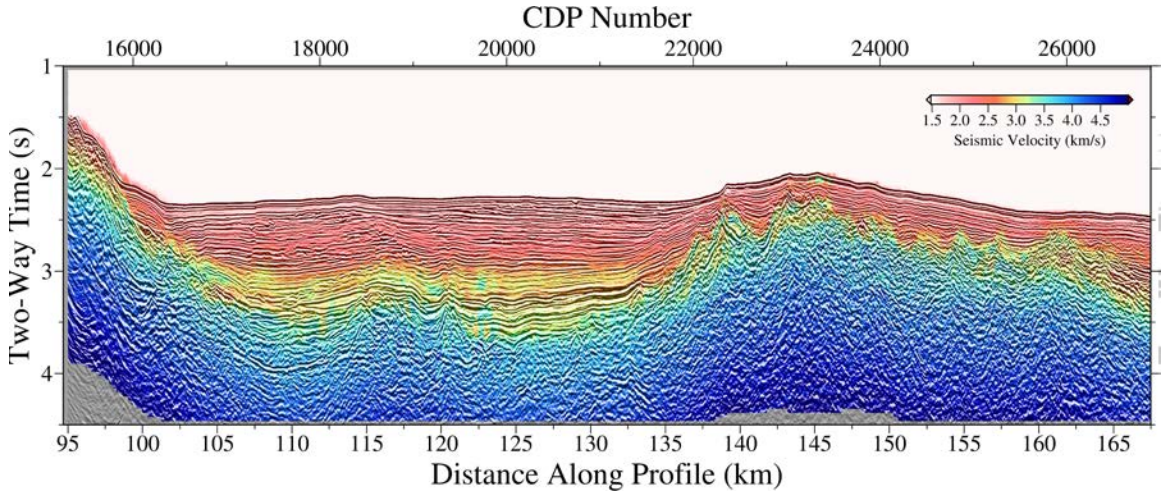

Figure 10.14: Two-way time-transformed Vp model obtained after the modelling sequence proposed in this paper (joint DC refraction and streamer reflection TTT-FWI) is shown superimposed on the time-migrated MCS image.

10.5. Pre-stack depth migration results

We apply a 2-D Kirchhoff depth migration to image the subsurface structures directly in depth by using the Vp models obtained and the high frequency content of the data set. The migration module applied is part of the Seismic Unix platform. We use the sukdmig2d command for the data migration. The travel-time table required for the depth migration is obtained with the rayt2d command, which calculates the 2-D ray tracing along the Vp model.

The seismic data used for the PSDM are not the same as for FWI, but data that have been processed to attenuate coherent and incoherent noise. Streamer field data were processed using a Wiener filter and a surface-consistent deconvolution to increase the vertical resolution attenuating the ringing of the source. Data were sorted in the common depth point (CDP) domain. An amplitude balance (quality factor of 100) was applied to recover the energy lost by geometrical spreading.

We interpolate the FWI result to a 3.125 m grid interval in the horizontal and 3 m in the vertical for the ray tracing. The receivers were spaced at 12.5 m, so the horizontal midpoint distance was 6.25 m for the migration. A total of 720,747 traces were migrated.

PSDM images using the TTT and FWI velocity models

First, we perform a 2-D Kirchhoff depth migration using the processed data set and the TTT velocity model (Fig. 10.15 a). The same PSDM image is also shown in Fig. 10.15 b superimposed with the TTT velocity model, providing additional information on the rock properties. The resolution of the velocity models obtained through TTT is similar to the typical velocity models built for PSDM, although the latter are based fundamentally on reflections. Thus, the PSDM result shown in Fig. 10.15 should be comparable to the one that would be obtained with conventional velocity analysis and PSDM. Although the main features are imaged, i.e. the basin geometry, some structures and interfaces are not as well defined as when the PSDM is performed using a high-resolution Vp model, as it is shown below.

Finally, we repeat the PSDM but using the final FWI Vp model instead, obtained after the processing-modelling sequence proposed in this work (Fig. 10.16). An accurate image of the real structure of the shallow subsurface is displayed directly at depth in Fig. 10.16 a. The sediment layer is thicker on the left side of the profile (~ 1.5 km), where we find the basin, than on the right (~ 0.5 km), where the basement gets shallower. As can be seen in both the FWI velocity model as well as the PSDM image, the basement is severely folded and cut by clear fault structures along the whole profile. The strong lateral velocity changes produced by the faults have caused some migration smiles at the TOB. The deepest part and edges of the profile where FWI and TTT have the largest uncertainties show also the largest misfit in the PSDM result. On the whole, the vertical section in Fig.

10.16 a shows the correct geometry of the structures at depth with a high resolution, clearer than in Fig. 10.15 when a TTT model was used. As an example, the depth and location of the TOB boundary is now comparatively more precise.

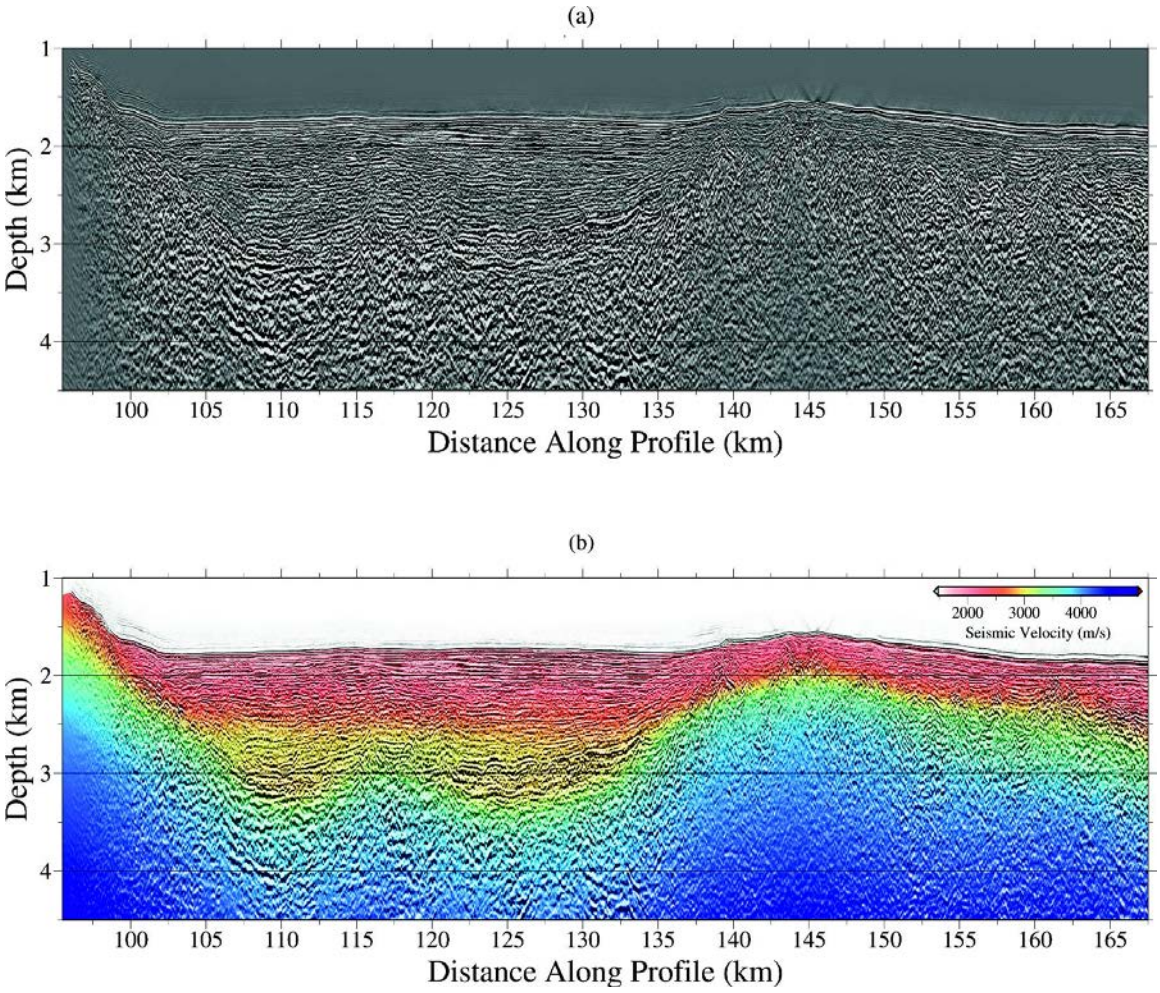

Figure 10.15: a) Kirchhoff depth migration result based on the velocity model shown in (b), obtained after the joint DC refraction and streamer reflection TTT.

A good fit is obtained between the shape of the geological features and the isovelocity contours in Fig. 10.13 b. The volcano-like structure and dipping faults, coincide with well-defined velocity anomalies. Furthermore, a high-velocity layer, which was not visible with TTT in Fig. 10.13 a, is also clearly imaged within the sediment package. The combined interpretation helps us to better define the geological structures and to obtain a proper characterization of the nature of the features.

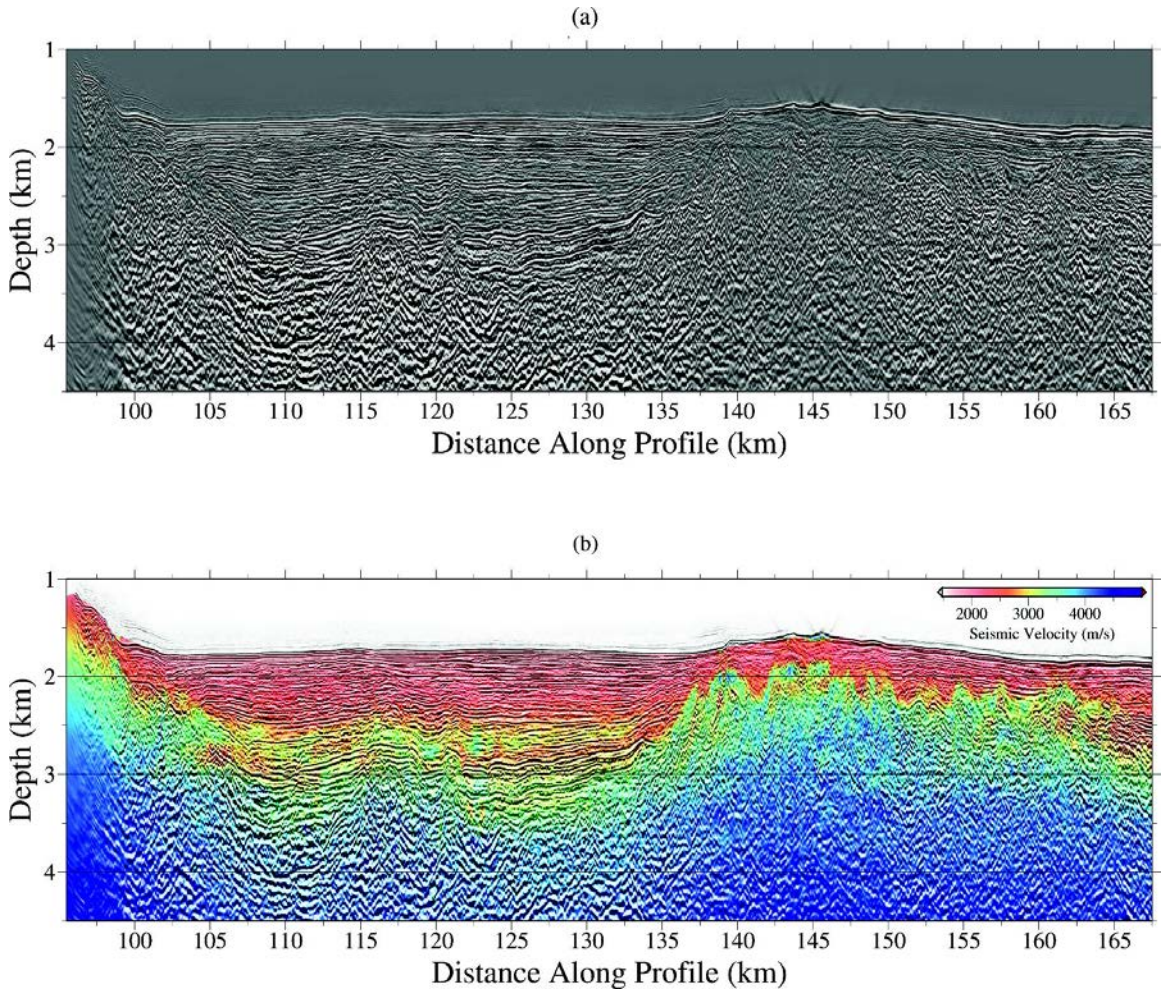

Figure 10.16: a) Kirchhoff depth migration result based on the velocity model shown in (b) obtained after the modelling sequence proposed in this paper (joint DC refraction and streamer reflection TTT-FWI).

10.6. Discussion

In order to avoid excessive repetition, the analysis of the above-presented results and geological interpretation of the Alboran Basin are included in the main discussion (Chapter 11).

Part V

DISCUSSION

Brilliant Disguise

(Bruce Springsteen)

Chapter 11. Discussion

This thesis presents a study that combines different seismic techniques to extract high-resolution information of the subsurface using band-limited, limited-offset MCS data collected in deep-water settings. The discussion of this thesis summarizes and analyses the previous mentioned observations of synthetic and field data results with other studies from the bibliography. We explain the importance of the strategy or workflow that we have implemented and tested to overcome the challenges that are intrinsic to this type of data. The results shown here support the validity of the workflow followed to obtain the best image of the subsurface by extracting all the possible information contained in the dataset. Therefore, they have significant implications showing how to proceed with data sets that were collected with standard equipment not designed for this type of approaches (Fig. 10.1), such as the TOPOMED data set (Fig. 10.3), acquired with a relatively short streamer. Finally, we include a brief summary of the geological interpretation of the Alboran basin based on the velocities and PSDM section obtained.

Validity of the workflow followed

This thesis has been innovative because is focused on integrating and adapting the inversion techniques available to the Barcelona-CSI group (TTT and FWI codes) to data acquired with limited-offset acquisition systems, first with synthetic and then with field data. The reason why they are used together is because it is the only way to achieve a reliable and high-resolution result with the FWI without a priori information, as shown in chapters Chapters 5 and 9. FWI applications require data with low-frequency content (<3 Hz) or good kinematical starting models from a prior information (e.g. Sirgue et al., 2004; Brossier et al., 2009a, 2014; Morgan et al., 2013, 2016). In their absence, to overcome the FWI problems the more robust TTT techniques are commonly used to obtain a proper initial model (e.g. Shipp and Singh, 2002; Dagnino et al., 2014; Qin & Singh, 2017, 2018). We show in chapter Chapter 9, that these two inverse techniques are complementary. In our case, the TTT models (Figs. 8.3 b, and 9.8 a), are shown to be essential to perform FWI from data lacking low frequencies (<4 Hz), especially when first arrival travel-time information is combined with the travel times of reflected phases in the same TTT approach (Fig. 10.7 d).

It has to be noted that the two synthetic models presented in Chapter 6 represent just two examples of the different tests made to develop the combined inversion strategy. Many other tests that cannot be presented in this work due to the limitations of space have been done to (1) check the effects and define the best set of inversion parameters, and (2) to define the optimal steps for the inversion procedure. This includes the downward continuation code, the joint refraction and reflection travel-time inversion, and the full waveform inversion. These previous tests have been key to identify the proper steps for

the multi-scale strategy in the FWI or the optimal regularization constraints to be applied on each step of the TTT.

Based on all these previous tests, we have developed a workflow combining a suite of methodologies developed in-house to retrieve detailed images of the subsurface properties (Vp) in depth with MCS data acquired in conditions that are far from ideal. For this, it has been essential to first apply a data processing, the so called downward continuation (Chapter 4). This step is crucial to reveal refractions as first arrivals, not seen in the original recordings (Fig. 6.2, 6.4 and 10.3 of Chapter 6 and 10) due to the limited length of the streamer and large seafloor depth. Without the Vp information contained on the refractions, neither first arrival or joint refraction and reflection travel-time tomography could be applied, thereby increasing the potential velocity-depth trade-off of the inverted models. While reflections are commonly used in academia and industry to build a Vp model from MCS data, to obtain a reliable model using reflection tomography it is necessary to identify and select specific reflections coming from several geological boundaries in a consistent manner in all the data set, which is an intense, interpretive time-consuming job. Due to the inherent velocity-depth trade-off and to the possible errors in the identification of the layer boundaries, we cannot expect a precise Vp model by travel-time inversion using only one or few reflectors with little lateral or vertical continuity. For that reason, the process to reveal the refractions as first arrivals is so important to construct a kinematically correct background model of the medium.

After adapting the acoustic propagation code of the Barcelona-CSI (Dagnino et al., 2016) to perform the DC (Chapter 4), it has been observed that the travel times of the first arrivals (generated with the TOMO2D) match those of the resulting shots after applying the DC code (Chapter 7). While some studies use waveform-modelling in downward continued data (Qin et al., 2018), here only the travel-time information is used for inversion. We follow this strategy because the wave field during the back-propagation is altered due to several factors that can in turn distort the FWI results. The wave field at the virtual positions obtained is affected by grid dispersion causing amplitude attenuation. As amplitudes are affected by the re-datuming process, it is not a straightforward process to perform FWI using DC data. However, arrival times of the different phases are correct (which is our main objective) if the Vp model of the water layer is accurate enough. Because we only consider the travel-time information, we did not apply amplitude corrections to compensate for 3-D effects. Moreover, the field data used to reconstruct the virtual seismogram are a discrete, single-sided recording, and, therefore, part of the signal is missing during the back-propagation, hindering the complete reproduction of the wave field. A better approximation of the target wave field, and thus a better result, would be achieved using denser and longer arrays. The proper source spacing and optimal recording time step are the ones that avoid aliasing issues, grid dispersion and reduce the effects caused by the discrete approximation of the wave field. For sparse data sets, the re-datumed arrivals are less focused due to a larger amplitude loss and noise effects, but nevertheless correctly located. This justifies using travel-time information from the DC shot gathers.

The data re-datuming allows recovering and identifying the refracted phases as first arrivals, but not all the energy collapses at its corresponding point, making the first arrival picking even more difficult (see Figs.7.3, 7.5, and 10.5). On one hand, at near offsets the energy collapses to an extended area instead of a single point (Figs. 7.3, 7.5, and 10.5). On the other hand, at far offsets the wavefronts may be affected by the presence of diffraction tails (Figs. 7.3, 7.5, and 10.5). Moreover, especially in deep-water environments, the total recording time of the input shot gathers must be long enough to reproduce virtual data covering the whole offset distance or streamer length with subsurface information (Fig. 7.5).

To check the first arrival travel-time errors introduced by the DC procedure we have simulated the shot gathers with the virtual acquisition geometry and the Vp target model in the synthetic cases (Chapter 7). We show that the arrival times are correctly recovered (Figs. 7.1, 7.3, 7.4 and 7.5). This implies that the DC process allows retrieving the first arrival times of the virtual shot gathers effectively. In the case of the DC application with field data, the DC procedure is also checked by reproducing the re-datuming process but using synthetic shot gathers simulated with the TOPOMED acquisition geometry and the final Vp model obtained from FWI (Fig. 11.1). As is shown in Figs. 11.1(a-c), the first arrivals identified in the field DC shot gathers (blue dots) coincide remarkably well for all offsets with the first arrival travel-times of the final TTT Vp model (red squares) and also with the ones in the DC wave fields that are obtained using the synthetic data. The similar results for the first arrivals justify the inclusion of the DC travel times even for large offsets.

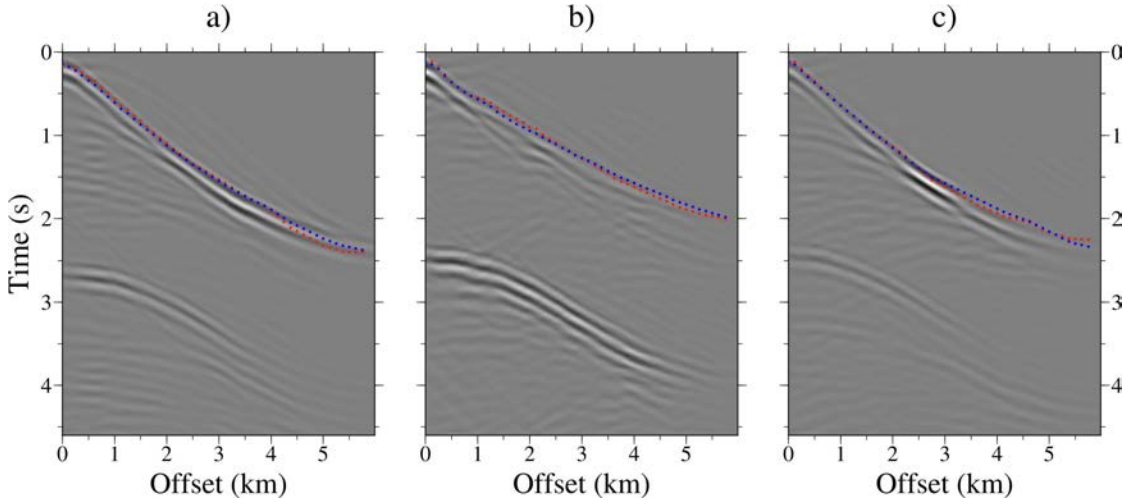

Figure 11.1: Panels (a)–(c) show synthetic seismic data obtained from the DC of the streamer shots simulated using the final FWI Vp model. From left to right, shot locations are at 171.1, 138.7, and 112.5 km along the profile. First arrivals used as input for the TTT are plotted as blue dots and the ones simulated with the final TTT Vp model as red squares.

As the code allows defining an irregular datum or virtual surface, which in our case is the seafloor, as well as heterogeneous Vp models of the water layer, their effects on the travel

times were also checked. While in other studies the virtual datum should be located at either a flat surface or at a surface several meters above the seafloor (e.g. Harding et al., 2016), here the new virtual surface is the seafloor relief extracted from bathymetric data. We have also tested the effect of the water Vp model used to the travel-time picks of the first arrivals identified in the DC shot gathers. In both synthetic (Chapter 7) and field cases travel-time differences are smaller than the associated picking uncertainty. Vp profiles obtained from oceanographic measurements in the Alboran region ranges from 1.507 to 1.526 km/s giving: (1) for a 1 km of water depth, travel times from 0.664 s to 0.655 s, or (2) for a 2 km of water depth, from 1.327 s to 1.311 s. These are smaller than the travel-time picking uncertainty (±0.035 s). Since Vp changes in the water layer of our study area are < 20 km/s, considering either a realistic or an homogeneous model has a minor effect in the first arrival travel-time picks, smaller than the picking uncertainty. However, it would probably be good to analysing the effects of a heterogeneous water Vp model more carefully if the objective were to perform FWI of the DC results.

We then applied TTT from first arrivals refractions provided by the simulation of a virtual acquisition system with both sources and receivers located at the seafloor. Due to the limited offset, these crustal refractions would correspond to ray paths in the upper region of the subseafloor section, and therefore provide structural detail mainly in the upper portion of the model. DC travel-time information alone is efficient and accurate enough to obtain kinematically correct background Vp models from no a priori information, as it is shown in Chapter 8 (Fig. 8.8 and 8.16).

To further improve the Vp model from a kinematic perspective, especially in the deepest part of the model that are less well resolved by first arrivals alone, I have included the travel-times from the geological discontinuity (TOB) (Fig. 10.6) observed in the original data into a joint refraction and reflection TTT approach. For the first time, both travel times from first arrivals in the DC data and from reflections at the original MCS data have been jointly inverted using a modified version of TOMO2D (Begović et al., 2017). Fitting two different phases increases the accuracy of the result because of the introduction of more constraints and extra information of the subsurface, particularly above the reflector. We have obtained a more accurate model of the deeper structure by performing a second TTT inversion step (Fig. 10.7 d) starting from the Vp and reflector geometry of the first TTT step (Fig. 10.7 b), but including a Vp contrast after the TOB reflector position (Fig. 10.7 c). Although the inversion result still suffers from velocity-depth ambiguity at deep regions of the model that are fitted only by the TOB reflection, the Vp result in the upper part of the model appears to be considerably better constrained during the inversion, showing robust results regardless of the initial model used. The shallow area is better defined than it usually is in wide-angle data models with receivers that are commonly separated several kilometers, so that strong smoothness regularization constraints should be used. The streamer TTT exploits the dense and evenly spatial distribution of MCS data, and it is further improved by DC, which allows for the inclusion of the main shallow refractions that are consistent throughout the whole model (Henig, 2013).

The validity of the input travel-time picks and of the TTT result is shown when the Vp and reflector models are converted to TWT and superimposed on the time-migrated image produced by standard imaging techniques (Fig. 10.10). The image shows the spatial agreement of major Vp contrasts with reflectivity changes, together with a good match of the TOB geometry.

The fact that the TTT result retrieves correctly the general Vp variations of the medium implies that shot gathers or seismic records simulated using this model are not cycle-skipped with respect to those observed at the lowest available frequency recorded in data set (see Figs. 8.8, and 8.16). This is a key point to reduce the effects of non-linearity during the multi-scale inversion approach and perform a successful FWI.

The target of applying FWI is to obtain a detailed model of the properties of the subsurface to characterize the medium. However, as discussed above, it has been shown that it is not possible to retrieve a correct Vp model using FWI to band-limited MCS data without a good initial model, (Chapter 9, Figs. 9.6 and 9.8 e) so that it is not cycle-skipped with the target one. If achieved, during FWI the Vp initial model is improved, in this case the TTT result, by introducing smaller wavenumbers (Fig. 9.2).

The final FWI model reproduce the Vp contrasts and anomalies of the target models in detail. It has been proved that TTT models (Figs. 8.3 b, and 8.11 b) obtained from DC first arrivals are adequate to obtain proper FWI results (Figs. 9.1 b, 9.2 c, and 9.8 b) using band-limited data. Most of the differences between the final FWI and target models are concentrated in areas where the initial TTT models are not well constrained due to poorer data coverage (i.e. the deeper part and especially the corners of the models). In practice, the survey area should be considerably larger than the target of the study to overcome this issue.

FWI allows fitting most seismic events in the seismic records (Figs. 9.4. and 9.10), obtaining in this way a high-resolution Vp model of the subsurface. Particularly, the FWI of MCS data mainly introduces high-wavenumber information from the near-vertical reflections that is absent in the coarse initial model. After the application of the whole workflow, the wave field generated using the final FWI model (Figs. 9.4 b, and 9.10 b) and its corresponding target seismic record (Figs. 9.4 c, and 9.10 c) match for all offsets and times (Figs. 9.4 e, and 9.10 e). So, FWI of band-limited and limited-offset shot gathers can be successfully applied.

The results of the synthetic tests encouraged recreating the strategy with field data. This thesis shows the result of the first application of the FWI with field data (Fig. 10.11) of the Barcelona-CSI group and at national level. The Vp model is the first high-resolution one obtained in the Alboran Sea region with inversion techniques.

If we compare TTT and FWI Vp models, in both we clearly identify the TOB as an abrupt Vp change. However, the shape of this discontinuity and its Vp contrast differs between the two models in some areas. The FWI result shows sharper boundaries with

pronounced dipping contacts at ~137-167 km along the profile, which are not displayed in the model obtained by TTT. Those dipping contacts, which may represent fault planes in some cases, are of short wavelength and separate zones of abrupt Vp changes that might be associated with lithological variations. This difference becomes more evident at ~115 km along the profile, where a volcano-like structure is imaged. This feature might be a volcano due to the location of the profile, which crosses an area where there is supposed to be a volcanic arc. Moreover, the geometry of the volcano-like structure and irregular TOB boundary is only clearly imaged at depth when the PSDM is performed with the high-resolution Vp model provided by FWI (compare Fig. 10.15 and 10.16). In addition, the high-Vp layer within sediments on top of this structure is only clearly identified in the FWI Vp model (Fig. 10.11).

The Vp model from FWI was converted to TWT and compared with the TMI from standard processing (Fig. 10.14). The two-way time-transformed Vp model has an excellent match with the MCS time migration; Vp changes follow major reflectivity contrasts and delineate fault locations (Fig. 10.14), which supports the quality of the inversion result and thus the workflow (Fig. 10.1).

Despite the higher level of detail introduced by the FWI, not all the observed signal is matched by the acoustic approach (Fig. 10.12). In the case of synthetic tests, the results are more accurate because the same acoustic solver is used to generate and invert the data. However, field data show larger mismatches that most likely originate from the combined effects of data noise, together with elastic (Warner et al., 2013, Marjanovic et al., 2019), anisotropy, or attenuation effects, which are not taken into account in the acoustic approximation. The seafloor reflection is one example of a discontinuity that is hard to fit to the acoustic formulation of the wave propagation. However, and despite the errors, we show that the FWI of limited-offset and realistic frequency content field data is feasible, and provides geologically meaningful Vp models with a much better resolution than travel-time tomography ones.

The results shown in this thesis have an important implication for the Marine Seismic community, suggesting that many of the existing data sets could be revisited and analyzed with new techniques to enhance our understanding of subsurface, as in the case of the Alboran basin shown here.

Geological interpretation

Information on the structure and properties of the subsurface in the Alboran basin has been retrieved by applying a combination of TTT and FWI (Chapter 10), for which I have followed the strategy described in Fig. 10.1, previously tested with synthetic data. The inverted model includes the Vp of the sedimentary basin and the geometry of the TOB discontinuity. The area has heterogeneous vertical and horizontal Vp gradients, with a Vp distribution showing sharp high-Vp contrasts delineating boundaries of this geologically complex area.

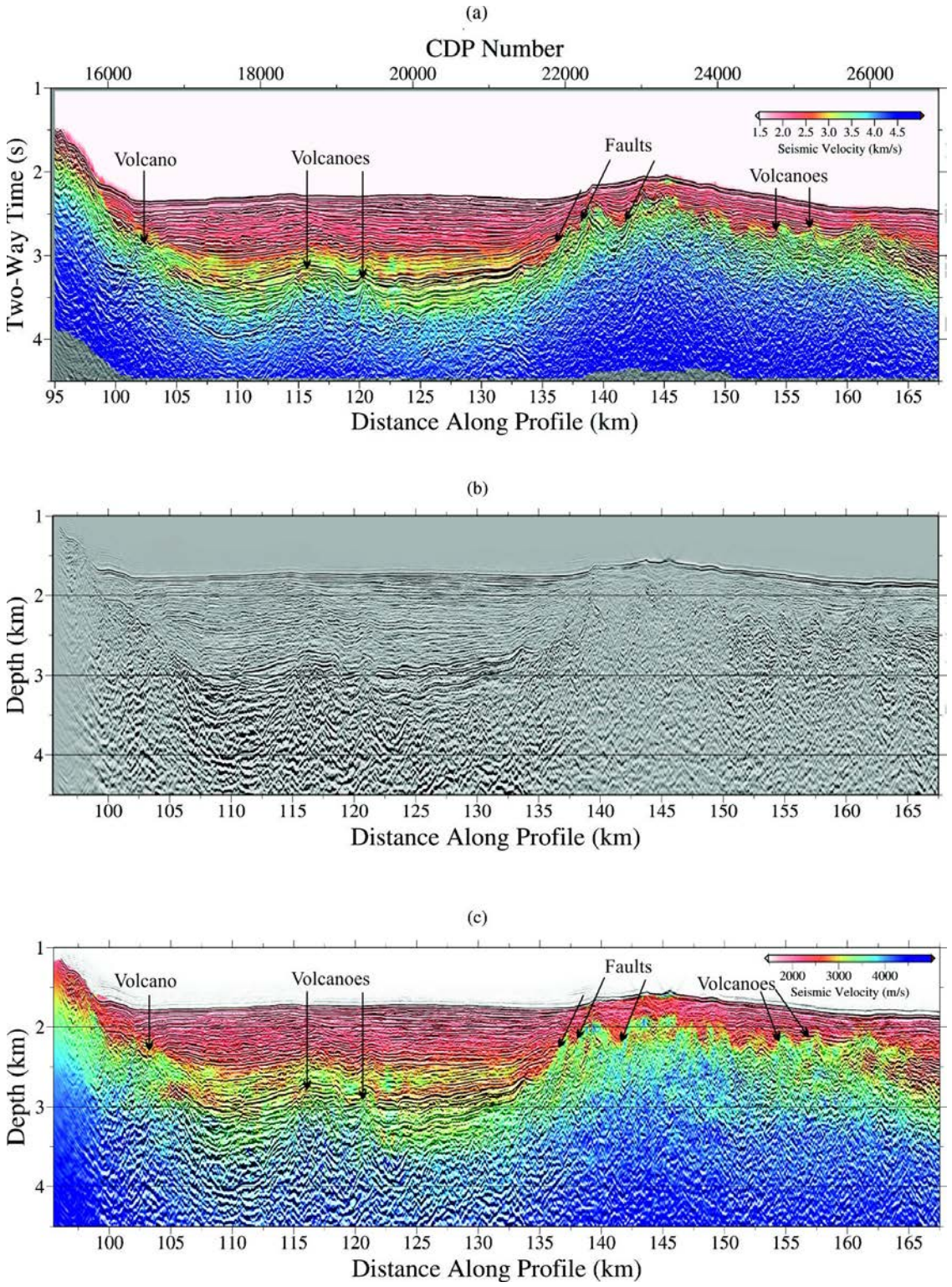

Figure 11.2: Geological interpretation superimposed onto Fig. 10.14. (b) Kirchhoff depth migration result based on the Vp model shown in (c) obtained after the modelling sequence proposed in this thesis (joint DC refraction and streamer reflection TTT–FWI). Geological interpretation is also superimposed onto (c).

The seismic line was collected to image the structure of the eastern Alboran Basin (Fig. 10.2) in a region where basement is interpreted to be made up of magmatic arc rocks (Booth-Rea et al., 2007, 2018 , Gomez- de la Peña et al., 2018). The time migration (Fig. 11.2 a) and PSDM (Figs. 11.2 b, and c) show a sediment basin with basement highs on either end of the image. The large basement highs in the flank display some indications of extensional faulting and block tilting, particularly in the NE. These faults worked during the formation of the basin, cutting the basement and may have some syn-tectonic sediment tilted above rotated fault blocks, but the faults were not active during the deposition of most of the sediment cover.

The basement top under the basin and along the southern ridge displays several small-scale highs with steep flanks and triangular shape. Their fairly symmetric flanks do not support tectonic rotation and may indicate small-scale volcanoes, so that the image supports the basement formation by the interplay between magmatic and extensional processes as expected in a magmatic arc.

The sediment cover displays several units bound by angular gentle unconformities and cut by small sub-vertical, currently active faults. Based on regional geology, we infer that most of the sediment sequence is possibly Pliocene but the oldest layers may be late Miocene, although no drill hole in the vicinity provides a calibration. The seismic Vp distribution in the basin infill may provide some further clues regarding the age and nature of the sediment. The Vp model of the largest basin shows a gradual increase in Vp with depth to ~3 km/s (depth change from reddish to orange colours in Fig. 11.2 a, and c) that is underlain by ~ 0.5 km/s slower-Vp body (change from orange to reddish colours in Fig. 11.2 a, and c). This high- to low-Vp change is marked by a high-amplitude reflection that marks an unconformity -possibly erosional- with the underlying unit. The high-Vp is anomalous because clastic material -turbidities in most of the basin- typically increases in Vp with a compaction-driven decrease in porosity. The high-Vp layer may indicate the presence of evaporites from the end of the Messinian period characterized across much of the Mediterranean by a relatively large drop-down of the water level and deposition of oversaturated deposits. In the deeper basin to the East there are considerably thick salt deposits that can be easily identified in seismic reflection images due to the mobility and formation of diapiric structures (Booth-Rea et al., 2007). Here, in the region of this study there are no known salt deposits, and the presence of Messinian deposits without drilling information is unconstrained. A possible interpretation is that the high-Vp layer represents an anhydrite-rich layer that has relatively high velocities (like salt layers), but that is not easily mobilized by gravity driven processes, so it remains static instead of creating domes or other diapiric-like structures.

Part VI

CONCLUSIONS

Thunder Road

(Bruce Springsteen)

Chapter 12. Conclusions

This thesis presents a detailed workflow of an inversion strategy for limited-offset seismic data lacking low frequencies (band-limited) that is based on codes developed in-house and is shown to be valid to recover high-resolution Vp models of the uppermost kilometers of the subsurface. The workflow provides the tools and a receipt book to apply the inversion strategy to streamer data collected in deep-water settings. The results shown in this thesis, which include both synthetic and field data, confirm that a combination of seismic data modelling and inversion techniques allows obtaining accurate high-resolution Vp models of the medium in a pseudo-automatic way. Below are the main conclusions:

1.- Based on a number of synthetic tests for the different steps of the procedure, we show that FWI of streamer data in deep-water settings is feasible following a three-step workflow strategy that includes: 1) data re-datuming or DC, 2) TTT and 3) FWI. This workflow is shown to allow recovering detailed subsurface information from the MCS recordings.

2.- We have successfully transformed the MCS seismic records to recover refractions in the uppermost levels of the subsurface as first arrivals by applying re-datuming DC techniques.

3.- First arrival travel times of DC data contain valuable information on the velocity of the media, mitigating the typical velocity-depth trade-off that is intrinsic to reflection TTT. Therefore, refractions tracked as first arrivals in the DC shot gathers allow recovering a coarse, but kinematically correct, background velocity model using TTT. Furthermore, performing joint refraction and reflection TTT enhances the resultant Vp distribution in addition to obtain the location and geometry of the reflector.

4.- We have proved that TTT models retrieved from DC of first arrivals are well-suited initial models that avoid cycle-skipping issues at the lowest inverted frequency available for FWI in the data set (4-5 Hz).

5.- We have been able to successfully apply FWI using band-limited MCS streamer data producing high-resolution Vp models of the subsurface.

6.- The application of a workflow including DC of MCS data to the seafloor, joint refraction and reflection TTT and FWI in the Alboran basin has allowed obtaining a high-resolution, geologically meaningful Vp model. The FWI converged satisfactorily providing a geologically meaningful velocity model to a depth of 3-4 km, despite the fact that streamer length is limited to 6 km, water depth is ~ 2 km, and seismic records lack frequencies below 6 Hz.

7.- The excellent match between the two-way time-transformed Vp model and the time-migrated MCS image of the Alboran basin validates the FWI result. Moreover, the PSDM image also shows that the energy is correctly focused at depth.

8.- Building a reliable and accurate Vp model has been essential to depth image the record sections and to obtain the real geometries of the seismic reflectors. This, in turn, makes the geological interpretation of the studied area more straightforward. The PSDM of the Alboran basin obtained with the TTT Vp model is not accurate enough to resolve the small-scale structures and interfaces. In contrast, the final FWI model provides a better defined, more accurate PSDM image that displays clearer the small-scale features, allowing to reproduce many details that cannot be retrieved with TTT.

9.- The PSDM image together with the final Vp model obtained with FWI allows reproducing the structures and properties of the sediment layers and of the uppermost part of the basement with a high accuracy. An abrupt and strong Vp contrast displaying a highly irregular geometry delineates the TOB. This reflector displays volcano-like structures and steeply dipping discontinuities at the flanks of the basin that may correspond to faults. These features support previous interpretation that the basement might be formed by the interplay between magmatic and extensional processes in a magmatic arc setting.

10.- The FWI Vp model allows identifying the location, geometry, thickness and velocity of a high-Vp body within the sedimentary layer. It likely represents a layer of Messinian evaporites embedded within sediments.

Through this workflow, I have been able to learn the fundamentals and use a number modern, start-of-the-art seismic techniques developed at the Barcelona-CSI group, as well as to modify some original codes to adapt them to the needs and characteristics of the experimental data set. The limitations of each seismic technique separately and the characteristics of the data used here have become essential reasons for the implementation of this workflow. The proposed workflow aims at increasing the amount of information that can be extracted from the data, focusing on recovering detailed information about the structural features and its relationship with rock properties that cannot be obtained otherwise. The positive results encourage to apply this workflow to other preexisting marine MCS data sets that have not been used for tomography. The idea is taking advantage of all the information that is typically left unused in the seismic records and, in turn, without additional experimental expenses.

Chapter 13. Forward look

The application of the workflow followed in this thesis shows the feasibility of obtaining high-resolution Vp information of the subsurface to band-limited MCS streamer data. Here we present several ideas to improve the technical and modelling aspects of the methods used in this workflow, and in the uncertainty assessment of the Vp results. Aside from the technical aspects, I identify an important yet poorly understood geological process that could be better studied with this approach.

Regarding the DC code, a more efficient and functional version can be programmed. We propose to change some subroutines in order to extract out of the code the input parameters characteristics of each practical application. These parameters should be introduced in external files. Moreover, we also propose to adapt the code to read and write the input and output data in a binary format to reduce computational costs. Apart from these technical aspects, it can be interesting to analyse the modelled DC wave fields to extract all the information contained on them apart from first arrivals travel times. Some studies use waveform modelling in DC data (Qin et al., 2018), although here only the travel-time information is used. Despite the fact that amplitudes are affected by the re-datuming process, other wave field attributes can be modelled and evaluated into the objective function, such as the phase. Additionally, the travel-times of secondary phases could also be used. Developing mathematical or modelling strategies to invert first arrival wavefronts, joint refraction and reflection travel-times or other attributes of the DC shot gathers can be a path for future research that would probably produce more accurate background Vp models.

As FWI is a complex method, we also propose to explore different objective functions to see which ones allow overcoming cycle-skipping and produce more robust results (Jiménez Tejero et al., 2015; Kormann et al., 2016). Moreover, we have used mainly the SD optimization method with field data because of its low sensitivity to noise, however other approaches as the Non-linear conjugate gradients or the quasi-Newton Limited-memory BFGS might accelerate convergence compared to SD, increasing in this way the efficiency of the inversion. Additionally, as the Earth is an elastic medium, to produce better results we propose fitting the wave field using an elastic FWI solver (Warner et al., 2013; Marjanovic et al., 2019). Depending on the studied area, it is also convenient to consider anisotropy and/or attenuation effects in the modelling process.

Aside for testing other inversion strategies, we also propose to add some uncertainty analysis to better assess the resolution of the different parts of the Vp models. We propose to implement for example Monte Carlo-type stochastic tests (Tarantola, 1987; Meléndez et al., 2013; Prada et al., 2015) for the TTT and/or the final FWI results. The motivation of this analysis is to check the influence on the inverse result of several factors, such as the errors on input data data (either travel-time picking errors or noise), initial model,

regularization parameters or the inversion strategy used. It consists on performing numerous inversions with different random initial models, input data sets with random noise and and/or picking errors, and using random inverse parameters or strategies and computing the average of all the solutions to identify the model that is statistically most likely. By assuming that all the Monte Carlo results have the same probability, the mean deviation of all the resultant models can be taken as a measure of the model parameters uncertainty (Tarantola, 1987). Figure 13.1c shows the final standard deviation for the Vp and Moho reflector geometry models (Prada et al., 2015). In this example, the assessment of the feasibility of the final inversion results (Fig. 13.1a) is made by a Monte Carlo analysis of 250 inversions (Fig. 13.1c).

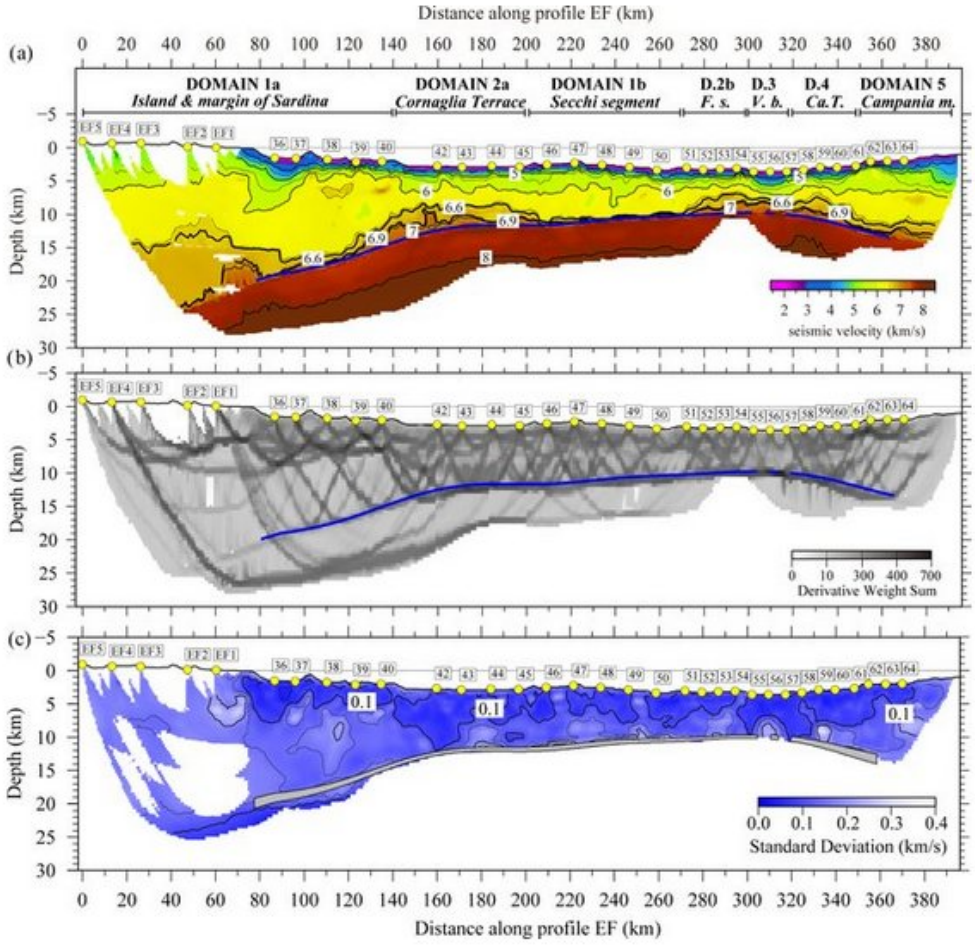

Figure 13.1: (a) Final 2-D P-wave tomographic model of the crust, uppermost mantle and geometry of the Moho obtained from the inversion of Pg, Pn and PmP phases along transect E-F. Yellow circles and blue line display the receiver location and the inverted Moho geometry, respectively. The seven regions are identified along profile on the basis of crustal seismic velocity distribution. F.S: Farfalla Segment, V.B: Vavilov basin, CaT: Campania Terrace. (b) Derivative weight sum (DWS) of tomographic model in (a). (c) Final standard deviation for P-wave velocity values and Moho geometry (grey band) result of the Monte Carlo uncertainty analysis (see Annex B in Supporting Information for details of this analysis) (Prada et al., 2015).

Additionally, the resolvability power of the data set could also be tested by applying series of checkerboard tests with different anomaly sizes (Davy et al., 2018). It consists on superposing positive and negative Vp perturbations onto a background model following a checkerboard pattern. Then, synthetic data are generated using the same source-receiver geometry through these reference models and inverted. The process is repeated for different anomaly sizes. The difference between these inversion results and the unperturbed initial model will determine the areas where the inversion properly reconstructs the media for the different anomaly sized, given an idea of the maximum resolution that can be reached with the available data set in the different parts of the model. Figure 13.2 shows the results for three checkerboard tests with different pattern dimensions to evaluate the resolvability power of the inversion on each case. Then the results can be combined to define the minimum size of the anomalies that can be resolved on each area.

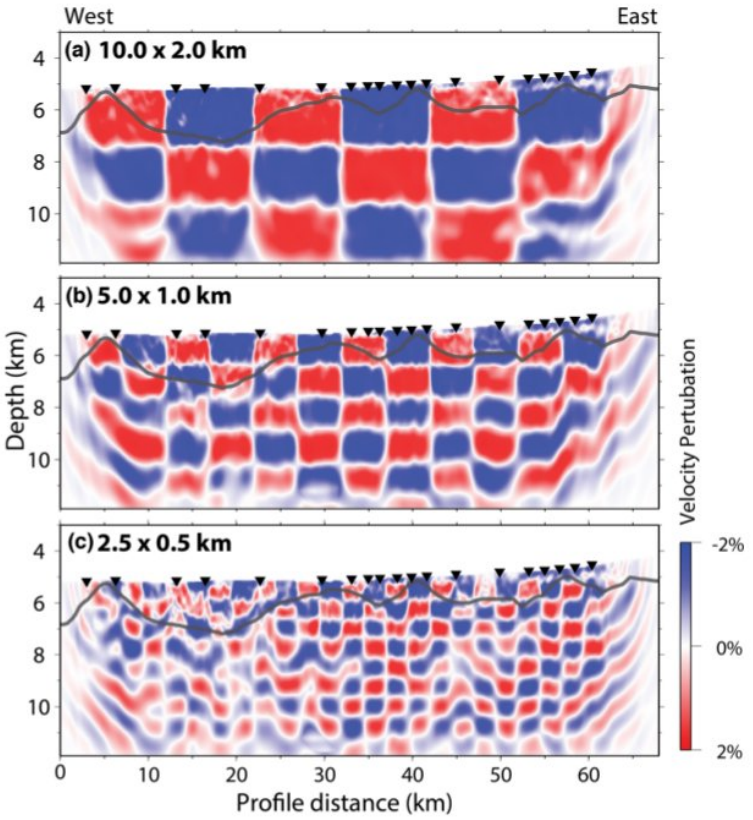

Figure 13.2: Checkerboard resolution test results. Anomaly check dimensions: (a) 10.0 x 2.0 km, (b) 5.0 x 1.0 km and (c) 2.0 x 0.5 km. Vertical exaggeration is 3.4. Grey line represents the top of the syn-rift sediments (Davy et al., 2018).

So, the uncertainty analysis gives information of the areas in the model that are or not well-constrained by the data and therefore, more influenced by the initial conditions and regularization constraints.

We also encourage to test the workflow presented in this thesis to other areas with new or pre-existing MCS data sets. Applying it to longer streamer data should improve Vp models and allow extending the models to greater depths. Future research can be directed to use longer offset data from wide-angle acquisition geometries to increase the coverage and to better constrain the model properties. It would be especially interesting to apply the strategy in areas covered by both MCS and WAS data. Due to the distinct characteristics of the acquisiton set ups, the information contained in both data sets are highly complementary. In this case, a joint refraction and reflection TTT of re-datumed and original MCS data plus WAS refractions and reflections could be applied following a layer-stripping strategy (Bartolome et al., 2019). Early refractions from the re-datumed MCS data, WAS refractions, and shallow (MCS) to deep (WAS) reflections, will be sequentially introduced in the input data set for inversion. The combination of these data sets would highly increase the coverage and resolution of the TTT model (Begović et al., 2017). By improving the background model, the FWI will be better-posed and the high-wavenumber information will be easily and correctly incorporated along the iterations.

A particularly interesting geological object to test the inversion procedure and strategies described above is the frontal part of a subduction zone, from the trench to a megathrust fault depth of ≥5 km. This could be resolved with great detail combining a large streamer of ≥10 km as well as densely spaced OBSs separated ≤2 km in average. The interest of this particular zone is that, while it is the fault segment generating the largest, most devastating tsunamis on Earth, the structure and physical properties of the rocks accumulating and releasing stresses, sliding, and deforming during rupture propagation are poorly known. We know from other studies that the Vp, Vs, density and hence rigidity above this shallow megathrust segment should differ considerably from those found at deeper seismogenic zone depths, but their specific distribution is known only for very few areas (Fig. 13.3) (Qin et al., 2018), and has never been analysed and exploited in full detail to date. As the above-mentioned elastic parameters critically affect key earthquake source properties such as amount slip, rupture duration, propagation velocity, energy content, etc., I identify this type of experiment as the perfect case study for the near future from a strictly geological/seismological view.

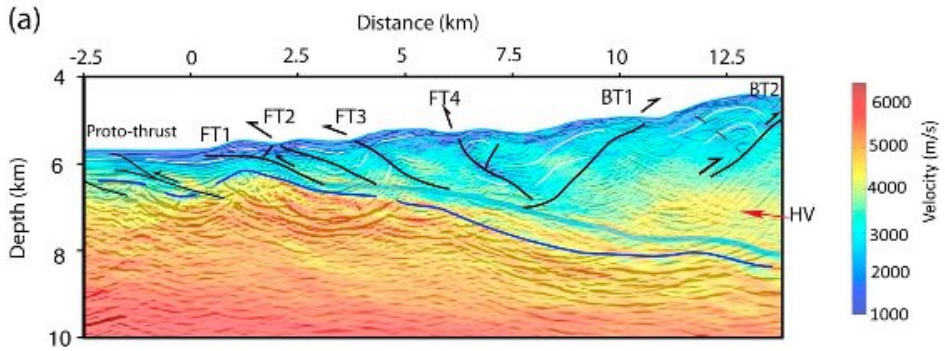

Figure 13.3: Blow-up of the superposition of velocity and PSDM results from the frontal section. The scale ratio of horizontal and vertical axes is 1:1 (Figure 11 a of Qin et al., 2018).

References

Arnulf, A.F., Singh, S.C., Harding, A.J., Kent, G.M., and Crawford, W.C.: Strong seismic heterogeneity in layer 2A near hydrothermal vents at the Mid-Atlantic Ridge, Geophys. Res. Lett., 38, L13320, http://doi.org/ 10.1029/2011GL047753, 2011.

Arnulf, A. F., Harding, A. J., Singh, S. C., Kent, G. M., and Crawford, W.: Nature of upper crust beneath the Lucky Strike volcano using elastic full waveform inversion of streamer data, Geophys. J. Int., 193, 3, 1471-1491, http://doi.org/10.1093/gji/ggt461, 2013.

Arnulf, A.F., Harding, A.J., Kent, G.M., Singh, S.C., and Crawford, W.C.: Constraints on the shallow velocity structure of the Lucky Strike Volcano, Mid-Atlantic Ridge, from downward continued multichannel streamer data, J. Geophys. Res.-Sol. EA, 119, 1119-1144, http://doi.org/10.1002/2013JB010500, 2014.

Bakulin, A. and Calvert, R.: The virtual source method: Theory and case study, Geophysics, 71, 4, 139-150, https://doi.org/10.1190/1.2216190, 2006.

Ballesteros, M., Rivera, J., Muñoz, A., Muñoz-martín, A., Acosta, J., Carbó, A., and Uchupi, E.: Alboran Basin, southern Spain-Part II: Neogene tectonic implications for the orogenic float model, Mar. Petrol Geol., 25, 1, 75-101, http://doi.org/10.1016/j.marpetgeo.2007.05.004, 2008.

Barison, E., Brancatelli, G., Nicolich, R., Accaino, F., Giustiniani, M. and Tinivella, U.: Wave equation datuming applied to marine OBS data and to land high resolution seismic profiling, J. Appl. Geophys.,73, 267-277, https://doi.org/10.1016/j.jappgeo.2011.01.009, 2011.

Bartolome, R., Prada, M., Gras, C., Begovic, S., Awkar, F., Bandy, W.L., Dañobeitia, J.J.: Interplay Between Megathrust Topography and Tsunamigenic Structures Offshore West Mexico, AGU Fall Meeting, San Francisco, CA, 9-13 December 2019, ID#: 611212, 2019.

Begović, S., Meléndez, A., Ranero, C.R., and Sallarès, V.: Joint refraction and reflection travel-time tomography of multichannel and wide-angle seismic data, EGU General Assembly, Vienna, Austria, 23-28 April 2017, EGU2017-17231, 2017.

Berkhout, A.J.: Pushing the limits of seismic imaging. Part I: prestack migration in terms of double dynamic focusing, Geophysics, Soc. Expl. Geophys., 62, 3, 937-953, https://doi.org/10.1190/1.1444201, 1997a.

Berkhout, A.J.: Pushing the limits of seismic imaging. Part II: integration of prestack migration, velocity estimation, and AVO analysis, Geophysics, Soc. Expl. Geophys., 62, 3, 954-969, https://doi.org/10.1190/1.1444202, 1997b.

Berkhout, A.J.: Wave field extrapolation techniques in seismic migration, a tutorial, Geophysics, 46, 12, 1638-1656, https://doi.org/10.1190/1.1441172, 1981.

Berryhill, J.R.: Wave-equation datuming, Geophysics, 44, 1329-1344, https://doi.org/10.1190/1.1441010, 1979.

Berryhill, J.R.: Wave-equation datuming before stack, Geophysics, 49, 11, 2064-2066, https://doi.org/10.1190/1.1441620, 1984.

Bevc, D.: Flooding the topography: wave-equation datuming of land data with rugged acquisition topography, Geophysics, 62, 1558-1569, https://doi.org/10.1190/1.1885634, 1997.

Bishop, T.N., Bube, K.P., Cutler, R.T., Langan, R.T., Love, P.L., Resnik, J.R., Shuey, R.T., Spindler, D.A. and Wyld, H.W.: Tomographic determination of velocity and depth in laterally varying media, Geophysics, 50, 903-923, https://doi.org/10.1190/1.1441970, 1985.

Booth-Rea, G., Ranero, C. R., Martínez-Martínez, J. M., and Grevemeyer, I.: Crustal types and Tertiary tectonic evolution of the Alborán sea, western Mediterranean, Geochem. Geophys. Geosyst., 8, 1525–2027, https://doi.org/10.1029/2007GC001639, 2007.

Booth-Rea, G., Ranero, C. R., and Grevemeyer, I.: The Alboran volcanic-arc modulated the Messinian faunal exchange and salinity crisis, Sci. Rep.-UK, 8, 13015, https://doi.org/10.1038/s41598-018-31307-7, 2018.

Bozdag, E., Trampert, J. and Tromp, J.: Misfit functions for full waveform inversion based on instantaneous phase and envelope measurements, Geophy. J. Int., 185, 845-870, https://doi.org/10.1111/j.1365-246x.2011.04970.x, 2011.

Brocher, T. M.: Empirical Relations between Elastic Wavespeeds and Density in the Earth's Crust, Seismological Society of America, 95, 6, 2081-2092, https://doi.org/10.1785/0120050077, 2005.

Brossier, R., Operto, S., and Virieux, J.: Seismic imaging of complex onshore structures by 2D elastic frequency-domain full-waveform inversion, Geophysics, 74, 6, WCC105-WCC118, https://doi.org/10.1190/1.3215771, 2009.

Brossier, R., Operto, S., and Virieux, J.: Velocity model building from seismic reflection data by full-waveform inversion, Geophysical Prospecting EAGE, 63, 1-14, http://doi.org/10.1111/1365- 2478.12190, 2014.

Bunks, C., Saleck, F.M., Zaleski, S., and Chavent, G.: Multiscale seismic waveform inversion, Geophysics, 60, 5, 1457-1473, http://doi.org/10.1190/1.1443880, 1995.

Cao, S. & Greenhalgh, S.: Calculation of the seismic first-break time field and its ray path distribution using a minimum traveltime tree, Geophys. J. Int., 114, 593-600, https://doi.org/10.1111/j.1365-246X.1993.tb06989.x., 1993.

Cheng, N. & House, L.: Minimum traveltime calculation in 3-D graph theory, Geophysics, 61, 1895-1898, https://doi.org/10.1190/1.1444104, 1996.

Cho, Y., Ha, W., Kim, Y., Shin, S., and Park, E.: Laplace-Fourier-Domain Full Waveform Inversion of Deep-Sea Seismic Data Acquired with Limited Offsets, Pure Applied Geophysics, 173, 749-773, http://doi.org/10.1007/s00024-015-1125-7, 2016.

Christensen, N. I., and Mooney, W.D.: Seismic velocity structure and composition of the continental crust: a global view, J. Geophys. Res., 100, 9761-9788, 1995.

Claerbout, J.F.: Fundamentals of Geophysical Data Processing, McGraw-Hill Inc., New York, 1976.

Clark, J.A. and Page, R.: Inexpensive Geophysical Instruments Supporting Groundwater Exploration in Developing Nations, Journal of Water Resources and Protection, 3, 768-780, https://doi.org/10.4236/jwarp.2011.310087, 2011.

Dagnino, D., Sallarès, V., and Ranero, C.R.: Scale- and parameter-adaptive model-based gradient pre-conditioner for elastic full-waveform inversion, Geophys. J. Int., 198, 1130-1142, http://doi.org/10.1093/gji/ggu175, 2014.

Dagnino, D., Sallarès, V., Biescas, B., and Ranero, C.R.: Fine-scale thermohaline ocean structure retrieved with 2-D prestack full-waveform inversion of multichannel seismic data: Application to the Gulf of Cadiz (SW Iberia). J. Geophys. Res.-Oceans, 121, 5452-5469, http://doi.org/10.1002/2016JC011844, 2016.

Davy, R.G., Morgan, J.V., Minshull, T.A., Bayrakci, G, Bull, J.M., Klaeschen, D., Reston, T.J., Sawyer, D.S., Lymer, G., and Cresswell, D.: Resolving the fine-scale velocity structure of continental hyperextension at the Deep Galicia Margin using full-waveform inversion, Geophys. J. Int., 212, 244-263, https://doi.org/10.1093/gji/ggx415, 2018.

Deal, M.M. & Nolet, G.: Nullspace shuttles, Geophys. J. Int., 124, 372-380, https://doi.org/10.1111/j.1365-246x.1996.tb07027.x, 1996.

Dean, T., Lane D., Tulett, J., and Puckett, M.: Improving quality and safety through the use of a purposely designed truck-mounted Vibroseis for VSP surveys. ASEG-PESA 2013, https://doi.org/10.1071/ASEG2013ab071, 2013.

Delescluse, M., Nedimović M. R., and Louden, K. E.: 2D waveform tomography applied to long-streamer MCS data from the Scotian Slope, Geophysics, 76, 4, B151-B163, https://doi.org/10.1190/1.3587219, 2011.

Dijkstra, E.W.: A note on two problems in connection with graphs, Numer. Math., 1, 269-271, https://doi.org/10.1007/bf01386390, 1959.

Farra, V.: Bending method revisited: a Hamiltonian approach, Geophys. J. Int., 109, 138-150, https://doi.org/10.1111/j.1365-246x.1992.tb00084.x, 1992.

Farquharson, C. G. and Mosher, C. R. W.: Three-dimensional modelling of gravity data using finite differences, J. Appl. Geophys., 68, 417-422, https://doi.org/10.1016/j.jappgeo.2009.03.007, 2009.

Fichtner, A., Bunge, H.P. and Igel, H.: The adjoint method in seismology, I. Theory., Phys. Earth. Planet. In., 157, 86-104, https://doi.org/10.1016/j.pepi.2006.03.016, 2006.

Fichtner, A., Kennett, B.L.N., Bunge, H-P and Igel H.: Theoretical background for continental and global scale full-waveform inversion in the time-frequency domain, Geophy. J. Int., 175, 665-685, https://doi.org/10.1111/j.1365-246x.2008.03923.x, 2008.

Fichtner, A., Trampert, J., Cupillard, P., Saygin, E., Taymaz, T., Capdeville, Y. and Villaseñor A.: Multiscale full waveform inversion, Geophy. J. Int., 194, 534-556, https://doi.org/10.1093/gji/ggt118, 2013.

Gadallah, M., Fisher, R.: Exploration Geophysics, Springer, https://doi.org/10.1007/978-3-540-85160-8, 2009.

Gardner, G. H. F., Gardner, L. W., and Gregory, A. R.: Formation velocity and density-the diagnostic basics for stratigraphic traps, Geophysics, 39, 770-780, https://doi.org/10.1190/1.1440465, 1974.

Gary Mavko, Tapan Mukerji, Jack Dvorkin: The Rock Physics handbook, Cambridge University Press 1998.

Gauthier, O., Virieux, J. and Tarantola, A.: Two - dimensional nonlinear inversion of seismic waveforms: Numerical results, Geophysics, 51, 1387-1403, https://doi.org/10.1190/1.1442188, 1986.

Gazdag, J.: Wave equation migration with the phase-shift method, Geophysics, 43, 1342-1351, https://doi.org/10.1190/1.1440899, 1978.

Godfrey, N. J., Beaudoin, B. C., Klempererthe Mendocino Working Group USA, S. L., and Klemperer, S. L.: Ophiolitic basement to the Great Valley forearc basin, California, from seismic and gravity data: implications for crustal growth at the North American continental margin, Geol. Soc, Am. Bull. 109, 1536-1562, https://doi.org/10.1130/0016-7606(1997)109%3C1536:obttgv%3E2.3.co;2, 1997.

Gómez de la Peña, L., Gràcia, E., Muñoz, A., Acosta, J., Gómez-Ballesteros, M., Ranero, C.R., and Uchupi, E.: Geomorphology and Neogene tectonic evolution of the Palomares continental margin (western Mediterranean), Tectonophysics, 689, 25-39, http://doi.org/10.1016/j.tecto.2016.03.009, 2016.

Gómez de la Peña, L.: The origin and tectono-sedimentary structure of the Alboran Basin, Ph.D., University of Barcelona, Barcelona, 2017.

Gómez de la Peña, L., Ranero, C., and Gràcia, E.: The crustal domains of the Alboran Basin (Western Mediterranean), Tectonics, 37, 3352-3377, https://doi.org/10.1029/2017TC004946, 2018.

Gràcia, E., Bartolome, R., Lo Iacono, C., Moreno, X., Stich, D., Martínez-Díaz, J. J., et al.: Acoustic and seismic imaging of the Adra Fault (NE Alboran Sea): in search of the source of the 1910 Adra earthquake, Nat. Hazard Earth Sys., 12, 11, 3255-3267, http://doi.org/10.5194/nhess-12-3255-2012, 2012.

Gras, C., Sallarès, V., Dagnino, D., Jiménez, C. E., Meléndez, A., and Ranero, C. R.: Full waveform inversion of short-offset, band-limited seismic data inthe Alboran basin (SE Iberia), Solid Earth Discuss., https://doi.org/10.5194/se-2019-46, in press, 2019.

Grippo, L. & Lucidi, S.: A globally convergent version of the Polak-Ribiere conjugate gradient method, Math. Program., 78, 375-391, https://doi.org/10.1007/bf02614362, 1997.

Guasch, L. & Warner M.: Adaptative Waveform Inversion - FWI without Cycle-Skipping - Applications. In 76th EAGE conference & Exhibition 2014, WeE10614, https:/doi.org/10.3997/2214-4609.20141093, 2014.

Haldar, S. K., Mineral Exploration, Principles and Applications, Elsevier, https://doi.org/10.1016/C2011-0-05550-3, 201**3.**

Harding, A.J., Kent, G. M., Blackman, D. K., Singh, S. C. and Cannales, J.-P.: A new method for MCS refraction data analysis of the uppermost section at a Mid-Atlantic Ridge core complex, Eos Trans. AGU, 88, 52, Fall Meet. Suppl., Abstract S12A-03, 2007.

Harding, A. J., Arnulf, A. F., and Blackman, D. K.: Velocity structure near IODP Hole U1309D, Atlantis Massif, from waveform inversion of streamer data and borehole measurements. Geochem. Geophy. Geosy., 17, 6, 1990-2014, https://doi.org/10.1002/2016GC006312, 2016.

Henig, A. S., Blackman, D. K., Harding, A. J., Canales, J. P., and Kent, G. M.: Downward continued multichannel seismic refraction analysis of Atlantis massif oceanic core complex, 30N, mid-Atlantic ridge. Geochem. Geophy. Geosy., 13, Q0AG07, https://doi.org/10.1029/2012GC004059, 2012.

Henig, A.S.: Seismic structure of shallow lithosphere at locations of distinctive seafloor spreading, ProQuest Dissertations And Theses, Ph.D. Thesis, University of California, San Diego, Publication Number: AAT 3558093, ISBN: 9781303023583, Source: Dissertation Abstracts International, 74-08(E), Section: B., 141, 2013.

Hicks, G.J., and Pratt, R.G.: Reflection waveform inversion using local descent methods: Estimating attenuation and velocity over a gas-sand deposit, Geophysics, 66, 2, 598-612, 2001.

Hildebrand, JA.: Anthropogenic and natural sources of ambient noise in the ocean, Marine Ecology-progress Series - MAR ECOL-PROGR SER. 395. 5-20. 10.3354/meps08353, 2009.

Hobro, J.W.D., Singh, S.C., and Minshull, T.A.: Three-dimensional tomographic inversion of combined reflection and refraction seismic traveltime data, Geophys. J. Int., 152, 1, 79-93, https://doi.org/10.1046/j.1365-246X.2003.01822.x, 2003.

Jannane, M., Beydoun, W., Crase, E., Cao, D., Koren, Z., Landa, E., Mendes, M., Pica, A., Noble, M., Roeth, G., Singh, S., Snieder, R., Tarantola, A., Trezeguet, D., and Xie, M.: Wavelengths of earth structures that can be resolved from seismic reflection data, Geophysics, 54, 7, 906-910, https://doi.org/10.1190/1.1442719, 1989.

Jiménez Tejero, C., Dagnino, D., Sallarès, V., and Ranero, R.C.: Comparative study of objective functions to overcome noise and band-width limitations in full waveform inversion, Geophysical, J. Int., 203, 1, 632-645, http://doi.org/10.1093/gji/ggv288, 2015.

Julian, B.R. & Gubbins, D.: Three-dimensional seismic ray tracing, J. Geophys., 43, 95-113, 1977.

Kearey, P., Brooks, M., and Hill I., An Introduction to Geophysical Exploration, Blackwell Science, 2002.

Korenaga, J., Holbrook, W.S., Kent, G.M., Kelemen, P.B., Detrick, R.S., Larsen, H.-C., Hopper, J.R., and Dahl-Jensen, T.: Crustal structure of the southeast Greenland margin from joint refraction and reflection seismic tomography, J. Geophys. Res., 105, B9, 21591-21614, 2000.

Korenaga, J., Holbrook, W. S., Detrick, R. S., and Kelemen, P. B.: Gravity anomalies and crustal structure at the southeast Greenland margin, J. Geophys. Res., 106, B5, 8853-8870, https://doi.org/10.1029/2000jb900416, 2001.

Kormann, J., Cobo, P., Recuero, M., Biescas, B. and Sallarés, V.: Modelling seismic oceanography experiments by using first- and second-order complex frequency shifted perfectly matched layers, Acta Acust. Acust., 95, 1104-1111, https://doi.org/10.3813/AAA.918242, 2009.

Kormann, J., Rodríguez, J.E., Gutierrez, N., Ferrer, M., Rojas, O., de la Puente, J., Hanzich, M. and Cela, J.M.: Towars an automatic full-wave inversion: Synthetic study cases. The Leading Edge, Special Section: Full-waveform inversion Part I, 1047-1052, http://dx.doi.org/10.1190/tle35121047.1., 2016.

Lailly, P.: The seismic inverse problem as a sequence of before stack migrations: Conference on Inverse Scattering, Theory and Application, Society for Industrial and Applied Mathematics, in edited by J. Bednar R. and Weglein, 206-220, SIAM, Philadelphia, Penn, 1983.

Lambert, J.D.: Numerical Methods for Ordinary Differential Systems: The Initial Value Problem, John Wiley, N. Y., 1991.

Landro, M. and Amundsen, L.: Marine Seismic Sources Part I. GeoExPro, 7, 1, 2010.

Langhammer, J. 1994, Experimental studies of energy loss mechanisms in air-gun bubble dynamics, PhD thesis, Norges Tekniske Hoegskole.

Li, X. and Chouteau, M.: Three-dimensional gravity modelling in all space, Surv. Geophys., 19, 39-368, 1998.

Loke, M.H.: Electrical imaging surveys for environmental and engineering studies. A practical guide to 2D and 3D surveys, 2001.

Lowrie, W.: Fundamentals of Geophysics, Cambridge University Press, 1997.

Ludwing, W.J., Nafe, J. E., and Drake, C.L.: Seismic refraction, in The Sea, A.E. Maxwell (Editor), Wiley-Interscience, New York, 4, 53-84, 1970.

Luo, Y and Schuster, G.: Wave equation traveltime inversion, Geophysics, 56, 645-653, https://doi.org/10.1190/1.1443081, 1991.

Marfurt, K.: Accuracy of finite-difference and finite-elements modeling of the scalar and elastic wave equation, Geophysics, 49, 533-549, https://doi.org/10.1190/1.1441689, 1984.

Marjanovic, M., Plessix, R.-E., Stopin, A., and Singh, S.: Elastic versus acoustic 3-D Full Waveform Inversion at the East Pacific Rise 9º50'N, Geophys. J. Int., 216, 1497-1506, http://doi.org/10.1093/gji/ggy503, 2019.

Martin, G. S., Wiley, R. and Marfurt, K. J.: Marmousi2: An elastic upgrade for Marmousi, The Leading Edge, 25, 156-166, https://doi.org/10.1190/1.2172306, 2006.

Mavko, G., Mukerji, T., and Dvorkin, J.: The Rock Physics handbook Tools for seismic analysis of porous media, Cambridge University Press, Cambridge, 1998.

McMechan, G.A.: Determination of source parameters by wavefield extrapolation, Geophys. J. Roy. Astr. S., 71, 613-628, https://doi.org/10.1111/j.1365-246X.1982.tb02788.x, 1982.

McMechan, G.A.: Migration by extrapolation of time-dependent boundary values, Geophys. Prospect., 31, 413-420, https://doi.org/10.1111/j.1365-2478.1983.tb01060.x, 1983.

Meléndez, A., Sallarès, V., Ranero, C.R. & Kormann, J.: Origin of water layer multiple phases with anomalously high amplitude in near-seafloor wide-angle seismic recordings, Geophys. J. Int., 196, 243-252, https://doi.org/10.1093/gji/ggt391, 2013.

Meléndez, A.: Development of a new parallel code for 3-D joint refraction and reflection travel-time tomography of wide-angle seismic data, Ph.D., Institut de Ciències del Mar (ICM-CSIC)/University of Barcelona, Barcelona, 2014.

Meléndez, A., Korenaga, J., Sallarès, V., Miniussi, A., and Ranero, C.R.: TOMO3D: 3-D joint refraction and reflection traveltime tomography parallel code for active-source seismic data-synthetic test, Geophys. J. Int., 203, 158-174, http://doi.org/10.1093/gji/ggv292, 2015.

Métivier, L., Brossier, R., Mérigot, Q., Oudet, E., and Virieux, J.: Measuring the misfit between seismograms using an optimal transport distance: application to full waveform inversion, Geophys. J. Int., 205, 345-377, http://doi.org/10.1093/gji/ggw014, 2016.

Mo, L.: Datuming by wavefield extrapolation. Stanford Exploration Project, Report 75, 181-202: 1997.

Morgan, J., Warner, M., Bell, R., Ashley, J., Barnes, D., Little, R., Roele, K., and Jones, C.: Next-generation seismic experiments: wide-angle, multi-azimuth, three-dimensional, full-waveform inversion, Geophys. J. Int., 195, 1657-1678, http://doi.org/10.1093/gji/ggt345, 2013.

Morgan, J., Warner, M., Arnoux, G., Hooft, E., Toomey, D., Brandon, V., and Wilcock, W.: Next-generation seismic experiments-II: wide-angle, multi-azimuth, 3-D, full-waveform inversion of sparse field data, Geophys. J. Int., 204, 1342-1363, http://doi.org/10.1093/gji/ggv513, 2016.

Moser, T.J.: Shortest path calculation of seismic rays, Geophysics, 56, 1, 59-67, https://doi.org/10.1190/1.1442958, 1991.

Moser, T.J., Nolet, G., and Snieder, R.: Ray bending revisited, Bull. Seismol. Soc. Am, 82, 1, 259-288, 1992.

Moser, T.J., Nolet, G. & Snieder, R. (1992a). Ray bending revisited, Bull. Seismol. Soc. Am, 82, 259 – 288.

Mulder, W. A.: Rigorous redatuming, Geophys. J. Int., 161, 401-415, https://doi.org/10.1111/j.1365-246x.2005.02615.x, 2005.

Nabighian, M.N. and Corbett, J.D.: Electromagnetic methods in applied geophysics, 1, Theory, Society of Exploration Geophysicists, 1988.

Nakanishi, I. & Yamaguchi, K.: A numerical experiment on nonlinear image reconstruction from first-arrival times for two-dimensional island arc structure, J. Phys. Earth, 34, 195-201, https://doi.org/10.4294/jpe1952.34.195, 1986.

Neal, A.: Ground-penetrating radar and its use in sedimentology: principles, problems and progress, Earth-Sci. Rev., 66, 261-330, https://doi.org/10.1016/j.earscirev.2004.01.004, 2004.

Niebauer, T.M., Sasagawa, G.S., Faller, J.E., Hilt, R., and Klopping, F.: A new generation of absolute gravimeters, Metrologia, 32, 159-180, https://doi.org/10.1088/0026-1394/32/3/004, 1995.

Nocedal, J.: Updating quasi-Newton matrices with limited storage, Math. Comput., 35, 773-782, https://doi.org/10.1090/s0025-5718-1980-0572855-7, 1980.

Nocedal, J., and Stephen, J.W.: Numerical Optimization, American Mathematical Society, Springer, Providence, Rhode Island, USA, http://doi.org/10.1007/978-0-387-40065-5, 2006.

Nocedal, J., and Wright, S.J.: Numerical Optimization, Springer Verlag, 2006.

Onajite, E.: Seismic Data Analysis Techniques in Hydrocarbon Exploration, Elsevier, https://doi.org/10.1016/C2013-0-09969-0, 2014.

Paige, C.C., and Saunders, M.A.: LSQR: An algorithm for sparse linear equations and sparse least squares, ACM T. Math. Software, 8, 1, 43-71, http://doi.org/10.1145/355984.355989, 1982.

Papazachos, C. & Nolet, G.: P and S deep velocity structure of the Hellenic area obtained by robust nonlinear inversion of travel times, J. Geophys. Res., 102, 8349-8367, https://doi.org/10.1029/96jb03730, 1997.

Pereyra, V., Lee, W.H.K. & Keller, H.B.: Solving two-point seismic ray tracing problems in a heterogeneous medium. Part 1. A general adaptive finite difference method, Bull. Seismol. Soc. Am, 70, 79-99, 1980.

Pila, M. F., Schleicher, J., Novais, A. and Coimbra, T. A.: True-amplitude single-stack redatuming, J. Appl. Geophys., 105, 95-111, https://doi.org/10.1016/j.jappgeo.2014.03.010, 2014.

Prada, M.: The structure and formation of the Tyrrhenian basin in the Western Mediterranean back-arc setting, Ph.D., University of Barcelona, Barcelona, 2014.

Prada, M., Sallarès, V., Ranero, C.R., Vendrell, M.G., Grevemeyer, I., Zitellini, N., and de Franco, R.: The complex 3-D transition from continental crust to backarc magmatism and exhumed mantle in the Central Tyrrhenian basin, Geophys. J. Int., 203, 1, 63-78, https://doi.org/10.1093/gji/ggv271, 2015.

Pratt, R. G., Shin, C., and Hicks, G. J.: Gauss-Newton and full Newton methods in frequency-space seismic waveform inversions. Geophys. J. Int., 133, 341-362, https://doi.org/10.1046/j.1365-246x.1998.00498.x, 1998.

Pratt, R.G.: Seismic waveform inversion in the frequency domain, Part I: theory and verification in a physical scale model, Geophysics, 64, 3, 888-901, http://doi.org/10.1190/1.1444597, 1999.

Qin, Y., and Singh, S.C.: Detailed seismic velocity of the incoming subducting sediments in the 2004 great Sumatra earthquake rupture zone from full waveform inversion of long offset seismic data, American Geophysical Union, http://doi.org/10.1002/2016GL072175, 2017.

Qin, Y., and Singh, S.C.: Insight into frontal seismogenic zone in the Mentawai locked region from seismic full waveform inversion of ultra-long offset streamer data, American Geophysical Union, http://doi.org/10.1029/2018GC007787, 2018.

Sallarès, V., Meléndez, A., Prada, M., Ranero, C.R., McIntosh, K., and Grevemeyer, I.: Overriding plate structure of the Nicaragua convergent margin: Relationship to the seismogenic zone of the 1992 tsunami earthquake, Geochem. Geophys. Geosyst., 14, https://doi.org/10.1002/ggge.20214, 2013.

Saragiotis, C.D., Hadjileontiadis, L.J., and Panas, S.M.: PAI-S/K: A robust automatic seismic P phase arrival identification scheme, IEEE Transactions on Geoscience and Remote Sensing, 40, 6, 1395-1404, https://doi.org/10.1109/TGRS.2002.800438, 2002.

Schuster, G.T., and Zhou, M.: A theoretical overview of model-based and correlation-based redatuming methods, Geophysics, 71, 4, SI103-SI110, http://doi.org/10.1190/1.2208967, 2006.

Shah, N., Warner, M., Nangoo, T., Umpleby, A., Stekl, I., Morgan, J., and Guasch, L.: Quality assured full-waveform inversion: Ensuring starting model adequacy, SEG Annual Meeting, Las Vegas, Nevada, 4-9 November 2012, https://dx.doi.org/10.1190/segam2012-1228.1, 2012.

Shipp, R.M., and Singh, S.C.: Two-dimensional full wavefield inversion of wide-aperture marine seismic streamer data, Geophys. J. Int., 151, 325-344, https://doi.org/10.1046/j.1365-246X.2002.01645.x, 2002.

Shtivelman, V., and Caning, A.: Datum correction by wave-equation extrapolation, Geophysics, 53, 10, 1311–1322, https://doi.org/10.1190/1.1442409, 1988.

Sirgue, L., and Pratt, R.G.: Efficient waveform inversion and imaging: a strategy for selecting temporal frequencies, Geophysics, 69, 1, 231-248, http://doi.org/10.1190/1.1649391, 2004.

Tarantola, A: Inversion of seismic reflection data in the acoustic approximation, Geophysics, 49, 8, 1259-1266, http://doi.org/10.1190/1.1441754, 1984.

Tarantola, A.: Inverse problem theory: Methods for data fitting and model parameter estimation, Elsevier Science Publ. Co., Inc, New York, 1987.

Tarantola, A.: Inverse Problem Theory and Methods for Model Parameter Estimation. SIAM, 2004.

Tegtmeier, S., Gisolf, A. and Verschuur, D. J.: A data-mapping approach to 3-D wavefield redatuming. Geophys. J. Int., 172, 759-769, https://doi.org/10.1111/j.1365-246x.2007.03675.x, 2008.

Telford, W. M., Geldart, L. P., and Sheriff R. E., Applied Geophysics, Cambridge University Press, 2004.

Toomey, D.R., Solomon, S.C., and Purdy, G.M.: Tomographic imaging of the shallow crustal structure of the East Pacific Rise at 9º30'N, J. Geophys. Res., 99, 24135-24157, https://doi.org/10.1029/94JB01942, 1994.

Van Avendonk, H.J.A., Harding, A.J., Orcutt, J.A. & McClain, J.S.: A two-dimensional tomographic study of the Clipperton transform fault, J. Geophys. Res., 103, 17885-17899, https://doi.org/10.1029/98jb00904, 1998.

Van Avendonk, H.J.A., Harding A.J., Orcutt, J.A. & Holbrook, W.S.: Hybrid shortest path and ray bending method for traveltime and raypath calculations, Geophysics, 66, 2, 648-653, https://doi.org/10.1190/1.1444955, 2001.

Vasconcelos, I., van Manen, D.-J., Ravasi, M., Wapenaar, K. and van der Neut, J.: Marchenko redatuming: advantages and limitations in complex media, Workshop W-11, 84th Annual Meeting, SEG, Expanded Abstracts, 2014.

Vidale, J.E.: Finite-difference calculation of travel times, Bull. Seismol. Soc. Am, 78, 2062-2076, 1988.

Vigh, D., Starr, E.W., and Kapoor, J.: Developing Earth model with full waveform inversion. The Leading Edge, 28, 432-435, 2009.

Virieux, J.: P-SV wave propagation in heterogeneous media: Velocity-stress finite-difference method, Geophysics, 51, 4, 889-901, http://doi.org/10.1190/1.1442147, 1986.

Virieux, J., and Operto, S.: An overview of full – waveform inversion in exploration geophysics, Geophysics, 74, 6, WCC1 – WCC26, http://doi.org/10.1190/1.3238367, 2009.

Vrolijk, J.-W., Haffinger, P., and Verschuur, E.: Multi-datum based estimation of near-surface full-waveform redatuming operators, J. Appl. Geophys., 82, 1, 30-45, http://doi.org/10.1016/j.jappgeo.2012.02.004, 2012.

Wapenaar, K., Thorbecke, J., van der Neut, J., Broggini, F., Slob, E. and Snieder, R.: Green's function retrieval from reflection data, in absence of a receiver at the virtual source position, J. Acoust. Soc. Am., 135, 2847-2861, https://doi.org/10.1121/1.4869083, 2014.

Warner, M., Ratcliffe, A., Nangoo, T., Morgan, J., Umpleby, A., Shah, N., Vinje, V., Stekl, I., Guasch, Ll., Win, C., Conroy, G., and Bertrand, A.: Anisotropic 3D full-waveform inversion, Geophysics, 78, 2, R59–R80, https://doi.org/10.1190/geo2012-0338.1, 2013.

Wapenaar, K., Thorbecke, J., van der Neut, J., Broggini, F., Slob, E., and Snieder, R.: Marchenko imaging, Geophysics, 79, 3, WA39-WA57, http://doi.org/10.1190/GEO2013-0302.1, 2014.

Wapenaar, K. and Thorbecke, J.: Review paper: Virtual sources and their responses, Part I: time-reversal acoustics and seismic interferometry, Geophys. Prospect. EAGE, 1-19, httpd://doi.org/10.1111/1365-2478.12496, 2017.

Warner, M., Ratcliffe, A., Nangoo, T., Morgan, J., Umpleby, A., Shah, N., Vinje, V., Stekl, I., Guasch, Ll., Win, C., Conroy, G., and Bertrand, A.: Anisotropic 3D full-waveform inversion, Geophysics, 78, 2, R59–R80, https://doi.org/10.1190/geo2012-0338.1, 2013.

Xu, S., Yashchuk, V. V., Donaldson, M.H., Rochester, S.M., Budker, D., and Pines, A.: Magnetic resonance imaging with an optical atomic magnetometer, PNAS, 103, 34, 12668-12671, https://doi.org/10.1073 pnas.0605396103, 2006.

Xu, W. and Chen, S.: A case study of forward calculations of the gravity anomaly by spectral method for a three-dimensional parameterised fault model. Computers and Geosciences, 111, 67-77, https://doi.org/10.1016/j.cageo.2017.11.001, 2018.

Yang, K., Liu, Y-Z, Geng, J-H and Ma, Z-T: Upward continuation with topographic datuming operator: the integrated wave equation datuming scheme revised, Geophys. Prospect., 57, 943-956, https://doi.org/10.1111/j.1365-2478.2009.00790.x, 2009.

Zelt, C.A., and Smith, R. B.: Seismic traveltime inversion for 2-D crustal velocity structure, Geophys. J. Int., 108, 1, 16-34, https://doi.org/10.1111/j.1365-246X.1992.tb00836.x, 1992.

Zhang, J. & Toksöz, M.N.: Nonlinear refraction travel time tomography, Geophysics, 63, 1726-1737, https://doi.org/10.1029/98jb01981, 1998.

Zhang, J., ten Brink, U.S. & Toksöz, M.N.: Nonlinear refraction and reflection travel time tomography, J. Geophys. Res., 103, 29743-29757, https://doi.org/10.1029/98jb01981, 1998.

Zhang, W., and Shen, Y.: Unsplit complex frequency-shifted PML implementation using auxiliary differential equations for seismic wave modeling, Geophysics, 75, 4, T141-T154, http://doi.org/10.1190/1.3463431, 2010.

List of acronyms

Barcelona-CSI: Barcelona Center for Subsurface Imaging

BVM: boundary value migration

CDP: common depth point

CC: cross-correlation-based

CCTT: cross-correlation travel time

CFS-PML: complex-frequency-shifted perfectly matched layers

CMP: common midpoint

CPU: central processing unit

CSIC: Consell Superior d'Investigacions Científiques

CST: constant separation traversing

DC: downward continuation

DWS: derivative weight sum

ρ: density

EM: electromagnetic

FD: finite difference

FS: forward star

FWI: full-waveform inversion

GPR: ground-penetrating radar

GPS: global positioning system

IP: induced polarization

L-waves: surface waves

l-BFGS: limited-memory Broyden - Flecher - Goldfarb - Shanno

LSQR: least square root

MCS: multichannel seismic

NIM: non-integration method

NLCG: non-linear conjugate gradients

OBC: ocean bottom cables

OBH: ocean bottom hydrophones

OBN: ocean bottom nodes

OBS: ocean bottom seismometer

P-waves: primary, compressional or longitudinal -waves

RK: Runge-Kutta

PML: perfectly matched layer

PSDM: pre-stack depth migration

RMS: root mean square

S-waves: secondary, transverse or shear -waves

SD: steepest descent

SH-wave: horizontal shear -wave

SNR: signal-to-noise ratio

SP: self-potential or spontaneous polarization

SV-wave: vertical shear -wave

TMI: time-migrated image

TOB: top of the basement

TTT: travel-time tomography

TWT: two-way travel-time

UTM: Unitat Tecnològica Marina

VES: vertical electrical sounding

Vp: velocity (P-wave)

Vs: velocity (S-wave)

WAS: wide-angle seismics

WED: wave equation datuming